Metallurgical Design of New Nanoporous Structures

Daria Barsuk

THÈSE

Pour obtenir le grade de

DOCTEUR DE LA COMMUNAUTE UNIVERSITE GRENOBLE ALPES

Spécialité : 2MGE : Matériaux, Mécanique, Génie civil, Electrochimie

Arrêté ministériel : 25 mai 2016

Présentée par

Daria BARSUK

Thèse dirigée par **Yannick CHAMPION**, Directeur du SIMAP, CNRS, et
codirigée par **Alberto MOREIRA JORGE JR**, Professeur de l'Université Federal de São Carlos

préparée au sein du **Laboratoire Science et Ingénierie des Matériaux et Procédés** dans **l'École Doctorale I-MEP2 – Ingénierie – Matériaux, Mécanique, Environnement, Energétique, Procédés, Production**

Conception Métallurgique de Nouvelles Structures Nanoporeuse

Metallurgical Design of New Nanoporous Structures

Thèse soutenue publiquement le **19 octobre 2017**
devant le jury composé de :

Monsieur Livio BATTEZZATI
Professeur de l'Università degli Studi di Torino (UNITO), Rapporteur

Madame Dominique POQUILLON
Professeur de l'École nationale supérieure des ingénieurs en arts chimiques et technologiques (ENSIACET), Rapporteur

Monsieur Yannick CHAMPION
Directeur de Recherche, CNRS, Université Grenoble Alpes (UGA), Directeur de thèse

Monsieur Alberto MOREIRA JORGE JR
Professeur de l'Université Fédéral de São Carlos (DEMa/UFSCar), Co-Directeur de thèse

Monsieur Marian CHATENET
Professeur de l'Université Grenoble Alpes (LEMPI/UGA), Président

Monsieur Frédéric THIBAULT-STARZYK
Directeur de Recherche, CNRS, Maison Française d'Oxford, Examinateur

SIGILLUM UNIVERSITATIS GRATIANOPOLITANAE
VERI TAS
LIBE RABIT
1339

Acknowledgements

First of all I would like to thank all the jury members who came to Grenoble, sometimes from remoted places and made my Doctorate degree possible. I thank Marian Chatenet from LEPMI-UGA for taking a role of a president of the jury and assure the whole process go smoothly. I am grateful for Livio Battezzati from UNITO and Dominique Poquillon from INP-ENCIASET to accept their roles as reviewers of my work, for their consistent remarks and overall positive reviews that kept my spirit up. I thank Frédéric Thibault-Starzyk from Maison Française d'Oxford for accepting the invitation to be a member of the jury and bringing interesting discussions and suggestions regarding the functionality of the target materials. I also thank my thesis supervisor Yannick Champion and co-supervisor Alberto Moreira Jeorge Jr for their dedication and great support during all stages of the preparation of my Ph.D. and for constituting a very competent jury for the defense.

There have been a number of people with whom these three years of thesis brought me together. But before mentioning further any names I would like to express my gratitude to those who participated in the preparation of my scientific fundament and sculpturing out of me the person that I became. On the first place it will certainly be my dear family, my parents. On their own example they demonstrated the allurement of exact sciences and accompanied me along this uneasy road with patience.

I am also thankful to my good friends from the faraway Moscow University and Obninsk Lyceum for their presence in my life even though you are far.

Eventually, I would like to thank all the teachers and professors that I had before entering this Ph.D. for their inspiring classes, commitment and rigorism.

Speaking more specifically about the last three years in SIMaP laboratory, I will certainly evoke the name of the late Professor Alain Reza Yavari, thanks to whom my Ph.D. became possible just as our whole research project VitriMetTech. His personality attracted people just as bright that is why I was lucky to share my everyday life with Nikos, Kostas, Min, and Alberto. I am thankful to you not only for professional advices and practical help, but for amity and hearty reception to your team. The sad event of two years ago reversed the course of things for many people. But not on any account can I regret finding Yannick Champion and Alberto Moreira to be my supervisors for the last two years of thesis. It was pleasant and interesting working with you, you subtly directed me to the true path and didn’t let me dissipate at the same time leaving me enough space for creativity.

Alberto, I would like to thank you separately for participating in this period of my life from the very beginning to the finish point and making friendship and supervision coexist.

I am also saying “merci” to all the residents of SIMaP: administrative personal, Sylvie for her positive attention and funny “ahchoo!”, Pascale for allowing us doing some more or less allowable things, and certainly Fabienne for your mothering care and participation, especially outside professional life.

I am thankful to the technical team of SIMaP for their efficiency, responsiveness and for their million dollar hands. I am especially grateful to Laurent for not letting me drawn in my dear HF, even though it caused some complicated paperwork. Stephane, thank you for being the way that you are. The day I heard your stupid gross songs in the corridor I knew everything was going to be fine.

I cannot forget to mention out sos-IT team, who was always coming to the rescue. Thank you Yannick for mixing with us and showing on your example that staying ever-young is easy.

Also I would like to thank all the researches and engineers of SIMaP, CMTC and Lepmi. Thierry Encinas, Stephane Coindeau, Frederic Charlot, we have spent a lot of time with you trying to make XRD and SEM work for the sake of research. I am thankful to Pierre Lhuissier, Jean-Marc Chaix for your time that you found for discussions and advices regarding the image treatment and tomography aspects, Gilles Renou for what concerns the production of TEM results and explanations, Alex Crisci for your positive Raman séances. People from two floors above who participates enormously in the production of valuable electrochemical results: Anicet Zadick, Guilaume Braesch under a wise supervision of Marian Chatenet, Vincent Martin for the active BET exploitation, and, finally Funny for some soft impedance theory and magnificent time in Brazil.

I thank all Ph.D. students from Grenoble and particularly from TOP group of SIMaP for the great time spent during polishing, barbeques, seminars, ski-weekends, pub-quizzes. Even though we are not a big community compared to many others, everybody knows that it is the quality that matters and I was very lucky to find friends among you.

I am very grateful to the VitriMetTech ITN MSCA community for the opportunities provided by this project, for the exceptional workshops and training we had in every part of the world, for discussions with brilliant scientists of our field, for all the conferences that we attended and for many more. Now that our ITN is over I will try to use wisely the acquired knowledges and continue promoting the MSCA spirit in the next MSCA program.

I would like to enclose these few pages by addressing one very important person, who was there for me from the very beginning and till I hope another 80 years. Even when separated, I always knew I have your shoulder. You comforted me when it was rough and you gave me confidence when I was lost. Our doctorates in two different cities were our challenges and I am proud of how we accomplished it. Now I know it is a beginning for another wonderful journey with you. Alexandre (and Rusty the Cat).

CONTENTS

LIST OF FIGURES

TABLE OF ACRONYMS AND ABBREVIATIONS

AB: Ammonia-Borane

AST: Acceleration Stress Test

BET (theory of): Brunauer, Emmett and Teller

BJH (theory of): Barrett, Joyner and Halenda

BMG: Bulk Metallic Glass

BSE: Backscattered Electrons

CCVIM: Cold-Crucible Vacuum Induction Melting

CE: Counter Electrode

CV - Crystal Violet

DABHFC: Direct Ammonia-Borane Half-Fuel Cell

DARPA: Defense Advanced Research Projects Agency

DMA: Dynamic Mechanical Analysis

DSC: Differential Scanning Calorimetry

EBSD: Electron Backscatter Diffraction

EDX/EDS: Energy Dispersive X-ray Spectroscopy

FEG-SEM: Field Emission Gun Scanning Electron Microscopy

FIB: Focused Ion Beam

FT: Fischer-Tropsch (synthesis)

H-W: Halder-Wagner (method)

ISD: Interface Shape Distribution

IUPAC: International Union of Pure and Applied Chemistry

LIB: Lithium-Ion Battery

LMD: Liquid Metal Dealloying

LN: less Noble (element)

MN: More Noble (element)

NBD: NanoBeam Diffraction (mode)

NPCo: Nanoporous Cobalt

NPCu: Nanoporous Copper

NPG: Nanoporous Gold

NPM: Nanoporous Metals

NPS: Nanoporous Silver

PGM: Platinum Group Metals

PSD: Pore Size Distribution

QSt: Quasistatic (mode)

R6G: Rhodamine 6 G

RE: Reference Electrode

RHE: Reversible Hydrogen Electrode

SAEDP: Selected Area Electron Diffraction Pattern

SDD: Silicon Drift Detector

SE: Secondary Electrons

SEM: Scanning Electron Microscopy

SERS: Surface-Enhanced Raman Spectroscopy

SHE: Standard Hydrogen Electrode

SPM: Scanning Probe Microscopy

TEM: Transmission Electron Microscopy

VAM: Vacuum Arc-Melting

WE: Working Electrode

W-H: Williamson-Hall (method)

XRD: X-ray Diffraction Spectroscopy

GENERAL INTRODUCTION

With the increase in world energy demand, together with environmental concerns, a boost in the research and innovation of new technological developments for alternative “clean-energy" solutions have been observed during the past several decades and still stays one of the hottest topics in the contemporary research. Much engineering efforts are needed to reduce energy consumption by improving the efficiency of the various components of the power system. The continuous pursuit of higher energy/lower cost/compact geometry technological solutions and the rapid progress in microelectronic devices just maintains the motivation for further advances.

Thanks to their extremely high surface area and low cost of the substrate, carbon-supported metallic particles have been commonly used as principle catalytic composites on electrodes for direct oxidation in liquid fuel cells. Recently, the viability of this type of catalyst was questioned due to its extreme instability and fast degradation in alkaline fuel cells – one of the most efficient categories of liquid fuel cells, producing potable water, heat, and electricity. In view of this finding, nanoporous metallic systems have been suggested as an alternative to the Pt/C type catalysts and other composites, since they demonstrated a good integrity of the structure and competitive performance in devices based on electrochemical functioning.

In addition to the above application featured in the present study, entirely or partially nanostructured nanoporous metallic materials are also favorable for utilization in the biomedical field to enhance biological interactions, to improve bactericidal properties of the medical parts or adjust their weight and strength according to specific needs. Their unique optical properties drive up the demand for the nanoarchitectured metals design for biosensors and detecting devices.

Given the above, it becomes apparent that studies focused on finding new nanoporous metallic materials with a desirable architecture, competitive physicochemical functionality, simple manufacturing ability, and economic viability are still a subject of the modern field of materials research.

Dealloying, or simply corrosion, historically has always been considered as an unwanted destructive process of metals and alloys. However, recent technological advances have adapted it to serve scientific purposes, notably to create porous metallic scaffolds by intentional selective leaching of (mostly common) less noble elements, sometimes, even avoiding the chemically aggressive media.

In present work, dealloying was also chosen as the primary tool for the synthesis of nanoporous metals, thanks to its overall simplicity compared to other alternative methods.

Three main systems, namely, nanoporous copper, silver, and cobalt were obtained as a result of dealloying in carefully selected conditions to compose the body of present research. These systems have been favored thanks to their relatively low cost, outstanding catalytic, optical and bactericidal properties and abundance of constituent raw materials.

The manuscript is composed of four chapters:

In Chapter I the reader will be introduced to the context of the study and will find comprehensive literature data, covering the subject of nanoporous metals. This bibliographic revision chapter will touch upon the methods of NPMs fabrication, focusing on the theory and practice of dealloying, microstructure formation and the role of precursors in the dealloying. Further will be outlined the existing approaches for the evaluation of their mechanical properties and peculiarities related to the nanoscale nature of materials. Finally, the motivation for the study of the selected systems and the range of their potential applications will be given at the end of this chapter.

A detailed protocol of the used experimental techniques for the fabrication, characterization, and test of target applications of the NPMs aimed for electrocatalysis and Surface-enhanced Raman spectroscopy (SERS) is described in Chapter II.

All main results supported by discussions are presented in the third key-chapter. This chapter is divided into four subsections, which go along with the concepts inserted in Chapter II. Such subsections are focused on the synthesis of NPMs, results of their microstructural, numerical and mechanical characterization, and, finally, completed by the accomplishment of practical tests in SERS and half-cell electrochemistry, and interpretation of obtained results.

The present work is enclosed by the fourth and last Chapter, which summarizes the achieved targets, the main adapted approaches and encountered drawbacks. It compiles all the significant findings, particularly, fabrication of novel nanoporous substrates by acidic or pure water dealloying (the latest being particularly attractive in the scope of “clean” production of constitutive technological components), an unprecedented demonstration of their potential in the field of chemical energy conversion and strong points for SERS-based technologies.

CHAPTER I. LITERATURE REVIEW ON NANOPOROUS METALLIC MATERIALS

I.1. Introduction

Nanoporous metals (NPM), or nanoporous metallic foams, represent a wide class of porous materials. In dimensions of macro scale, one can easily imagine a foam taking examples from everyday life: dishwashing sponge, various shock absorbing materials, water filters, etc. Some of them possess an impressive mechanical rigidity: one may think of the Eiffel Tower and how carefully is positioned every single detail in its construction to keep the monument's integrity for years. If one decides to calculate its density, it will give ≈ 9,24 x 10^{-3} g.cm^{-3}.[1] It is peculiar that Eiffel's tower relative density (ρ/ρ_0, density ρ as mass per unit volume of the structure divided by the density ρ_0 of a material of which it is made) is close to those of modern superlight aerogels and microlattice cellular materials. One of them (Figure I.1), with a density (ρ) smaller than 10 mg.cm^{-3}, was initially developed for the Defense Advanced Research Projects Agency (DARPA) and could be used as battery electrodes, catalyst supports, and acoustic, vibration or shock energy damping.[2]

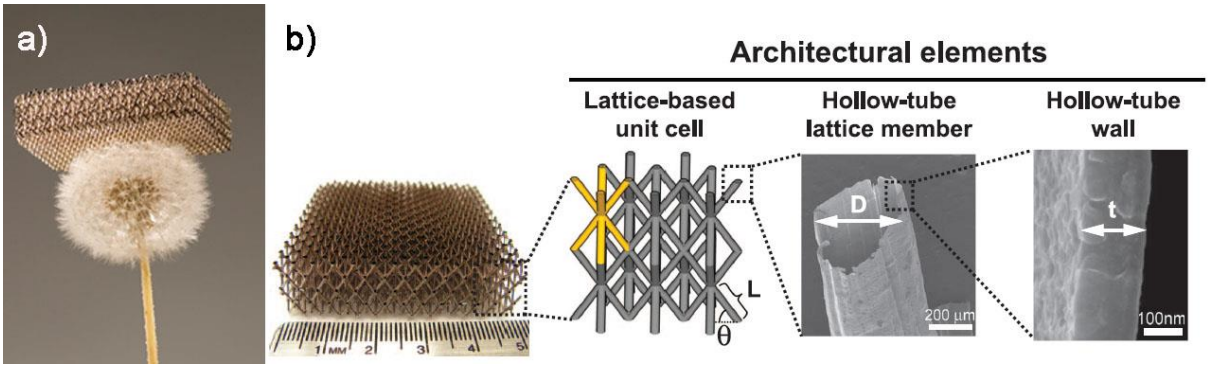

Figure I.1. a) Photo of the light microcellular material on the blowball by Dan Little © HRL Laboratories, LLC b) Images of as-fabricated microlattices along with a breakdown of the relevant architectural elements. Adapted from [2].

A common set of properties correlates these objects [3]: 1) Low density, due to the important volume fraction of voids distributed within the material 2) High surface area 3) High strength of the entire structure 4) Others functional properties (optical, magnetic) more or less pronounced in different structure-forming materials. For instance, high electrical conductivity and electrochemical activity for metals, effective impact energy absorption ability and shape adaptation for polymers, thermal resistance and biocompatibility for ceramics and metals; alternatively a combination of all of them for obtaining the required set of properties that cannot be provided by a single class of material.

Now, going down from the macroscale dimensions to sub-micron and nanoscale dimensions will approach us to the concept of nanoporous materials.

Nanoporous metallic foams can be envisioned as a 3-dimensional network of interconnected metallic wires (or so-called ligaments) surrounded by hollow spaces (pores). All together, they define a representative unit of such porous system – a unit cell. Figure I.2 presents the nomenclature of such model open-cell nanoporous metallic network/foam, illustrating the common constituent elements.

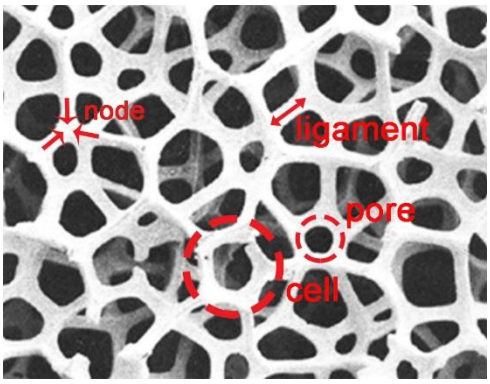

Figure I.2. A schematic illustration and nomenclature of NP metallic structure.

From the definition adopted by the International Union of Pure and Applied Chemistry (IUPAC)[4], porous materials hierarchy is the following: microporous (pore size < 2 nm), mesoporous (2 nm < pore size < 50 nm) and macroporous (pore size > 50 nm). However, due to practical reasons, it is generally accepted that NPMs are those with the characteristic length scale ≤ 100 nm. Further, in the experimental results section, it will be shown that, depending on the chosen method for geometric measurements of the structure, the constituents' values of NPM can span across multiple length scales.

In nanoscience, it is common knowledge that an assembly constituted of building blocks, which have at least one dimension with sizes in the range of 1–100 nm can exhibit very different properties in comparison to their bulk counterparts.[5] The fact is that the effects of quantum confinement on electrical, thermal, and optical properties become important at about this scale.[6] The fact that the structural organization of NPM lays in nanometer range defines physicochemical properties of the materials. Metallic foams that have a length scale of several microns to more than 1 cm are usually limited to use in damping and acoustic materials. As the material constituents undergo the transition from macro to nanoscale, the total surface area increases drastically, so does the ratio S_{tot}/V_{tot}, leading to the growth of the impact of surface processes to the system behavior, such as, but not limited to, the critical adsorption and specific catalytic activity highly pronounced for nanoporous metals [7]. Here, the focus is given to dealloyed nanoporous metals mainly due to their wide range of applications (fuel cells, catalysis, sensors, actuators, etc.) and because of their unique properties (catalytic, electrocatalytic, mechanical, sensing, optical, etc.).

I.2. Fabrication of NPM

When it concerns nanoporous metallic objects, such characteristics as compositional homogeneity, uniform or complex distribution of final structural parts, or simply atomistic characteristics of the metal can indicate the further route of scaffold synthesis. Generally speaking, smart design and fabrication of NPMs have been a manufacturing challenge over at least the last two decades.

The intended synthesis of porous metallic foams goes back to 1926 to the American engineer Murray Raney, who patented a fabrication of fine nickel catalyst for hydrogenation of oils which has become one of the most important industrial catalysts [8]. Back then, he used dealloying as the principle fabrication means, which will be properly introduced later.

By today the list of available methods to produce NPMs is rather rich: hydrothermal synthesis, catalytic chemical deposition, surface-mediated synthesis, laser-etching, powder sintering, electrophoretic deposition, lithography, and others.

Some of the methods are worth being described in more details due to the role that they play in current field of materials synthesis.

I.2.1. Template method

Template synthesis is an effective method of fabrication of NPMs. It is widely used when the precise control over the final structure/particle architecture, morphology, and size is crucial [9], although it must be kept in mind that this method is mold-destructive (sacrificial). The principle of the template method for porous systems fabrication is easily understood in the following example: one defines a configuration of the mold with the desirable architecture of vicinities. Next step is to fill the mold with a target alloy (for metallic NPMs), which will then solidify. Lastly, the initial solid template has to be removed by dissolution or other appropriate means, leaving a self-standing porous material.

Depending on the template's material, this method is subdivided into hard (for example, porous structure of anodic aluminum oxide template for fabrication of noble metals nanorods [10,11]), soft (with high polymer, surfactant being an easy removable soft template),[12] and multiplate method, combining both above-mentioned types of templates in the simultaneous process of NP materials fabrication. For instance, as well-known in its field group of a laboratory of the University of New-Mexico, headed by Plamen Atanassov, designing of industrial nanocatalysts for fuel cells makes use of dispersed silica particles as a sacrificial template. After metal deposition on silica particles, they are dissolved in KOH, leaving the convex porous structure [13].

Even though template method can provide high precision and reproducibility, the separation process of the matrix from the synthesized product can be damaging for the last. In addition, limited number of template materials for the hard template method and their stability restrict its use [12]. In contrast with others, template method applied in metals can accurately adjust pore sizes, their distribution, and morphology. However, its modulation flexibility is almost impossible, while dealloying allows structure adjustment through its parameters control [14].

I.2.2. Dealloying (chemical/electrochemical/liquid metal)

Dealloying certainly finds its place among the top most conventional methods for the preparation of nanoporous metals.

Dealloying will play a major role in present work. As it is the main way for producing nanoporous systems from bulk metallic precursors, it will require some more careful description in this chapter.

In a very general way, a selective dissolution of an element out of an alloy describes dealloying (or preferential corrosion), therefore, classifying itself as a destructive synthesis [15]. In a given binary alloy, dealloying will occur as a result of the removal of one of the elements, preserving a desirable one when placing the alloy in an appropriate etching bath solution. Figure I.3 shows a schematic illustration of the dealloying of a binary model alloy. Figure I.4 contains examples of the typical top and cross-sectional morphologies of resultant NPMs. Dealloying can also be applied to ternary and multicomponent alloys, where a range of elements are removed, and the rest is reorganized in a way to form a stable porous matrix.

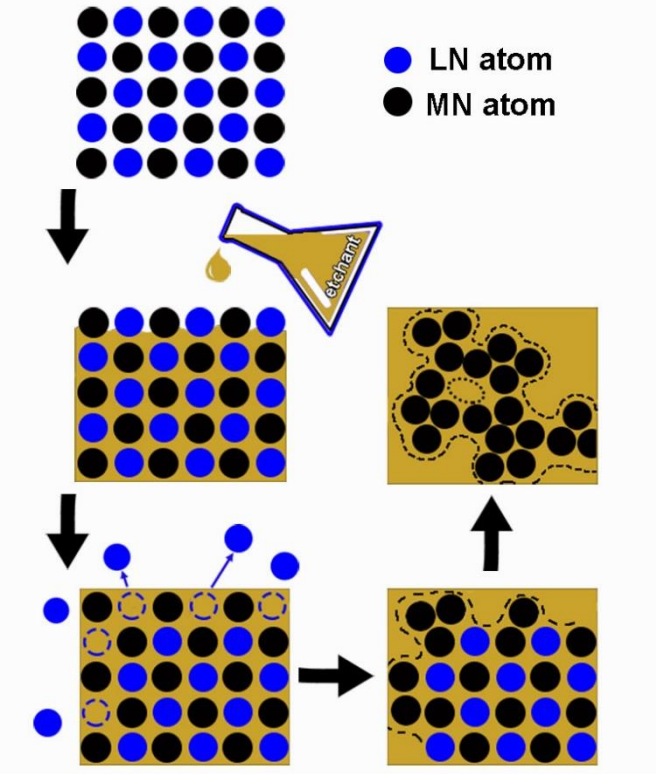

Figure I.3. Illustration of dealloying in homogeneous single phase binary alloy, LN – less noble, MN – more noble atoms.

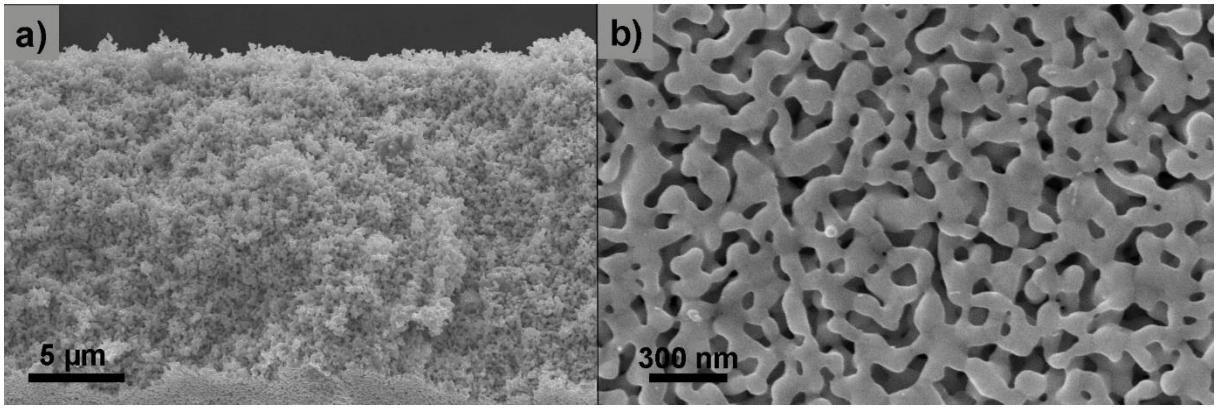

Figure I.4. Typical cross-section (a) and top view (b) of dealloyed metallic sample.

Dealloying can be split into two types: electrochemical and free corrosion, depending on whether a voltage is applied.

In electrochemical dealloying (also referred to as potentiostatic method), a constant electric potential is used to selectively electro-oxidize the more active alloy component [16].

The issue with electrochemical dealloying is that there is a limited amount of alloys with a sufficiently large difference in reduction potential enabling porosity formation [15]. Even though dissolution with a prescribed potential offers higher control over pore morphology, there are instances where the use of electric current is not practical. In such cases, free corrosion is preferred. For example, micro-patterns that are not electrically connected cannot be dealloyed in this manner and are usually immersed directly in the acid [17]. Commercially available white gold leaves (Au/Ag alloy with a 1:1 weight ratio) are generally dealloyed without applying a potential [18].

In addition, observations showed that, in the case of nanoporous gold (NPG), free corrosion results in a lower density of crystal defects in the NP structure comparing to those obtained electrochemically. It was suggested that the application of a potential provokes more intensive pattern formation, resulting in residual stresses and plastic deformation while dealloying [19].

Recently, a new type of dealloying, the Liquid Metal Dealloying (LMD), emerged in the field of NPM synthesis. The peculiarity of this method is that, a liquid metal is used instead of an acid bath as conduit for the selective dissolution of one element of a multicomponent alloy. The process is based on the negative enthalpy of mixing H_{mix} of the liquid metallic "etchant" with the target metal atoms of the alloy and positive H_{mix} with the sacrificial atoms. One of the related examples is a synthesis of porous α-Ti from a binary Cu-Ti alloy in magnesium melt. When the Cu–Ti binary alloy solid precursor contacts the Mg liquid, Cu atoms selectively dissolve into the melt while the mutual repulsing of the remaining Ti atoms and the melt results in a nanoporous structure [15,20].

Delving into details, there exist a number of empirical rules for dealloying to occur that will be introduced in the following example for a binary alloy, which is extendable for more complex systems:

1) First of all, the two elements of a binary alloy must have sufficiently different equilibrium potentials $\Delta\varphi$, allowing the electrochemically active one (less noble element - LN) to dissolve

away, while the other (more noble element - MN) remains intact [10]. This principle works for the majority of the cases. However, a minor dissolution of the nobler element is also possible during dealloying [21].

2) Another important process is surface diffusivity D_s of MN element, which among others defines the speed of the porous structure formation and its timescale. It is highly important for the remaining nobler atoms to possess sufficient mobility for reorganization within the dealloying time to a stable self-standing porous form. Following a coarsening mechanism of the ligaments, D_s of adatoms along the solid/solution interface can be quantitatively estimated by the equation [22,23]:

$$D_s = \frac{[d(t)]^4 kT}{32\gamma t a^4},$$

Where $\boldsymbol{\gamma}$ is the surface energy of an alloy, $\boldsymbol{a}$ is the lattice parameter, $\boldsymbol{d(t)}$ is the ligament size at a time $\boldsymbol{t}$, $\boldsymbol{k}$ is the Boltzmann constant (1.38 x 10^{-23} $J.K^{-1}$), $\boldsymbol{T}$ is the dealloying temperature. In this way, one calculated D_s as being within the range of the order of 10^{-11} to 10^{-19} $cm^2.s^{-1}$ for some noble metals.

3) The compositional balance between LN and MN elements (often called parting limit) defines a threshold when the dissolution becomes possible [24].
4) The dissolution rate of LN element, as well as surface diffusivity, affects the speed of nanoporous pattern formation and, in its turn, depends on the activity of the LN element and etching solution parameters (temperature, time, concentration, pressure) [25,26].
5) Capillary process, related to the mass transport through the bulk of the alloy and electrolyte [27].

As a method for materials fabrication, dealloying will play the primary role in this work. Hence, by default, a meticulous attention will be given in further sections of this chapter on the systems obtained by this means.

I.3. Pores and ligaments formation

Since the second part of the 20th-century scientists try to reveal the complex mechanism of dealloying and the consequent porosity formation. Numerous mathematical theories, supported by computer modeling and practical experiments were developed to bring together pieces of the puzzle to approach the real picture of the phenomena.

Among all nanoporous metals, nanoporous gold (NPG) attracted particular attention of researchers being a highly adaptable system for the fundamental study of a wide range of mechanical and surficial properties [17]. At present, the amount of works on NPG has reached a four-digit number.

Most remarkable contribution in advancing of understanding the processes has been made by Forty et al. [28] followed by Erlebacher et al [27]. They were one of the first to look into the intrinsic process of porosity formation upon dealloying on the example of a model Ag-Au binary alloy, which is due to the similar lattice of the fcc structure of Ag and Au and to the distinct electrochemical properties of both elements [29].

In his corrosion disordering/diffusion reordering model, Forty [28] demonstrated the importance of surface diffusion of gold in the corrosion process by dealloying $Au_{50}Ag_{50}$ alloy in 50 % Nitric acid

solution. With the dissolution of surface silver atoms, the residual gold atoms reorganized into gold-rich islands, gradually exposing fresh silver atoms to the etching environment. The schematic process, adapted from the original work of the author, is presented in Figure I.5. Later, in the 90s, basing on percolation theory Sieradzki et al. [30,31] have built a sustainable Monte-Carlo model trying to combine all the processes accompanying dealloying (coarsening of porosity, sharp dealloying thresholds or partitioning limits, and the development of intermediate compositions).

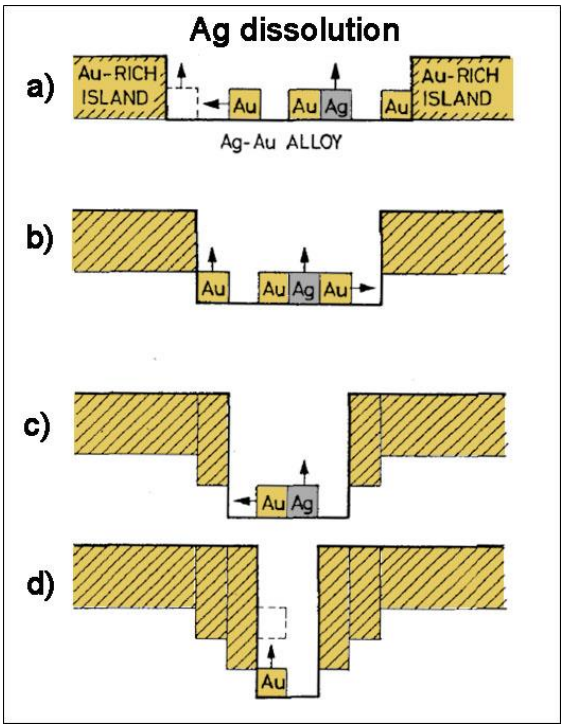

Figure I.5. Schematic view of several consequent stages of dealloying in noble metallic alloy. Reproduced from [32].

In 2001 happened the latest breakthrough when Erlebacher et al. created a successful continuum-atomistic model and demonstrated that nanoporosity in metals abide by an intrinsic dynamical pattern formation process [27]. In other words, pores form because the gold atoms are chemically driven by uphill diffusion to be aggregate into two-dimensional clusters by a phase separation process at the solid-electrolyte interface. Thus, the surface area continuously increases due to the etching diffusion. Convection phenomena also play an important role in the dealloying process, preventing the corrosion products to re-adsorb on the surface of the alloy [27,33]. The model that they used was based on processes happening on the solid-electrolyte interface and corresponded to the spinodal decomposition in the form of the Cahn-Hillard law [34]:

$$\frac{\partial C}{\partial t} = \nu_n C_0 - \nu_n k C - \nabla \cdot J_s$$

This law describes the process of phase separation, by which the two components of a binary mixture are spontaneously separate and form domains rich in each component. The left-hand part of the

equation is the concentration accumulation rate, where $\boldsymbol{J_s}$ is the flux of diffusing adatoms, $\boldsymbol{v_n}$ is a normal component of the velocity at the interface, and C_0 is the Au concentration in the bulk.

Patterns created by spinodal decomposition are random, but they have a characteristic length scale given by:

$$\lambda_c = \left(\frac{-8\pi^2 k}{d^2 G/dX^2}\right)^{1/2}, \text{ [34]}$$

Where $\boldsymbol{k}$ is a material's gradient energy coefficient and $\boldsymbol{G}$ is a free energy of a system. Figure I.6 exhibits patterns resulted from a simulation of spinodal decomposition.

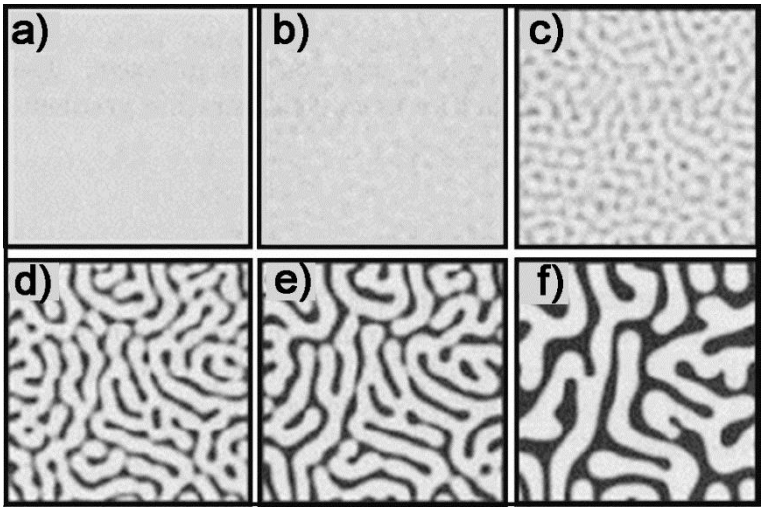

Figure I.6. A result of the numerical modeling showing patterns of different stages of spinodal decomposition, described by the Cahn-Hillard linear equation. The system evaluates from an unstable concentration (a), and decomposes into two different phases with a characteristic length scale (b, c); as the time progresses, the length scale coarsens (d-f). Reproduced from [35].

In addition, it was shown that the coarsening process away from the dealloying interface impacts on the final pattern formation [36].

Geslin et al.[15], in their phase-field modeling study on LMD in Ta-Ti system, also successfully relied on the theory of spinodal decomposition for depicting the process of solid-liquid front pattern formation on nanometric scale, but extended it to the diffusion-coupled growth theory to describe the phenomena on microscale [15].

Although morphological aspects of the dealloying process have become clearer with the recent studies, its underlying physical mechanism still leaves many open questions [27].

Among factors playing a key role in the formation of final architecture, one can certainly emphasize the initial composition and phases present in the bulk precursor. Indeed, in some cases, it is considered that the pores geometry is pre-established in the original bulk alloy and revealed after the chemical etching [37]. This supposition is not true for all alloys as, for instance, in the case of dealloying of bulk metallic glasses (BMGs). Unlike crystalline alloys, BMGs exhibit only short-range order, thus not showing any phase separation pattern that can direct any future porous architecture.

Once fixing the precursor composition, one can play with environment parameters during dealloying. As mentioned before, it may be the etching solution temperature, ambient pressure, etching composition, dealloying time and even introduced mechanical constraints and resultant stress states [17].

When the product of dealloying is ready, there still exist some post-treatment procedures to affect its geometry. One of the most conventional is the thermal treatment that leads to the coarsening of ligaments and pores. Upon sufficient increase of thermal energy, surface atoms tend to diffuse, resulting in growth of ligaments and, consequently, increasing pore size. Using thermal treatment, pore and ligament sizes can be controlled within a wide range from 5 nm to a few microns [17]. Acid aging is another way to affect coarsening of ligaments and structure agglomeration [38].

I.3.1. Quantitative characterization of porous structure

One of the most important parameters of NPMs that define their fineness and potential for such applications as catalysts is the specific surface area (S_{spec}) normalized by the weight.

The commonly used experimental method is the Brunauer, Emmett, and Teller (BET) [39]. It is based on physical adsorption of nitrogen gas molecules on the materials' surface and mainly applied to nanometer-scale systems. The limited sensitivity leading to lower accuracy [40,41] and requirement of a considerable amount of material for analysis are its main disadvantages. This method will be described in more details in the related chapter.

Due to the drawbacks of experimental techniques for S_{spec} determination, the need to estimate this parameter by theoretical mean appeared.

One of the existing solutions, confirmed to be in good agreement with experimental measurements for different families of porous structures, was proposed by De Hosson and co-workers [42].

The expression to describe specific surface area is quite simple [42]:

$$S = \frac{C^*}{\rho^* d}$$

It contains information about porous bulk density of material ρ^*, about the size of the characteristic feature (ligament/pore) – d, and C^* is a dimensionless constant that needs to be defined for each of porous families. These equation can be rewritten as:

$$S = \frac{C}{\rho d}$$

Where porous bulk density ρ^* is replaced by $\rho_r \rho$ – relative and solid bulk densities, and with $C = C^*/\rho_r$. Further values of this constant are derived for common porous structures and are presented in Figure I.7.

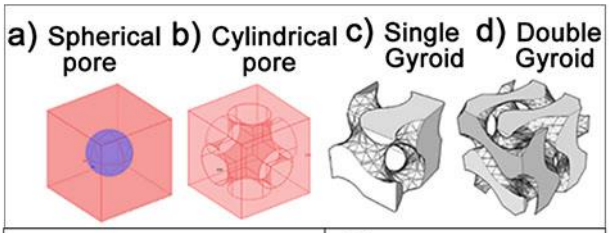

Nanostructures	**C**, dimensionless constant
Spherical pores	0,4
Cylindrical pores	2,1
Single gyroid	3,4
Double gyroid	5,8
Disordered nanoporous structures	3,7

Figure I.7. Table of constants "C", used to determine specific surface area by eq. I.3, experimentally derived for various interconnected structures. Adapted from [42].

Based on investigation of eight nanoporous gold samples of different ligament sizes (d) and porous bulk density by BET and electrochemical methods, the dimensionless constant C was calculated to be 3.7 for "disordered nanoporous structures", conventional meaning of nanoporous metals [42].

I.4. Role of precursor alloys

As mentioned before, the state of the bulk mother alloy defines the mechanism and evolution path of dealloying process. That is to say, the reorganization of remaining atoms after corrosion proceeds in a different way depending if the precursor was crystalline, if it already had a predefined pattern of "frozen" interconnected phases, and if the alloy was in a disordered – amorphous state. In present work, both types of precursors will be considered.

I.4.1. Crystalline precursor

To date it was shown that NPMs with desirable porosity can be obtained preferably from binary single phase solid solution alloys, for example Au-Ag [27], Au-Cu [43], Cu-Mn [18,44], Ag-Al [45].

The mechanism of porosity formation during dealloying of multi-phase alloys will differ from that for single-phase precursors, and dealloying route will depend on composition, arrangement in space, activity, and electrochemical properties of each phase in the alloy. In the work of Q. Zhang and Z.

Zhang classification of different dealloying behaviors was suggested for such class of alloys with coexisting phases [46].

Regarding the question of etching of multi-phase alloy: as it was already said, nanoporosity is formed by a self-assembly process through surface diffusion, and it is generally considered that an excavation of one phase from a pre-separated multiphase system is not the mechanism of porosity formation [47,48] Such pre-architecture of phases and grain sizes can, to a great extent, affect future reorganization of porous phase as, for example, observed in our work [49] on the nanoporous surface formed on the nanostructured chill-zone surface layer of a copper-based system, which will be considered in details in another chapter.

Similar pre-formation of distinct regions inside the alloy, induced by spinodal decomposition, gave an impulse for the formation of the morphology with defined parameters, like in case of the binary $Ti_{50}Sc_{50}$ alloy. [50] The authors of this work found characteristic sizes of the final porous pattern, for the lamellar-type Ti-rich structures, similar to the size range of the spinodal pattern (Figure I.8). The calculated values agreed with the spinodal mechanism, with a typical wavelength of repeated patterns of about 30-40 nm, without considering the impact of coherent strains.

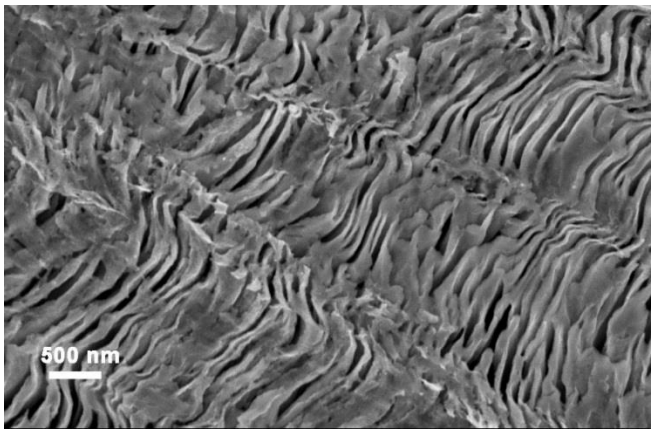

Figure I.8. SEM image of NP Ti after dealloying of spinodally decomposed Ti-Sc alloy precursor. Figure 2 (b) in [50].

One of the remarkable facts about dealloying of crystalline precursors, highlighted in a number of works, is that the original grain configuration is retained in the final NP structure, [51,52] thus, the configuration of future ligaments is not completely random and predefined by the mother alloy.

One of the drawbacks of crystalline precursors is that only limited amount of them can provide a uniform NP structure. Moreover, through one-step dealloying, only single-scale porosity can be achieved [47].

I.4.2. Amorphous precursor

Dealloying of amorphous precursors is relatively less reported in the literature, but with the apparition of opportunity of fabrication of NPMs from amorphous alloys, enthusiastically impulsed the field of NPMs.

Amorphous metals possess some unique advantages for fabrication of uniform NP structures due to their monolithic microstructure. They exhibit highly disordered atomic arrangement with high chemical homogeneity, which is one of the reasons to expect to initiate a very fine microstructure. Such precursors usually have wider composition range than crystal-solid solutions that allows one to better adjust consequent porosity formation [53].

Amorphous metals usually have a complex elemental composition. Additionally, they do not exhibit grain boundaries and other defects, such as dislocations [41] that are necessarily present in crystalline alloys. Therefore, generally speaking, such systems are poor in activation sites for dealloying, if not only produced by occasional chemical inhomogeneity and casting imperfections [52,54].

Upon dealloying of amorphous alloys, ligaments are expected to be formed by the development of multiple crystals when an amorphous precursor is extensively dealloyed. The size of crystalline domains is expected to be of the order of the diffusion distance in a given condition of temperature and electrolyte concentration [55]. Such behavior is unlike that of crystalline precursors that tend to preserve the initial size and orientation of the initial grain of the mother alloy [56]. This morphological difference of final microstructure obtained from crystalline and amorphous precursors are well depicted in Figure I.9, taken from a recent work of research group [55] from Torino University.

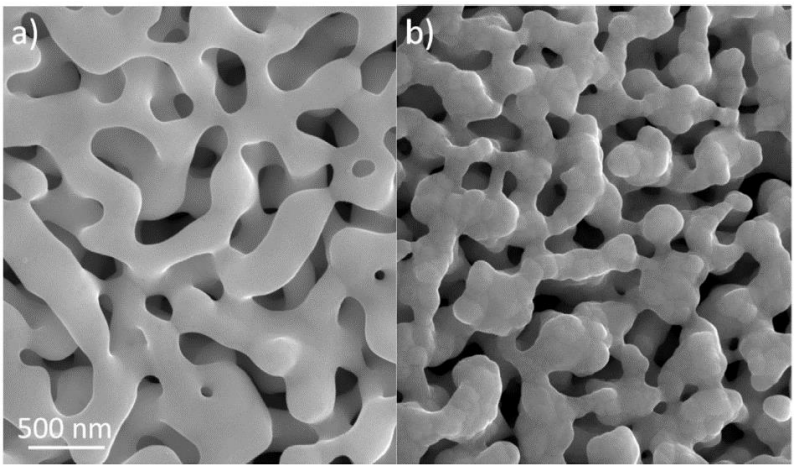

Figure I.9. SEM image of porous structure obtained from de-alloying of a) $Au_{31}Cu_{41}Zn_{12.8}Mn_{15,2}$ crystalline and b) $Au_{40}Cu_{28}Ag_7Pd_5Si_{20}$ amorphous alloys. Adapted from [55].

According to the general concept, glassy and amorphous alloys cannot remain in those states after dealloying. The removal of LN atoms creates a misbalance in their compositions, bringing such atoms outside of amorphous region. It is the remaining phase that nucleates and grows into a 3D-porous matrix [56].

Since this type of precursors has been exploited, a considerable amount of metallic systems, important for the applications, has been produced by dealloying of MGs, NPs: platinum, gold, silver, palladium, copper and others [47,57–59].

I.5. Mechanical deformation of nanoporous materials.

Integrity and mechanical stiffness of the material is an indispensable requirement for any successful target system that, at a certain point, may be applied in a real device. Therefore, it is crucial to be able to describe theoretically via existing formal approaches and measure quantitatively via experiments physical characteristics of nanoporous metallic foams.

I.5.1. Scaling laws of NPM

Most studies carried out on mechanical properties of NPMs are, in the end, boiled down to the most common Gibson-Ashby model for solid foams. This model allows estimating the effective Young's modulus, Y, and the yield strength, σ. The following "scaling equations" presented in the general form describe the mechanical behavior of metallic foams [60]:

$$Y^* = C_1 Y_b(\varphi)^q \qquad \textit{(eq. I. 1)}$$

$$\sigma^* = C_2 \sigma_{b,y}(\varphi)^p \qquad \textit{(eq. I. 2)}$$

Here, **b** is reffered to the bulk material and * to the porous one, $\boldsymbol{C_1}$ and $\boldsymbol{C_2}$ are fitting constants that depend on the geometry of the porous structure (sponge, lamellas etc) and are assumed as $\boldsymbol{C_1}$ =1 and $\boldsymbol{C_2}$ = 0.3, $\boldsymbol{\varphi}$ is a volume fraction of a solid, it can also be expressed as the ratio of the density of porous structure to the density of the bulk material, $\boldsymbol{\rho^*/\rho_b}$. The exponents $\boldsymbol{q}$ and $\boldsymbol{p}$ depend on the deformation mechanism of the cell and its solid fraction. Initially, Gibson-Ashby equations were used for foams with a cell size of several micrometers and larger. However, since they do not depend on geometrical features of the foam such as cell/pore/ligament size, by extension, if the model is accurate enough, it is supposed to be valid for nanofoams as well [24]. For the case of open-cell foams with the small solid fraction $\phi < 0.3$, q and p parameters = 2 and 3/2 respectively.

I.5.2. Deviations from scaling equations and role of nanoscale

From the previous formalization, one should expect that the mechanical properties of the foam ligaments are assumed to be bulk-like and size-independent, implying that the strength of foam materials always decreases with increasing porosity. Nevertheless, Biener et al.[61–65] remarked that existing nanomechanical experiments revealed that the yield strength of the material predicted by Ashby and Gibson's equations is lower than the ones found experimentally. This phenomenon is not surprising since it is easy to attribute such behavior of NPMs to the strong size effect in mechanical properties of nanosized ligaments. Therefore, in order to apply the scaling equation to nanoporous metal foams, they need to be modified correspondingly. One of the solutions is to consider σ_y as a variable of the ligament size $\sigma_{b,y}(d)$ [66]. In particular, the power law $\sigma_{b,y} \sim d^m$ ($\boldsymbol{m}$ – is an empirical

exponent) proved to be effective, with some examples of specific cases of m = 1/2 (Hall-Petch type dependence [66]) and m = -0,6 [64].

Moreover, in NP metals, the strut strength $\sigma_{b,y}$ is not only a function of the strut thickness but may also depend on details of the internal microstructure (such as grain size *d* and/or grain orientation)[67].

I.5.3. Elastic and plastic deformations

When a force is applied to a metallic sample, it will evidently undergo certain deformation. With the removal of the force, the material can fully recover, thus, material's atoms will return to their initial position. This type of deformation is called elastic. When the deformation is high enough, plastic deformation, which is the non-recovered constituent of the total deformation, may occur, and the material's atoms will adapt to a new permanent position. Since macroscopic foams are fully compressible materials, the dominant mechanical impact is converted into ductile plastic densification, and it is assumed that hardness H ~ σ_y, [60] while for bulk it is ~ 3 $\sigma_{b,y}$.

Upon compression in macroporous foams, two dominant deformation mechanisms are suggested to occur according to Gibson-Ashby model: so-called elastic buckling and plastic collapse [60]. Here, the elastic constituent of deformation reflects only bending of the ligaments of the foam. Generally, two phenomena describe plastic deformation: plastic collapse (dominant) at junctions and axial yielding of ligaments. The Gibson-Ashby model solely describes the first mechanism. Later, scaling equations were adapted to nanoscale foams by the phase-field method and molecular dynamics simulations [68]. Corresponding equations were derived for Young's modulus and yield strength by considering tensile deformation and axial yielding of nanoscale ligaments. These properties start playing an important role in the deformation mechanism, particularly for high-density foams ($\rho \geq 0{,}6$) [69].

I.5.4. Tools to measure mechanical properties of NP foams

I.5.4.a. Indentation

Indentation test is a well-reported technique for investigating porous metallic systems [51,65,67,70–74]. This method allows obtaining the elastic (Young's modulus) and plastic (hardness) properties of the material from indentation load-unloading displacement data using Oliver and Pharr method [75]. Indentation test can be distinguished into microindentation and nanoindentation.

Microindentation hardness testing, or microhardness test, is a conventional technique used to observe changes in hardness on the microscopic scale of materials, being more appropriate for the bulk materials because it carries the information on mechanical behavior of different crystal orientations and it shows less accuracy on small load and displacement.

Nanoindentation, on the other hand, is appropriate for nanoscale systems and allows overcoming sample size and thickness limitations.[70]

For NPMs, nanoindentation is an optimal choice as a testing method because, by varying the indenter penetration depth, it allows balancing the border between measuring mechanical properties on an ensemble of ligaments and pores and approaches the properties of an individual ligament.

Moreover, using nano- instead of microindentation allows decreasing densification impact, which disturbs the analysis of porous materials.

In addition to standard data, nanoindentation experiments can provide more complex information, like the presence of pop-ins, the evolution of properties with depth, etc.

In order to understand the principles of material characterization using instrumented indentation technique, one would certainly turn to the review of cognominal method of W.C. Oliver and G. M. Pharr [72].

Figure I.10 schematically represents nanoindentation test with Berkovich indenter type and the resulting imprint on NPS surface. An example of a typical nanoindentation cyclic curve and cross-sectional view of indent imprint in the sample surface after unloading are given in Figure I.11 (a) and (b) accordingly.

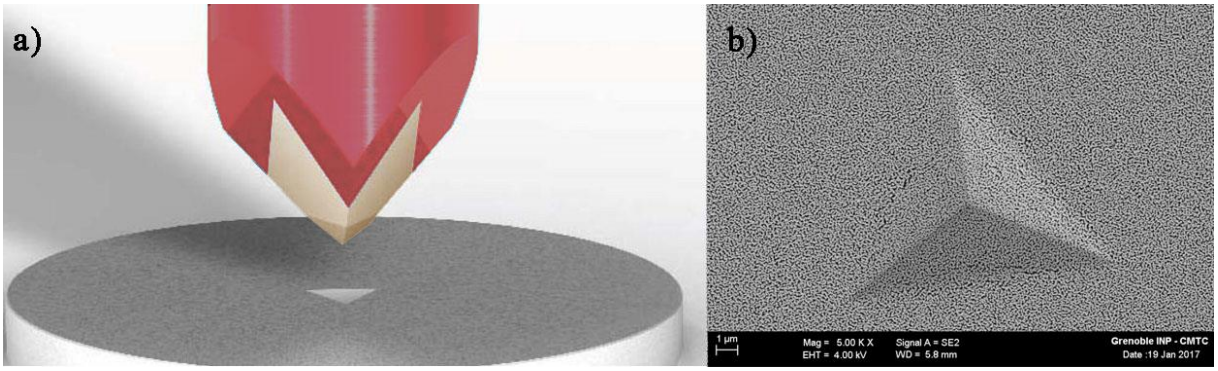

Figure I.10. General view of Berkovich-type indenter above the sample surface (a); and magnified SEM image of its imprint (b).

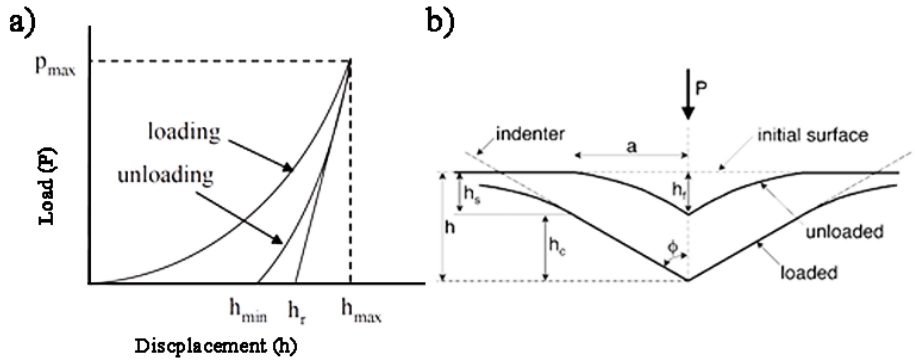

Figure I.11. A schematic view of the load – displacement curve of nanoindentation experiment performed with a Berkovich indenter (a). Image adapted from [72]. Parameter P designates the load and h the displacement relative to the initial undeformed surface; an illustration of the unloading process showing parameters characterizing the contact geometry (after [76]) (b). h_f is a final depth, ϕ is a half-included angle of the indenter, h_s is a sink-in depth, $h_c = h_{max} - h_s$

The slope of the unloading curve on the Figure I.11, dP/dh is indicative of the stiffness S of the contact. Further, the stiffness can be used to calculate the reduced Young's modulus E_r (*Y* here). The hardness *H* is estimated from: $H = P_{max}/A$, where P_{max} is a maximum load and *A* is the contact area of the indenter and a sample, that should include the correlation for the non-flat imprint punch [75].

As an example of application of this characterization technique to the nanoporous materials, the ZrO_2–4 mol% Y_2O_3 nanoporous coatings of different porosity were investigated, and the authors [72] managed to describe the dependence of hardness and Young's modulus in the particular regions of the coating on porosity. It was reported that *H* and *Y* of coatings showed a significant dependency on the porosity, and, predictably, their values on the side regions of coatings decreased with increase in porosity of specimens, as exhibited on the Figure I.12.

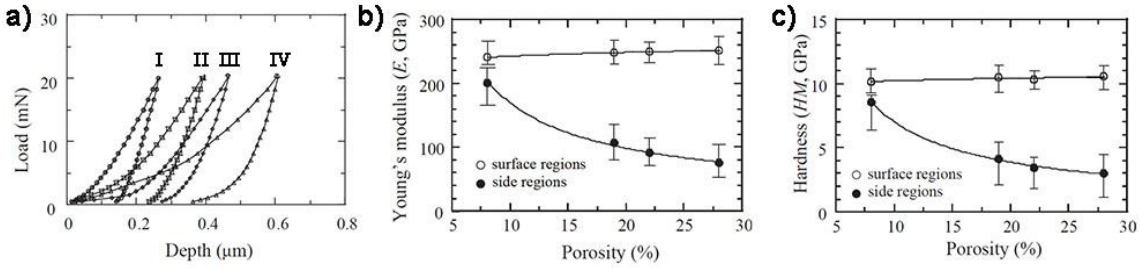

Figure I.12. a) Load– depth curves for side regions of nanoporous ZrO_2–4 mol% Y_2O_3 coating specimens obtained by nanoindentation: (I) 8%, (II) 19%, (III) 22% and (IV) 28% of porosity, respectively; b) Young's modulus and c) Martens hardness as a function of porosity for ZrO_2– 4 mol% Y_2O_3 coatings. Adapted from [72].

Another previously mentioned work of Biener et. al [65] on study of mechanical properties of NPG using nanoindentation has attracted considerable attention to the question of adequate description of mechanical response of NPM. It has been shown that while the experimentally determined Y of 42% nanoporous Au is of the same order as predicted by the scaling laws, the value of the yield strength is almost one order of magnitude higher than the value predicted by equation (2). Authors claim that an inconsistence of the theory with the experiment might indicate a new class of high yield strength / low density materials, although a more comprehensive study of the scaling equations at the nanoscale could be required first [70].

More details about this experimental method and corresponding data treatment will be provided in Chapter II.

I.5.4.b. Other methods

Other existing techniques include : a compression test (usually applied to macrofoams); uniaxial column microcompression stress test with an indenter of flat punch [61] ; a wrap bend test, typically assessed by bending the sheet around increasingly severe radii until the observation of fracture on the outer bent surface; a three-point bending test that allows investigating ductile-to-brittle transition of NPMs.[77] These methods stay out of the scope of this work, however, new data obtained from these

tests and regarded together with results from nanoindentation should provide a better understanding of mechanical behavior of NPMs.

I.6. Systems of interest and their applications

I.6.1. Notes of consideration

Nanoporous metallic materials are becoming a growing trend in an increasing range of applications. However, to create an adequate solution to a given problem, one will need to consider the following general aspects and recognize whether the purpose is "functional" or "structural":

- *Required morphology (open or closed pores),*
- *Required extent of porosity,*
- *Required size scale of porosity,*
- *Required total internal surface area,*
- *Required metallurgy (metal or alloy its microstructural state),*
- *Processing feasibility: possibilities for previous items,*
- *Economy (cost and adequacy of large volume production).*

Many applications require a medium (liquid or gaseous) to be able flowing through a nanoporous material, and the architecture of porosity may need to be very complex: the amounts of open pores, which can range from widely opened pores (high rate of fluid/gas flow, for example, in heat exchangers [78]) to completely closed ones (load-bearing structural applications). The following diagram in Figure I.13 gives a visual interpretation to it [79].

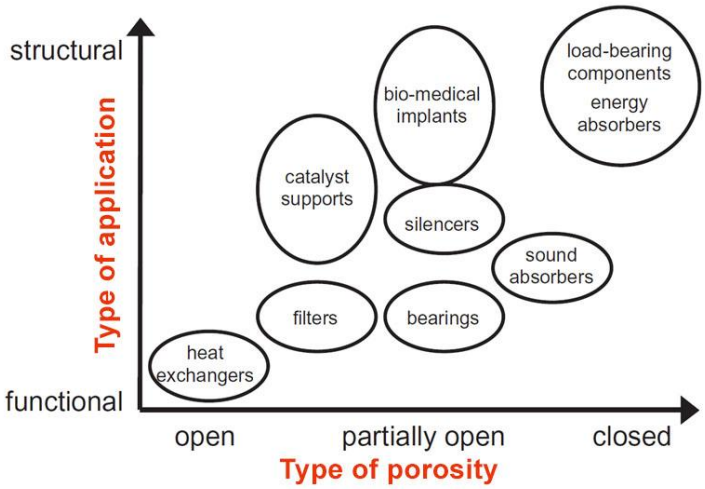

Figure I.13. Applications of porous metallic materials grouped according to type of porosity. From [79].

Usually larger-sized pores (hundreds of nm) are good for microfluidic flow control [80], while smaller pores (tens of nm) are practical for increasing the surface area of the device as, for instance, in sensor and catalytic applications [81]. For microfluidic-based sensors, a bimodal pore size distribution, composed of large porosity channels with highly porous channel walls, is advantageous to attain fast

time response and high sensitivity [9]. In catalytic systems, for example, hierarchical porosity is very favorable for a correct mass-transport: the access and evacuation of products from the reaction into the and out of the material [82,83].

Another question of fundamental importance is whether a given metal or alloy of a given type of nanoporous structure is manufacturing feasible as, for example, for structural applications in load-bearing parts the structure must be lighter than conventional bulk metals or alloys. In this way, one prefers porous aluminum, magnesium, and titanium for such applications. For biomedical applications for tissue growth, due to the biocompatibility and related mechanical properties Ti or Mg and their alloys are desirable [80], and for usage in corroding media and/or high-temperature applications it would be stainless steels or again titanium.

At last but not the least, the industrial feasibility of materials must be considered. In other words, a technology for production with reasonable prices must be available for the material to remain in the market. By precursors design and control over the dealloying process, nanoporous metals with different structures and morphologies can be fabricated: homogeneous structure, bimodal pore distribution, composite structure, ultrafine porous structure, etc. Moreover, both nanostructures (nanowires, nanotubes) and monolithic forms (films, ribbons, and bulk samples) can be obtained. However, any of the processing routes must be competitive when compared to conventional materials for the same application.

I.6.2. Noble NPM

It is a relevant fact that the greatest amount of works on nanoporous metals has been carried out particularly on Platinum group metals (PGM), i.e., six noble elements: ruthenium, rhodium, palladium, osmium, iridium, and platinum. It is presumed that partially filled d-orbitals cause high catalytic efficiency of PGM-based catalysts [84]. Due to this intrinsic feature and low activation energies, they are the most extensively used as the exhausted gas treatment catalysts [85] and are the best for various catalytic reactions involving the oxidation of small organic molecules such as methanol, ethanol, formic acid, etc. However, they often suffer from poisoning by strongly chemisorbed carbonaceous intermediates such as CO [86].

Until recently, gold was considered as a rather inert metal until it showed unusual catalytic properties with the size range changes down to the nanoscale. Such chemical activity should be ascribed mainly to intrinsic properties of these special nanoporous structures, the creation of specific CO-adsorption sites and a high fraction of low-coordinated gold atoms [87]. Au and Au-based functional catalysts have proved to have a potential to replace PGMs for electro-oxidation of methanol in fuel cells and alternative reactions [88]. Different innovative designs have been exploited to increase their natural activity: fabrication of nanopowders, deposition of powders on super-high surface carbon substrates, increase the convex curvatures of substrates, which are believed to have the higher impact on electrochemical activity, addition of second noble metal to achieve some synergistic effect[88] and bifunctional mechanism based on a concept of electronic structure modification of one metal by another [89], etc.

The most important drawbacks of noble metals family are certainly their price and the fact that PGM will be scarce in the near future. In order for the final NPM to remain in the market and find real

implementation in industrial devices, they should have competitive pricing. These drawbacks are the reasons why this work will focus on non-PGM alternatives.

I.6.3. Non-PGM alternatives: Ag, Cu, Co

Primarily, market prices of Ag, Cu, and Co are nearly 800 times lower than those of Platinum or Gold. Table 1 will help to estimate current values for metals of interest:

Table 1. Market prices of some PGM and non-PMG metals as on Feb. 7th, 2017. Extracted from [90].

Metal	Price, USD/ozt
Au	1,226.26
Pt	1,008.75
Ag	17.6
Cu	2.26
Co	1.17

Nanoporous analogs based on these metals open doors for a much wider range of systems fabrication if one can provide competitive physicochemical properties of the material.

I.6.3.a. Nanoporous silver (NPS)

Pure silver is a very soft semi-precious metal. It possesses some remarkable natural properties as, for example, it is an excellent heat and electricity conductor and one of the best refractors of visible light [91]. Silver has relatively low toxicity to the body and also exhibits antimicrobial properties. That is why it is often used in coatings of medical devices, treatment of injuries, and disinfection of water.[92]

Synthesis of NPS is known for several binary systems as, for instance, Ag-Al system via dealloying of Al from a single α-Ag(Al) phase precursor in diluted hydrochloric (HCl) media [45,93–95] (related SEM graphs, Figure I.14), via electrochemical double-step dealloying of Zn-Ag alloys in HCl and subsequently in NaCl solution [96] or by its dealloying in H_2SO_4 [97]. Microstructure control of NPS is performed via phase control over phases in precursor alloys and etchant state (concentration/T). However, morphology feature sizes of NPS is typically one order greater (100-500 nm) than for NPG (5-50 nm), which limits functional properties of NPS. The larger length scale of pore-ligament block is presumed to be due to the more intense surface diffusion of Ag along the alloy/solution interface [98].

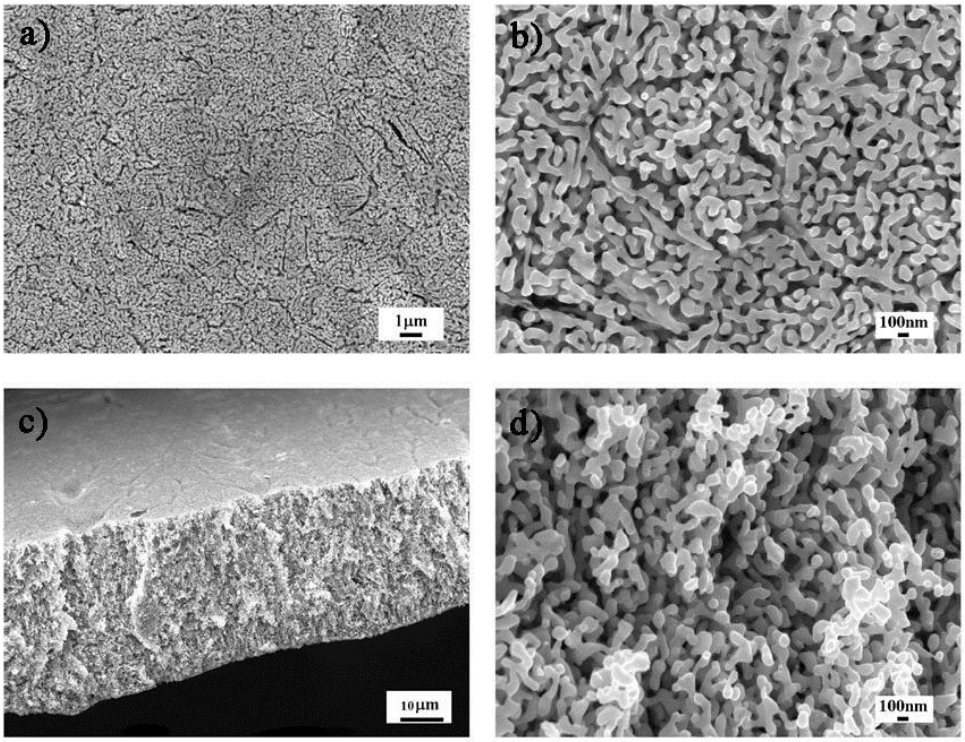

Figure I.14. SEM images showing the microstructure of NPS through chemical dealloying of the Al-25 Ag alloy in the 5 wt % HCl solution. (a,b) Plan-view and (c,d) section-view SEM images. (Adapted from [94]).

Considerable refinement of porous architecture was achieved by dealloying of amorphous silver-based precursors. A family of binary Ag-Ca alloys of a glass-forming range permitted producing an NPS upon dealloying in water with a characteristic average ligament size of ≈ 30 nm that showed a tendency to decrease down to 22 nm with the decreasing of Ag concentration in the precursor [99]. Another successful synthesis of a competitive morphology was performed in our laboratory on the basis of an amorphous ternary Ag-Cu-Si alloy. After selecting the appropriate etching condition in HNO_3 media, it was possible obtaining grain sizes ranging between 20 and 30 nm and asymmetric pores of around 30 nm [57].

Size limitations of the morphology can also be caused by an exothermic chemical reaction that takes place during dealloying, and an intense release of bubbles accompanies it. However, using an amorphous alloy as a starting material allows one to obtain finer porosity when comparing with a conventional method of dealloying of a solid single-phase binary alloy.

Up to date, NPS was shown to be a good candidate for a number of applications.

As a catalyst, it has already become a conventional commercial solution, widely available on the market in the form of nanoparticles [100]. It was proved that NPS is active towards CO_2 reduction to CO with a very high selectivity (81%) [101]. NPS displays high enhancement of catalytic activity during the formaldehyde electro-oxidation reaction and even outperforms the commercial nano-Pt catalyst. The electro-oxidation of formaldehyde and other alcohols is important in view of applications within the

field of soluble organic fuel cells [102]. Since the end of the last century, silver is well-known to be a good catalyst for this purpose [103].

Detsi et al.[104] studied the behavior of NPS under applied current and charge-induced reversible dimensional changes, and have shown that NPS is an appropriate electrochemical actuator.

In the research group of Z. P. Lu et al.[105] scientists showed that nanoporous silver, synthesized via electrochemical dealloying of Ag-Mg-Ca metallic glass, has excellent surface-enhanced Raman scattering (SERS) for potential applications in molecular detection. In particular, the detection limit of NPS is close to the detection of a single molecule of a probe Rhodamine 6G corresponding to 10^{-12} mol.L^{-1}.

I.6.3.b. Nanoporous Cu (NPCu)

Synthesis of nanoporous copper has been successfully practiced via both free corrosion and electrochemical dealloying since the elaboration of the Raney copper catalyst in 1980 by the Raney method [106], although, less effective and thermally stable copper catalysts had been known even earlier, since the 1921 patent by Patart [107]. Raney copper was obtained as a result of the removal of LN metals from ternary $Al_{50}Cu_xZn_{50-x}$ alloys by immersion in 20 wt% of NaOH base solution and took place in the methanol synthesis [108], which was previously made through three-step catalysis [109].

As the dealloying method started gaining popularity, the number of possible ways of NPCu fabrication increased drastically: in 1980 D. S. Keir and M. J. Pryor [110] successfully produced by electrochemically dealloying Cu–Mn alloy in a sodium chloride electrolyte, although the minimum atomic percentage of Cu in initial alloy did not drop below 50% [110]. Later, Hayes et al.[111] reported the fabrication of monolithic NPCu by dealloying $Mn_{0.7}Cu_{0.3}$ in diluted HCl acid, although due to the high concentration of cracks, originated from fracture morphology, its mechanical properties have been significantly reduced. Furthermore, monolithic NPCu were synthesized through dealloying of various Cu-M melt-spun crystalline alloys (where M = Al[112,113], Mg[114], brass Zn[115,116] etc.).

Since the class of metallic glasses emerged as a new promising type of precursor, not only noble NP metals such as Pd, Pt, Au, and Ag were produced via dealloying of MG, but recent works have proven that it is possible for quite a large number of Cu-bearing binary and multi-elemental systems as well[117,118]. In particular, Luo et al.[119] synthesized a uniform NPCu with open pores by electrochemical dealloying of ternary Mg–Cu–Y metallic glasses in H_2SO_4 aqueous solution. Due to the large standard electrode potential difference between the LN (Mg and Y) and MN (Cu) elements (-2.372 V vs. standard hydrogen electrode (SHE) for Mg/Mg^{2+}, -2.375 V vs. SHE for Y/Y^{3+} and +0.342 V vs. SHE for Cu/Cu^{2+})[120], the driving force of dissolution favors the porosity formation. Wide glass-forming range linked to a wide variation of the copper amount (20-40 at %) allowed to study the effect of variation of chemical composition and etchant state on the formation and stability of porous microstructure during electrochemical dealloying. The study of this system was accompanied by the research group of T. Zhang [117] with a more qualitative description of ligaments formation mechanism while dealloying and its variation with the composition change.

A. Inoue et al.[121] observed the formation of NPCu through free corrosion of $Cu_{60}Zr_{30}Ti_{10}$ metallic glass in HCl media and investigated the rate of dealloying on acid concentration. The authors of [122]

have performed another interesting study on NPCu, where, in addition to its synthesis from a Cu-Hf-Al metallic glass, they studied the accompanying chemical process during the dealloying, such as the formation of spherical Cu particles, CO microwires and CO_2 nanoplates on the surface of formed NPCu.

Researchers from Tohoku University [123] performed dealloying of amorphous $Ti_{60}Cu_{40}$ and $Ti_{60}Cu_{40-x}Ag_x$ (x = 1, 2 at.%) alloys and observed that pore sizes of NPCu, dealloyed from Ag-added alloys was smaller (8-55 nm) than the ones for the Ti–Cu alloy (130 nm), proving that a small addition of silver atoms to the mother alloy promotes the refinement of the final NP ligament structure. On the contrary, the effect of the addition of Al to the Cu-Zr alloy [124] caused widening of the ligaments. A review of T. Zhang et al.[118] gives more detailed information on dealloying of various MG families to produce NPCu and corresponding etching conditions.

Among the three coinage metals, Au, Ag and Cu, the latest one is the less investigated. A good systematic research on optical application properties of NPCu was studied by the teams of T. Fujita and M.-W. Chen [125] obtained from the same rapidly cooled single-phase $Mn_{0.7}Cu_{0.3}$ precursor as in the earlier work of Hayes et al [44]. They have shown that the pore size can be tailored as 15-120 nm and the SERS effect on the detection of R6G and CV by an NPCu with the ligament size of 30-50 nm can be comparable to that of NP gold with a ligament size of 5 nm.

Possessing an excellent electrical conductivity, one can think of using the NPCu/ NPCu+Metal-Oxide composite as a current collector for energy storage devices. The bimodal porosity of the Cu structure with large channels and nano- roughened channel walls was fabricated and successfully tested in a simulant Lithium-Ion battery (LIB) as an anode substrate [126,127]. The porosity of NPCu, among other, provides space to accommodate the huge volume change during lithiation/de-lithiation, while large channels facilitate the transport of Li+ ion. The authors of the series of related works found the application of NPCu in LIBs. An example of NPCu as a part of LIB is given on Figure I.15 [127]. Meanwhile, researchers admit the importance of further structure strengthening and improvement of its mechanical integrity for successful implementation in real devices [128]. Therefore, some investigations have been focused on the stability of NPCu structure and on the possibility to retain good mechanical properties of the initial MG precursors [118] and on the observation of ductile-to-brittle transition depending on the thickness of the NPCu foil [53].

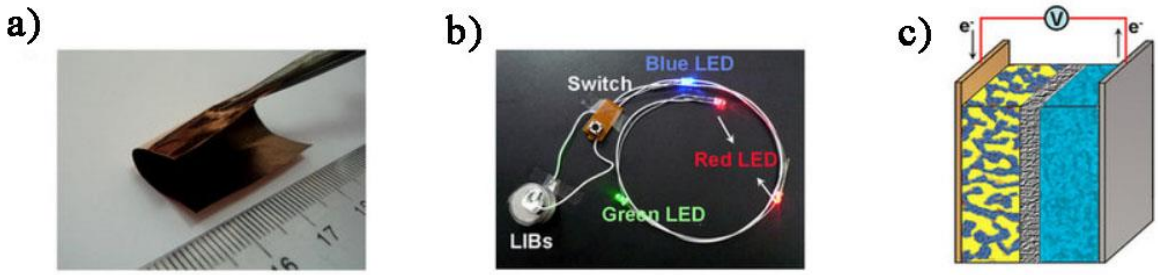

Figure I.15. Photograph of a flexible S/NPCu/MnO_2 hybrid bulk electrode (2 × 3 cm2). (a), four batteries assembled with S/NPCu/MnO_2 bulk electrodes power blue, red and green LEDs (b), Schematic battery constructed with S/NPCu/MnO_2 and lithium foil as electrodes (c). Adapted from [127].

NPCu has several useful attributes for studying nanoporous structures, such as low density, high thermal conductivity, large elasticity modulus, and low-cost precursor materials, [111] which one can compare in the table in the previous subsection. Moreover, copper, similarly to silver, have demonstrated outstanding anti-bactericidal properties [129–131], although, it is also considered as a toxic element. According to the present knowledge, increasing the surface area of copper-, silver- and titanium-based alloys improves bactericidal efficacy and, therefore, metallic nanofoams can prevent the growth of bacteria [132,133]. Furthermore, in view that the surface roughness of 1 μm range is believed to be a critical value for bacteria adhesion due to their similar size [134], NPCu is expected to exhibit better bactericidal properties comparing to bulk ones and to ones with the large characteristic size of pores. These facts support the use of reasonable cost copper-based materials in medical parts and devices (door handles, etc.), and in related fields. One of the quite important disadvantages of this metal is the easy formation of copper oxide on its surface that diminishes the charge transferability, and may stop a charge transfer across electronic vacancies generated upon sacrificial metal atoms' solubilization.

I.6.3.c. Nanoporous Cobalt (NPCo)

Cobalt is a transition group VIII magnetic metal. Generally, cobalt is a strong oxidizing agent and readily reduces to the +2 state, being the most stable oxidation state of this metal, which means that it is somewhat a reactive metal, not stable in acids (except nitric acid) in the metallic state comparing to noble metals and results in producing hydrogen gas.

$$\text{Ex: } Co_{(s)} + H_2SO_{4(aq)} \rightarrow Co^{2+}{}_{(aq)} + SO_4^{2-}{}_{(aq)} + H_{2(g\uparrow)} = CoSO_4 + H_{2(g\uparrow)}$$

Therefore, in most dealloying processes, cobalt plays a role of a LN element. A limited number of systems, allowing the formation of soluble solid phase, where cobalt would be the nobler species is one possible reason why there have not been reported any nanoporous monolithic cobalt fabricated through dealloying to date.

Other probable reasons for that are physical barriers for potential precursor production. Such precursor, in analogy with previously considered Ag- and Cu- based systems, are likely to have single phase solubility of components or to exhibit the presence of a eutectic point on the phase diagram to make a rapid quenching of alloy possible, avoiding intermetallic formation and promoting dealloying effect. For example, Figure I.16 presents the binary Co-Cu alloy phase diagram with solid solubility in the cobalt-rich side. As one can observe, the main drawback of this system is that it will be challenging or even impossible to find an etchant that would react with copper without removing cobalt, and, secondly, the melting temperatures for alloys in the cobalt-rich side approaches to 1400 °C. Such high temperature makes it technologically complicated to perform good alloy homogenization with further quenching, in addition, our laboratory facilities do not allow fabrication of alloys with melting point above the annealing temperature of quartz (1215 °C) [135]. Similar issues exist for a number of other potential binary systems: Co-Fe, Co-Ni, Co-Cr.

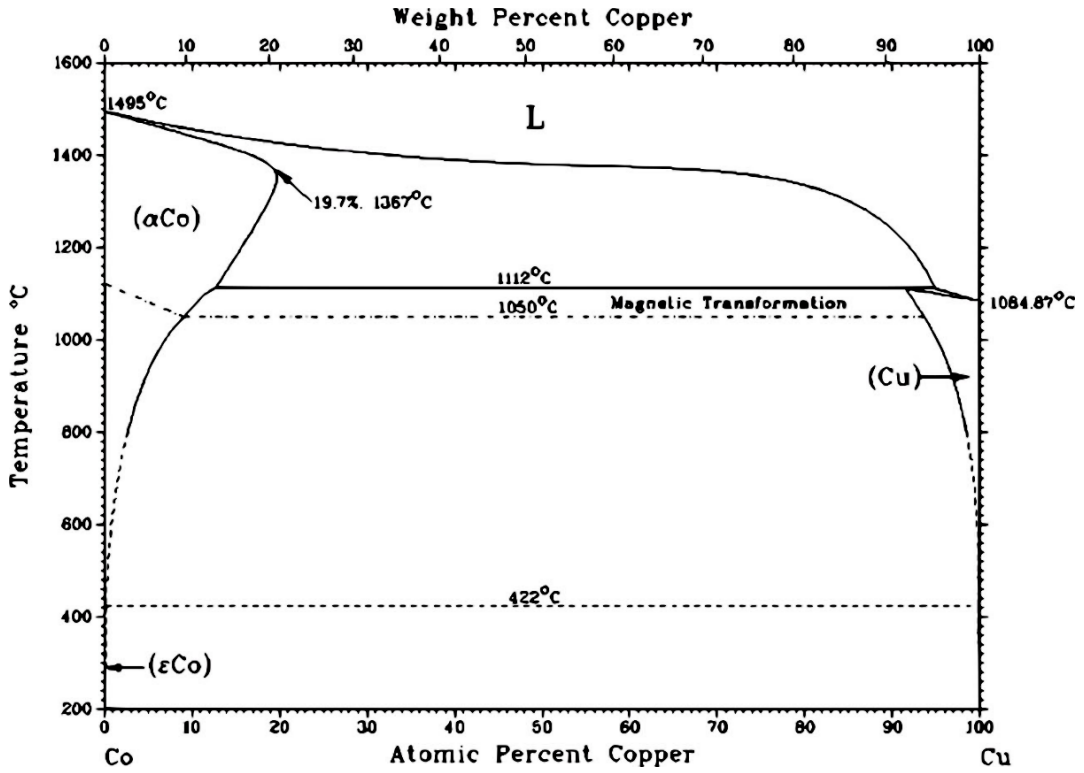

Figure I.16. Phase diagram of Co-Cu system. Extracted from [136].

Nevertheless, in spite the fact that dealloying is admitted as one of the simplest methods in terms of realization, there exist a big variety of other industrially available methods for producing NPCo and other nanofoams: for example, in 2006, the Los Alamos National Laboratory has produced nanoporous Co- and Cu-based foams by combustion synthesis. [137] Another reported way was heating of consolidated carbon nanotubes *CNT*/Co_3O_4 nanocomposite powders that resulted in the reduction of metallic cobalt and formation 3D nanostructured matrix for further use as a conductor [138].

One of the highly featured applications of Cobalt together with other group VIII metals is in the Fischer-Tropsch (FT) synthesis. Shortly speaking, FT is a catalyzed process that converts a mixture of CO and H_2 into liquid hydrocarbons (ideally alkanes (C_nH_{2n+2}) (see eq. I.3) through a series of chemical reactions [139]. The product of reactions is a synthetic oil or fuel:

$$n\mathrm{CO} + 2nH_2 \rightarrow C_nH_{2n} + nH_2O \qquad \textit{(eq. I. 3)}$$

It is considered that catalytic activity in the FT process proceeds into the metallic Co phase and not into the oxidized species. On the contrary, oxide formation leads to the deactivation of the catalyst [140]. Some of the existing FT catalyst fabrication ways, known to date, are the impregnation (deposition of particles on a porous substrate), precipitation of Co ions on the active support [141], sol-gel [142], colloidal [143], and other methods. Nevertheless, there is still no available information about a successful synthesis of monolithic nanoporous Co via dealloying. Hence, it could be of great importance to find an approach to it.

I.7. Applications: Catalysts and electrocatalysts.

Rapid industrialization and ubiquitous vehicle ownership raise demands for higher capacities of the transportation means and portable and on-board electronics. The importance of ecological problem has kicked off fast development of catalyst market. Nowadays, the field of fabrication of higher-value catalyst products, which are of a remarkable efficiency, facilitate product differentiation and provide flexibility to manufacturers, is one of the most economically interesting as the world demand for chemical synthesis, petroleum refining, and polymerization catalysts will rise ~ 4,8 % per year to US$ 20.6 billion in 2018 [144]. As mentioned previously, the first successful synthetic catalyst was the Raney® nickel, obtained via dealloying of aluminum from Ni-Al alloy which gave a burst for analogs industrial skeletal catalysts mainly based on PGM.

Because the catalysis is a surface phenomenon, its effectiveness significantly depends on an interface area between the catalyst and the gasses or liquids to be reacted. Consequently, one of the possible solutions is that the catalyst is either processed into a highly porous structure or, in the case of impossibility, they are applied to another porous system, commonly a porous ceramic material. Thus, the chemical reaction takes place on the surface of nanoparticles.

However, the main inconvenience of such assembly is instability and detachment of particles from the substrate during the electrochemical reaction. Therefore, a self-supporting integral nanoporous matrix can be an advantageous alternative solution, possessing good thermal and mechanical stability and conformability. In such NP frame, each pore represents the so-called nano-reactor, where the target reaction takes place in the active site of the cavity (S), as depicted in Figure I.17, which presents an example of a heterogeneous mechanism of oxidation of carbon monoxide CO to carbon dioxide CO_2 over a precious metal surface [145]. The key steps that take place in this reaction are chemisorption of O_2 and its further dissociation into $2O^{2+}$ as O atoms' bond to the active sites on the metal surface, adsorption of CO molecules to same active sites, thus completing the transformation to CO_2.

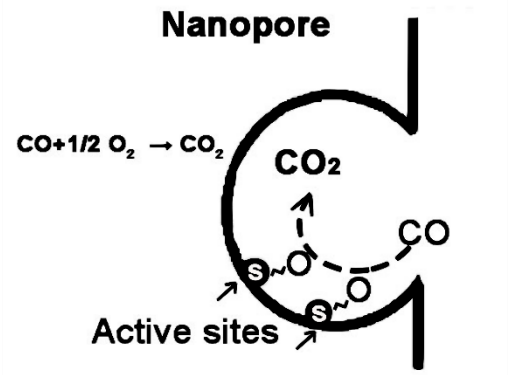

Figure I.17. Schematic view of CO oxidation on the surface of a nanopore of a catalyst.

After this example, it is simple to summarize the overall heterogeneous catalytic reaction in the following steps:

1) Adsorption of the reactants on the surface of the solid, which in its turn can be divided into physisorption: adherence of a molecule to a surface without the formation of a chemical bond (2-10 kJ/mol), and chemisorption – binding through the chemical interaction with the energy well above 50 $kJ.mol^{-1}$. Both the host and adsorbate are chemically changed in the process, and the initial compound is usually trapped on the surface or within the bulk of the solid media. This process involves an electron transfer between the metal and the hydrogen, may requiring thermal or catalytic activation due to the dissociation energy barrier [146];
2) Diffusion on the surface;
3) The breaking of some reactant bonds (in the present example, adsorption of O_2 requires dissociation into two oxygen atoms O_{ads} on the catalyst surface.);
4) Creation of new bonds to form the product molecules ($CO_{2\ ads}$);
5) Desorption of product from the surface and diffusion away to the gas/liquid phase.

In the present case of CO oxidation, the noncatalytic route (see Figure I.18) is slow and energy-consuming. However, thanks to the catalyst, the reaction takes a low energy path and makes the dissociation of usually stable O_2 possible [147]. This process basically reflects the general purpose of any catalyst.

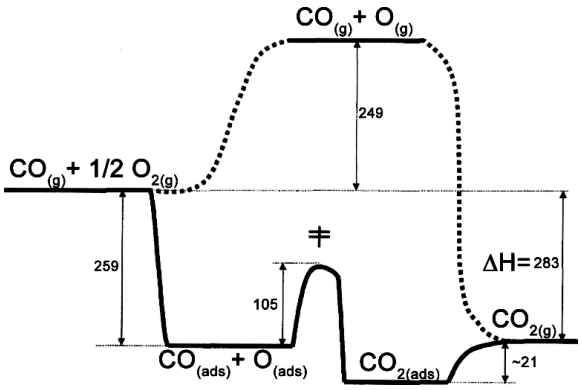

Figure I.18. Schematic energy diagram for the oxidation of CO on Pt catalyst. Adapted from [148]. Energies are given in $kJ.mol^{-1}$.

In addition to the complexities of the mentioned processes one should add the challenges of catalyst design. Considering the creation of a catalyst one should gather all following characteristics: its activity, selectivity towards desirable reactions, durability, cost, availability of fabricating materials, availability of forming techniques, compatibility with other parts within the system and its recyclability, which is especially important for rare and expensive metals.

For a better understanding of general concepts of heterogeneous catalysis and the essence of activity of certain metals, it could be helpful to refer to a careful study by B. Hammer and J. K. Nørskov [84] with an accent on computation methods and to a book by Caltech researchers Mark E. and Robert J. Davis [147].

I.8. Optical applications: SERS.

When the metal's surface is modified in a nanometric scale, it is no longer interacting with the incident light in a way as the bulk due to the appearance of complex electromagnetic modes. When the size of the metal is much smaller than the wavelength of light, nanostructured metals exhibit significantly different optical properties compared with their bulk counterparts due to the surface plasmon resonance (SPR), i.e., the collective oscillation of the free conduction electrons excited by visible light (λ = 400-700 nm) [19]. The resonance condition develops when the frequency of incident photons matches the natural frequency of oscillating surface electrons. Materials multifunctionality for optical sensing of adsorbates has obvious advantages: in addition to the potential for greater sensitivity, the different length scales associated with a variety of optical phenomena allow a numerous diversity of adsorption characteristics that deserve a deep study. In this field there exists applications mainly in Raman scattering [149] acknowledged as one of the promising techniques of molecular diagnosis, trace detection, pharmacology and others [150–152].

Surface-enhanced Raman Scattering is a powerful non-destructive technique for identification of chemical and structural information from small numbers of molecules[153]. Generally speaking, this technique requires the appropriate interaction of the three basic components: 1) the enhancing substrate 2) the excitation source 3) and the detection target molecules.

First SERS observations were reported in 1974 by Fleischmann et al. The researchers observed the pyridine molecule adsorbed from aqueous solution onto a roughened silver electrode reduction cycles [154] (see Figure I.19). Their precipitate conclusion was that the untypical strong signal of pyridine was due to the increase of the surface area of the electrode and, therefore, a higher number of attached molecules. Later studies showed that surface roughening and concentration of particles could not account alone for the enhanced signal and had to involve a more complex approach [155–158].

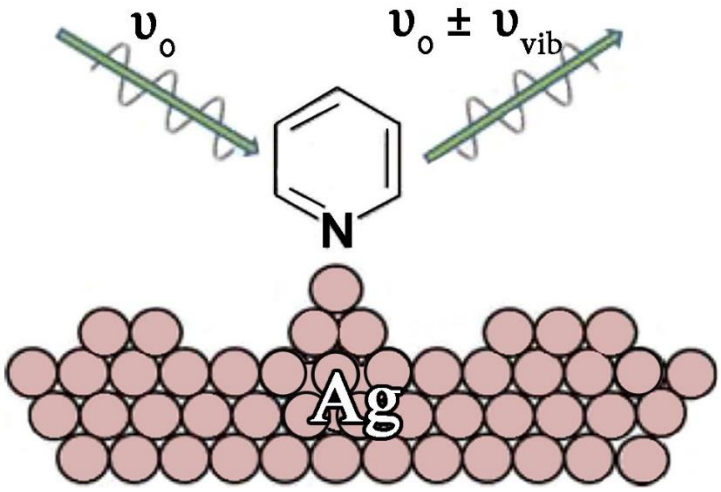

Figure I.19. A schematic model of a SERS experiment with pyridine molecules adsorbed on roughened silver. The intensities of the incident laser and Raman scattered light are both influenced by the enhanced field at the Ag surface resulting from surface plasmon excitations. (Edited from [159]).

Even though there are no strict rules applicable to a good optical sensor, it is possible to select several main factors that are important to make NPMs valid materials for optical applications, particularly for surface-enhanced Raman scattering. These factors should be considered collectively:

- The electromagnetic enhancement factor: electromagnetic enhancement from the localized surface-plasmon resonance, induced by the appropriate wavelength of visible or near infrared light wavelength λ [158,160–162]. Qualitatively, this impact can be approximately expressed as the fourth power of the ratio of the total electric field $\boldsymbol{E}(r_m,\omega)$ at the molecule location $\boldsymbol{r_m}$, to the incident excitation plane wave $E_{inc}(\omega)$, where ω is the radiation frequency [163]:

$$\rho(\boldsymbol{r_m},\omega) = \left[\frac{\boldsymbol{E}(\boldsymbol{r_m},\omega)}{E_{inc}(\omega)}\right]^4$$

  In order for scattering to occur, the plasmon oscillations must lay in the plane perpendicular to the surface of the metal; if they are in-plane with the surface, there will be no scattering.
- Chemical factor: chemical composition of the target molecule and its binding with the metal's surface [162]. This factor directly affects charge transfer between chemisorbed species and the metal surface. It is more prone to think that new electronic states of the adsorbate, caused by chemisorption, serve as resonant intermediate states in Raman scattering [164].
  The impact of chemical enhancement in the total SERS effect is considered to be a factor of about 10-10^2, which is considerably smaller than the impact of electromagnetic enhancement (10^{-4}-10^7) [164].
- Surface-morphology-induced effects: appropriate morphology, size, and assembly of the nanostructure, described by characteristic length smaller than the λ of the incident light [125,151,154].

Particularly high SERS effect capable of detecting molecules, present in a very low concentration, nearly single-molecule one, is believed to be possible thanks to the presence of the so-called "hotspots" – regions of the NP substrate where intense electromagnetic fields are believed to be generated at interparticle fissures or in pores of a rough surface [165]. These sites can promote enhancements as large as 10^7 in the Raman signal of the adsorbed molecules. Hence, it was suggested that the major Raman effect would be governed by these non-uniform locations with maximum roughness [163].

Enhanced Raman scattering effect and its demonstration upon the morphology and different commonly studied molecules (Crystal violet - CV, Rhodamine 6G – R6G, Pyromellitic Dianhydride) have been observed for a number of metals, the particularly high effect was confirmed for platinum, gold, silver, and copper [105,149,151,154,166,167]. This effect is due to the fact that their SPR frequencies fall within these λ ranges, providing maximal enhancement for visible and near-infrared light.

As a demonstrative example, the work of M.W. Chen et all [167] featured the amplification signal from CV and R6G molecules by plane and wrinkled nanostructured gold films (Figure I.20).

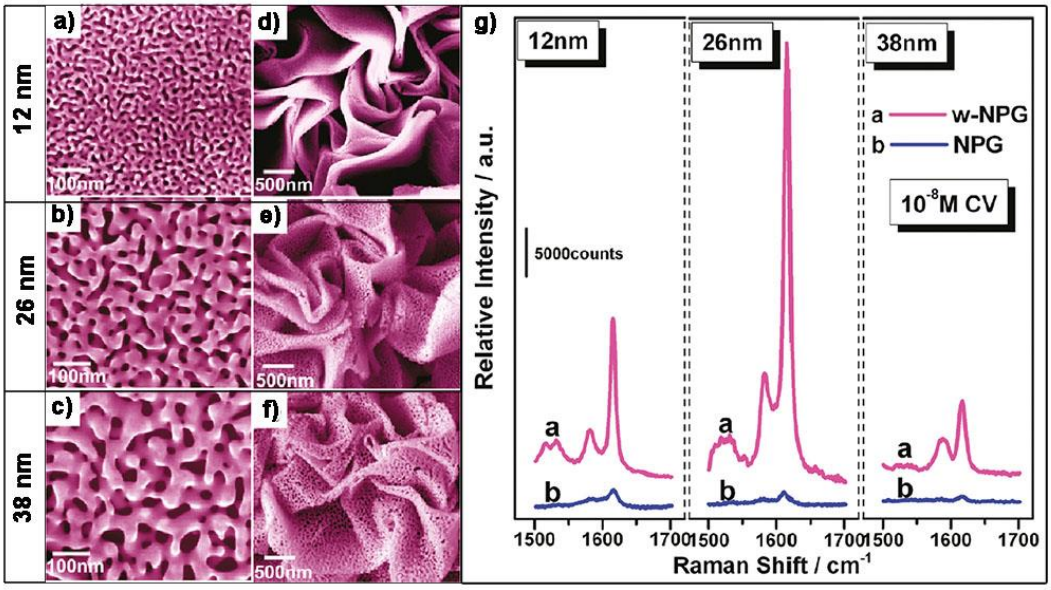

Figure I.20. SEM micrographs of the as-prepared and of the wrinkled NPG films with different nanopore sizes of~12 (a, d), 26 (b, e), and 38nm (c, f). Overview and horizons for applications. SERS spectra of CV molecules on corresponding NPG films (g). (Adapted from [167]).

It was observed that wrinkling of NPG substrate leaded to the considerable improvement in the CV detection that was evident at the concentrations of CV as low as 10^{-8} M, with the best result achieved for the average pore size of ~ 26 nm. Such upgrade in SERS substrate's performance is presumably due to the generation of new electromagnetic "hot-spots" in the sharpen tips and gaps between the creases.

Up to now, SERS studies and optical phenomena of nanostructured metals and their substrates are still in the mainstream of research [153]. The future of SERS comprises the introduction of new plasmonic materials (graphene, semiconductors, quantum dots etc.)[168–170], commercialization of new cheaper substrates, enlargement of working frequency diapason and finally the search of standardization procedure for SERS-type materials characterization.

I.9. Overview and horizons for applications.

The above brief descriptions of applications of nanoporous metals are only a part of the whole spectrum of possible useful utilization of this family of materials. Catalysts and optical substrates will be in focus in our experimental work, described in the applications section, and such introduction will facilitate the reader to probe into the matter.

By analyzing the literature of the precedent topics, it was possible to observe that the majority of them is linked to energy applications and related to (electro)catalysis and related to them sensors and actuators, thus reflecting the overall tendency of current researches on NPM. Applications, other than catalysis or electrocatalysis, are still on the border, i.e., optical applications are practically linked to the group of M.-W. Chen [149,151,171–175] and the biomedical ones [176–181] are mostly limited to patents,

which are related to nanoporous coatings and therapeutic agents delivering. The structural complexity of NPM in its turn offers an opportunity to play a role of template for fabrication of other structures with 3D porous morphologies.

It is often very difficult to search and find applications for new materials. This also applies to this relatively new and fascinating area of nanoporous metals. After analyzing the literature, it is possible to say that the keyword for the most promising applications is "mixing of functionalities". In other words, one needs to make use of a combination of properties of nanoporous metals. In this way, most probably, if the interest is only in the lightweight of the material there will be an already conventional cheaper material. If, conversely, lightweight combined with energy absorption, or heat resistance, or mechanical properties, or electrical conductivity or self-supporting characteristics is necessary, then the competitive edge of nanoporous metals will be considerably increased. It is therefore of utmost importance that each new idea of an application is evaluated first on identifying the requirement of essential properties and then determine whether there is a nanoporous metal with the desired set of properties and whether any established materials already exist with similar properties. If this is the case, cost will have to be considered to decide which solution is the best.

CHAPTER II. MATERIALS AND METHODOLOGY

II.1. Materials

For producing nanoporous materials based on copper (NPCu), silver (NPS) and cobalt (NPCo), precursor materials were prepared in the form of ingots (Topic II.2) from the ternary systems: Cu-Hf-Zr, Ag-Cu-Si, and Co-Cu-Si. After following procedures described in Topic II.2, the precursor alloys were dealloyed to produce NPCu (Chapter III.1.1-III.1.2), NPS (Chapter III.1.3) and NPCo (Chapter III.1.4), respectively. For the preparation of those precursor materials, high purity metals (at least 99.9+% purity, Alfa Aesar®) in the form of shots and pieces have been used. Finally, to estimate weight losses after the melting step, the differences in weight between the final ingot and initial pure elements were traced. For all the ingots, weight losses were less than 0.5 %.

II.2. Techniques for precursor preparation.

Fabrication of a precursor for a future nanoporous metal is a starting point of the sample preparation process. Depending on the required microstructure for the bulk precursor, equipment availability, geometrical specifications of an experimental setup for further materials characterization, a precursor alloy of an NPM may be synthesized by various means.

Figure II.1 presents a general sequence for precursor fabrication used throughout this work to produce NPMs, which starts with pure metals as raw materials (1). Raw materials are melted by vacuum arc melting (2) and/or by cold-crucible vacuum induction melting (3), producing ingots. Finally, melt spinning is used for producing ribbons from ingots. Characteristic shapes of samples after each processing step are presented underneath its specific equipment for production.

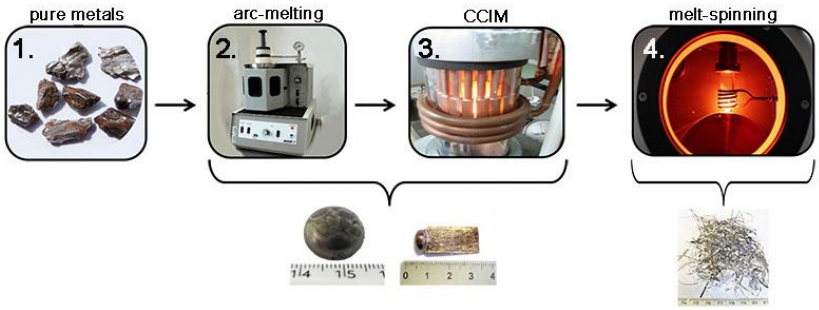

Figure II.1. Steps of precursor fabrication and typical sample shape after processing in arc-melter and cold crucible (2.-3.) and in melt-spinning (4.)

Topics II.2.1 to II.2.3 will describe each one of the types of equipment as follows.

II.2.1. Vacuum arc-melting (VAM) furnace

Vacuum arc-melting (VAM) furnace is the most conventional melting process for producing metal ingots with high chemical homogeneity for technically challenging applications. In the VAM furnace, metals are melted with an electric arc using a non-consumable tungsten electrode in a water-cooled copper crucible inside a vacuum chamber.

In this work, raw materials were melted in an Edmund Buehler Compact Arc Melter; model MAM-1 (Figure II.2), in which the following procedure was used to produce ingots for preparing precursor materials:

(i) The vacuum chamber preliminarily undergoes at least 5 cycles of Ar gas circulation. Before each Ar charge, the chamber is evacuated down to 10^{-3} bar by a small roughing pump, and then the vacuum is purged with Ar up to the atmospheric pressure.

(ii) At the end of the last cycle, just before the melting, Ar is purged down to 450 mbar, keeping an inert atmosphere to avoid oxidation and to facilitate the electric arc formation. Between each remelting, the ingot is turned over, the procedure (i) is repeated, and then the ingot is remelted.

Several Ti getters served as oxygen-traps inside the vacuum chamber to reduce the oxygen reactivity during arc-melting of the target alloy. The resulting microstructure and grain sizes will depend on the cooling of the freshly-formed alloy that takes place inside the chamber through its contact with the water-cooled copper crucible and depends on the contact area and the quality of cooling. Therefore, if a refined microstructure is necessary, suction casting may be used. In this case, specially shaped molds can be used, for instance, the thin sheet-like one, as described in the section III.1.1.

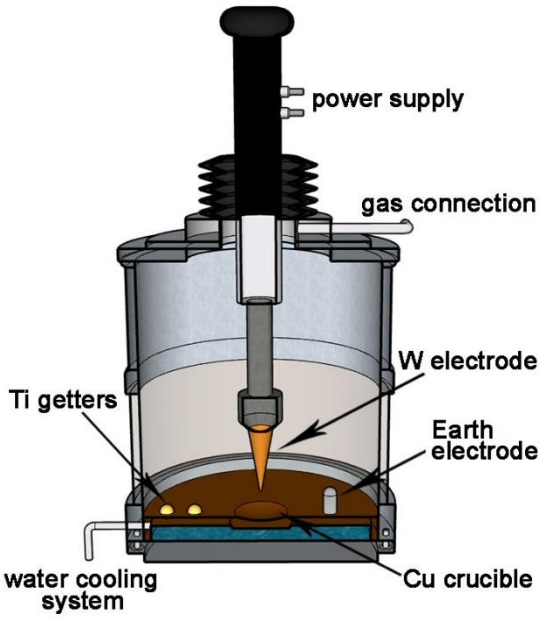

Figure II.2. Schematic view of the chamber of vacuum arc-melting furnace.

II.2.2. Cold-crucible vacuum induction melting (CCVIM)

CCVIM offers the possibilities to melt, cast, and rapidly solidify the alloy at once. Vacuum or gas flowing atmosphere can be used during processing. In this work, the vacuum (~ $7 \cdot 10^{-6}$ mbar) was used for induction melting. Figure II.3 presents an image of the home-made CCVIM chamber used in this work.

Materials to be melted are placed in a water-cooled copper crucible of a half-spherical shape (1). A special cylindrical quartz cap (2) isolates the crucible from the external environment. This whole assembly forms a vacuum chamber being evacuated to the necessary secondary vacuum pressure by a pumping system connected to the main vacuum chamber (3). The crucible is surrounded by an induction coil (4) connected to an induction generator. The coil will then transforms the high-frequency output from the generator into an alternating magnetic field. Such a field produces eddy (Foucault) currents within the material inside the crucible, thus heating it by Joule effect and melting the crucible content [182].

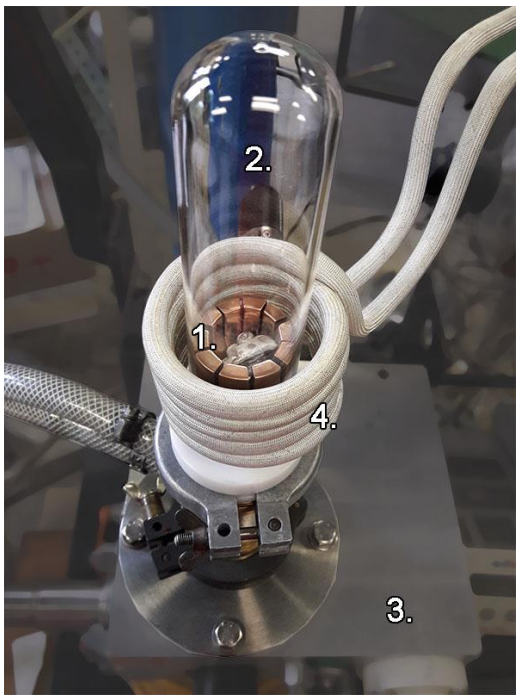

Figure II.3. An image of the home-made CCVIM chamber used in this work.

CCVIM has not been used for homogenization of Cu-Ca due to the risk of Ca evaporation at a given pressure and temperature.

For other alloys, the melting temperature was determined from a phase diagram, and an overheating of about 100 ^{0}C was kept for ~ 2 minutes after melting.

The fast shutdown of the induction current was used to rapidly solidify an ingot inside the cooled crucible.

Once the alloy is melted in CCVIM, it is kept under vacuum during cooling and then removed from the crucible. After that, to remove possible surface oxides and contamination produced as a result of contact with the copper crucible, the button-shaped ingot's external “shell” is ground with SiC paper.

II.2.3. Melt-spinning

Once all pure components of the target precursor are alloyed via VAM, homogenized via CCVIM, and possible contamination from the ingot surface is removed, ribbons can be fabricated by melt-spinning, which produces rapidly quenched thin metallic ribbons, according to the procedure depicted in Figure II.4. The advantage of this technique is the possibility of producing samples with an amorphous structure or crystalline ones with refined and uniform microstructure, which is beneficial for pores formation by dealloying. All final samples, except the ones from the system Cu(Hf-Zr), studied in the present work were produced via melt-spinning with distinct casting parameters.

Our current facility for melt-spinning technique (Figure II.4) consists of the following essential parts:

1) Main casting block, composed of main chamber and sample-evacuation pipes;
2) Copper wheel, maximum linear wheel speed 65 $m.s^{-1}$;
3) Crucible and coil assembly;
4) Atmosphere control system (vacuum pumps, Ar/He gas supply);
5) Water-cooling system (not present here);
6) Power generator Celes Lautenbach MF25AP.

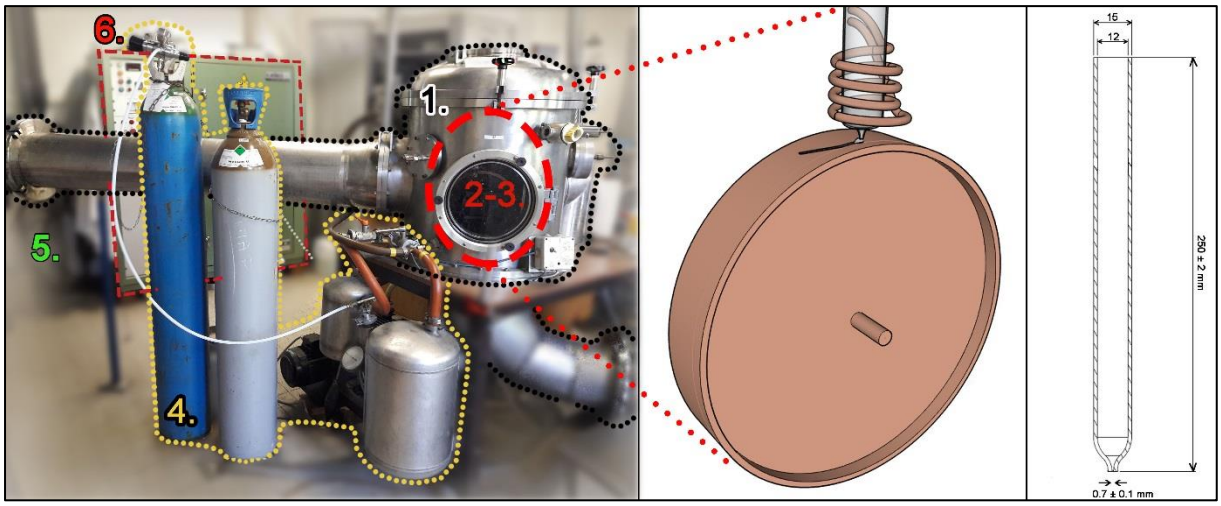

Figure II.4. Melt-spinning setup with a magnified schematic view of the crucible- coil assembly and a geometry of a casting quartz tube.

In short, the formation of a metallic ribbon is the result of the ejection of an induction-heated liquid precursor alloy onto the cooled copper wheel spinning rapidly. The quench speed obtained via melt-spinning technique can be of the order of 10^5-10^6 $K.s^{-1}$.

The induction heating of the sample takes place within a quartz tube having specific geometrical parameters, as on Figure II.4, which will affect the ribbon's thickness and width. Once the metal reaches its melting temperature, the sample is overheated (ΔT_{cast}) in a range between 80 C^0 to 100 C^0 for approximately 10 seconds. Afterwards, an overpressure ranging from 300 mbar to 600 mbar is applied from one of the dedicated chambers of the setup. Thus, a thin stream of the overheated liquid is then dripped through a narrow nozzle of the quartz tube onto the rotating wheel and, subsequently,

cooled. As a result of the interaction between the liquid metal and the highly heat conductive Cu wheel, a puddle consequently transforming into the thin metallic ribbon is solidified on the wheel surface and then detached thanks to the centrifuge force into the sample outlet pipes.

Ribbon's thickness varies depending on the alloy composition, ΔT_{cast}, wheel speed and other procedure parameters [183]. The ribbon's width may vary between 1 and 3 mm depending on the quartz tube's nozzle diameter and on the overpressure of ejection.

II.2.4. Dealloying

For dealloying of binary Cu-Ca precursors to produce NPCu, a simple immersion in distilled water for 6-10 minutes allowed dissolving and removing the Ca species from the alloy. In particular cases, for better assurance of the complete removal of Ca the time was increased up to 1 hour. For all other corrosion procedures, a small volume (~50 ml) of an appropriate etchant has been prepared by diluting and mixing commercial chemicals in distilled water. Subsequently, ribbons or metallic precursors were fixed by corrosion-resistant tweezers and immersed into the solution, which was continuously steered (magnetic steering in 250 rpm mode) for maintaining the mass transport and prevent a re-precipitation of dealloying products. All the experiments were conducted at the room temperature and atmospheric pressure.

In this work, a mix of acid solution of 0.05 M of hydrofluoric acid HF (Alfa Aesar, 48-51 %) with 0.01 M of nitric acid HNO_3 (Alfa Aesar, 68-70 %) has been used for selective leaching of less noble atoms (Hf and Zr) from chill-zone of a quasi-binary $Cu_{90}(ZrHf)_{10}$ alloy at room temperature for 300-600 seconds. The selection of this etchant was partially based on the EH-pH diagram, targeting to get in the region of stable Cu species in the taken acidic solution.

The dealloying of the as-cast ribbons of the $Ag_{38.75}Cu_{38.75}Si_{22.5}$ alloy was performed in 13.4wt% (2.12M) of HNO_3 and in the solution of 0.67 M of HNO_3 and 0.64 M of HF in deionized water. Such etchants has been selected according to the previous work of our research group[57] and adjusted by trying different concentrations ratio and dealloying times to find an appropriate dealloying rate of secondary phases. The etching time ranged from 10 to 90 minutes and was chosen as a way to leave a non-etched layer, with a desirable thickness, in the middle of the ribbon and to allow the formation of a complete NPS structure in the rest of its volume (Chapter III.1.3). Such a layer was preserved in some cases to mechanically reinforce the NPS structure, allowing its use in moving liquids.

Taking into account that cobalt is extremely slowly attacked by a diluted nitric acid, the same solution of 13.4wt% of HNO_3 showed good results after 1 hour of dealloying of Cu-rich phase of Co-Cu-Si precursors. Meanwhile, after trying a number of etchants in diverse concentrations, it was impossible to leach the silicon completely. Therefore, a pure NPCo material was not obtained.

For some samples (Ag- and Cu-based) bubbles were released during dealloying process. Ribbons bleaching occurred almost every time for every type of study material (for example, Figure II.5) meaning that the roughness of the reflecting surface enhance the absorption and "traps" the incident light.

In addition, the dissolution of copper and cobalt in nitric acid media results in the solution coloring. Hence, initially transparent solution acquires a green-blue hue (Figure II.6) during the dealloying of

Ag-Cu-Si and Co-Cu-Si ribbons. Such color change is a common process when it concerns the dissolution of copper metal in aqueous solution of nitric acid because water molecules displace the nitrate ions in the coordinate sites around the copper ions in $Cu(NO_3)_2$ compound [184].

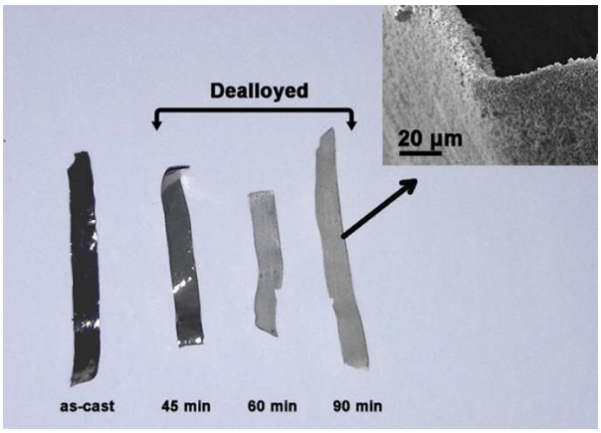

Figure II.5. Evolution of the Ag ribbons color with the etching time. In the inset a magnified SEM image shows a profile of completely dealloyed ribbon.

Figure II.6. Etchant color change during the dealloying of Cu-containing precursors.

II.3. Characterization techniques

II.3.1. Microstructural, elemental and thermal analysis

II.3.1.a. Scanning electron microscopy (SEM)

Scanning electron microscopy is one of the indispensable tools to study nanoporous metallic systems. First of all, no special sample preparation that could damage of drastically modify the

structure is required. Secondly, depending on a particular detector, it is one of the few techniques that can provide both topographical and compositional contrast imaging of the scanned area on the materials' surface. Finally, depending on the electron gun and positioning of detectors (in-lens or not), it can reach the nanoscale resolution.

The SEM uses a beam of accelerated electrons as an illumination source. This beam is scanned across the exposed surface of the sample in sync with the imaging system, thus producing the associated topographical or compositional contrast image. The topographic contrast is obtained by the collection of secondary electrons (SE) and is the most important imaging mode used in this work. SE result from the inelastic interaction of the beam with the specimen, where the energy loss is enormous, but, as a result, SE come out from the outermost surface of the sample, providing images with high spatial resolution. The compositional contrast is perceived by a backscattered electron (BSE) detector. The signal from these elastically scattered electrons depends on the atomic number (Z). Materials composed of elements with highest atomic numbers produces more backscattered electrons than with lower Z elements. Therefore, image areas where the material has a higher average Z are brighter than those where the material has a lower average Z.

The electron microscope used in this work is the high-resolution Carl Zeiss Ultra 55 equipped with a field emission gun (FEG-SEM) and coupled to an energy dispersive X-ray microanalysis (EDS/EDX) system equipped with a 30mm² silicon drift detector (SDD), BRUKER AXS, used for qualitative and quantitative elemental analyses. The microscope resolution is about 1 nm at the intermediate voltage of 15 KV, at 1KV the resolution is of 1.7 nm, allowing the microscope to reach magnifications up to about 1 M times. Figure I.4 of Chapter I presents a trivial example of an image of porous morphology, which was taken in the SE mode at the beam accelerating voltage of 15 kV and has a magnification of 50,000 times (compared to standard Polaroid picture size).

II.3.1.b. Transmission electron microscopy (TEM)

Alternatively to SEM, in the TEM, a high-energy beam of electrons passes through a very thin sample. The interactions (elastic and inelastic) between such electrons and the material can be used to examine the interior of the sample, showing its peculiarities such as the crystal structure and characteristics of the structure like dislocations, substructures and grain boundaries.

The TEM has two operating modes: imaging and diffraction. After passing through the sample, the electron beam experiences Bragg scattering and electrons are dispersed in the back focal plane. By adjusting electromagnetic lenses to the back focal plane of the lens, a diffraction pattern can be generated and projected on a fluorescent screen. For thin crystalline samples with large grain sizes, the diffraction image consists of a spot pattern. As grain sizes are reduced, a series of dotted rings starts appearing. For amorphous materials, a series of closed rings is formed. For large grains, the diffraction pattern is dependent upon its crystalline structure and on the orientation of the specimen in relation to the electron beam. Thus, the formed spot pattern will provide data about space group symmetries in the crystal and its orientation relative to the beam direction.

In the image mode, the lenses are adjusted to the imaging plane rather than the back focal plane. Therefore, depending on the position of the objective aperture, a bright or a dark field image is obtained and provides morphological information in the case of bright field images. Besides morphological

information, among others, dark field images can give information regarding the orientation of precipitates, second phases and, also, for instance, determine the type and position of lattice defects in crystals.

Similarly to the SEM, the TEM can also give a related compositional information and also compositional mapping, when coupled to an EDX system.

TEM technique requires a thin (~100 nm) sample, for the high energy electron beam penetrate through. In this work, to achieve such required thickness, a focused ion beam (FIB) tool (please, refer to section II.3.2.) was used to extract a thin cross-sectional slice of the ribbon, which was fixed to a special TEM-compatible FIB lift-out grid (Figure II.7).

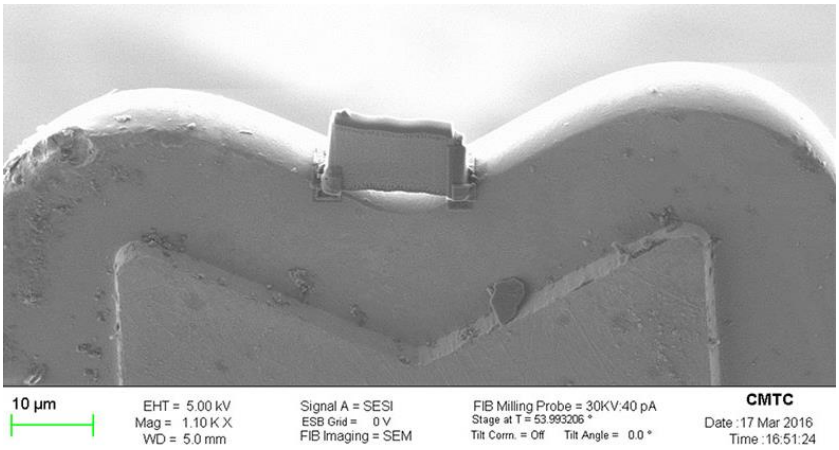

Figure II.7. View of a piece of NPCu ribbon on the tooth of TEM left-out grid.

The equipment used in the experiments was a TEM-FEG JEOL JEM-2100F coupled to an EDX system JEOL Centurio. The acceleration voltage was 200 kV and the beam size was about 1 nm diameter in the NanoBeam Diffraction (NBD) mode. In scanning mode (STEM) it is possible to reach a magnification of several millions, although, in our work a magnification of x400k already allowed to distinguish clearly nano-grains of NPM ligaments. Chemical cartography via EDX was made at up to 40 keV energy of electron transition.

Another relatively recent tool that was used for grain analysis is an Automatic Crystal Orientation and phase Mapping hardware /software package for TEM, commercially known as ASTAR. It consists in scanning the electron beam (with precession or not) in NBD mode over the selected area of the specimen, thus producing a collection of electron diffraction spot patterns, which are recorded by a CCD camera, to be further indexed automatically by cross-correlation of all experimental electron diffraction patterns with all templates from available databases [185].

II.3.1.c. Classic reflection X-ray Diffration (XRD)

Analysis of the microstructure of synthesized alloys has been carried out on PANalytical X'Pert Pro Multipurpose Powder Diffractometer. Primary purpose of XRD analysis is identification of phases with the extension to lattice parameter adjustment and crystallite size calculations. A configuration of diffractometer setup is shown on Figure II.8. An X-ray source and detector are positioned at θ/2θ

Bragg-Brentano goniometric geometry. X-ray of Cu Kα =1.5419 Å wavelength is provided by a Cu tube working at 45 kV/40 mA, 1800 W, a graphite monochromator, associated with the fast X'Celerator detector, is placed before the detector to narrow the band of Cu X-rays wavelength and avoid the fluorescence. The sample is fixed on the stage that rotates at 15 rpm rate and the angular scanning speed varies as 0.6 -1.26 °.min^{-1}. Measurements can be performed in the 2θ range of 10-140 degrees. In present work data collection modes corresponds to the high-speed high-resolution divergent beam diffraction, where programmable divergence slits can maintain a constant irradiated area on sample surface. Further diffraction pattern analysis is performed via PANalytical HighScore Plus software.

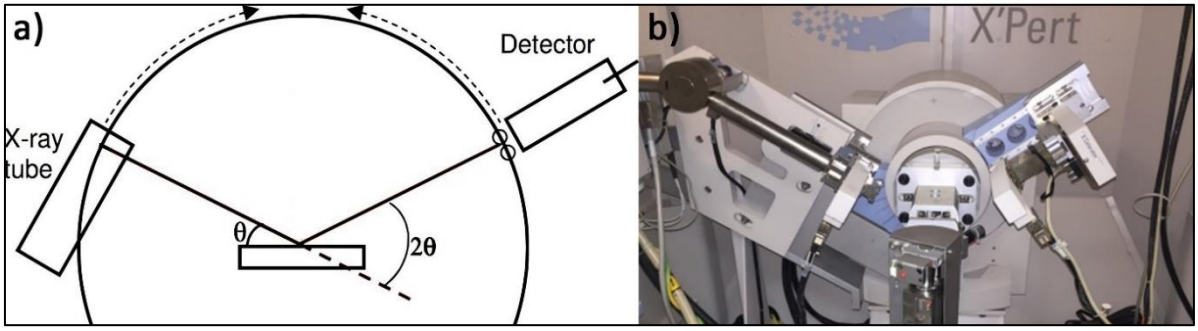

Figure II.8. a) Schematic view of XRD diffractometer in Bragg-Brentano configuration; b) and a photograph of exploited instrument.

II.3.1.d. Thermal analysis

Thermal analysis was conducted by means of differential scanning calorimetry (DSC) in a Perkin Elmer Diamond DSC Q2000 calorimeter with working temperature range [-90 C^0; 400 C^0].

The main purpose of DSC in this work was to characterize the amorphous state of as-melt-spun Cu-Ca (and Co-based) ribbons by observing endothermic and exothermic events, thus determining their glass transition temperature (T_g) and crystallization onset temperature (T_x). A typical curve exhibiting phase transformations in metallic glass and the method of T_g and T_x determination is presented in Figure II.9.

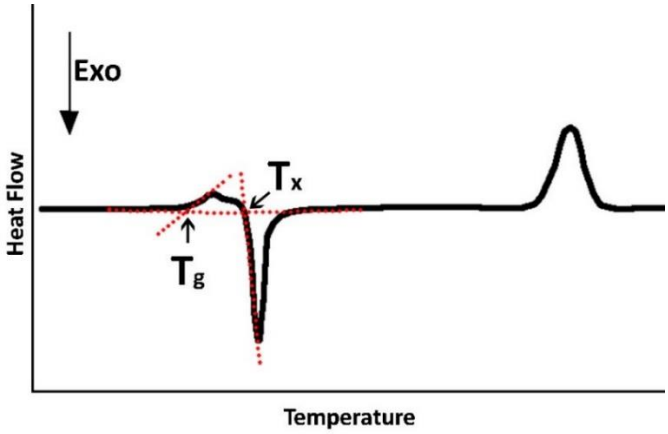

Figure II.9. Typical phase transformation curve for MG during heating and an approach for T_g and T_x definition.

In these experiments, samples were heated from ambient temperature up to the upper temperature limit of the equipment at a heating rate of 20 $K.min^{-1}$ in a nitrogen atmosphere (50 ml/min flow). Samples were held at the given temperature for 3 minutes and then cooled at the same rate down to the room temperature.

II.3.1.e. BET (Brunauer, Emmet, and Teller)

BET is a commonly-used experimental method to determine the specific surface area (S_{spec}) of a porous matter based on a model of physisorption of gas molecules onto the materials' surface at a given pressure and temperature [39]. This technique is valid for materials with a pore diameter > 2nm.

Measurements were carried out in a Micromeritics ASAP 2020 instrument working in nitrogen gas flow at the cryogenic temperature of 77 K. Prior to N_2 adsorption/desorption cycle, the material's interface is "cleaned" of ambient contaminants like CO_2 and H_2O, which may occupy potential pores vacancies, by outgassing the cell for 2 hours at 320 C^0 for NPCu and NPS, and for 5 hours at 120 C^0 for NPCu to avoid structural changes.

The pore size distribution (PSD) can be approached using the method of Barrett, Joyner, and Halenda [186]. The PSD is calculated from experimental isotherms using the Kelvin model of pore filling*.

Even though the BET method has presented a correlation with the numerical approach for S_{spec} determination, its main disadvantage is in the excessive need of examined material (at least a 100 mg and $S_{spec} \geq 1$ m^2 in the experimental cell for an adequate S_{tot} calculation), which was challenging to compromise in current work due to the lack of material.

II.3.1.f. Focused Ion Beam Scanning Electron Microscopy (FIB-SEM) tomography.

Focused ion beam tomography has been proven as a powerful tool for 3D visualization of materials in the nanometer range. Conventional laboratory equipment to perform x-ray tomography is useful only for resolutions down to ~ 1µm, which is about two orders of magnitude larger than our materials' building unit. Hence, the compromises on equipment availability, sample preparation procedure and resolution limit were reached using the FIB-SEM tomography. This type of tomography is based on the repeated removal of the material by a finely focused beam of ions (Gallium source). Between each removal, the imaging of the freshly exposed material cross-section is performed using the SEM mode. Recorded stack of images is processed to generate the dissected volume of interest, which contains the

* According to the research groups of the laboratory of Matériaux Divisés, Interfaces, Réactivité, Electrochimie (MADIREL, Uni. Aix Marseille) and characterization platform of the Institute of research on catalysis and the environment of Lyon (IRCELYON), the recommendation based on unpublished data is to have at least 20 m^2/g for application of BJH method

three-dimensional representation of the microstructure. Schematically this process is presented in Figure II.10.

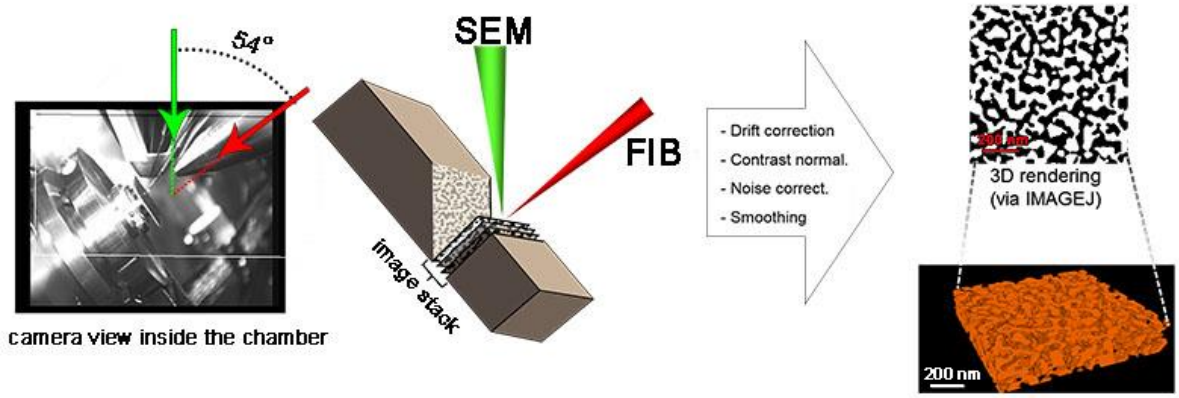

Figure II.10. Principle of FIB-SEM tomography.

FIB slicing, imaging, and tuning of setup parameters were performed in a Carl ZEISS Cross Beam NVision 40 by F. Charlot (CMTC platform, Grenoble). The ion beam acceleration voltage corresponded to 30 kV and the current to 300 pA. The sample is oriented in the sample holder such that the ion beam is perpendicular to the top surface of the sample. The removing cross-section is imaged at the angle of 36° with respect to the beam. However, this distortion is automatically corrected by the built-in software (tilt correction during SEM image). The point of coincidence between SEM and FIB fields of view is a working distance of 5 mm. Each image is recorded, collecting SE at low voltage (5kV), using the SE detector inside the column (in-lens detector). FIB setup parameters were kept as mentioned above for all the studied systems. In case of detected variations in abrasion the defaults were compensated by adjusting the speed of abrasion.

The lowest possible slice thickness was ~ 5 nm that allowed us to achieve a three-dimensional resolution, characterized by a voxel size of 5 nm^3. The slicing of 5 nm corresponds to the z-step between each image. During milling, there is an automatic correction of the focus based on this z-step. The milled-away volume of the studied material needs to represent the entire structure and the processing time needs to be reasonable. Therefore, a total amount of 100 – 150 sectioning have been performed depending on the sample type that makes it a block with z-dimension width of 500-750 nm (containing at least 10 unit porous cells).

The corresponding dimension was kept for the x-direction, while the ribbon's thickness (typically 20-30 µm) limits the y-dimension. The entire acquisition time depends upon a milling time and an imaging time. The average milling time for a step of 5 nm is around 10 % - 20% of the imaging time. The scanning speed of the beam must be low to allow a high signal-to-noise ratio. The imaging time of one image is around 1 min. This time is a good compromise between image quality and duration of the whole experiment. Moreover, if the scanning is too long, some drift could appear in the image due to a larger electronic dose per point.

A raw stack obtained after multi-slicing is post-treated to correct defaults (drift, contrast illumination, the gradient of background, sharpness, etc.) and to obtain a 3D reconstruction. Such

processing, 3D visualization and quantitative analysis of the microstructure, is performed using the ImageJ/Fiji [187] and Avizo Light 9.2.0 Softwares.

II.3.2. Image analysis

Throughout this work, a significant contribution of data comes from images obtained mostly via SEM and FIB-SEM facilities. These images include information on the microstructure of samples such as nanopore substrate's ligament and pore size, connectivity, porous fraction, etc. Thus, to extract required parameters adequately, a particular image treatment procedure needs to be applied. The easily accessible and user-friendly image processing software ImageJ (Windows version, Ver. 1.50b, 64 bits) and its extended version with built-in plug-ins package Fiji Life-Line version (2015) was our first choice for this task. Some of the implemented plug-ins have been developed in SIMaP-GPM2 by P. Lhuissier, L. Salvo and V. Boulos [188] and are described hereafter:

- Structural elements like ligament and pore size were measured using the "straight line" function. All marked elements are registered in "Region of Interest Manager" window, from where they can be exported to Excel or Origin for further treatment (average value, statistical distribution, etc). An average of at least 100 measurements was made for microstructure characterization of each sample. Figure II.11 presents an example of length measurement of NPS ligaments using Fiji;

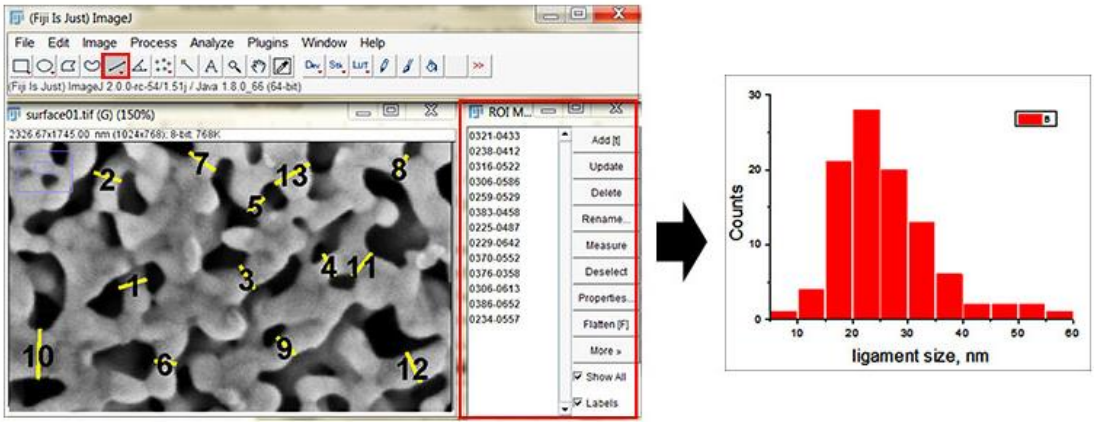

Figure II.11. An example of length measurement of NPS ligaments using Fiji. Each measurement is enumerated and displayed in the ROI manager window.

- Some standard image treatment procedure can be applied to reduce the noise; smooth the image; tune brightness and contrast to reveal informative details;

- A thresholding command (Figure II.12) is applied to estimate the solid/porous fraction of the material, (Image → Adjust → Threshold). Thresholding works by choosing a cutoff value, such that every pixel less than this value is attributed to one class, while every pixel greater than that value is considered the other class. Thresholding value is chosen by the eye of the user and can be supported by the image histogram (Analyze → Histogram) that gives a

number of pixels of each color (0 – black; 1 - white). The thresholding error can reach up to 10%.

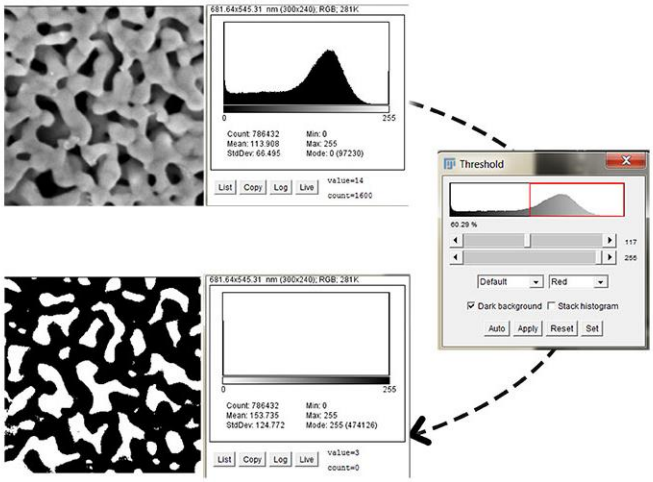

Figure II.12. Thresholding applied to SEM image of NPS to estimate a porous and solid phase fraction.

- Creation of image stack, obtained by FIB-SEM (Plug-in → Registration → StackReg) and correction of possible noises and drift ("Median filter" to remove bordering pixel noise, "Normalize local contrast", "Linear stack alignment with SIFT", "Bilateral filter" plug-in). The last step, after the stack, is successfully registered and corrections are introduced, is to apply a threshold to all the images of the stack and to visualize via Java plug-in (Plug-in → 3D viewer). This process is resumed in Figure II.13.

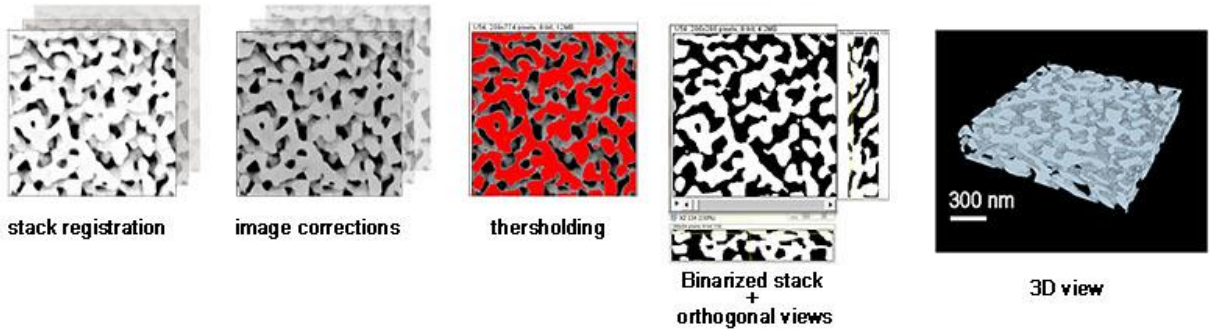

Figure II.13. Scheme to realize 3D model reconstruction via Fiji software on the example of NPS.

A combination of Fiji and Avizo (3D visualization and analysis software FEI™) functions was used for 3D volume analysis of compiled 3D nanoporous model.

Granulometry and connectivity measurements are performed in Fiji by "Analysis 3D" plug-in Version 1.3.2 (01/02/2016). Granulometry is a tool to extract size distribution from binary images by performing series of morphological openings of voxels of increasing size. In present work, we made 3D granulometry using octahedron structural element. Connectivity of the structure carries the information about the isolated voxels that constitute the total free-floating volume.

Binary 3D volume model file can be imported into Avizo software where, through the combinations of various modules, a 3D surface of the corresponding volume segment can be generated. The morphology of the NPM is characterized by discretizing the interface into many small triangles' patches and, if an appropriate smoothing is applied, one can calculate the total surface area ("Measure and Analyze" module); principal curvatures, $\kappa 1$ and $\kappa 2$, of every patch ("Curvature" → "Both curvatures" module); its curvedness $C=\sqrt{\frac{k_1^2+k_2^2}{2}}$ and shape index $S = \frac{2}{\pi}\arctan\frac{k_1+k_2}{k_2-k_1}$ ("Curvature" module with "nLayers" = 8, "nAverage" = 5 parameters values). Using the obtained information, the interface shape distribution (ISD) can be determined.

In this work, the ISD is represented as a 2D-histogram and gives a probability of finding a patch of interface with a given shape factor, and curvedness.

Variation of the shape S is represented in Figure II.14 and runs from concave cup (S = -1) to convex cap (S=1).

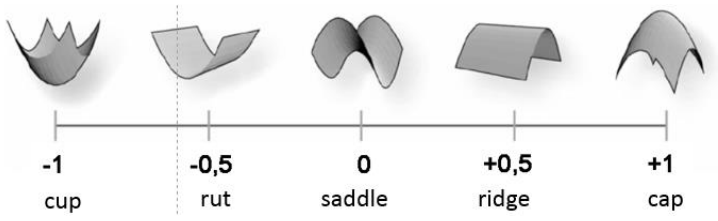

Figure II.14. Evolution of surface shape, depending on S value.

While the shape index captures the intuitive notion of 'local shape', curvedness is always a positive number that specifies the amount or "intensity" of curvature, for example, C = 0 is a flat surface [189,190].

II.3.3. Mechanical characterization

Nanoindentation experiments were carried out to determine Young's modulus, hardness and reveal possible pop-ins of the nanoporous silver ribbons of two different microstructures. An instrumented TI 950 TriboIndenter from Hysitron equipped with a Berkovich tip was used. Prior to indentation test, SPM (Scanning Probe Microscopy), which consists in scanning the sample with the indentation tip, is used to record a topographic image and thus to assure flatness of the investigated surface and absence of surface anomalies. An area of 10 μm^2 is imaged at 10 $\mu m.s^{-1}$ speed.

Indentation depth was kept around 400 nm due to several reasons. First of all, in order to make representative measurements of the material, the displacement should be enough profound compared to its pore size (~ 50 nm). Secondly, since some samples are only partially dealloyed, they possess an intermediate bulk non-porous layer. To reduce the influence by this dense layer, the displacement cannot exceed $1/10^{th}$ of the studied porous layer's thickness (~ 4 µm). Lastly, roughness of the surface affects the precision of the measurements at low displacements (< 30 nm), imposing to use deeper indents.

Nanoindentations were carried out in two modes: Quasistatic (QSt) and Dynamic Mechanical Analysis (DMA) for which an oscillating force is applied. For each DMA measurement, an increasing

normal load was applied up to a maximum value of 10 mN. To simulate a constant strain rate, the loading rate was exponentially increases from 31 to 1192 $\mu N.s^{-1}$. To keep a nearly constant displacement amplitude (around 1-2 nm), the oscillating load amplitude varied from 5 to 100 µN. The oscillating frequency was 220 Hz (Figure II.15.b). QSt measurements were made at a constant loading rate of 100 $\mu N.s^{-1}$ up to a maximum force of 900 µN which was maintained for 2 s and then unloaded at the same rate (Figure II.15.a). At least 8 DMA and 30 QSt measurements at different positions were carried out for each sample.

Lastly, for the study of possibly present pop-ins and surface deformation effects, a series of slow-rate quasistatic nanoindentation tests has been performed on one of the nanoporous substrates with the highest porous fraction. The experimental parameters are: 1 $\mu N.s^{-1}$ loading rate up to a maximum load of 80 µN which was held for 5 s (loading/unloading time of 80 s). The maximum penetration depth was 120 nm (Figure II.15.c).

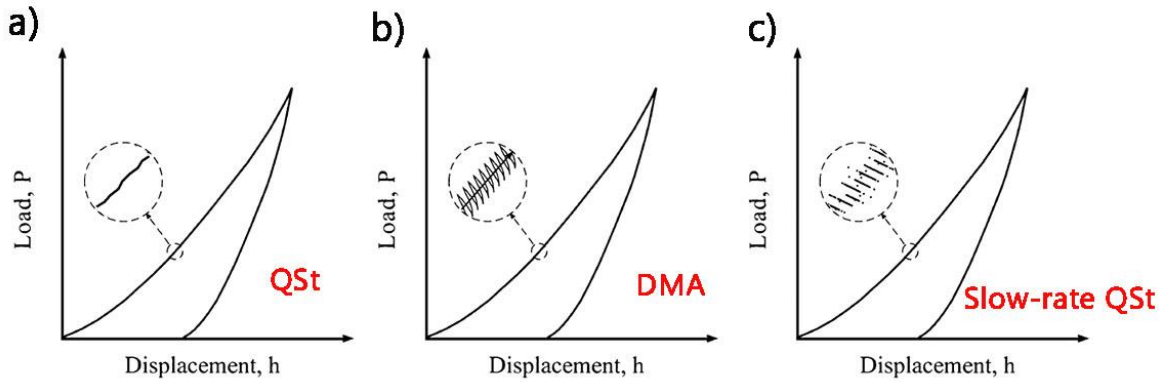

Figure II.15. Schematic of the a) Quasistatic b) Dynamic Mechanical Analysis c) Slow-rate QSt loading cycles.

Hardness H and reduced Young modulus E_r (which represents elastic deformation that occurs in both sample and indenter tip) are calculated from the unloading process of depth-sensing indentation tests as:

$$H = F_{max}/A \text{ and } E_r = \pi^{1/2}S/(2A^{1/2})$$

$\boldsymbol{F_{max}}$ is the maximum applied load to the indentation area, $\boldsymbol{A}$ is the contact area between the indenter and the specimen, projected into the plane of the surface and dependent on the contact depth $\boldsymbol{h}$ of the indenter with material, $\boldsymbol{S}$ is a stiffness defined via the slope of the upper portion of the unloading curve. Reduced modulus is related to the Young modulus of the material through the formula [191]:

$$\frac{1}{E_r} = \frac{1-\nu_i^2}{E_i} + \frac{1-\nu_s^2}{E_s}$$

Where $\boldsymbol{\nu}$ is the Poisson ratio, $\boldsymbol{E}$ is the Young modulus, $\boldsymbol{i}$ and $\boldsymbol{s}$ stand for indenter and sample.

Thus:

$$E_s = \frac{1 - \nu_s^2}{\frac{1}{E_r} - \frac{1 - \nu_i^2}{E_i}}$$

The $\frac{1-\nu_i^2}{E_i}$ component ≈ 0.0009 GPa^{-1} for the used diamond indenter, and the Poisson ratio $\boldsymbol{\nu_s}$ of the material is taken 0.38 [192].

Samples of nanoporous silver were prepared by dealloying according to the procedure described in the section II.1.3. Different etching times resulted in the formation of different average ligament and pore sizes. For nanoindentation tests two microstructures with the porosity of ~ 45.5 ± 5 % and 53 ± 6 % have been produced. Prior to dealloying, each NPS specimen was polished to improve surface flatness and to remove surface oxides. After dealloying, samples were fixed to the small piece of glass sheet using a thin layer of cyanoacrylate glue. Final view of samples, prepared for nanoindentation experiments, is present on Figure II.16.

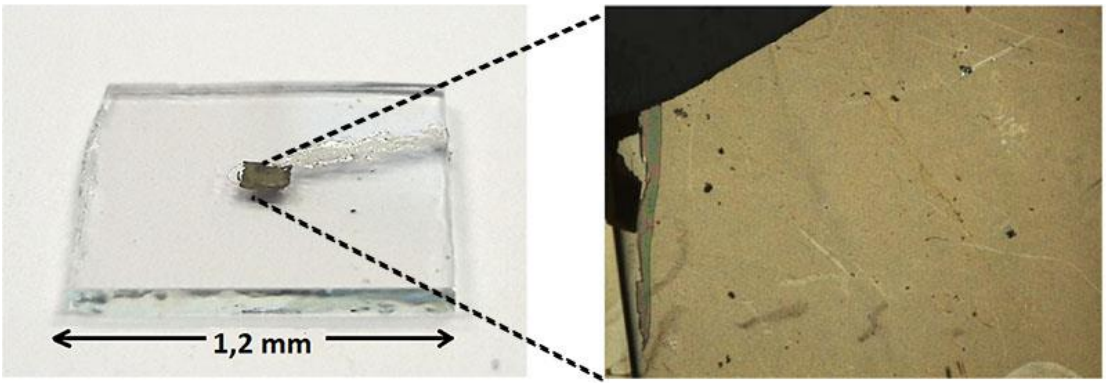

Figure II.16. General and magnified surface view of NPS sample glued to the glass substrate.

II.3.4. Electrochemical characterization

The general approach of electrochemical characterization of studied integral nanoporous substrates was based on testing the functionality of so-called "half-cell" assembly. A complete fuel cell of any type is composed of anode, cathode and electrolyte. Catalyzed oxidation of appropriate fuel on anode of the cell results in energy conversion. In half-cell method we make a simulation only of these anodic processes, and high surface nanoporous materials play a role of anode catalyst.

Such practical valorization of synthesized nanoporous metallic substrates was the result of collaboration with the Laboratory of Electrochemistry and Physicochemistry of Materials and Interfaces (LEPMI), Anicet Zadick and Guillaume Braesch with the lead of Pr. Marian Chatenet.

Experimental procedure for electrochemical tests has been motivated by the current interests of LEPMI in liquid fuel cell operation, notably, the direct valorization (electrooxidation) of chemical hydrogen storage compounds (e.g. ammonia-borane (AB), NH_3BH_3). The direct electrooxidation of AB is very energetic, owing (i) to the high inherent capacity of H_2 of AB and (ii) to the fact that the reaction can proceed at very low electrode potential. Classical Pt-based fuel cell catalysts are however

not the materials of choice for this reaction. Firstly, the alkaline stability of carbon-supported noble electrocatalysts is really questionable [193–196], in addition, the direct AB oxidation reaction on Pt is competed by its chemical decomposition and hydrogen evolution/oxidation reactions, overall consisting of a quantitative current only above the reversible hydrogen potential [193–195]. On the contrary, non-noble electrocatalysts are less subjected to these bias [197]. Hence, it became attractive to integrate our Ag- and Co-based catalytic substrates into the Direct Ammonia-Borane Half-Fuel Cell (DABHFC) assembly and verify materials catalytic activity, onset potential for AB oxidation V_{onset}, stability of performance and degradation rate. The results of electrocatalytic performance of NPMs are presented via cyclic voltamperograms in the section III.4 of this manuscript. DABHFC setup is displayed on the Figure II.17.

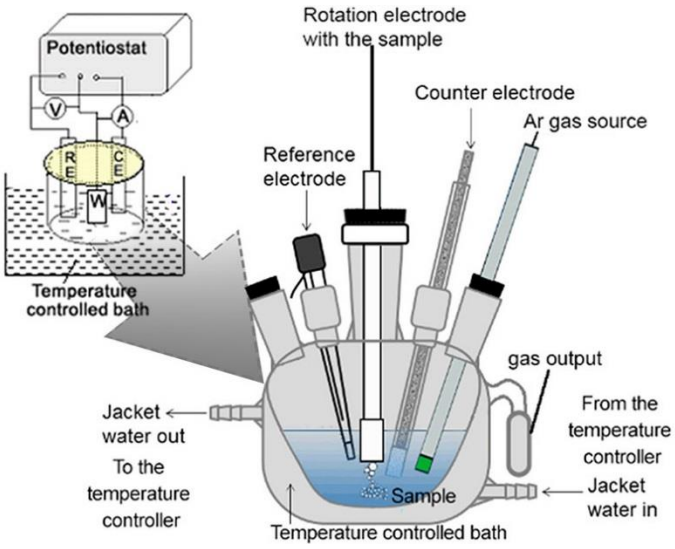

Figure II.17. A schematic view of electrochemical setup: 3-electrode cell in a temperature controlled water bath, connected to argon gas supply and to the power source.

In a three-electrode electrochemical cell setup, used in this case, we applied a potential difference between the working electrode (WE) and the reference electrode (RE). As this potential varied in a cyclic way within the fixed limits (-0.3 V; 0.5 V vs. RHE), we measured the current change between the electrodes. Recording of I(V) variations results in cyclic voltamperograms that carry information on the catalytic properties of our NPM substrate. In this study WE is an electrode of rotation type (Rotation Disk Electrode - RDE), this is to provide an adequate mass transport through the porous substrate in the contact with the WE. Rotation speed ω may vary between 0 and 2500 rotations per minute (rpm).

For the electrochemical experiments, NPM materials were carefully cut and placed on a glassy carbon electrode to be used as working electrode (see Figure II.18); geometrical surface of NPM in contact with the electrolyte was calculated prior to experiment. The counter electrode (CE) was a carbon plate, and the reference electrode was a mercury/mercury oxide electrode (Hg/HgO) filled with 0.1 M NaOH solution; to ease the comparison with the literature, all potential values are given versus the Reversible Hydrogen Electrode scale (RHE). Electrolytes were freshly prepared with NaOH

monohydrated provided from Merck (Suprapur), ammonia-borane provided from Sigma-Aldrich (AB complex, 97%) and MQ-grade water (18.2 MΩ cm, 3 ppb total organic carbon, Elix + Milli-Q Gradient, Millipore). The electrochemical set-up was thermostated at 25 °C. Potentiostat model is BioLogic VSP.

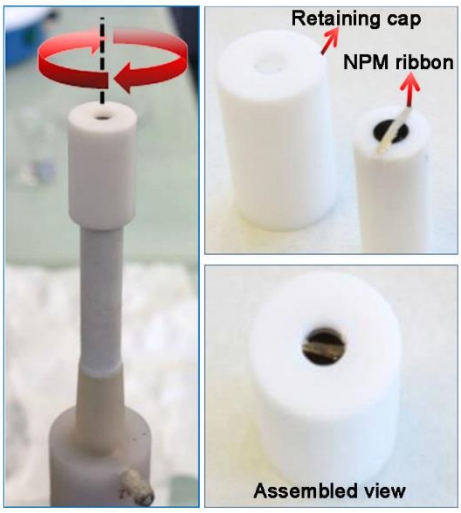

Figure II.18. A rotation disk electrode and sample assembly. A special Teflon cap is used to provide a sample contact with the carbon surface.

II.3.5. Raman Spectroscopy

The principles of surface-enhanced Raman spectroscopy and the role of each constituent in the enhancement have been introduced in the section I.8 of the first chapter. The Raman spectroscopy is based on the inelastic (Raman) scattering of a monochromatic light (laser) by the molecule of interest. The shift in the reflected wavelength carries the "fingerprint" of the target molecule. Plotting the intensity of the shifted lighted versus the incident light frequency, one will obtain a Raman spectrum of the material.

The main part of presented SERS experiments was performed in the framework of collaboration with the Laboratory of Metallurgy at the University of Turin by Dr Alessandro Damin. Micro-Raman measurements were performed with a Renishaw in Via Raman Microscope using a laser line of 514 nm, with an acquisition time of 10 and 60 s, a power at the sample of 0.5 and 0.25 mW, and an ULWD objective of 50 ×. Laser's spot diameter (d) was approximately 2 µm. Rhodamine 6G was chosen as a probe molecule since it is photostable, suitable for the standard blue-to-green excitation. The validation for this type of experiments on Ag- and Cu-based substrates has been confirmed by other works.[173,198,199] Prior to SERS experiments, the NPM samples were immersed in the water solution of R6G with concentrations ranging from 10^{-4} to 10^{-14} M for a time ranging from 10 seconds to 48 hours, enabling the probe molecules to be adsorbed on the surface. Measurements were performed on the surface of sample after drying in air. Each sample was measured at six different surface spots, and the average representative spectrum is exhibited (section III.4.3). All solutions of this experiment were prepared from chemical grade reagents and de-ionized water.

CHAPTER III. EXPERIMENTAL RESULTS AND DISCUSSIONS

III.1. Materials precursors, synthesis and characterization of their nanoporous counterparts

As it was highlighted previously, the state of a precursor for nanoporous metal, its composition, phases present, the scale of phase separation, and other numerous parameters of chemical dealloying affect the final nanoporous structure of the system. In the present section precursors for copper-, silver- and cobalt-based systems are introduced and characterized by XRD, DSC, scanning and transmission electron microscopy coupled respectively with EDX, and automated crystal orientation mapping in TEM (ASTAR). The dealloying process is described for each material correspondingly. Basic characterization of constituent parts of resulting nanoarchitecture structures (pores and ligaments) is further presented. An intermediate comparison among the studied systems and preliminary conclusions are made at the end of this chapter.

III.1.1. Nanoporous copper surface from the chill-zone of bulk $Cu_{90}(ZrHf)_{10}$ alloy.

Results presented in this subchapter are founded on the earlier work carried out by our research group and reported in [200].

Synthesis of the nanoporous copper surface from a copper-based alloy was performed via leaching the less-noble (LN) element rich-phase out of locally nanostructured ternary Cu–Hf–Zr alloys. The precursor used in these experiments was a rapidly solidified ingot of the $Cu_{90}(ZrHf)_{10}$ quasi-binary composition family alloy. Copper mold casting was performed by injection of liquid alloys into the cavity of cylindrical shape, placed into the massive copper mold. A fragment of the as-cast $Cu_{90}Zr_5Hf_5$ is presented in Figure III.1. Initially, the idea behind the development of this family of alloys was to increase the hardness of existing copper alloys with a possibility of color tailoring, since this may prolong the material lifetime and affect the demand for everyday human usage objects (door handles, coins et other countless things). Moreover, these reported specimens were the hardest copper-based ones known to date. Such advantageous mechanical properties were related to the formation of a scratch-resistant thick isotropic nanocrystalline chill-zone (Figure III.2 next to the area where the copper mold touches the sample surface).

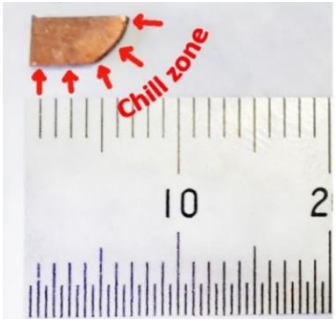

Figure III.1. A photograph of an as-cast $Cu_{90}Zr_5Hf_5$ sample fragment, with an indication of the chill-zone localization.

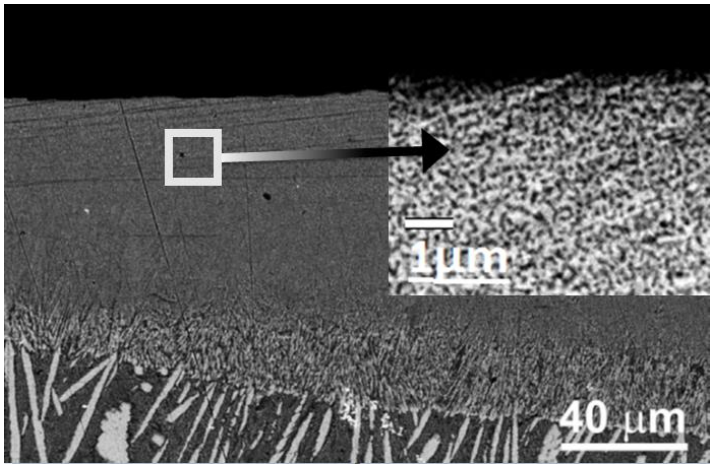

Figure III.2. SEM image of a cross-section perpendicular to the mold surface of the as-cast hypereutectic $Cu_{90}Zr_5Hf_5$ alloy. A 200–300 µm thick isotropic layer appears next to the mold contact surface and wraps the core of the casting. Magnified insert demonstrates a phase variation on the scale of ~ 100 nm. Images are acquired in QBSD mode.

As a matter of fact, looking at the material from the structural point of view and keeping in mind the possibilities offered by corrosion, one may suggest achieving a nano-roughening of the present specimen by appropriate chemical treatment. According to the data reported in the previous work[200], and as it is confirmed by SEM picture in Figure III.2., there are two phases composing the chill-zone - Cu_5Zr and Cu_5Hf intermetallics in the Cu-fcc matrix. The typical size of the Zr- and Hf-rich compounds lay in nanometer scale. Therefore, selective leaching of the chill-zone layer will theoretically result in the creation of nanocavities (pores) in the zones, previously occupied by less-noble phases.

Samples of $Cu_{90}Zr_5Hf_5$ alloys were placed in the chemical solution and treated according to the procedure in section II.1.3. The evolution of the surface morphology of $Cu_{90}Zr_5Hf_5$ alloy chill-zone with the leaching time is shown in the Figure III.3 (a, b). After leaching the chill-zone for more than 300 s, Zr- and Hf- rich intermetallic compounds start to be removed from the alloy, and the material surface becomes nano-roughened. The most homogeneous structure was obtained after leaching for 600 s (Figure III.3.b). The EDX spectra presented in Figure III.3.c shows that after 600 s only Cu peaks are detected (O and C come from the residual atmosphere). Zr and Hf atoms bonded with some copper atoms have been removed and are associated with the porosity in the Cu skeleton. The average size of surface pores is below 100 nm, while the grain size is below 50 nm. The thickness of the porous layer can be controlled by varying the etching time, while maintaining the bulk material with intact structural features and good mechanical properties. In the conditions used to perform EDX (15 keV), the X-ray range from the sample depth was estimated to be at least ~0.4 µm. This value was calculated according to the following formula, which was modified from the Kanaya and Okayama's one [201] and is available in the EDX user's manual from Link Systems [202] (nowadays Oxford):

$$R = \frac{4120}{\rho} E^{(1.265-0.0954\ln(E))}$$

$\boldsymbol{R}$ is the penetration in microns, $\boldsymbol{\rho}$ is material density (g.cm^{-3}) and $\boldsymbol{E}$ – primary electron energy (MeV).

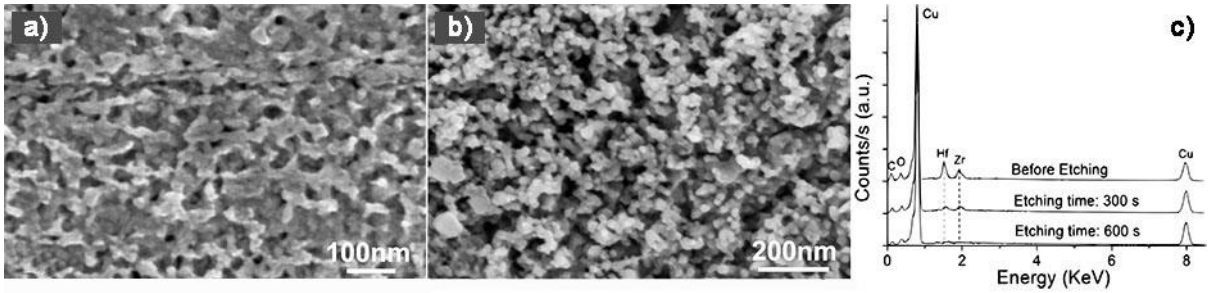

Figure III.3. High magnification SE-SEM images of the $Cu_{90}Zr_5Hf_5$ surface after leaching in 0.05M HF 0.01 M HNO3 water solution for 300 and 600 s respectively (a and b); EDX spectrum showing the evolution of elemental composition before and after leaching (c).

The fact that surface porosity is principally formed thanks to dissolution of Zr and Hf intermetallics and not of the copper matrix can be supported by E/pH diagram of corresponding elements in the present chemical medium (Pourbaix diagrams) [120,203,204] (Figure III.4).

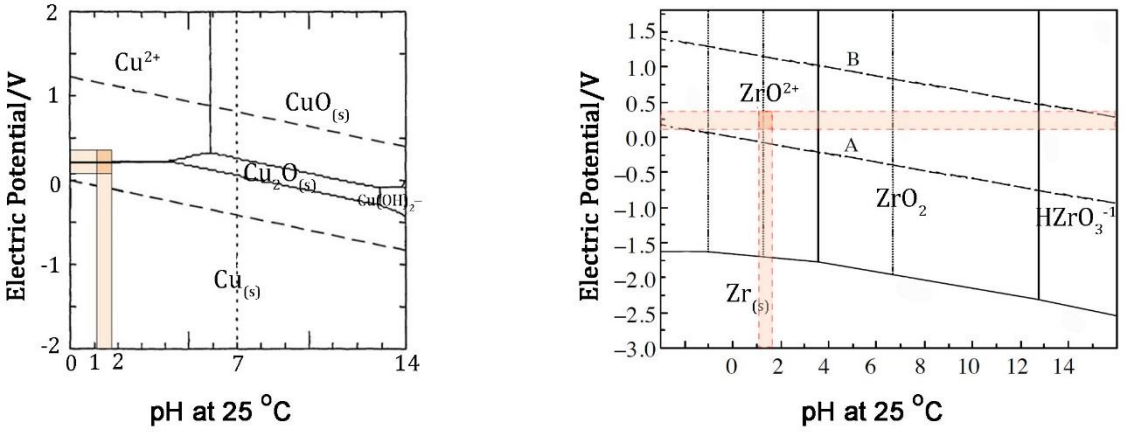

Figure III.4. Pourbaix diagrams of copper (left) and zirconium (right), showing the regions of immunity (for Cu) and corrosion (for Zr/Hf) state in the pH and potential region of interest.

In our experiment, we used a control carbon electrode and a saturated calomel electrode as the reference one. The whole etching process conditions were repeated. During the alloy etching, the electric potential variation was recorded in the range 0.09-0.39 mV, the solution's pH was about 1.22. Having a pH<5, according to Pourbaix diagram, one expect to have either stable copper (Cu^0) or aqueous species after reaction with the medium (Cu^{2+}), which dissolves into the solution. In any case, at given conditions, copper stability is higher than the stability of Zr and Hf, whose Eh-Ph diagrams are similar at pH<5 [204,205]. That gives us a reason to assume that the porosity initiates in Zr and Hf-rich phase.

III.1.2. NPCu from initially amorphous family of Cu-Ca alloys

III.1.2.a. Formation and microstructural characterization of as-spun Cu100-xCax ribbons

The role of the amorphous state of the precursor in dealloying and advantages for fine and homogeneous terminal porosity has been discussed in I.4.2 section. Other facts such as easy amorphization in a wide range of compositions, the convenient melting temperature of the alloy, commercial availability and non-toxicity of constituent elements favored the choice of further study of Cu-Ca binary system. A series of amorphous $Cu_{100-x}Ca_x$ precursors were fabricated via melt-spinning (section II.1.3.) of binary alloy ingots. Such alloys were obtained by direct induction melting of pure Ca and Cu elements inside a quartz tube crucible before casting and skipping pre-alloying via VAR or CCIM. Shunning of these intermediate steps was due to the high reactivity of Ca metal, which has low evaporation pressure at high temperatures. Moreover, when in contact with a piece of pure copper metal with cooled copper crucibles of VAR and CCIM, the heat transfer to crucibles was huge, preventing the metal from melting and avoiding its alloying with calcium. Thus, the only viable way for Cu-Ca alloy synthesis was achieved through direct melt-spinning. Casting took place in a reduced argon atmosphere, at the rotation wheel speed of 60 m/s and a casting temperature (T_{cast}) between 500-750 ^{0}C. Samples acquired a shape of ribbons of 10 - 20 µm thickness and 2 mm width, as shown in Figure III.5.

Figure III.5 A photograph of binary Cu-Ca melt-spun ribbon.

The studied interval for $Cu_{100-x}Ca_x$ (at%) alloy compositions varied with x ranging from 35 to 80, as indicated by arrows in the phase diagram of Figure III.6.a.

According to the work of R. St. Amand and B.C. Giessen [206] selected compositions fall within the glass forming (G.F.) ability range for the given alloy system (Figure III.6.b). As-cast samples have exhibited perfect bending ability and brilliance, showing first signs of the amorphous state. Eventually, such an amorphous state has been confirmed by XRD (Figure III.7) and selective DSC measurements for $Ca_{40}Cu_{60}$, $Ca_{50}Cu_{50}$, and $Ca_{70}Cu_{30}$ compositions.

XRD patterns in Figure III.7 shows those compositions with amounts of Ca higher than 35 at% present broad diffuse peaks typical for amorphous structures. Besides, the position of the main amorphous halo shifts to the left with the growth of Ca amount, reflecting changes in atomic density, and giving a sign that different amorphous phases have been formed.

The nature of a crystalline peak at 18 degrees is not completely understood yet, but according to reported data, all indications are that it might be $Ca(OH)_2$ [207] surface compound, formed as a result of Ca reaction with humid air according to the sequence of reactions [208]:

$$2Ca_{(s)} + O_{2(g)} \rightarrow 2CaO_{(s)} \text{ (calk)}$$

This reaction is exothermic with the ΔH = -221 kJ/mol. On air and calcium oxide CaO has a probability to react with diffused water molecules and form calcium hydroxide:

$$CaO_{(s)} + H_2O_{(g)} = Ca(OH)_{2(s)}$$

With the ΔH = -109 $kJ.mol^{-1}$.

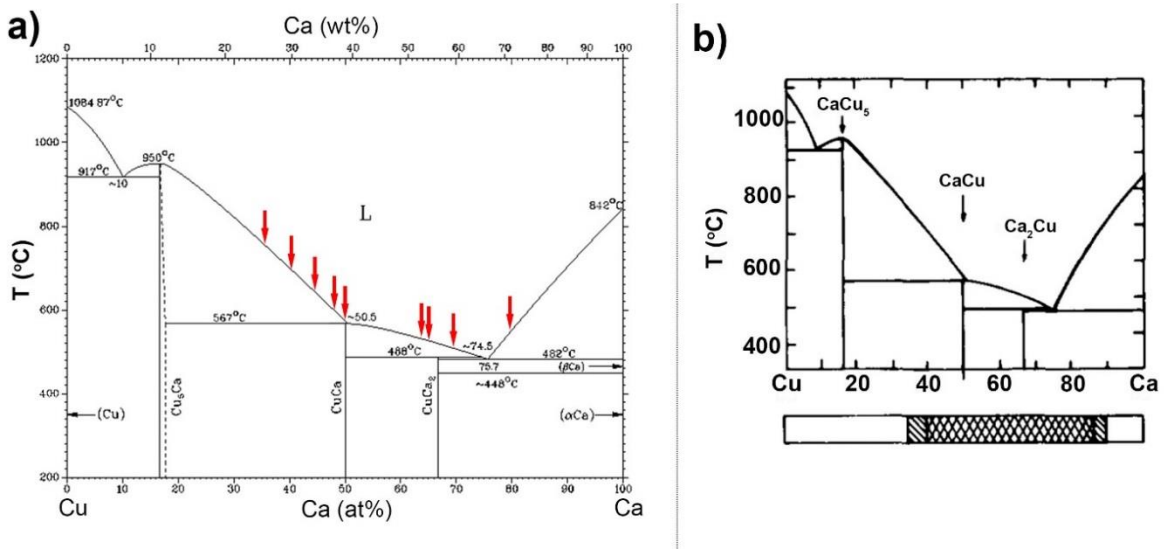

Figure III.6. a) A binary Cu-Ca phase diagram with indicated casted compositions; b) Ca-Cu diagram with corresponding composition ranges of easy glass formation (cross-hatched range: complete G.F. observed; hatched regions: G.F. possible), adapted from [206].

Figure III.8 presents DSC scans for $Ca_{40}Cu_{60}$, $Ca_{50}Cu_{50}$, and $Ca_{70}Cu_{30}$ compositions showing that, before a large exothermic crystallization peak, every DSC curve exhibits a small endothermic event, thermally manifesting a rise in specific heat (C_p) and characterizing a glass transition temperature (T_g). Also, one can see that T_g of all specimens is very low, < 140 ^{0}C. Between 150-170 ^{0}C materials start crystallizing, and at temperatures higher than 300 ^{0}C, they become fully crystallized.

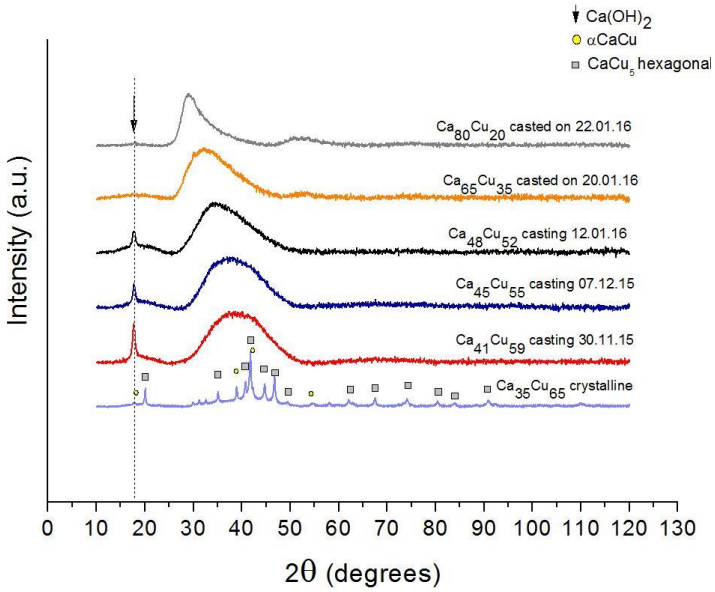

Figure III.7. X-ray diffraction patterns of as-spun $Cu_{100-x}Ca_x$ samples, showing wide G.F. region of compositions. $Ca_{35}Cu_{65}$ corresponds to crystalline precursor, as in agreement with literature [206].

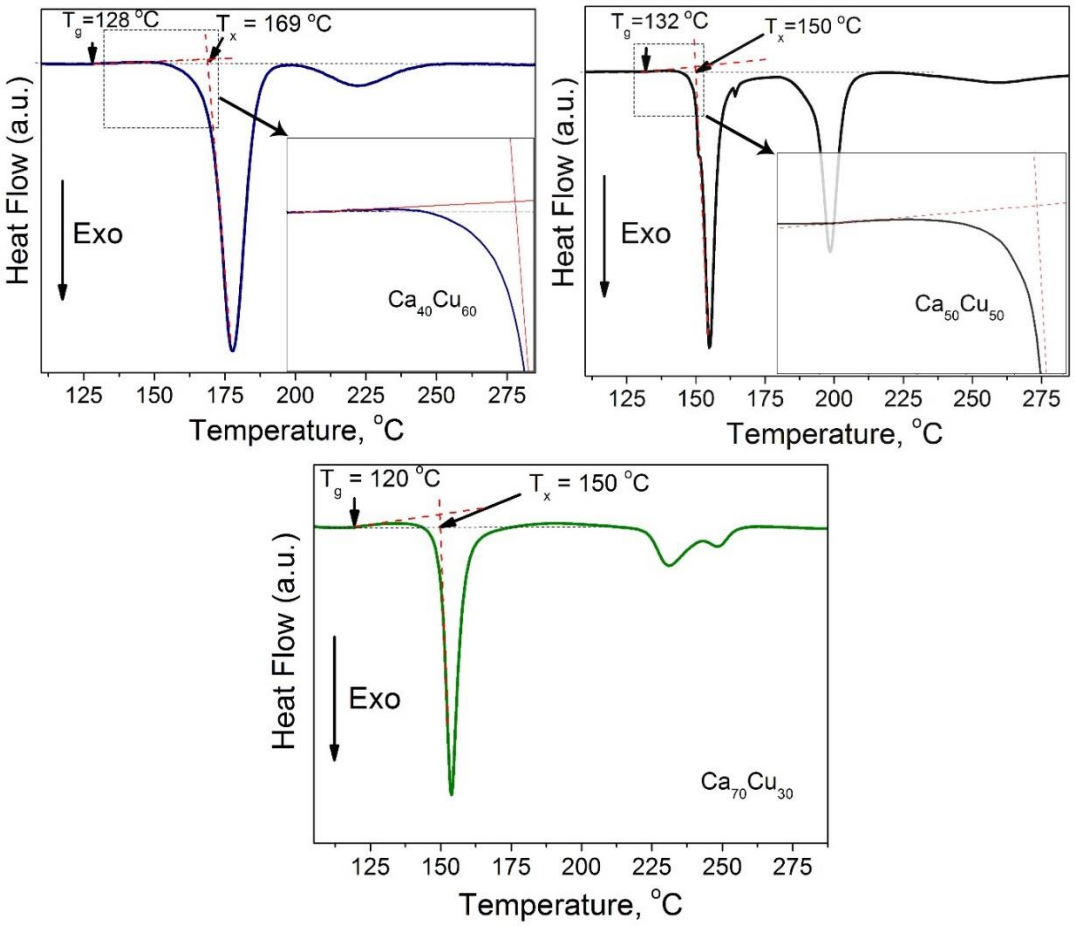

Figure III.8. DSC scans of three representative Cu-Ca compositions up to above the crystallization temperature, containing the endothermic (pointing upwards) glass-transition peak and identified T_g temperatures.

III.1.2.b. Dealloying of amorphous $Cu_{100-x}Ca_x$ ribbons

Calcium is the fifth element in abundance on the Earth, and pure Ca metal can directly react with water at room temperature [209]. If one considers such features, Cu-Ca alloys should be excellent candidates as precursors to be dealloyed to nanoporous metals using harmless and low-cost chemicals.

Among a series of synthesized ribbons, selective samples have been taken for the preliminary trial of dealloying. Samples were placed in a glass beaker filled with distilled water and held there till up to 1 hour at ambient temperature. After samples have been removed from the water, they were taken for SEM examination to reveal morphological and compositional changes (Figure III.9). SEM images clearly reveal a formation of interconnected nanoagglomerates and eventually huge cracks across the whole sample. Such behavior can be explained by simultaneous rapid dissolution of Ca through the entire sample, by the fast and intense release of the H_2 gas bubbles accompanied by heat release, which altogether led to multiple fractures of the ribbon. As presented in the EDX graphs (Figure III.9.d), after 5 minutes of dealloying almost all Ca was already removed from the ribbon. Practically, this means that water is a very effective etchant for Ca. Dilution of water either with ethanol or glycerol was tried but without any improvement of the behavior.

Given the present results, which showed the absence of a homogeneous nanostructured morphology, appropriate adjustments were introduced to the NPCu synthesis, which will be described hereafter.

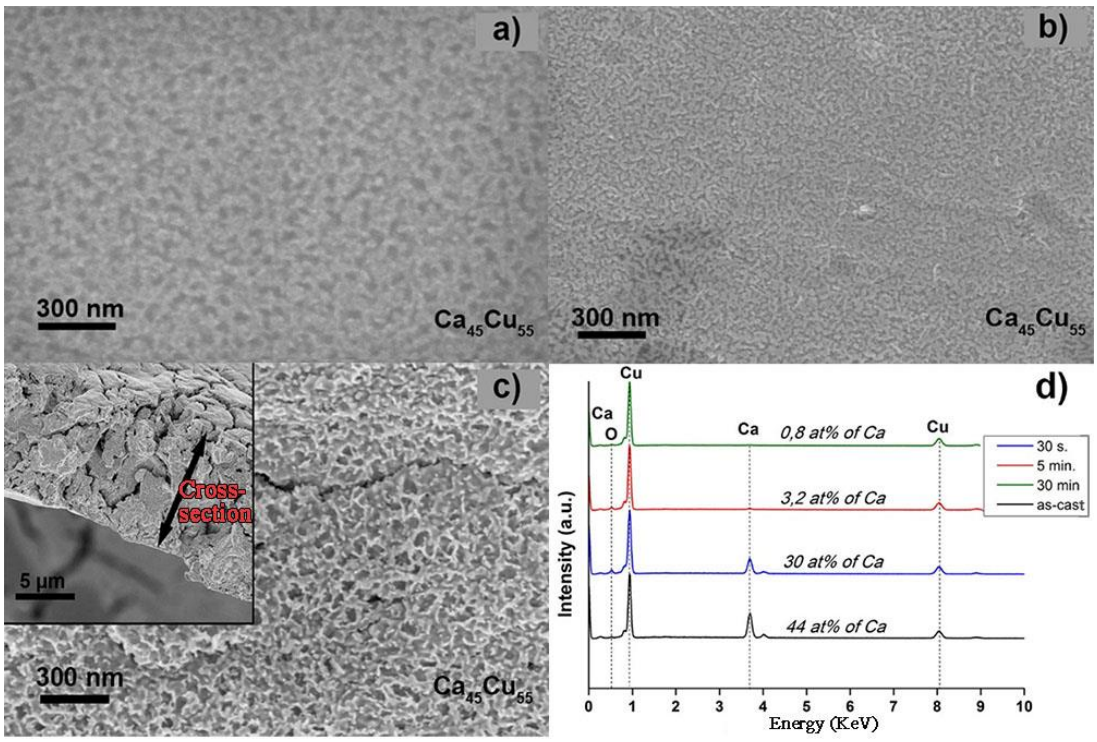

Figure III.9. Surface morphology of as-cast $Cu_{55}Ca_{45}$ amorphous sample (a) and surface evolution with the dealloying time in water for 30s and 30 min (b and c respectively). EDX spectrums (d) exhibit the decrease of surface Ca content with the dealloying time.

III.1.2.c. Cu-Ca alloy reactivity and effect on dealloyed morphology

The evolution of visual aspects of the as-cast sample became noticeable already after several hours after the casting. The first remarkable feature was the color change from bright metallic to dark brown as in Figure III.10.

Figure III.10. A photograph of a Cu-Ca melt-spun ribbon 3 days since casting.

Figure III.11 presents time-spaced XRD patterns of the $Cu_{55}Ca_{45}$ alloy, taken during 19 days after casting and compared with a representative amorphous diffractogram. These results confirm structural changes as the material was exposed to open atmosphere conditions, which crystallizing due to the exposition to air humidity. Results presented in Figure III.12 shows that crystallization and relaxation of the amorphous structure are initiated primarily on the surface of the sample since the crystallinity of material decreases after a slightly polishing of ribbons' surface to remove its top layer. The surface layer is further driving the crystallization process starting from forming a calcium hydroxide. Similarly to a dealloying process, when Ca is removed from the Cu-Ca amorphous matrix, Cu is left alone in the matrix, which finally starts reflecting the Cu crystalline structure.

Finally, the above discussion is further confirmed by the changes in the surface chemical composition determined by EDX data presented in Figure III.13, which shows an increase of the oxygen with the exposure time of the sample to the atmosphere.

The effect of structural relaxation on dealloying is highly pronounced (Figure III.14) and results in more effective nanopattern formation at short dealloying times (6 minutes). Although, the fact of general embrittlement of the materials, caused by heat treatment and dealloying cannot be unnoticed. This loss of ductility was already observed before [210] for copper alloys, heat treated roughly between 300 and 600 °C.

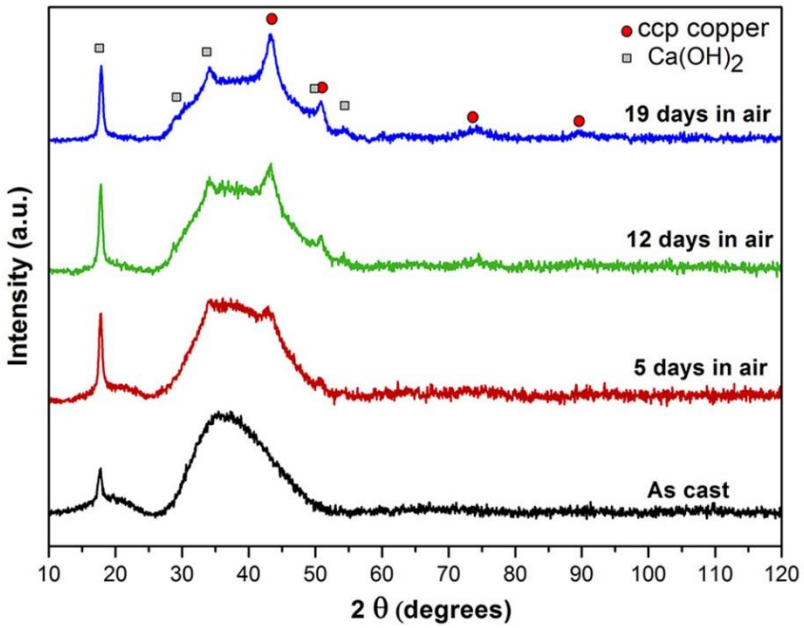

Figure III.11. Evolution of XRD patterns of initially amorphous $Cu_{55}Ca_{45}$ ribbon kept in the air during 19 days.

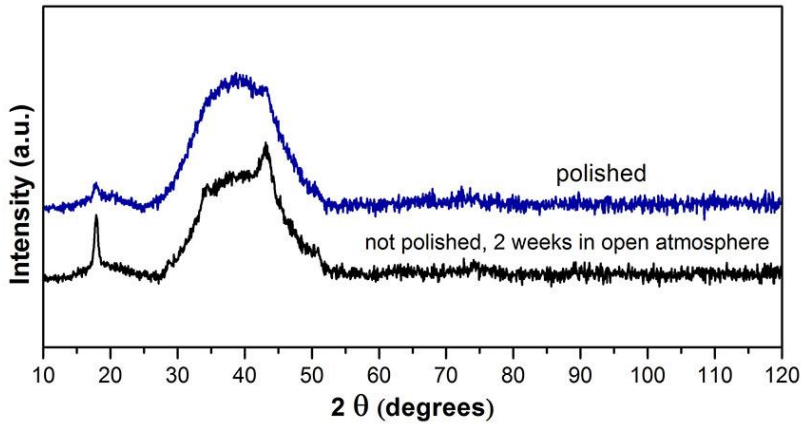

Figure III.12. Comparative x-ray diffraction plots of the $Cu_{55}Ca_{45}$ sample, kept in open atmosphere for 14 days before and after light polishing.

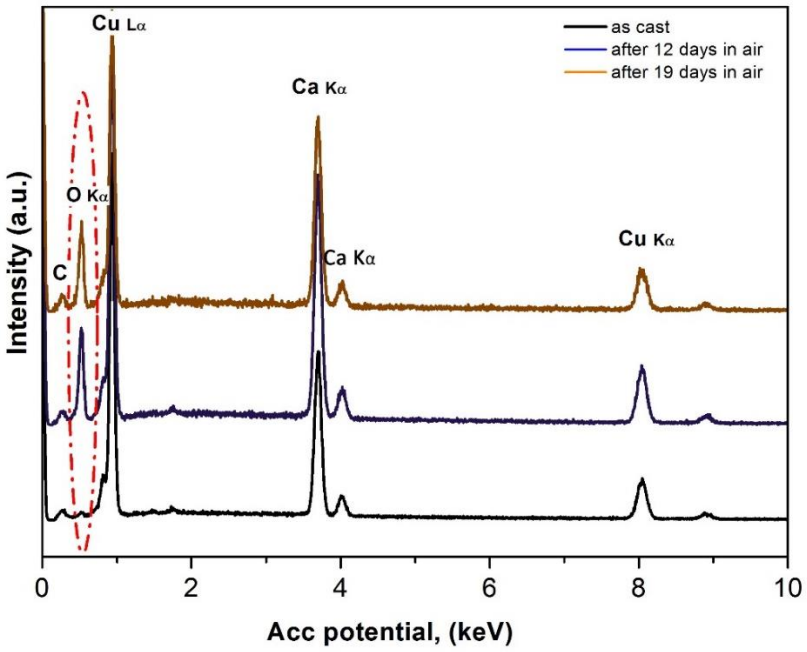

Figure III.13. Evolution of EDX spectrum of as cast sample exposed to air during 19 days.

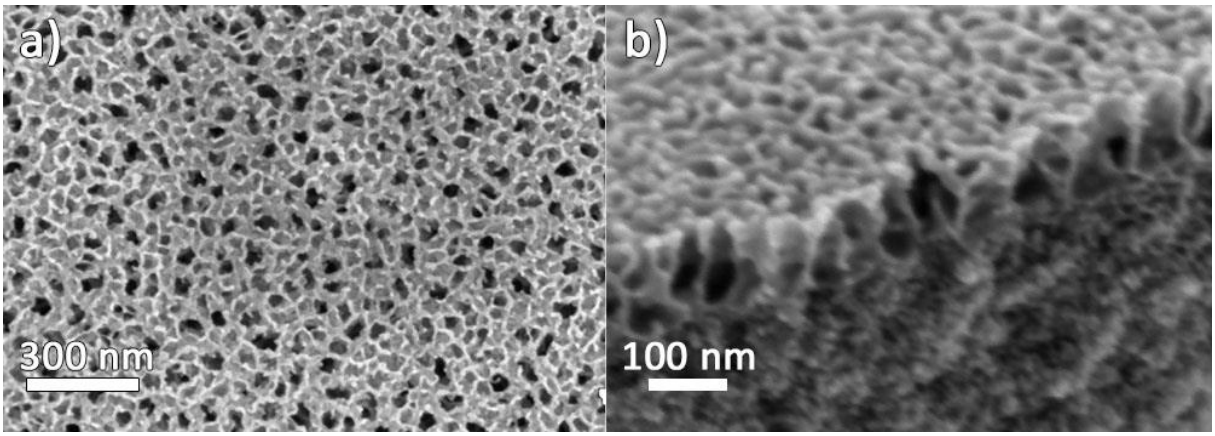

Figure III.14. SEM image surface (a) and cross-section (CS) (b) of as-dealloyed for 6 minutes reference $Cu_{55}Ca_{45}$ ribbon, relaxed in ambient conditions for 2 weeks.

Given the above observations, the next step was to apply heat treatment to crystallize the samples in an attempt to modify the kinetics of the dissolution of calcium and Ca-rich compounds from the ribbons and to produce a uniform porous morphology. Temperatures were chosen according to results obtained from DSC measurements. Therefore, 120 °C, 160 °C, and 300°C were selected, the latest showing best effect on later dealloying. In other words, full crystallization was more prone to produce good NPCu materials than a mix of nanocrystals with the amorphous matrix. X-ray pattern in the Figure III.15 describes new phases formed as a result of thermal annealing, comprising $CaCu_5$, CaCu and Cu predicted by the phase diagram, and newly formed CaO and $Ca(OH)_2$ resulted from the intereaction

with atmosphere before and after the heat treatment, because the presence of water spicies is almost impossible at 300 °C. $Ca(OH)_2$ – is a strong base, slightly soluble in water (at 20 C^0 1.56 g per liter [208]).

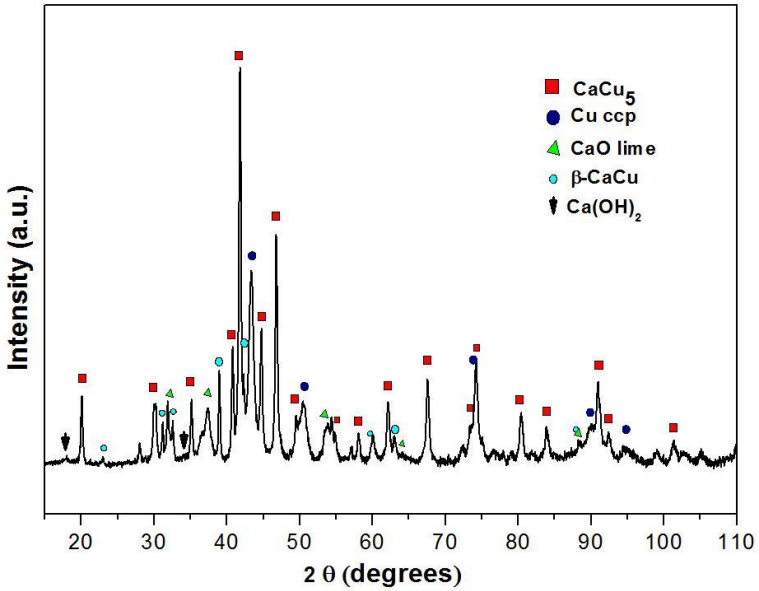

Figure III.15. XRD pattern of a $Ca_{40}Cu_{60}$ sample after annealing at 300°C. Complete relaxation of amorphous structure results in formation of new crystalline phases.

Resulting microstructures with different Cu/Ca ratios after dealloying in water for 10 minutes are presented in Figure III.16.a-c. The dealloying time has been selected as 10 min, according to gas bubbles release termination (one of the indicators of dealloying process). Besides, cross-section images show that ribbons are entirely etched, and no bulk middle layer is left. Although, locally calcium concentration in the center of the ribbon can attain up to 12 at%, as was measured for the case of Figure III.16.a cross-section middle). Therefore, in cases where good purity of the nanoporous copper matrix is desirable, longer dealloying times can be applied to remove residual calcium. It must be borne in mind that a longstanding dealloying may result in an increase of structure's brittleness.

The average surface pore size of the NPCu from Figure III.16.a and III.16.b is ~ 140 nm, and internal pores are below 20 nm. As one may notice, an approximately 1 µm thick surface layer demonstrates a remarkable microstructural difference between surface and in depth material. A possible cause for that is a more effective oxidation of this top layer of the ribbon combined with casting imperfections due to the contact with the copper wheel. Although such morphological feature is initially unplanned, it renders to the nanoporous scaffold a hierarchical quality, which is advantageous from the point of view of catalyst design. Shortly, such gradient-like porosity facilitates the infusion of the electrolyte with reactants and evacuation of converted products.

The average surface pore size of the bi-porous structure (Figure III.16.c) is ~ 130 nm, with the underneath porosity of ~ 11 nm. However, the irregular shape and unclear borders of pores and

ligaments make this estimation difficult, similar to the case of surface porosity of samples $Cu_{50}Ca_{50}$ and $Cu_{60}Ca_{40}$. The upper limit of cross-sectional pore size is approximately estimated as 200 nm.

For a more sound representation of typical NPCu internal structure of the dealloyed specimen, a focused ion beam cut slice of NPCu obtained from $Cu_{60}Ca_{40}$ is analyzed quantitatively via Fiji in 2D space. Further TEM observations are carried out to characterize grain size and distribution and obtain a mapping of elemental distribution across the specimen.

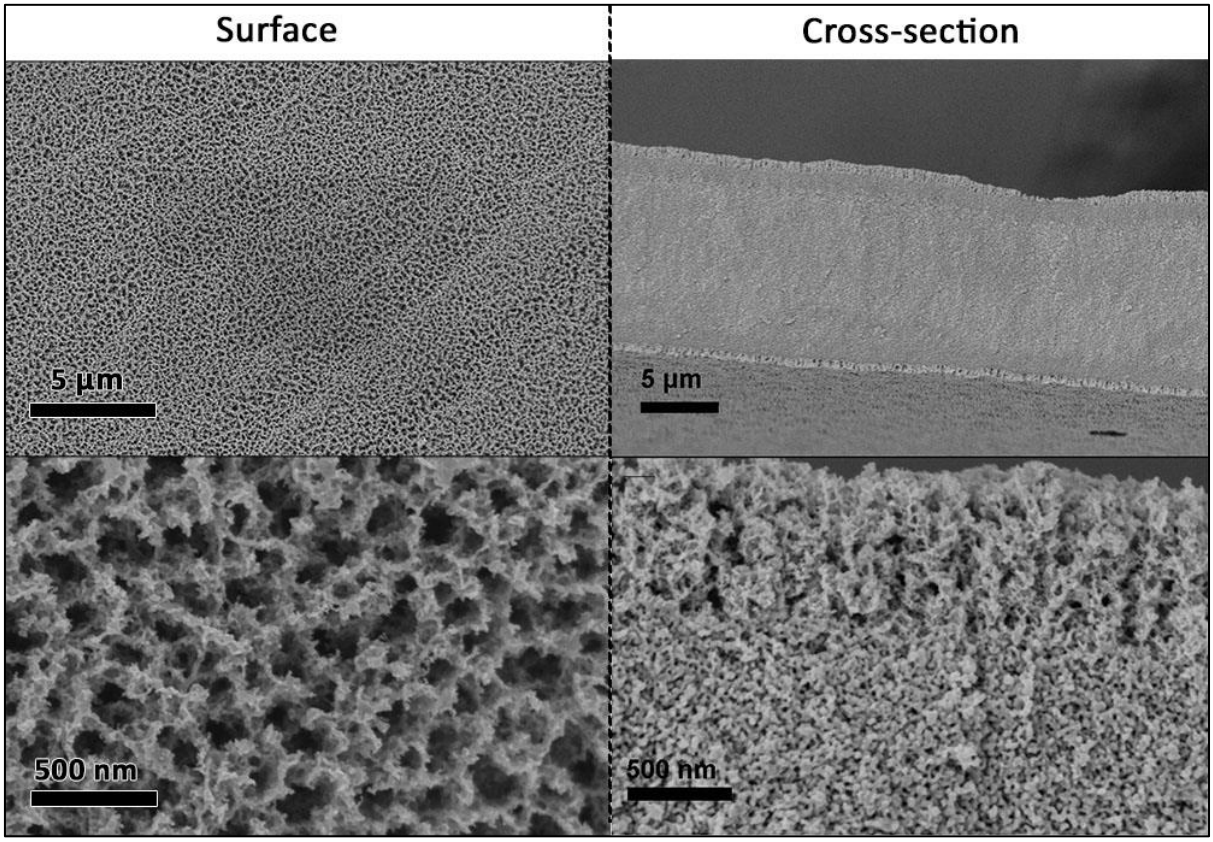

Figure III.16. a. Microstructure of as-dealloyed Cu60Ca40 ribbon, previously exposed to open atmosphere heat treatment at 300°C for 2 hours.

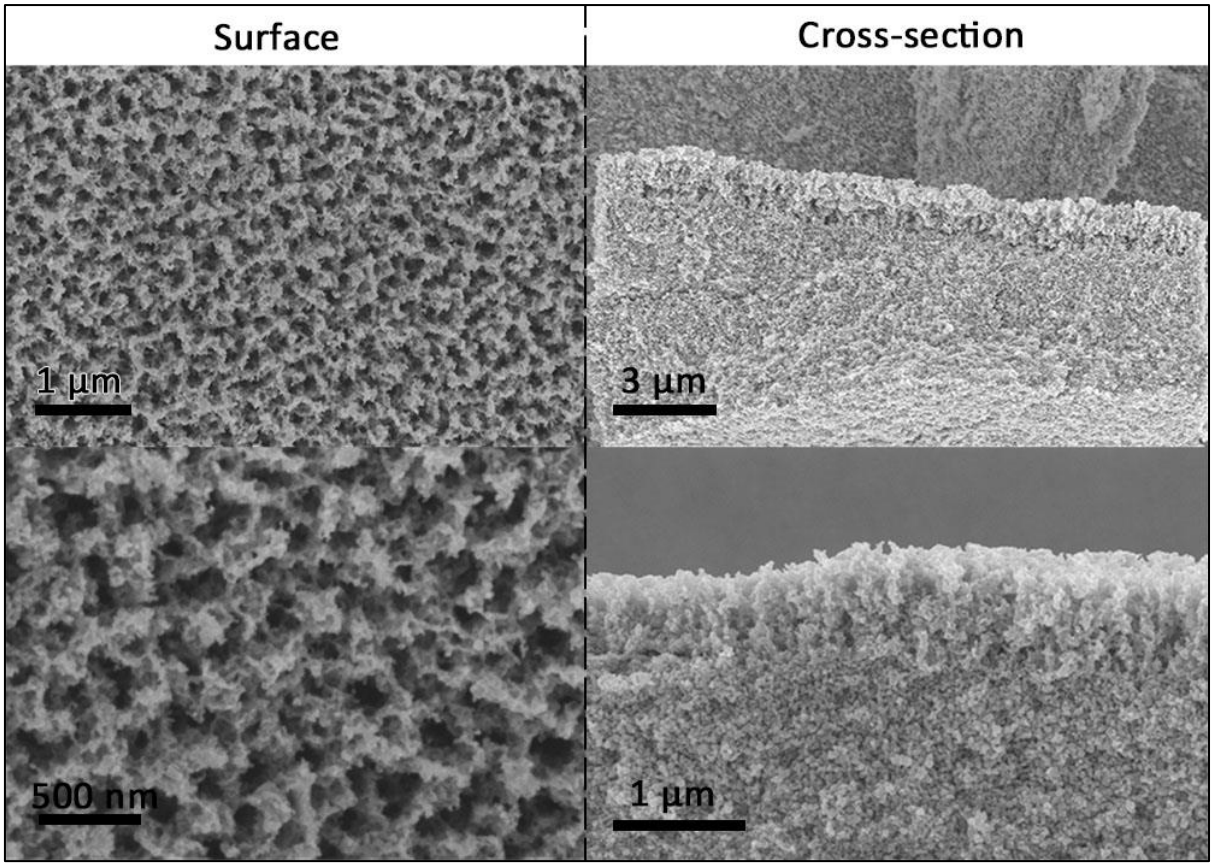

Figure III.16.b. Microstructure of as-dealloyed Cu50Ca50 ribbon, previously exposed to open atmosphere heat treatment at 300°C for 2 hours.

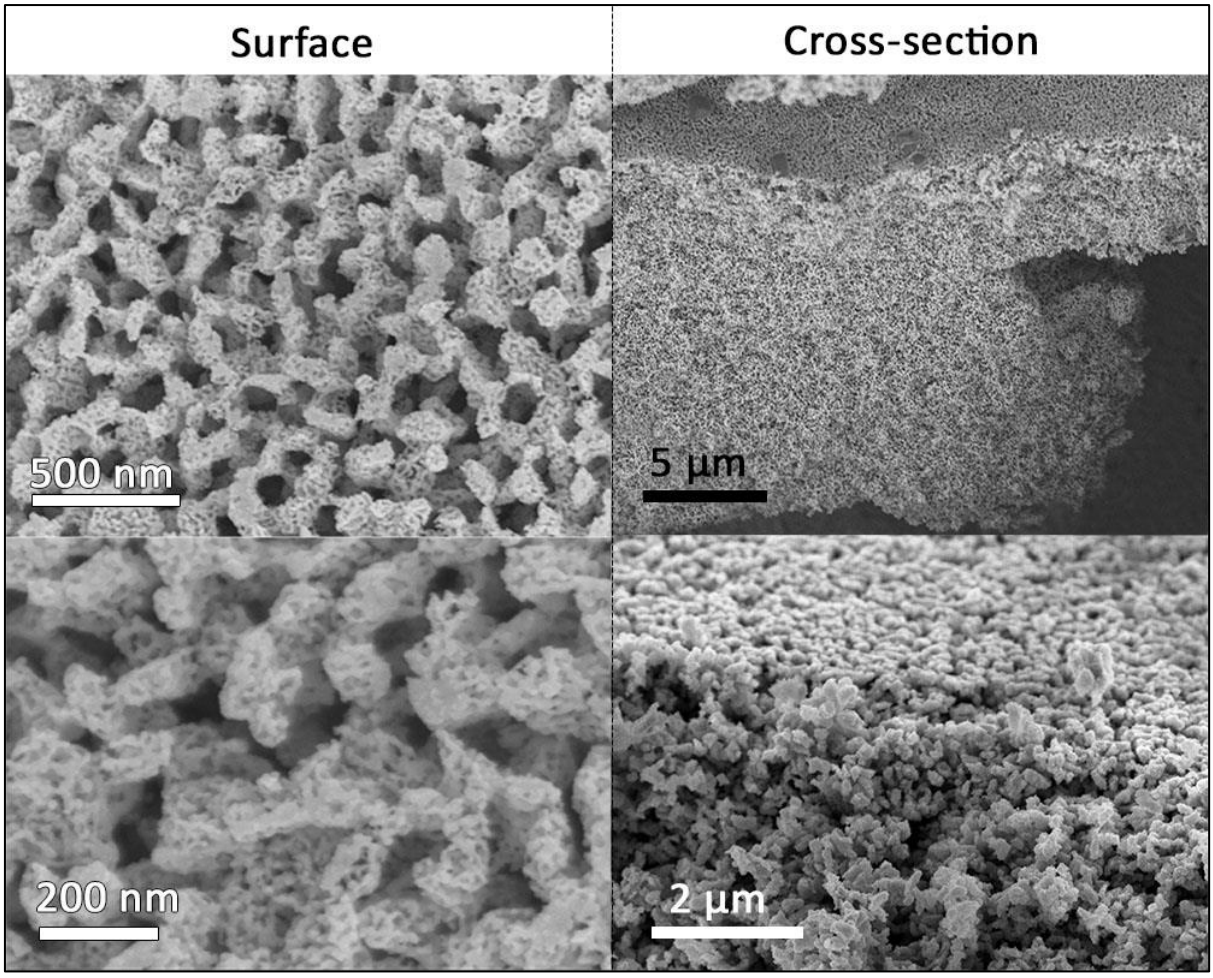

Figure III.16.c. Microstructure of as-dealloyed Cu20Ca80 ribbon, previously exposed to open atmosphere heat treatment at 300°C for 2 hours.

FIB-cut of up to 20 nm thickness is made by milling off a former 2 µm thick slice as described in section II.2.2. The SEM images in Figure III.17 depict the nanostructure in dark and bright-field mode (DF, BF). Further statistical analysis of ligament and pore-size distribution gave average dimensions of internal microstructure; an arithmetically average ligament width <l> = 22 ± 7 nm, while the one for pores <p> = 18 ± 9 nm. The ligament/pore width was measured according to the diameter of randomly selected ligaments/pores at their center part. The average value was adopted by identifying and averaging 100 data at least. Solid fraction was estimated with the help of the threshold function, which was set in the range of 50.6 – 57 %, and is the inverse for the pore phase fraction. It is worth noting that present NPCu structure is one of the finest among the reported copper-based systems [123,124,128,173,211] and is promptly obtained via non-toxic dealloying and relatively simple experimental procedures, comparing to those where aggressive etchants, longer etching times and electrochemical equipment are required.

TEM data of the same material in as-cast and final dealloyed states confirm transitions from amorphous to finely crystalline microstructure (Figure III.18.a-b). Selected area electron diffraction pattern (SAEDP) shown in Figure III.18.a presents only amorphous halos, characterizing the amorphous state of the sample, while in the SAEDP of Figure III.18.b it is possible to observe spot-

ring pattern, typical for nanocrystalline material. The small crystallite size of the entirely dealloyed NPCu sample is supported by XRD results (Figure III.19.a). Their size can be determined from peaks profile by well-known Scherrer's [212] and related Williamson-Hall [213] (W-H) methods. Although, in this study, it was favored the Halder-Wagner [214] approach (H-W), which we believe reduces the error of crystallite size *D* determination. The H-W method is based on the equation III.4:

$$\left(\frac{\beta cos\theta}{sin\theta}\right)^2 = \frac{K\lambda}{D} \cdot \frac{\beta cos\theta}{sin^2\theta} + 16\varepsilon^2 \qquad \textit{(eq. III.1)}$$

Where $\boldsymbol{K}$ is a dimensionless shape factor, $\boldsymbol{\lambda}$ the wavelength of the x-ray beam, $\boldsymbol{\varepsilon}$ is microstrain and $\boldsymbol{\beta}$ (in radians) is the integral breadth due to both small crystallite sizes and microstrains. $\boldsymbol{\beta}$ is determined as a result of Rietveld analysis of sample peak broadening, while the LaB_6 crystal is used as a reference for the determination of instrumental broadening.

Equation III.1. has a form of a straight line $y = ax + b$. Plotting $(\beta cos\theta/sin\theta)^2$ versus $\beta cos\theta/sin^2\theta$ for characteristic diffraction angles θ (Figure III.19.b) one gets a slope $\alpha = K\lambda/D$ and an intercept $b = 16\varepsilon^2$, Scherrer's shape factor *K* is assumed here as 1 [215]. Unlike the W-H method, where *D* size is determined from the intercept of the experimental curve, the H-W method suggests higher reliability for the D value since data for reflections at low and intermediates angles are given more weight than those at higher diffraction angles, which are often less reliable [214]. From the obtained straight line fit (eq. III.1), *D* was determined as 12 nm, which is in good agreement with STEM-FEG observations (Figure III.20).

Apart from local representation of crystalline state of studied material via diffraction ring patterns, Automated Crystal Orientation Mapping on TEM (section II.2.1.b) allows to see that locally nanostructured ligaments of porous matrix are constituted of smaller crystallites of 6-25 nm size. Such phenomena is typically observed for NPM obtained by dealloying of amorphous precursors [55]. Owing to this technique, fcc Cu grain orientations, their boundaries and grain/subgrain size were determined and a corresponding mapping is present on Figure III.21. Orientation mapping was performed using TEM in the same regions of the alloy as shown in Figure III.20. For comparison purposes, Figure III.21.a shows the equivalent bright field images obtained by regular TEM. This image shows a homogeneous distribution of grains/subgrains. It should be noted that, although this image was taken in the same region as in Figure III.20., the two sets of images are not identical because Figure III.21 was taken under conditions where orientation information can rapidly differentiate between boundaries and sub-boundaries. The misorientation angles of grain boundaries were indexed and Figure III.21.c shows high-angle boundaries (blue) with misorientation angles equal to or greater than 15° and low-angle grain boundaries (red) having misorientation angles less than 15°. The high-angle boundaries are associated with new grains and the low-angle boundaries denote subgrains. By indexing these colored boundaries, it can be seen that the sample contain ~85% of high-angle boundaries. This indicates that the sample is free of deformation. The observed sub-boundaries may be related to the final stage of dealloying were new grains are being formed. Figure III.21.c presents phase mapping for NPCu. As one can see, after dealloying, the sample is almost composed by pure Cu (~99%), which is agreement with the XRD analysis of Figure III.19.a. The grain size distribution is shown in Figure III.22. The measured average grain size was ~20 nm. This value is similar to that obtained from analysis of the images in Figure III.20. Figure III.21.b shows orientation imaging mappings (OIM) for the NPCu sample. It is apparent that there is no a tendency for any preferential texture, which is confirmed by the Pole Figures (Figure III.21.d) (the maximum was only ~3.6 times the random value). This is the same trend observed in the X-ray diffraction pattern in Figure III.19.a (as-dealloyed). The random grain orientation suggests a homogeneous structure formation upon dealloying.

As an intermediate conclusion of this subsection, it may be stated that it was for the first time that nanoporous copper was synthesized starting from an amorphous Cu-Ca precursor by simple dealloying in pure water. Applying thermal treatment above T_g and full crystallization point of the material is justified by further homogenization of as-dealloyed microstructure of NPCu and disappearance of major cracks.

For Ca-rich compositions, a clear bi-porous nanostructure was manifested. Such peculiar morphology could be a significant advantage for catalytic applications of the studied system, except for its enormous brittleness. In fact, the majority of the dealloyed $Cu_{20}Ca_{80}$ specimen was decomposed into sponge-like pieces and does not represent an integral substrate. Other presented specimens resemble in their morphological features (pore-ligament size), although, the exact measurement is limited by the microscope resolution and edges definition.

We suppose that in the present case a general mechanism of porosity formation may be based on i) infiltration of air species and ii) formation of new water-soluble phases such as CaO, $Ca(OH)_2$ iii) while a sufficient mobility of Cu atoms allow pores' formation upon dealloying. The mobility of atoms is proportional to the diffusion rate of Cu and a timescale, and can be estimated as $x \sim (Dt)^{1/2}$. Where the volume self-diffusion of Cu atoms, according to Rothman and Peterson [216,217] is approached as :

$$D = 0.78 \cdot exp(\Delta H/RT), \text{ cm}^2.\text{s}^{-1}$$

Where $\boldsymbol{R}$ is a universal gas constant (8.31 $J.K^{-1}.mol^{-1}$). In order to allow the rearrangement of the atoms at a length scale of current system (~20 nm) at a room temperature T = 300 K, copper atoms need to acquire the energy ΔH of the order of 80 kJ/mol. Such energy is supplied as a result of exothermic reaction of dissolution of Ca-rich phases in water.

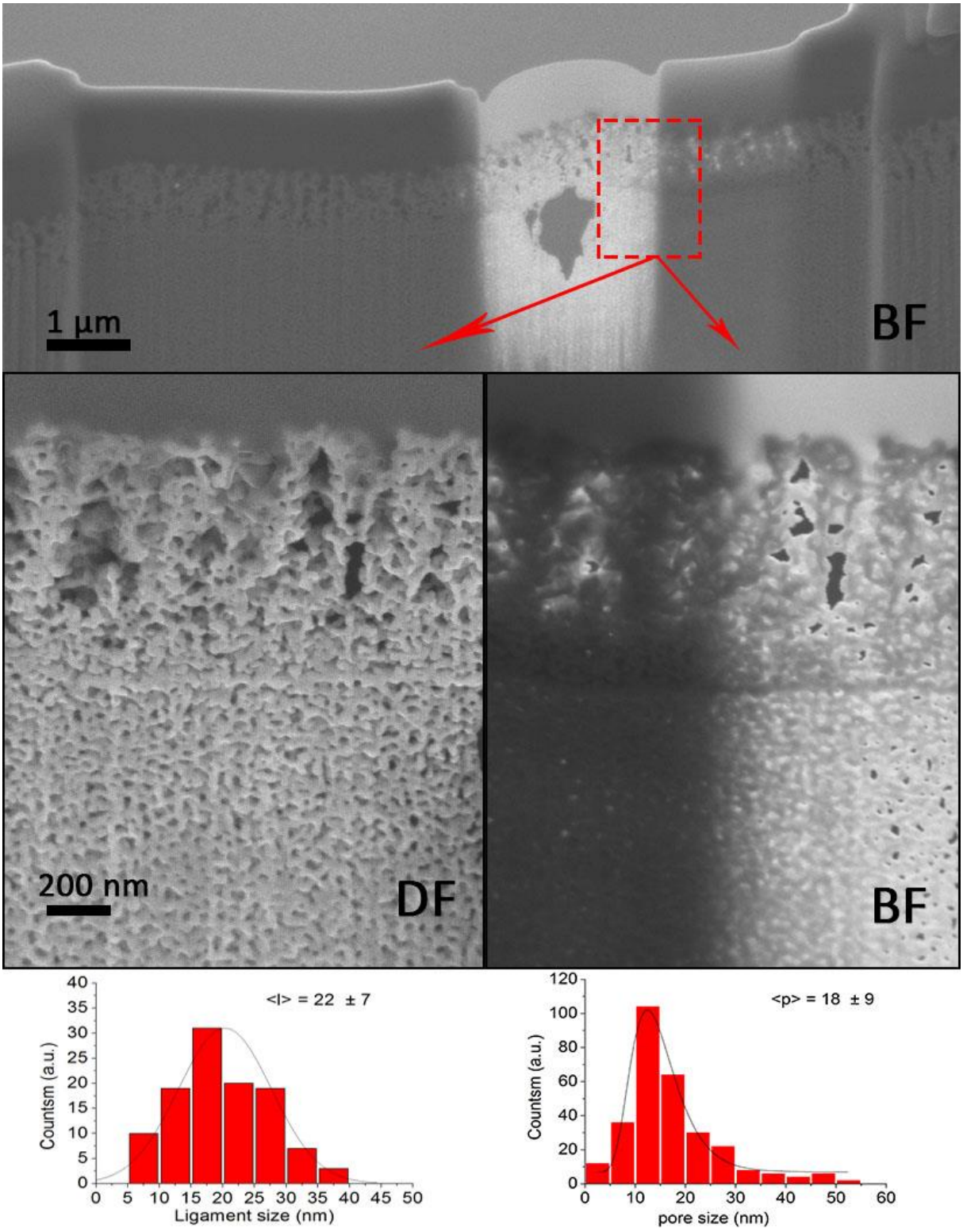

Figure III.17. BF SEM image of NPCu ribbon CS with magnified BF and DF view of a zone of interest. Pore/ligament size distribution histograms quantitatively characterize fine porous matrix below the inhomogeneous surface layer. (BF – bright-field, DF – dark-field).

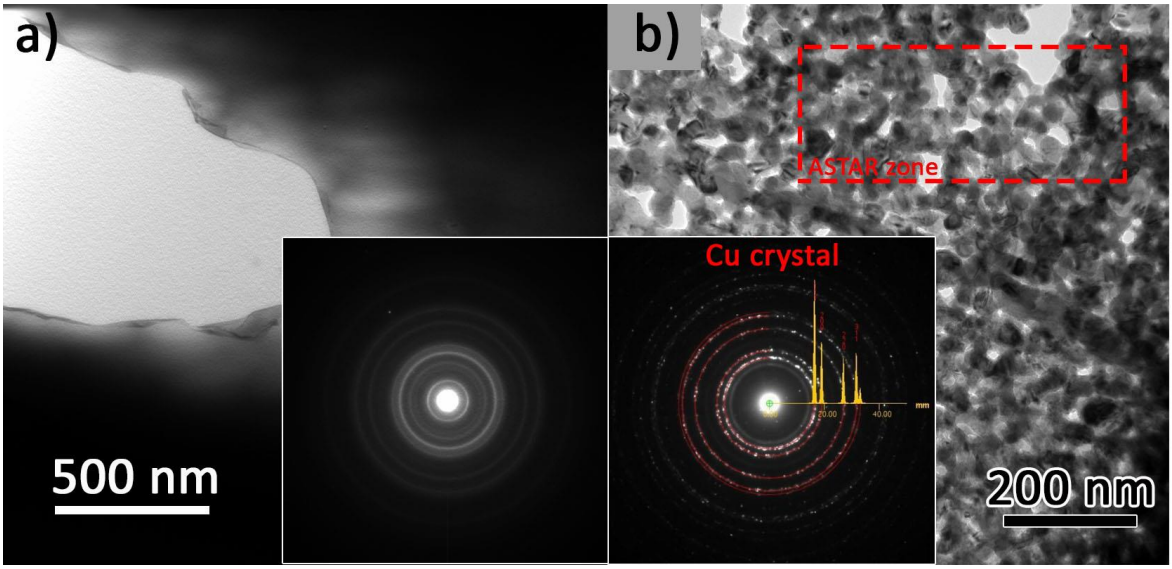

Figure III.18. BF STEM images of a) the amorphous $Cu_{60}Ca_{40}$ sample with an electron diffraction pattern consisted of continuous rings; b) as-dealloyed NPCu matrix.

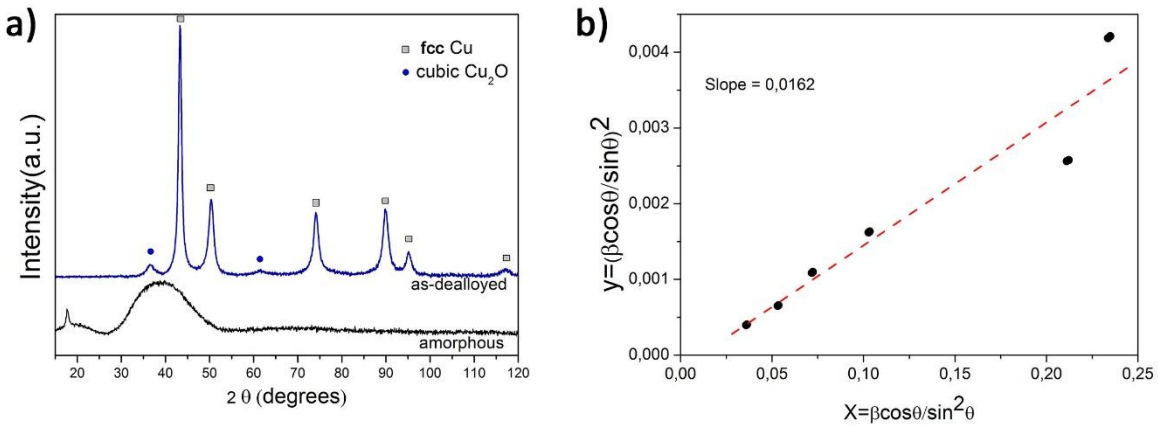

Figure III.19. a) XRD diffraction pattern of as-cast $Cu_{60}Ca_{40}$ amorphous ribbon and its dealloyed crystalline counterpart; b) the Halder–Wagner plot for the NPCu sample. The straight line was obtained by linear regression analysis

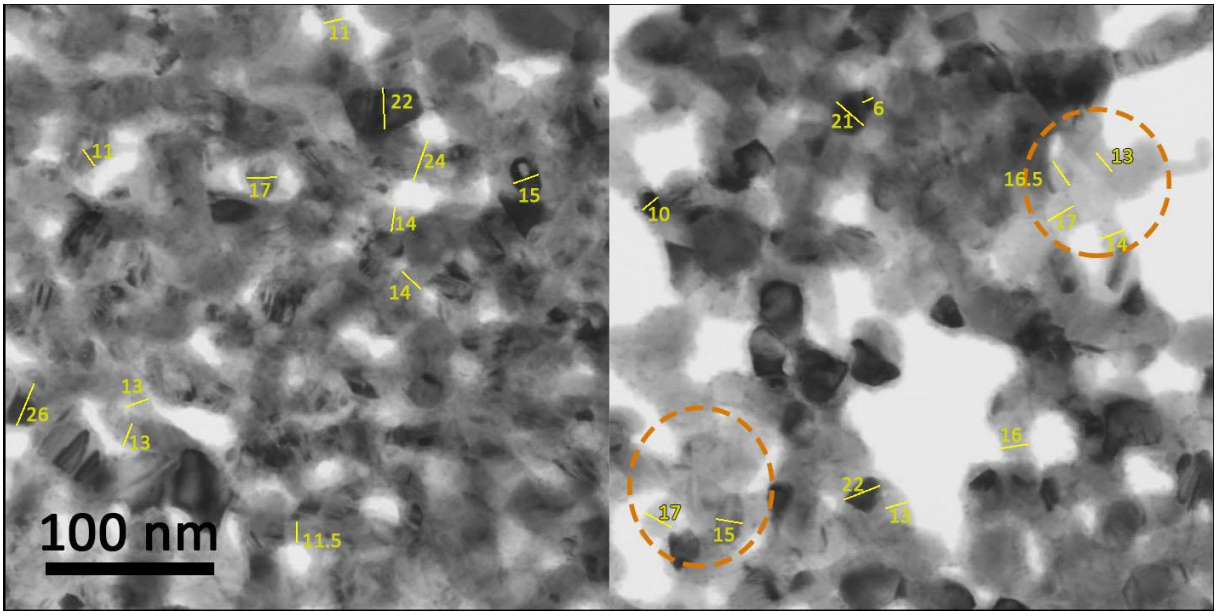

Figure III.20. STEM-FEM BF images of finely porous NPCu and linear measurements of single-crystallite sizes (in nm).

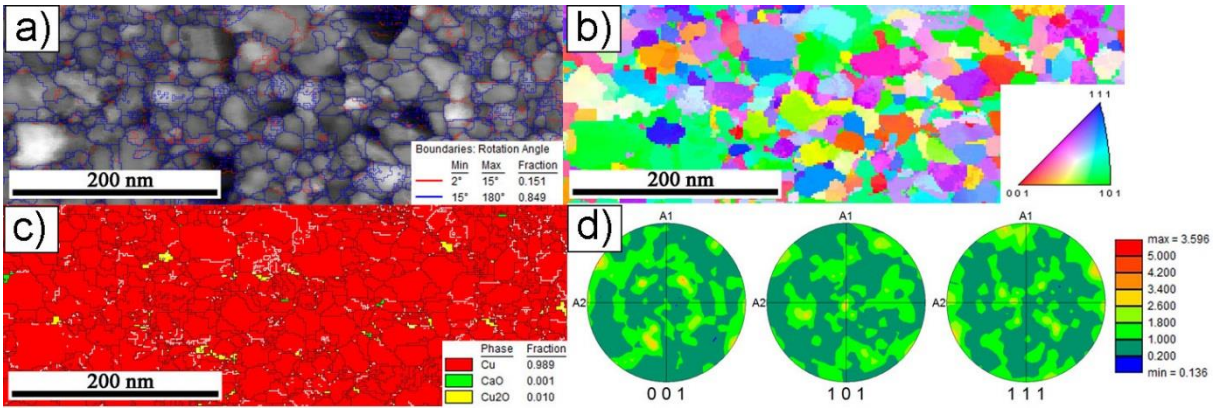

Figure III.21. a) Equivalent bright field image obtained by TEM for the NPCu. High-angle boundaries are represented by blue lines (misorientation angles of over 15^o) and low-angle grain boundaries are represented by red lines (misorientation angles of below 15^o); b) Orientation imaging mapping (OIM) c) Phase mapping for NPCu superimposed to boundaries; d) Pole figures for the NPCu sample.

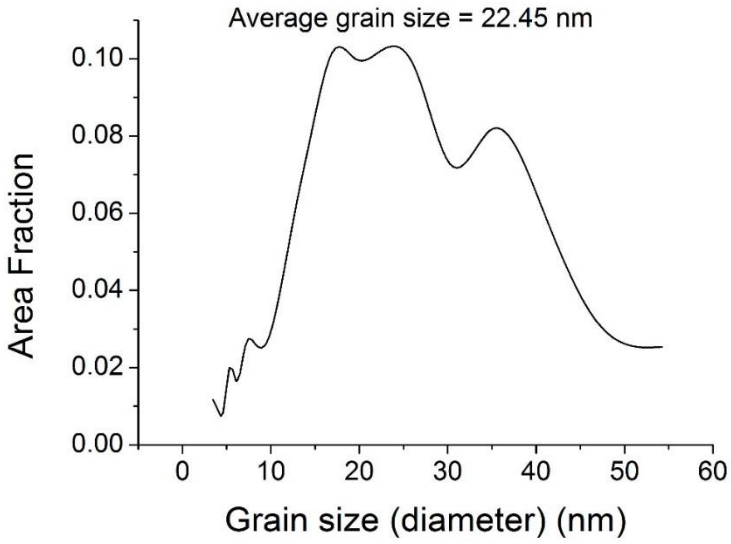

Figure III.22. Grain size distribution for the NPCu.

III.1.3. NPS from crystalline precursor

In the previous work by our research group, authored by M. Zhang et al.[57], was reported the fabrication of a porous silver material with a submicron pore size. The precursor of the given work was an amorphous rapidly solidified $Ag_{38.75}Cu_{38.75}Si_{22.5}$ alloy [218] that was exposed to an appropriate etching condition to eliminate Cu and Si atoms, leaving a single Ag porous framework. A ternary Ag–Cu–Si alloy according to the preceding work [57] was selected over other binary candidates because Cu and Si elements exhibit very low solid solubility in fcc silver (Figure III.23) at ambient temperature due to atomic mismatch, when compared to Ag-Al, Ag-Mg, and Ag-Zn candidates.

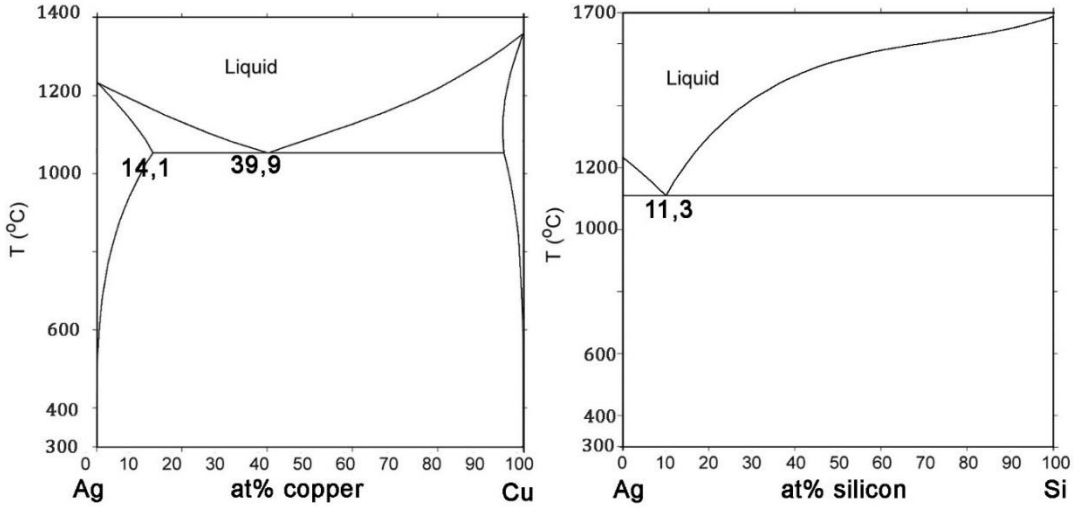

Figure III.23. Ag-Cu and Ag-Si phase diagrams showing eutectics at 39.9 and 11.3 at.% solute content. Ternary alloy eutectic is achieved for $Ag_{30}Cu_{44.7}Si_{25.3}$ composition [219].

The homogeneous distribution of elements in the amorphous state is a key to obtain a fine ultimate porous architecture upon the reorganization of Ag atoms while etching. On the contrary, when crystalline precursors are used, the final characteristic features are determined by the phases present in the ingot [220]. In spite of fine and a uniform porosity, the bulk material produced from the amorphous precursor did not possess sufficient mechanical integrity and robustness to allow any further experiments that could reveal its advantages, particularly in the field of catalysis, where good self-supporting ability is required. To be precise, after complete dealloying, it was impossible to introduce this NPS ribbon vertically inside the solution since its inherent stiffness was not sufficient to break a surface tension of the liquid. The general aim of this part of the study is first to approach the structural composition of previously elaborated NPS foils so as to enhance their mechanical characteristics, particularly by synthesizing the nanostructured crystalline precursors of identical composition.

A set of Ag-based polycrystalline of $Ag_{38.75}Cu_{38.75}Si_{22.5}$ mother alloys were prepared firstly by arc melting of pure elements as described in section II.1.1. However, in this case, the melting was performed in a helium atmosphere. To homogenize the alloy, a minimum of five additional melting steps were made before its casting and rapid solidification in the melt spinning. Foils with 2 mm width and thicknesses ranging between 20 and 60 μm were produced by varying the rotation speed of the copper wheel (14-28 m/s), with a He injection overpressure in the casting chamber (350-500 mbar). After preliminary corrosion tests on the obtained samples, the 25 μm thick foils showed a finer porous architecture, thus being chosen for further careful characterization and study for practical applications. The resulting composition of as-cast ribbon, determined by EDX at 15 keV was $Ag_{37.58}Cu_{37.54}Si_{24.88}$ (at.%). Its XRD pattern (Figure III.24) suggests that the majority of the samples were constituted by the crystalline face-centered cubic (fcc) silver and the hexagonal η (Cu_3Si) phase.

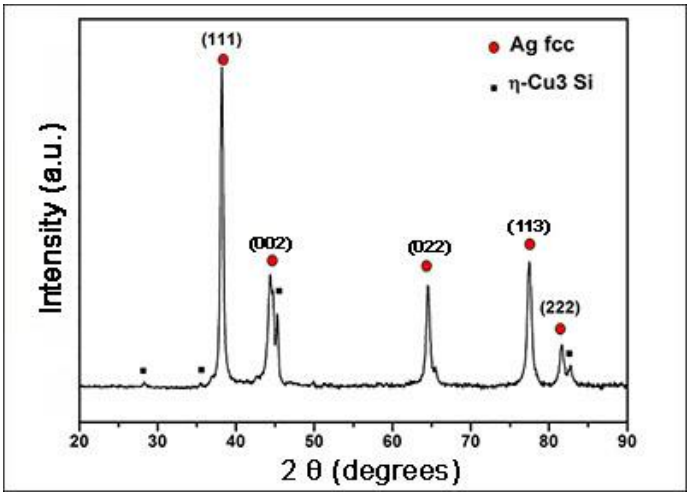

Figure III.24. XRD pattern of as cast $Ag_{38.75}Cu_{38.75}Si_{22.5}$ ribbon.

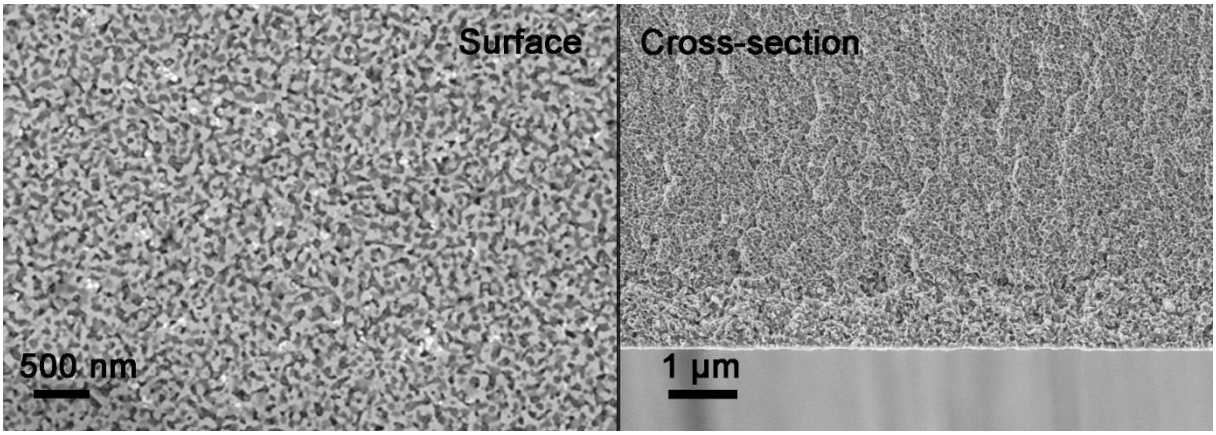

Figure III.25. SEM-FEG secondary electrons images of as-cast $Ag_{38.75}Cu_{38.75}Si_{22.5}$ ribbon. Eutectic microstructure of precursor is composed of alternating phases, bright is an Ag-rich and dark is a Cu-Si-rich phase.

Current state of the precursor represented an ideal situation for further dealloying, due to its little separation into two distinct phase: the nobler fcc-Ag and the less noble η phase with a typical segregation wavelength of about 60 nm (Figure III.25). As a first approach for corrosion of the less noble η phase, a 3.32 M of HNO_3 acid solution as in [57] has been tried out. According to [209] nitric acid is an effective etchant for both Cu and Si metals and their redox potential assured their dissolution before silver. Figure III.26 presents a micrograph obtained after 10 minutes of etching of the as-cast crystalline sample. It reveals an irregular morphology and difficulties for solution penetration, producing an indefinite tridimensional porous structure. The compositional analysis showed that the atomic concentration of the residual Si atoms was at least 19 at.% and copper residues were of a negligible amount of about 1.4 at.%.

Another solution, a mixture of 0.67 M of HNO_3 and 0.64 M of HF, was tested as an etchant for as-spun ribbons to accelerate the dissolution of the Si atoms. Figure III.27 reflects the evolution of the porous structure/thickness of the porous layer/EDX analyses of the material with the etching time up to 90 minutes. During the first stages of dealloying, the electrolyte attacks the Cu_3Si phase, initiating concave paths propagation at the length scale of the phase. Progressively removal of atoms extends across the whole surface and continues into the bulk of the material (Figure III.27.a-e), forming crystalline interconnected ligaments in some way duplicating original grains of the precursor. Final parameters of coarsened ligaments depended primarily on the temperature at which the dealloying was performed, duration of dealloying, and on the electrolyte type. These parameters can be adjusted to obtain the desired microstructure.

As one may see from Figure III.27.h, above 60 minutes of corrosion the intermediate bulk layer is completely dealloyed. A prolonged interaction of silver matrix with the etchant results in acidic aging of NPS matrix and self-precipitation of Ag-based agglomerates, which bring resemblance with a sponge-like structure. Such phenomena are because nitric acid is also a corroding media for silver metal, although in a much smaller extent comparing to copper and silicon. Therefore, morphology and arrangement of silver ligaments were not only due to the removal of η phase but also due to reorganization, dissolution and partial re-precipitation of Ag atoms.

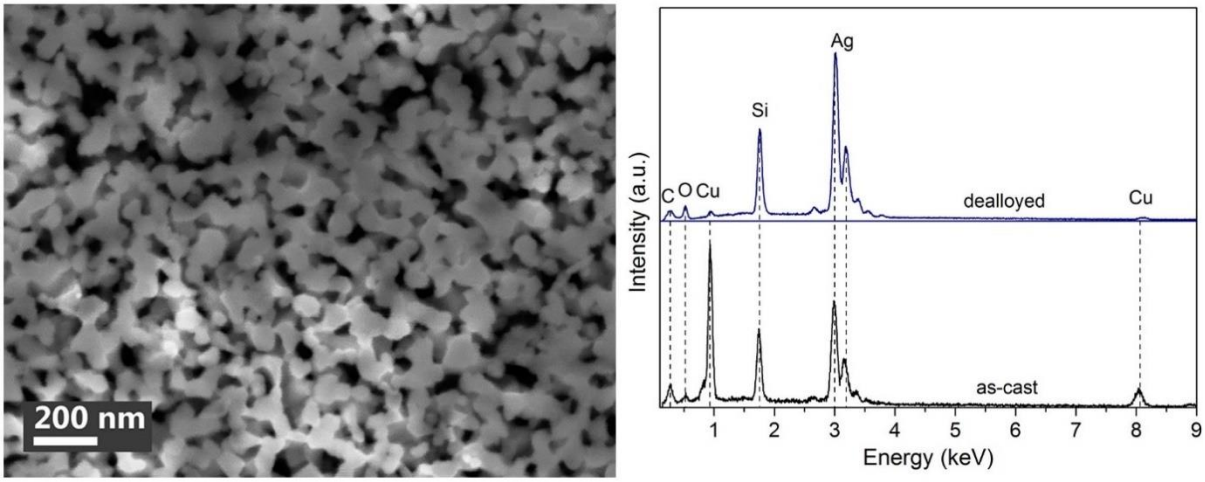

Figure III.26. SEM micrograph of a porous Ag-based pattern after dealloying in nitric acid solution for 10 minutes and corresponding EDX spectrums (beam energy = 15 keV) of as cast and dealloyed surface.

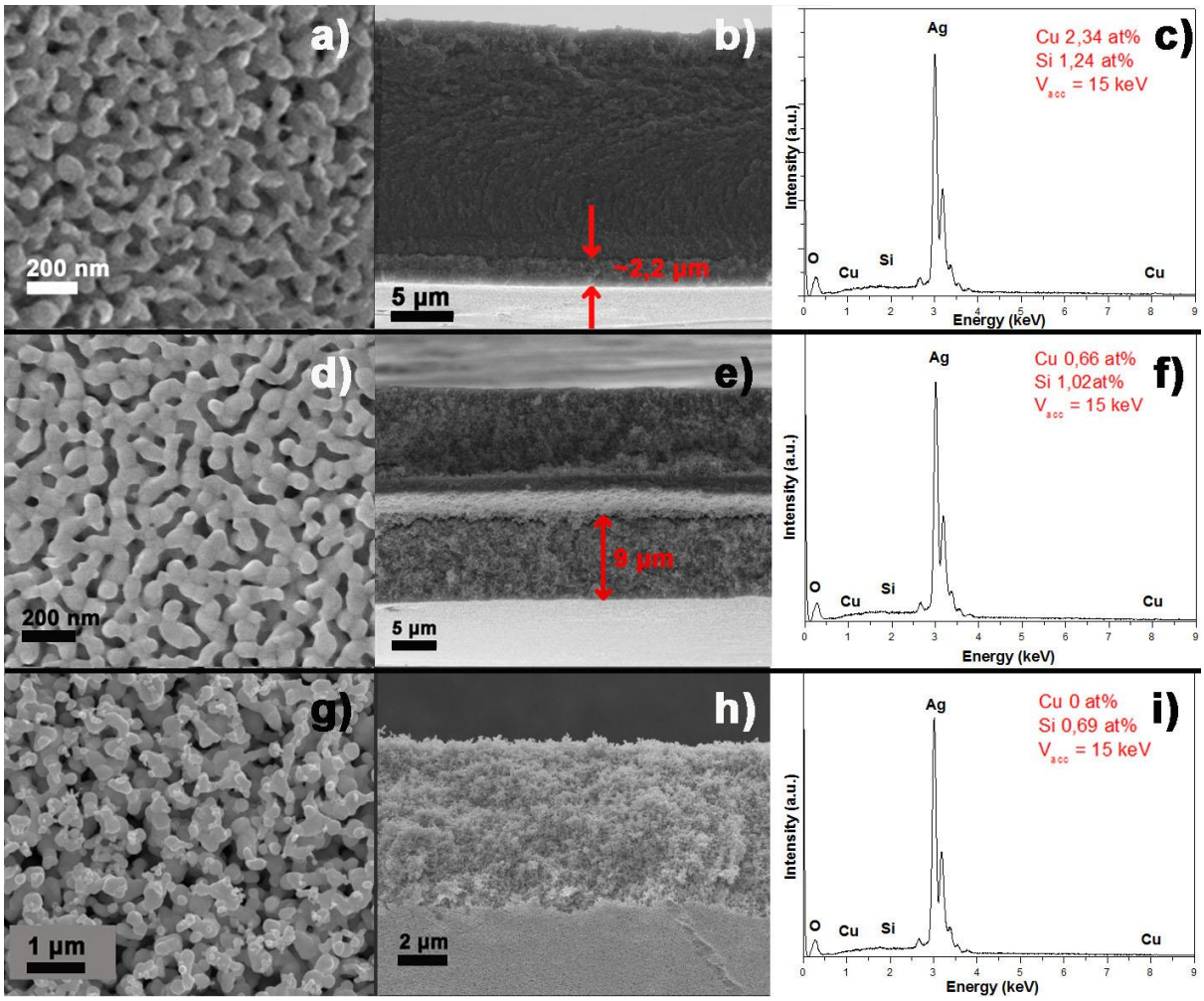

Figure III.27. SEM images of the surface porous structure, cross-section view of the etched ribbon and surface EDX analyses of the ribbons, immersed in the etching solution for 10 (a-c), 45 (d-f) and 60 minutes (g-i) respectively.

The fact of Ag atoms' dissolution could be proved from the mass evaluation of silver ribbon in the mixed acid solution with dealloying time (Figure III.28). Upon 60 minutes of dealloying, it was no longer possible to determine any Cu/Si residues in the cross-section of the dealloyed ribbon, although the corresponding graph still indicates the decrease in mass, meaning that it can only be due to the Ag dissolution. Indeed, after 5 hours of dealloying, all the material was dissolved in the acid bath.

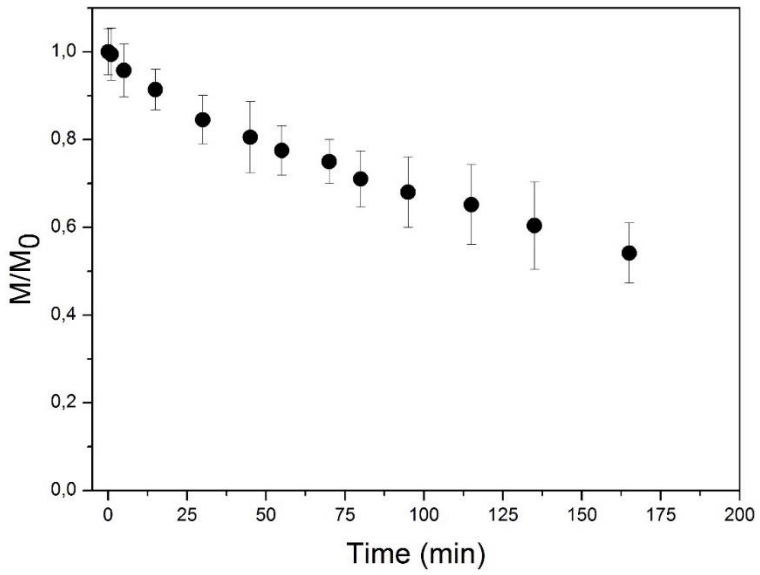

Figure III.28. Normalized mass evolution of as-cast Ag-Cu-Si ribbon while dealloying in HNO_3 and HF acid bath. M is an actual mass of the sample at a certain dealloying time, M_0 is its initial mass before the beginning of the experiment.

The etching time of 45 min was selected as an optimal time to generate a fairly regular asymmetric porous structure (Figure III.27.d andFigure III.29.b), which was entirely formed by a crystalline fcc silver scaffold (Figure III.30). By using image analysis, the average surface ligament width and length were measured, giving values of ~ 46 and ~107 nm, respectively, and a pore size of ~ 38 nm in width and ~95 nm in length. The quality of such geometry appears to be inferior to the one obtained using an amorphous precursor [57] of the same composition Figure III.29.a), which was characterized by a uniform pore size distribution of smaller dimensions (almost twice finer with a characteristic ligament and pore size of 20 and 30 nm respectively). The high-resolution SEM image permitted concluding that, similarly to the case of NPCu described in the previous section III.1.2, ligaments of NPS structure obtained from amorphous precursor were also formed by clustering of many fine grains.

Calculated dimensions of NPS obtained from crystalline precursor matched surprisingly well with characteristics of the phase distribution pattern of the crystalline precursor, which gives a reason to imagine that such phase separation left some sort of morphological fingerprint.

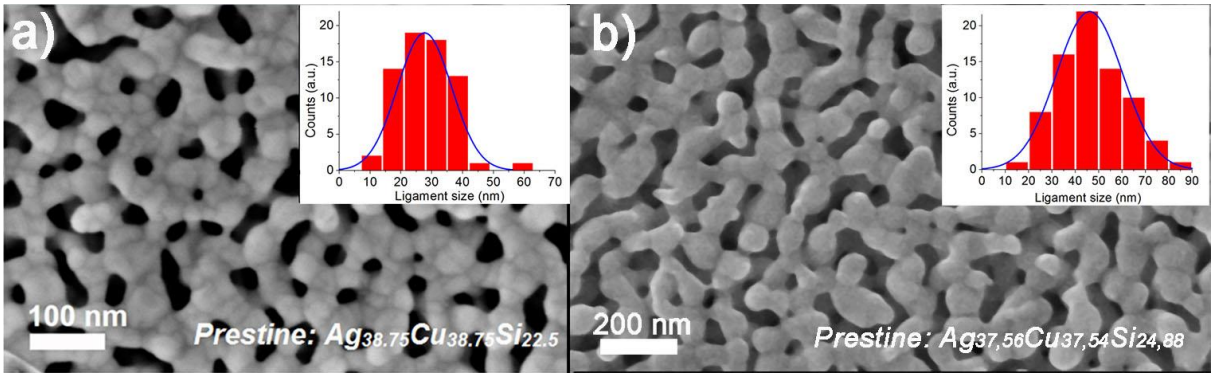

Figure III.29. Microstructures of rapidly solidified a) amorphous $Ag_{38.75}Cu_{38.75}Si_{22.5}$ foil after immersion in 13.4 wt.% nitric acid for 6 min; b) crystalline $Ag_{37.56}Cu_{37.54}Si_{24.80}$ after dealloying in mixed nitric and hydrofluoric acid solution for 45 min. Related histograms of ligaments width distribution are presented in the inserts.

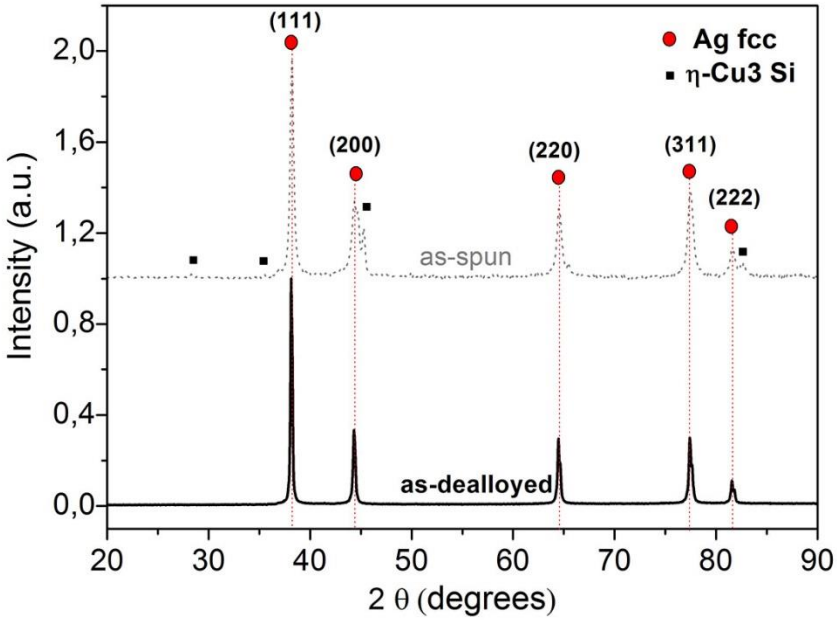

Figure III.30. XRD pattern of as-dealloyed NPS ribbon. Whole material is composed of a single fcc Ag phase.

Concluding this sub-section, it should be added that dealloying parameters such as temperature, pressure, the volume of etching bath, the intensity of solution steering were kept fixed. Dealloying time has been selected as the principal parameter of microstructural control. If an appropriate time is selected, one may control the thickness of an intermediate bulk layer as in Figure III.27.e. Such layer assures an additional integrity of the dealloyed material and simplifies further manipulations.

III.1.4. NPCo from crystalline precursor

A Co-based ternary system (Co-Cu-Si) was the last exploratory study of the present work. Such choice has been partially discussed in section I.6.3.c which, in short, was motivated by the potentially high catalytic activity of the metallic cobalt for industrially important reactions such as the Fischer-Tropsch synthesis, a competitive cost of raw materials, and technical holdbacks in the synthesis of alternative Co-based precursors for dealloying to NPCo. The idea behind synthesis of Co-Cu-Si alloy precursor is similar to the one of the $Ag_{38.75}Cu_{38.75}Si_{22.5}$ alloy. In spite of the possibility of formation of a metastable liquid miscibility below the liquidus line [221], Co-Cu-are immiscible and phase separation behavior is expected. As a result of rapid solidification, we would expect phase segregation into Cu-Si phase inside Co-rich matrix. Previously ternary Cu-Co-Si system has been principally studied from the perspective of hardening of Cu-based alloys by precipitation of Co_2Si phase [222]. Despite a lack of reported data for this system in the range of intermediate compositions with at least 30 at.% of Co (which is required to produce an integral porous matrix, according to parting limit requirement of dealloying), hence, it was challenging to guarantee the resulting microstructure of casted alloy, although several attempts of synthesis have been carried out.

Polycrystalline of Co-Cu-Si mother alloys with the nominal composition of $Co_{39}Cu_{38}Si_{25}$ were prepared by arc melting with consequent cold-crucible homogenization at 1100 ^{0}C for 1 minute. Additional casting by melt-spinning was performed at the wheel speed of 46 m/s in Ar atmosphere, casting temperature T_{cast} was recorded as 1150 ^{0}C. Obtained ribbons were characterized by having dimensions of 2-3 mm width and 15-27 µm thickness. Characterization of as-cast material was performed by Dr. Yaofeng Guo and Dr. Nikolaos T. Panagiotopoulos in the Department of Materials Engineering of the University of Sao Carlos (DEMA-UFSCar), Brazil via the dedicated characterization instruments, which include EDX, TEM and TEM/ASTAR, and XRD data (Figure III.31-33). The latest demonstrated that, besides σ-Co and $Cu_{0.9}Si_{0.1}$ phases, Co_2Si also precipitated. In the present study this last phase is disadvantageous since it captures target cobalt atoms indented for further catalytic activity after dealloying. The resulting composition of the as-spun ribbons was $Co_{42.1}Cu_{36.23}Si_{21.67}$, which was averaged from several areas of EDX measurements at 25 kV.

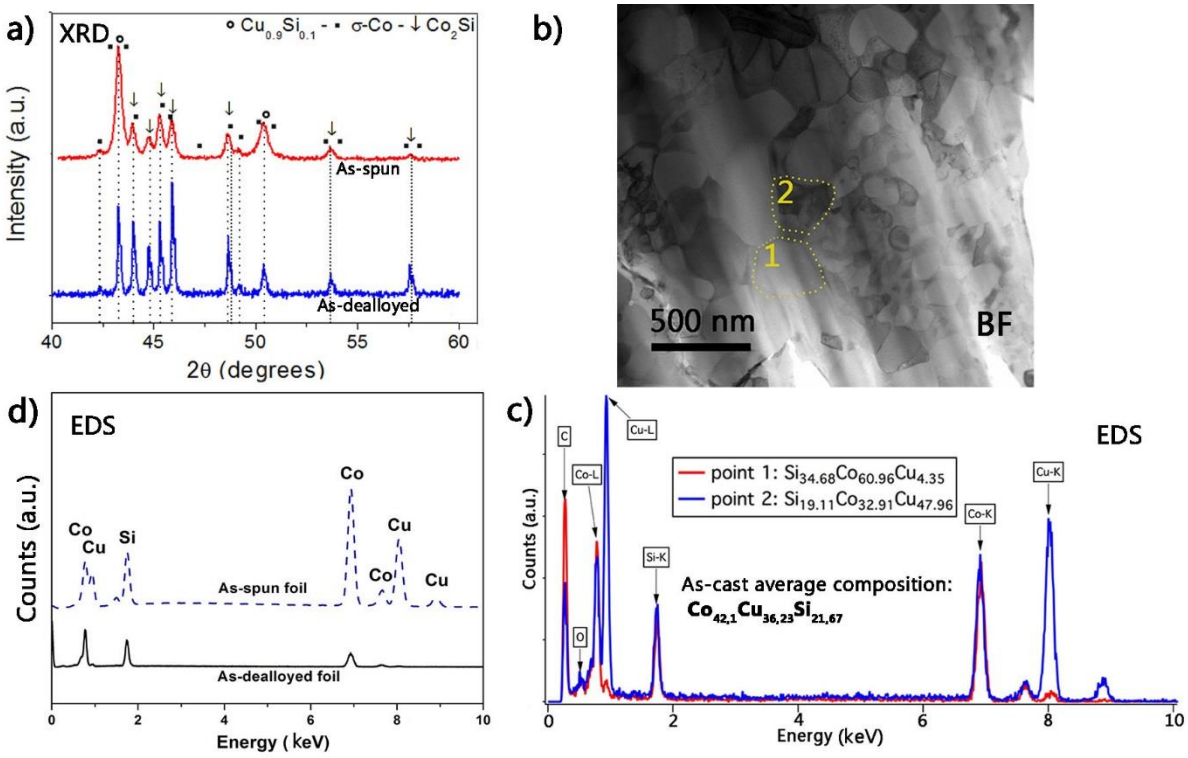

Figure III.31. Primary microstructural characteristics of the pristine Co-Cu-Si alloy. XRD of as-spun ribbon (a-red); STEM BF micrographs with the two outlined zones for local elemental analysis (b-c); EDX spectrum of large region gives an estimation of average composition of as-cast sample (d-blue).

As in the TEM mode, the scanning transmission microscopy (STEM) mode allows identifying grain boundaries. Also, as it is always performed using nanobeam, high-resolution EDX is achievable and allows determining local compositions in nano size range. For example, point 1 and point 2 in Figure III.31 represent two different grains with different chemical compositions. As confirmed by ASTAR, the majority of grains were composed of σ-Co and $Cu_{0.9}Si_{0.1}$ phases (Figure III.32.b). Probably a cobalt silicide phase could be present, but the ASTAR software could not identify it in analyzed areas. The average grain size of the pristine material was calculated as ~ 130 nm (Figure III.32.a) using the EBSD software EDAX OIM Analysis 7. Analyzed nanobeam diffraction pattern (Figure III.33) of as-cast material confirm that the detected phase is σ-Co.

Dealloying of the as-cast material was performed in a range of etchants (mixed nitric and hydrofluoric acid solution, ammonia, diluted nitric acid) where 13.4 wt.% nitric acid solution was the best to produce the desirable morphology. According to quantitative EDX measurements (Figure III.31.d-black), the as-dealloyed composition of the material was $Co_{64.54}Cu_{4.71}Si_{30.75.}$ The copper amount can locally vary from 3 to 17.1 at%. While HNO_3 supports the dissolution of Cu from the pristine material, Co was also diluted and the Co_2Si phase started prevailing. When dealloying was completed (no bulk layer in the middle of the ribbon was longer observed), almost all the specimen was constituted of cobalt silicide and σ-Co phase (XRD of Figure III.31.a-blue). Co_2Si phase is chemically very stable even in strong acids. Further etching by NaOH or KOH with the purpose of removing silicon resulted only in the formation of unwanted surface precipitates (Figure III.34.d).

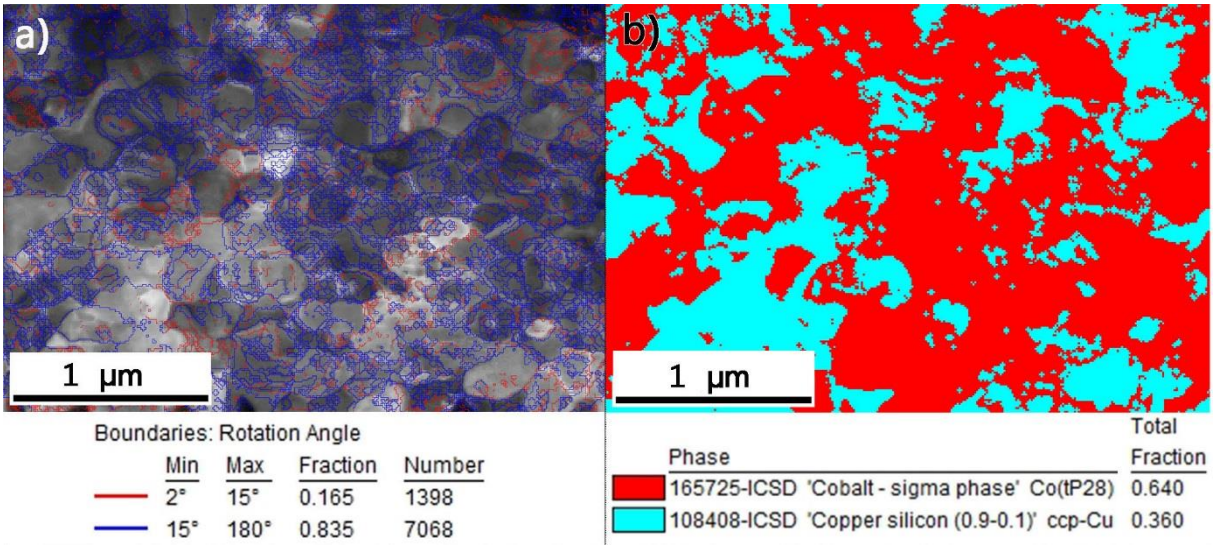

Figure III.32. Evaluation of grain/subgrain boundaries of as-cast $Co_{42.1}Cu_{36.23}Si_{21.67}$ sample (a) and phase distribution along the sample (b) via ACOM-TEM.

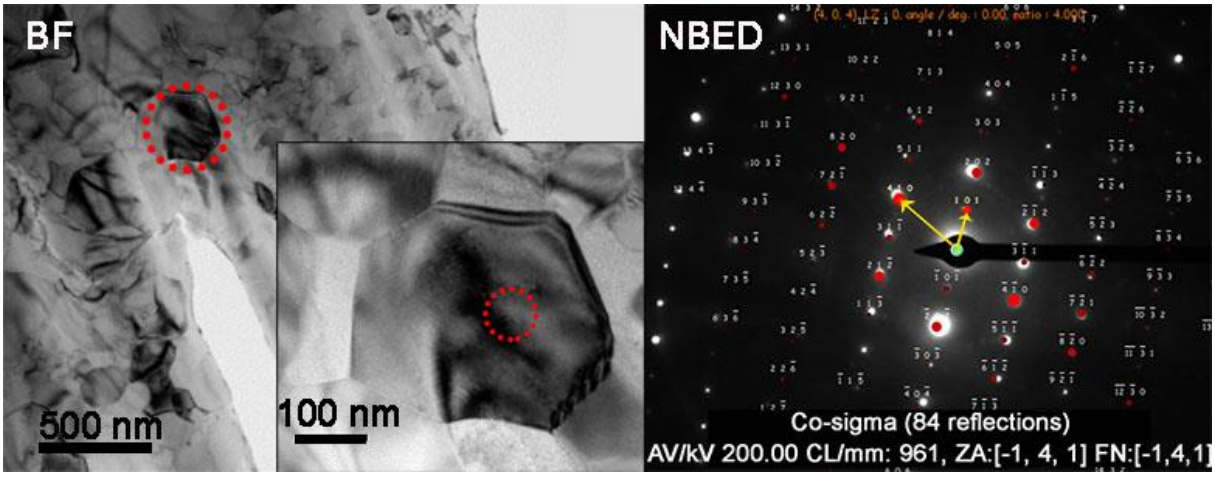

Figure III.33. Bright field STEM micrographs of the analyzed area of the as-spun Co-Cu-Si ribbon and corresponding nanobeam diffraction pattern (NBED), revealing sigma cobalt phase.

Surface and cross-sectional SEM observations of as-dealloyed ribbon revealed the porous morphology presented in Figure III.34.a-c, characterized by an average ligament width of ~ 190 ± 70 nm, circular pores ranging from 30 to 400 nm, and an average diameter of ~ 140 ± 90 nm. The porous fraction, estimated from the surface and cross-section views, gave at least 9.5 and 28 volume % of the material, respectively, which was mainly due to the dissolution of $Cu_{0.9}Si_{0.1}$ and σ-Co phases.

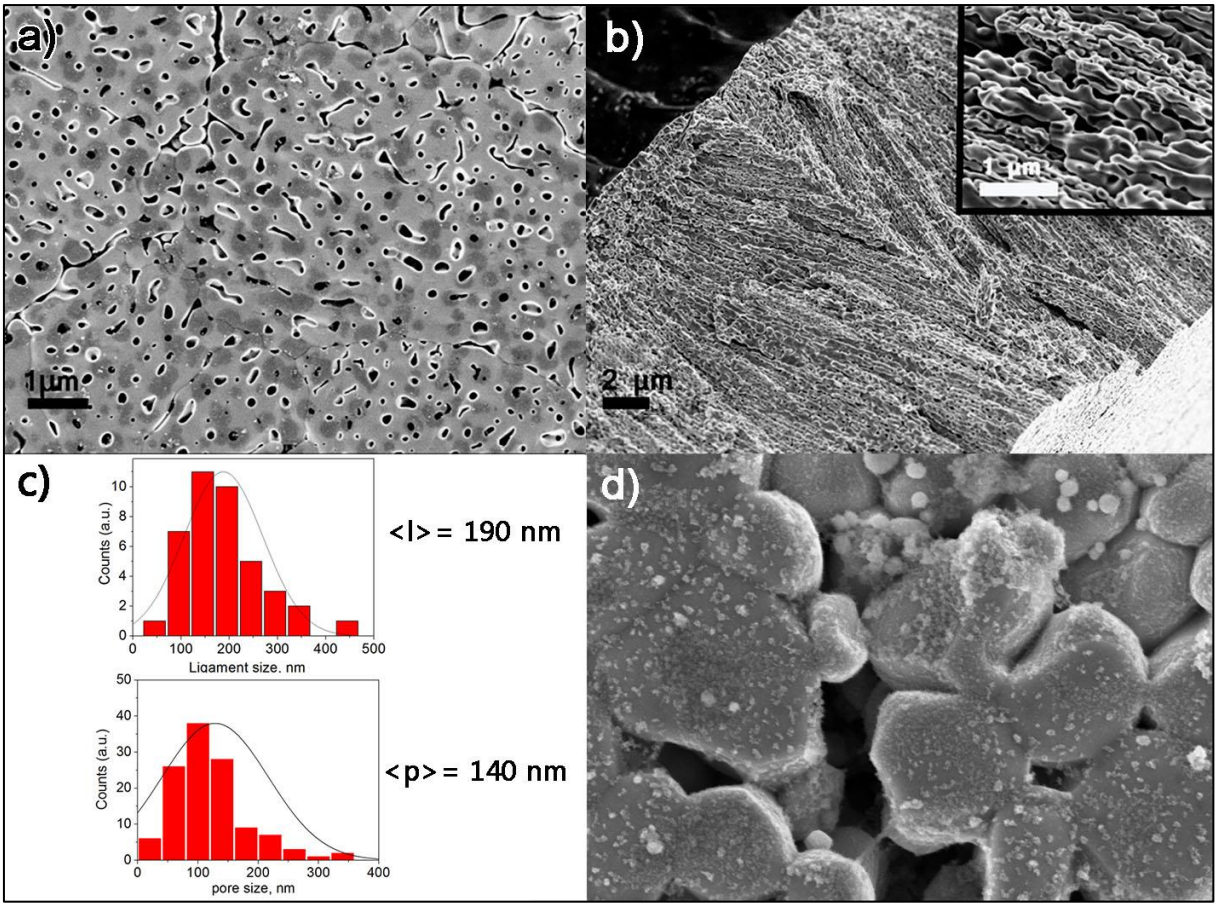

Figure III.34. Nanoporous surface (a) and CS (b) morphology of NPCo after corrosion in 13.4 wt% HNO3 for 1 hour and corresponding geometrical ligament and pore size distribution (c); effect of complemented etching in KOH for additional 10 minutes (d).

During dealloying of present system, there was no any noticeable gas bubbles release, but an external sign of corrosion was expressed through the change of etchant's color, similar to the phenomena described in the section II.1.3 which is due to dissolution of Cu. The sequence or reactions, that take place upon copper dissolution in nitric acid is:

(i) $Cu + HNO_3 = CuO + HNO_2$;

(ii) (a) $CuO + 2HNO_2 = Cu(NO_2)_2 + H_2O$;

(b) $CuO + 2HNO_3 = Cu(NO_3)_2 + H_2O$.

Nitrous acid, produced as a result of copper oxidation (i) greatly enhance the rate of the reaction. The soluble products of reaction (ii.a) and (ii.b) contain green copper nitrite as well as the blue copper nitrate, and part of it is decomposed to oxides of nitrogen, which are the gases evolved [223].

In addition to previously introduced characteristics of synthesized NPCo, it should be noted that nanoligaments are directed preferably along the plane perpendicular to ribbon's surfaces and geometrically are close to a rode-type. Similar phenomenon of columnar morphology formation during melt-spinning has already been observed in earlier reports on various rapidly solidified alloys [224–226]. It is suggested that such structuration is initiated from the wheel side of the melt-spun specimens and

propagates across the thickness of the ribbons, and is related to the melt puddle convection and regulation of the casting parameters that affect the solidification process. At the expense of smaller surficial area, the obtained nanostructure showed better mechanical strength in comparison to previous systems. NPCo is easy to handle without any risk of structure failure, which is important for following materials exploitation. One of the unforeseen phenomena upon dealloying was the dilution of Co and the consequent prevalence of cobalt silicide in the final composition, which is undesirable because it can affect the chemical activity of the material.

III.1.5. Conclusions

The process of precursor preparation for the synthesis of nanoporous metallic foams is an essential step of the current study. It is rather challenging to make an appropriate selection of potential systems that can guarantee an appropriate behavior upon applied corrosion within reasonable external parameters (t, T, P, pH). In the present chapter, the elaboration of four different prospected systems of crystalline and amorphous type, based on abundant non-Pt group metals, have been studied.

a) Nanoroughened copper surface, obtained through selective corrosion of less-noble intermetallics in the chill-zone of $Cu_{10}(HfZr)_{90}$ alloy was the first successful demonstration of possible modifications of existing alloys. Simple corrosion of nanostructured bulk pieces resulted in an effective surface design that may find real demand in fields where hard textured alloys with bactericidal properties are required.
b) Another Cu-based case study is a good example of achieving nanostructured materials via dealloying of formerly amorphous alloy. Binary Cu-Ca system allowed a broad range of compositional variations for the casting of amorphous ribbon precursors that can be easily dealloyed in pure water. The main drawback was the eventual brittleness of as-dealloyed nanoporous structure, most probably caused by intermediate temperature embrittlement, typical for copper alloys and, eventually, by hydrogen release from the sample upon dealloying. With this knowledge in the perspectives of this system modification of the procedure of annealing the as cast amorphous samples, previously sealed in a vacuum or treated in Ar/He atmosphere would be a justified step to be made.
c) An alternative way to synthesize nanoporous morphology was realized through dealloying of ternary crystalline $Ag_{38.75}Cu_{38.75}Si_{22.5}$ precursor that presents phase separation on the sub-100nm scale. Moreover, two constituent phases separate the target Ag matrix and Cu_3Si less noble phase that was further removed from by dealloying in 0.67 M HNO_3 and 0.64 M HF etching solution. Resulting NP material was entirely constituted of regular and continuous fcc silver crystalline ligaments with minor Cu and Si traces. The obtained NPS ribbons presented good integrity, which can be tuned via dealloying time/thickness of the bulk load-bearing layer. Although larger geometries characterized present NPS morphology compared to the one obtained through dealloying of the amorphous material of identical composition, we believe that our material demonstrates the competitive potential for successive applications.
d) The fabrication of the last system of interest was based on the same principles as in the previous NPS case, but with the idea of substitution of pricey components such as silver, and to explore the catalytic possibilities of the cobalt metal. $Co_{42.1}Cu_{36.23}Si_{21.67}$ crystalline metallic ribbons were dealloyed in diluted nitric acid to remove elements other than Co. As a result of Cu and partially σ-Co dissolution, Co_2Si phase started prevailing over the others. Finally, a self-supporting Co-

Co_2Si nanoporous matrix was formed. It was for the first time that an attempt of NPCo synthesis via dealloying of melt-spun ribbons was undertaken and can be considered successful. A possible solution of synthesis of fully cobalt-based metallic matrix would be (technically more challenging) fabrication and study a phase separation processes in the family of metastable, Si-free Co-Cu alloys and selection of appropriate etchants for more noble Cu-rich phase.

e) Throughout this section on materials preparation, two classes of materials have been considered for NPMs preparation: amorphous and crystalline ones. It was demonstrated here and confirmed by other studies, that dealloying of amorphous precursor results in finer interconnected ligaments microstructure, than in the case of dealloying of crystalline alloys. Such phenomena is considered favorable from the point of view of increased specific surface area, but may also affect the strength of the structure.
f) As an essential remark, it should be noted that all mechanical properties given about the synthesized NPMs were not strictly measured values (such as strength, Young's modulus, bendability, etc.). However, observed materials response to manipulations and handling resistance.

…

Finally, main quantitative results of representative structural dimensions of NPM are gathered in the Table III.1.

Table III.1. Geometrical characteristics of studied nanoporous metallic systems. NPS from amorphous precursor is given for comparison with its counterpart. Due to the irregular interconnection of NPCu ligaments, their length and porosity fraction of the materials are estimated from the cross-sectional view.

Type of NPM	Precursor	Ligament (nm)		Pore (nm)		Porous fraction (%) (from threshold)
		width	length	Width	Length	
NPS	Amorphous $Ag_{38.75}Cu_{38.75}Si_{22.5}$	20	40	30	100	29-36
	Crystalline $Ag_{38.75}Cu_{38.75}Si_{22.5}$	46	107	38	95	31-39
NPCu	Thermally annealed amorphous $Cu_{60}Ca_{40}$	20	40	23	38	43-49.4
NPCo	Crystalline $Co_{42.1}Cu_{36.23}Si_{21.67}$	190	> 1 µm	140 (circular)		9.5-28

III.2. 3D Visualization and quantitative analysis of 3D structures

A proper strategy for morphological analysis of nanoporous metallic structure and its quantification is essential for a better understanding of the properties that are associated with their high surface-area-to-volume ratios. In this chapter, we introduce an approach mostly adapted to our type of materials: a FIB-SEM nanotomography technique. Three-dimensional numerical prototypes, reconstructed on the basis of this techniques and quantification of materials' structural parameters such as specific surface area, pore fraction, connectivity, curvedness and shape index were determined for nanoporous copper, silver and cobalt supports and consequently presented in the following sections of this chapter. The results of experimental analysis of specific surface and pore-size

distribution were performed via BET method. A corresponding comparison of calculated surface characteristics was made for each of the studied systems in the conclusion of this chapter where a good correlation between the numerical and physical approaches was established. An importance of three-dimensional characterization for quantitative evaluation of porous media and catalytic supports should be highlighted since it represents a powerful tool for the profound insight into the unexposed intrinsic properties of the class of nanoarchitectured systems.

III.2.1. FIB nanotomography for a 3D model

As it has been introduced to the reader in section II.3.3, Fiji is a built-in ImageJ image-processing package, which enables one to treat consequent series of images to render a corresponding image stack. By using an appropriate plugin, this stack can be further visualized as a 3D object of the volume of interest (V_{oi}).

In present work, such image stacks were obtained with the help of FIB-SEM technique according to the procedure in section II.3.2 for all 3 types of NPM systems. The main advantage of such relatively new type of tomography is its high resolution within adequate timescales and performed on a representative volume of the sample for the case of nanosystems, which cannot be achieved either by X-ray, neutron- or TEM-tomography means. Although, some studies has been actively using high-angle annular dark field scanning transmission electron microscope tomography for analogous characterization of mesoporous silica supports for catalytic nanoparticles [227]. However, in this case, one should be aware of the limitations of the sample's thickness ($\leq$ 100 nm) implied by TEM technique. With the development of synchrotron capacity, the X-ray tomography resolution has considerably improved in recent years. Still, voxel dimensions below 1µm can hardly be attained and therefore, in many cases, the resolution of X-ray absorption tomography is insufficient for the study of nanostructured materials. It can be presumed from the increasing number of related publications that FIB-SEM is the most appropriate tomography tool that allows observing and characterizing the interior of nanoporous metal foams of a representative volume. Nevertheless, among the drawbacks of this technique should be named its destructive nature, since the ion beam milled-off part of the sample can no longer be restored.

III.2.1.a. Nanoporous copper in 3D and its quantification via Fiji

For the reconstruction of NPCu 3D model, a total of 154 cross-sectional as-dealloyed ribbon cuts has been made. Although, due to occasional malfunctioning of built-in drift correction function during the *in-situ* data registration, only 30 consequent images were executed to create a corresponding 3D volume model (Figure III.35) which allowed a satisfactory resolution of nanostructured features.

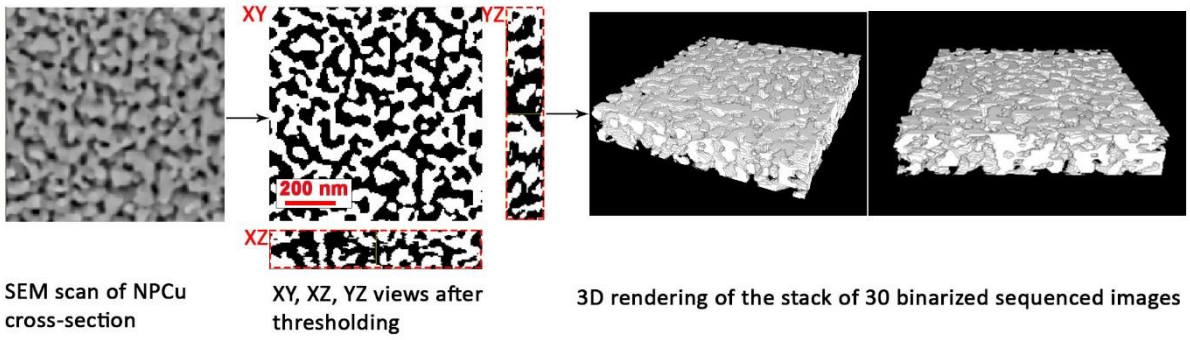

Figure III.35. FIB-SEM tomography of fully dealloyed NPCu ribbon. The sequence exhibits a similar procedure of the numerical model restoration as in Figure II.12 and realized in Fiji.

Present structure possesses a pore fraction φ_{pore} = 50.3 ± 4 % calculated as the fraction of pixels belonging to the copper ligaments (white phase on Figure III.35). A large margin of error was caused by the uncertainty of the definition of contrast between the ligaments of the top and underneath layers, which is called "shine-through" artifact. This problem is often solved by infiltration of polymeric substances or special nanocomposites inside the porous phase, which gives good contrast with metallic phase when visualized by SEM and therefore, facilitates thresholding [228,229]. Unfortunately, the knowledge of such optimization procedure reached us simultaneously with the experiments being under execution and was not applied in this work.

A useful procedure that gives an estimation of "particle" size distribution (by particles here we mean ligaments) is granulometry by opening contained within the object (solid phase of porous matrix)[230]. Application of the corresponding filter to the binarized stack, associated with NPCu, resulted in the following ligament size distribution (Figure III.36).

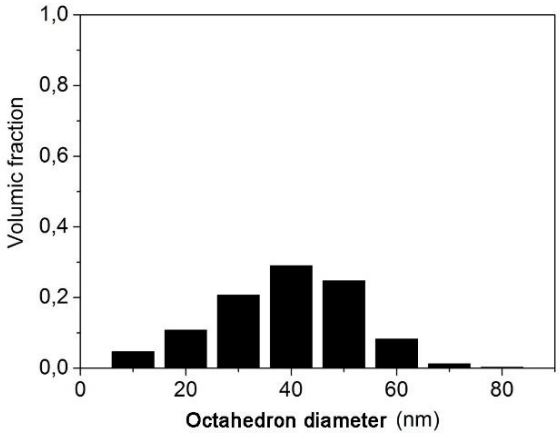

Figure III.36. Ligament size distribution according to granulometry by octahedron opening. Y axis indicates the volume of the solid phase, occupied by each corresponding size of the ligament.

As one may see from the obtained histogram, the average size of the ligaments is 40 nm, which corresponds to the arithmetic average ligament length, statistically found from 100 measurements in the section III.1.2. of the previous chapter.

Another important characteristic of nanoporous metals is the connectivity of the structure. In numerical 2 dimensions it is expressed through pixel connectivity, i.e., all pixels in a connected component share similar pixel color value and are in some way connected with each other. Once all groups have been determined, each pixel is labeled with a gray level or a color code (color labeling) according to the component it was assigned to black (0 color code) and white (255 color code). In three-dimension the principle is similar, but a voxel term is used instead. In this work, connectivity was calculated using the reconstructed numerical model by the Fiji "labeling" plug-in with "26" 3D connectivity (meaning that voxels are connected if their cubes share a common vertex).

Labeling solid phase (255) gives almost complete connectivity with only 0.015% of free-floating volume. Inverse labeling of porous phase gives a similar result. Therefore, the structure can be considered bi-continuous.

After labeling the bulk phase of the model, it is possible to determine the surface area, created by Marching-cube algorithm.[231] Knowing this surface in marching cubes (S_{mc}), physical V_{oi}, the density of porous silver matrix (ρ_{nps}) it is possible to calculate a specific surface S_{spec} of NPS:

$$\rho_{nps} = \varphi_{pore} \times \rho_{Ag} = 4.45 \text{ g/cm}^3$$

$$V_{oi} = XY \times XZ \times ZY \times 125 \text{ cm}^{-21} = 1 \cdot 10^{-13} \text{ cm}^3$$

$$\text{The mass of } V_{oi},\ m = V_{oi} \times \rho_{nps} = 4.45 \times 10^{-13} \text{ g}$$

$$S_{spec} = S_{mc}/m$$

Where S_{mc} is calculated by the corresponding plug-in and for indicated V_{oi} is equal to 188637 pixels = 0.47 x 10^{-11} m^2. Therefore, S_{spec} = 10.56 $m^2.g^{-1}$, and can further be compared with an experimentally measured value (section III.2.2).

III.2.1.b. 3D surface visualization of nanoporous copper in Avizo

As it has been detailed in chapter II.3.3, an image stack registered via Fiji can be imported in another software suite Avizo, FEI™ that allows surface reconstruction and adequate visualization quality.

The generated NPCu surface is presented in Figure III.37 in different perspectives. The object was created by "generate surface" module with a grid smoothing level 5 of "unconstrained smoothing" type. Such parameters have been chosen, based on the representation of a "test" 3D model of a sphere with a diameter equal to 6 voxels (≈ 30 nm), which corresponds to the characteristic length scale of the NPCu microstructure (see Annex, Figure A.1). We consider that correct visualization of such basic object would approach one to the proper representation of a more complicated structure, such as present nanofoam. After trying out multiple combinations of the level and type of the surface smoothing, selected parameters were found to give the most adequate representation of a spherical surface without loss of the size or symmetry of the object. Smoothing is important since it defines how

sharp one wants to keep angles between triangles of the surface forming a grid. Smoothing algorithm can be found in the user-assisting guide [232] of the software and will not be specified in this work.

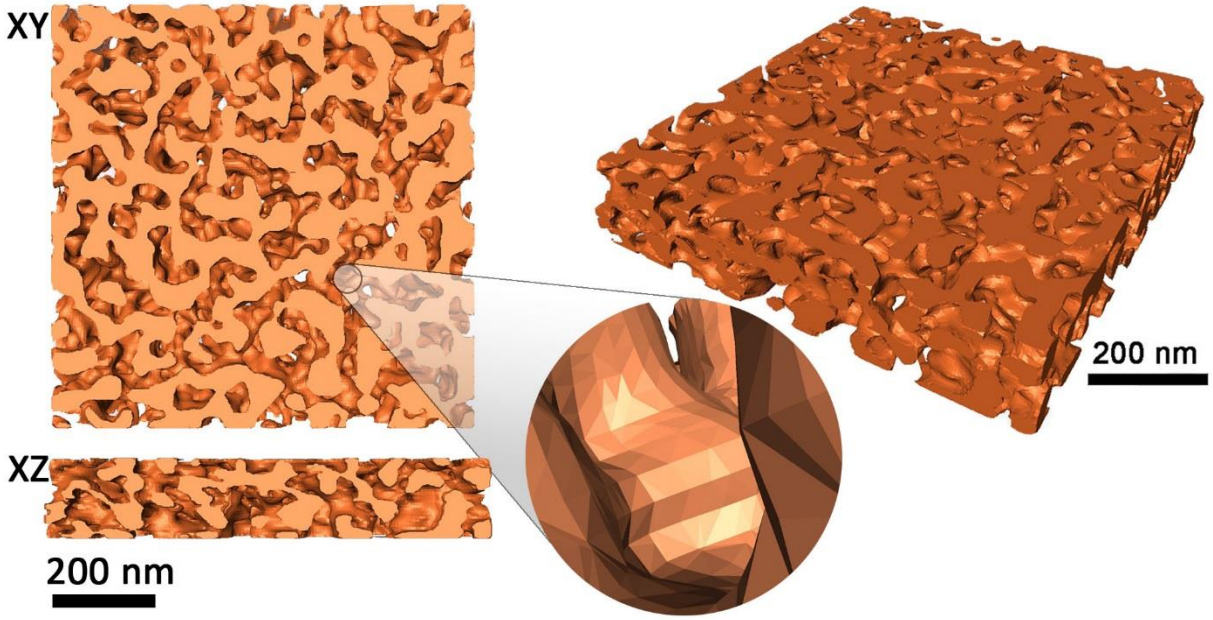

Figure III.37. Smoothened three-dimensional surface morphology of the NPCu in one perspective and two orthogonal XY and XZ views executed via Avizo software upon the image stack, created via FIB-SEM and Fiji. The inset presents magnified view of the triangle-patch surface grid. Physical volume dimensions are 820 × 820 × 150 nm.

Surface and volume analysis integrated function renders the total surface of the solid phase in pixels, which can be transferred into nm^2. Same as in the previous section, S_{spec} of the interface between the solid phase and porosity was calculated as 9.2 $m^2.g^{-1}$ which is 15 % different from the value, calculated by Fiji. It should be admitted that taking into account the initial resolution of the SEM scans, where 1 pixel is considered equal to the 5×5 nm^2, and the average ligament size is ~ 6 pixels (30 nm), such correlation of S_{spec} is a fairly good result. As the solid fraction was evaluated as a ratio of some pixels, restrained within the solid phase (V_s) to the total number of pixel in the physical $V_{oi,}$ the pore fraction $\varphi_{pore} = 1 - V_s/Vtot = 0.51$. This value is consistent with the result obtained by simple histogram analysis of the initial binary image stack in Fiji (Figure III.35).

Surface "curvature" utilities, implemented in Avizo, allows one to estimate the *curvedness* (*C*) and *shape index* (*S*), as introduced in the end of the section II.3.3. Corresponding color mapping of C and S values along the selected surface area of NPCu segment is presented in Figure III.38. From visual inspection, it seems that the shape index is homogeneously distributed and no particular shape of the interconnected network is prevailed over others, except that extreme cases of "cap"-"cup" shape (typical result of ligaments pinch-off) are minimal. As for curvedness, its values lay principally below 0.1 nm^{-1} and is in agreement with reported data for analogs nanostructures, including catalytic nanomaterials [233,234]. From a practical point of view, it is an extremely small value of object's curvedness, for comparison, a curvedness of a standard football of 22 cm diameter is 4.5 m^{-1}, almost eight orders superior to our system.

Better quantitative estimation of *S* and *C* surface characteristics can be made with the help of interfacial shape distribution function (ISD). ISD indicates a probability of finding a patch of interface with an attributed pair of *S* and *C* coordinates. By plotting the distribution of points with *x* coordinate corresponding to the shape index, and *y* coordinate to the curvedness, one may obtain a 2D histogram that reflects the ISD (Figure III.39). The above described quantitative characterization of tortuous structures is extremely useful in the domain of catalytic materials, in particular for the evaluation of fluid transport mechanism inside the system driven by the Gibbs-Thompson effect (i.e., the local chemical potential is proportional to the local radius of curvature) or dependence of the effective catalytic sites concentration on substrate's shape.

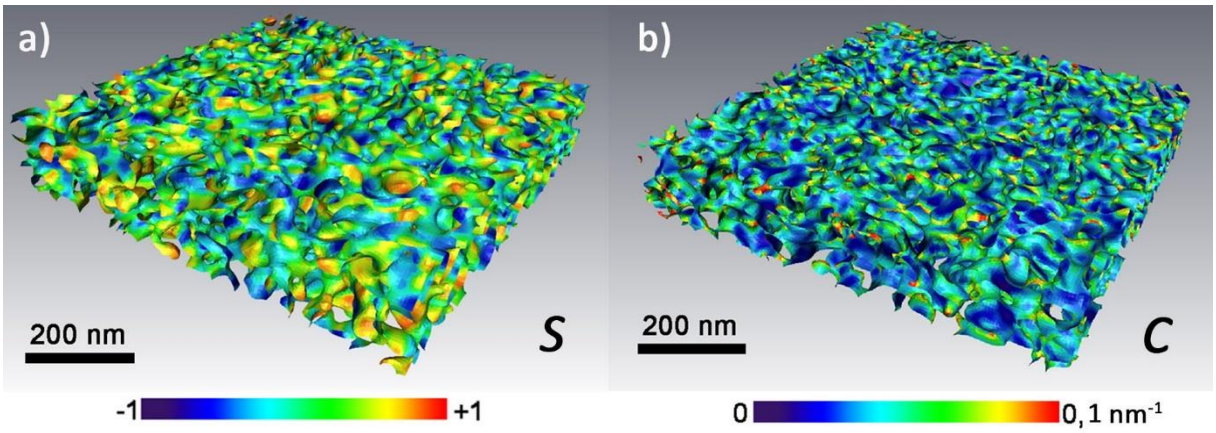

Figure III.38. A geometric surface of NPCu excluding the edge borders colored according to its classification using the Koenderink-van Doorn shape index (a); and the curvedness (b). Red-orange and green-blue regions on (a) correspond to convex and concave areas respectively, while intermediate color values represent saddle and saddle-like regions. The shape classifications are described in the section II.3.3.

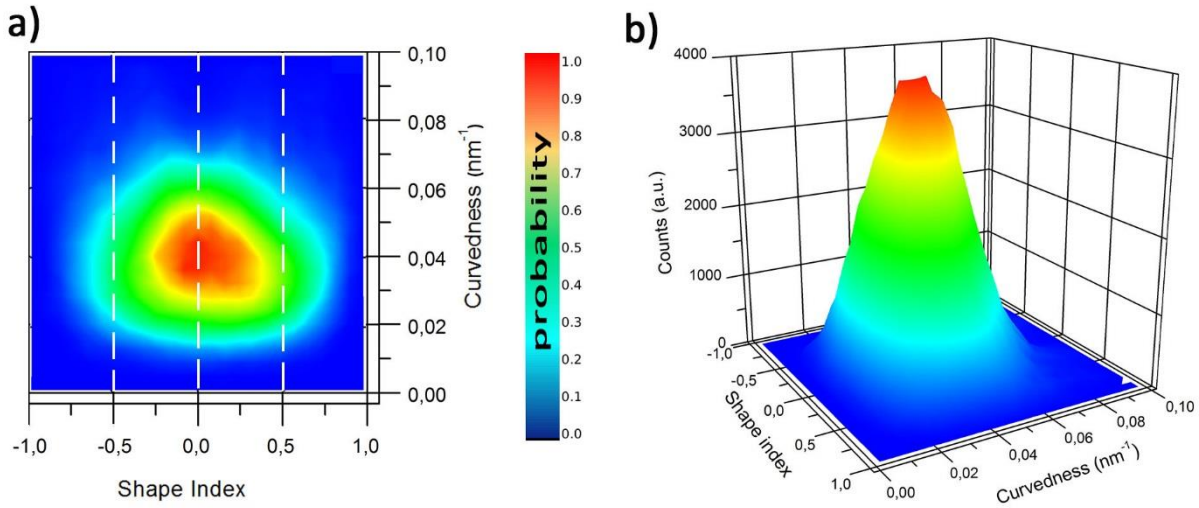

Figure III.39. Two-dimensional (a) and three-dimensional (b) interfacial shape distributions of nanoporous copper segment. The most representable patch of surface possesses a shape index that ranges from -0.6 to 0.8 with a curvedness ~ 0.04 nm^{-1}. The majority of present shape are anticlastic "saddle-type" surfaces with extension to "saddle rut" and "saddle ridge".

III.2.1.c. Estimation of uncertainties related to FIB nanotomography

As in any characterization technique, 3D model reconstruction FIB nanotomography also has several possible sources of errors. Due to the non-negligible mismatch of data, it was considered necessary to introduce some explanations.

Firstly, the FIB-SEM calibration may lead to an error in image recording of up to 5% in x-y axis, which is equal to 0.25 nm per pixel. The roughness of milling technique and precision of ion beam is another source of z-axis error, since the ion beam may produce curved slanting surfaces as it advances into the depth of the sample. Roughness rate can also be influenced by the state of milled material and its capability to preserve its characteristics during ion beam milling. The described phenomena can violate the assumption of flat milled sections and affect the z-error value. In the [235] study of porous $BaTiO_3$ ceramics in comparable FIB nanotomography experimental conditions it has been established by AFM analysis that for a voxel resolution of 6nm an upper limit of z-axis error while milling was ~ 1nm. The z-directional drift phenomenon together with its autocorrelation procedure can lead the z-axis error to exceed 17 %. Lastly, a partial distortion of real object's characteristics was introduced in the step of image treatment (median and bilateral filters, contrast normalization, etc.) and its binarization (threshold). The first part of image treatment procedure can be considered negligible in comparison with the threshold step, which completely depends on image quality and contrast. It was tested for a set of exploited images that in this work the threshold reaches 12% uncertainty error of phase definition that consequently affects a 12% error of phase's volume and surface calculations. The simultaneous calculation of all methodical errors, produced along the reconstruction of a 3D model of the nanoporous metallic structure is complex and would require an additional measurement and comparison with the etalon sample, studied under similar conditions, which has not been done in the frames of present work. Although, from the arguments given above, it is possible to conclude that the error/distortion of the picture can locally reach > 20% and, thus, contribute to the differences in quantitative results.

III.2.2. Physical gas adsorption for porosity evaluation of NPCu

Alternatively, the internal specific surface area of the NPM and pore size has been measured by the model-dependent Brunauer, Emmet, and Teller method (section II.1.3.e.), based on analysis of nitrogen gas adsorption-desorption isotherms. Figure III.40 displays the nitrogen adsorption/desorption type IV (according to IUPAC classification [236]) isotherm curve performed on 156.9 mg NPCu sample of $Cu_{60}Ca_{40}$ cast sample. The part of the curve at low relative pressures is associated to the monolayer adsorption, and according to BET method [236] the quantity of N_2 gas adsorbed in that pressure range ($0.05 < P/P_0 < 0.25$) was used for the evaluation of the S_{spec}. Hereafter, BET surface area was calculated 14.05 ± 0.06 $m^2.g^{-1}$, which from the first sight appears to overestimate the real picture.

Determination of the pore size distribution was evaluated by Barrett, Joyner and Halenda method [186] (BJH) (DIN standard 66134) which is usually used for mesoporous materials with the pore radius r = 15-1000 Å. It uses the modified Kelvin equation [237] to relate the amount of adsorbate removed from the pores of the material, as the relative pressure (P/P_0) is decreased from a high to a low value,

to the size of the pores. Obtained pore size distribution of porous copper substrate is exposed in Figure III.41.

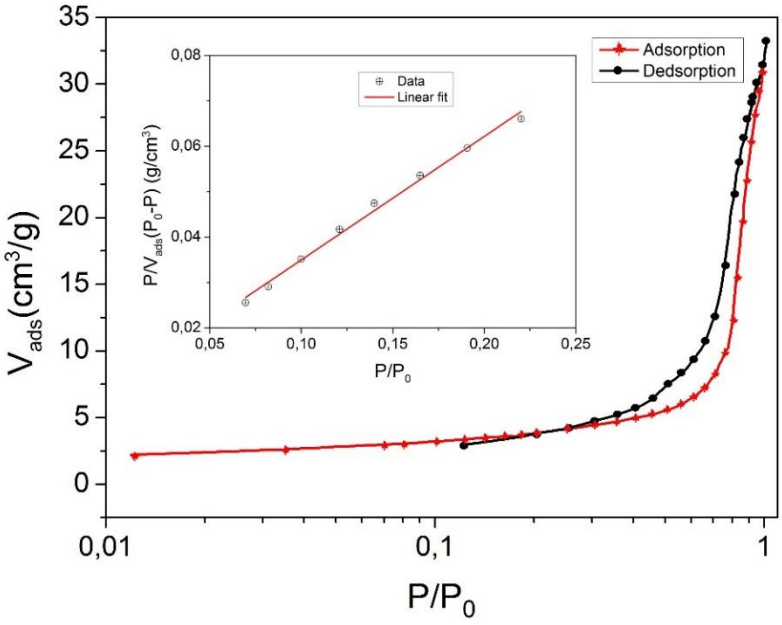

Figure III.40. BET nitrogen adsorption/desorption isotherm curves for NPCu sample. The initial linear part of the isotherm curve at low relative pressures corresponds to monolayer adsorption. The BET surface area and constant were deduced from the slope (0.305 ± 0.001 g.cm^{-3}) and offset (0.0046 ± 0.0002 g.cm^{-3}) of the linear part of the nitrogen adsorption isotherm. Here V_{ads} is a volume of adsorbed gas per unit mass of the sample.

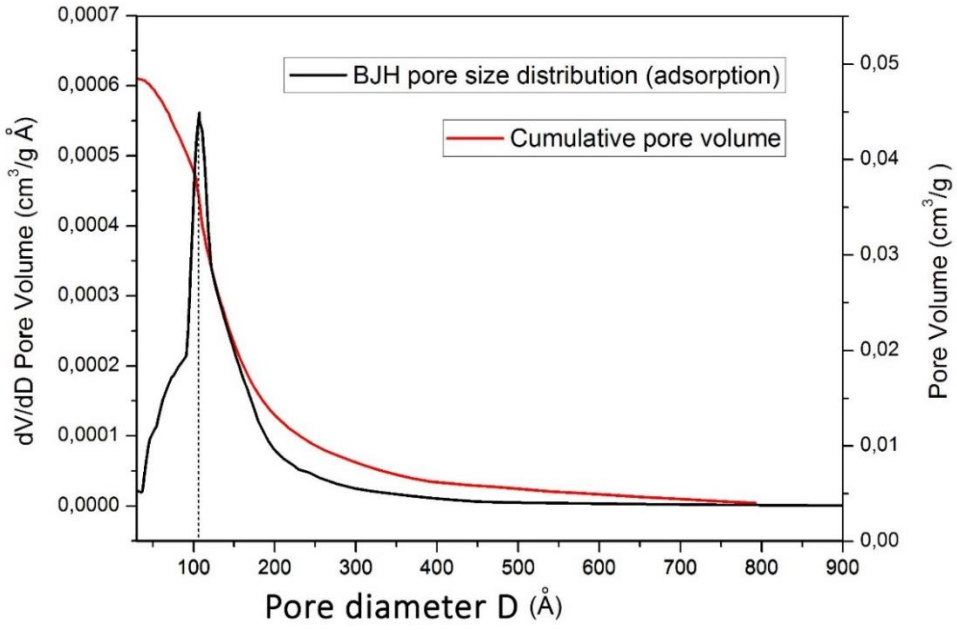

Figure III.41. Cumulative pore volume (red) and differential pore size distribution (pore volume density) (black) plots; dV is the change in adsorption volume; dD is the change in pore diameter size.

From BJH graph one may see that the maximum of adsorbed gas volume falls within the pore diameter range of 5- 20 nm with the maximum at 12 nm, and the average pore diameter value for adsorption-desorption curves is 10 nm. Such value is twice less than in previous granulometry of 3D model and a statistical SEM/TEM image analysis, where the numbers were obtained as a result of visual observation of microscopy images limited in resolution. In that case, sub-10nm features (less than 2 pixels in FIB nanotomography experiments) were more likely to be missed, and, therefore, not accounted for the calculations related to numerical analysis, whereas BET method does not experience such limitations and is likely to be more accurate in the domain of fine porosity.

III.2.3. Comparison and limitations

Resultant surface and pore size distribution analyses have been performed via two different approaches. A first numerical approach based on a calculation of 3D model realized with the help of FIB nanotomography gives a S_{spec} = 10.56 $m^2.g^{-1}$ (Fiji) and 9.2 $m^2.g^{-1}$ (Avizo). The pore size distribution based on granulometry calculations is similar as in Figure III.36 since porous and solid phases are complementary to each other for a bi-continuous structure at the φ_{pore} = 50,3 %. The corresponding average pore size gives a value of 40 nm, while, in statistical image analysis (as in section III.1.2.c, Figure III.17), the average value is 18 nm. This last result correlates fairly well with the experimental BJH pore size distribution plot, where the pore size of the distribution has a maximum = 12 nm. S_{spec} determined by the gas adsorption/desorption method = 14.05 m^2/g and exceeds previously obtained S_{spec} values. This discrepancy may indicate a certain shortfall of the BET technique because of the assumptions inherent in modeling the mesoporous systems [227]. The additional surface may be attributed other than to the internal porosity (for example, ribbons cracks, borders of V_{oi}, other defects), or also because of overestimation of true gas monolayer loading on the internal pore walls. [238] The last has less probability due to the absence of orientation effect of N_2 molecules on nonpolar metallic surfaces. It is also possible that the volume studied by FIB nanotomography is not a representative part of the macroscopic sample, differently from the analyzed via BET mass of 0.156 mg, where come the differences of obtained data.

Of no less importance is the fact that FIB-SEM tomography method possesses an important error margin and certainly contributes to the observed incompatibility of quantitative structural characteristics of investigated nanoporous structures.

Generally speaking, BET is an appropriate technique for an overall macroscopic characterization of the sample and comparative measurements of different samples of the same type, while FIB nanotomography is more precise about rather local information of the structure (mean curvature, curvedness, shape and so on.).

III.2.4. 3D visualization and quantification of nanoporous silver and cobalt systems

After a thorough examination of NPCu system by FIB-SEM tomography combined with visual software and experimental BET technique, corresponding results related to NPS and NPCo samples will be briefly given and summarized in present sub-chapter.

For the creation of the 3D model of a 45 minutes dealloyed reference NPS sample (Figure III.29.b) from a series of SEM images, a mechanism similar to the case of NPCu has been adapted. In the case of NPS, a stack of maximum 28 consequent sectionings guaranteed a minimal z-axis image drift. After applying a threshold filter, the porous fraction φ_{pore} is determined 51.6 ± 6 %. Java plug-in visualized NPS model on the base of the image stack, and built-in surface view in Avizo are presented in Figure III.42.

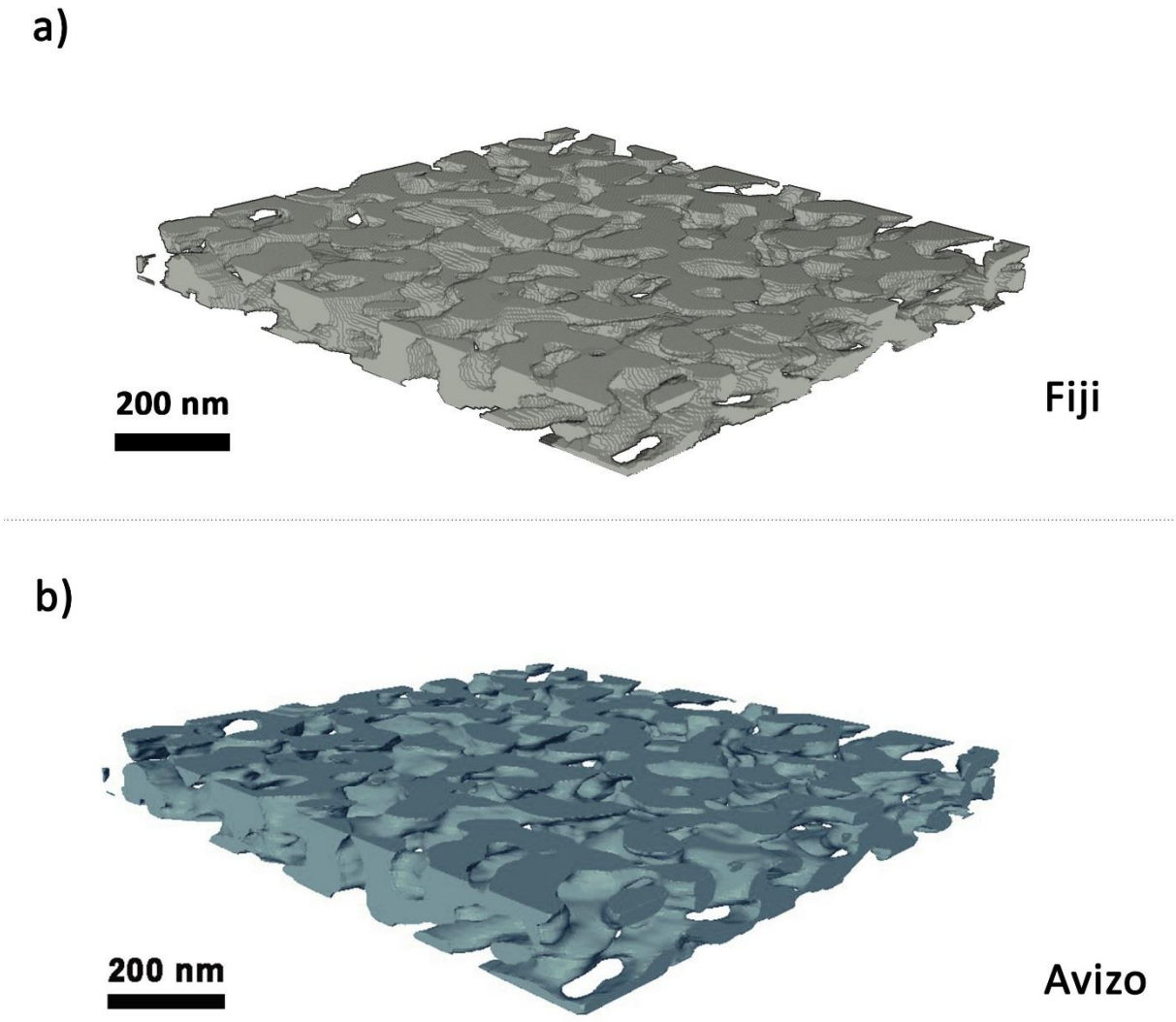

Figure III.42. 3D rendering of the stack of 28 binary sequenced images of the nanoporous silver matrix (a) and a corresponding surface visualization in Avizo based on triangular mesh grid (b). Physical volume dimensions are 1430 × 1430 × 140 nm.

Granulometry calculations of octahedron opening, performed on the hollow phase of the reconstructed NPS model give a peak size distribution value at a particle diameter of 18 pixels (~90 nm), which is roughly consistent with the straightforward Fiji measurements of pore geometry (section III.1.5). Specific surface area, calculated from this 3D model was 4.02 $m^2.g^{-1}$, while BET measurements on 0.2335 mg of material predict a S_{spec} of 5.01 $m^2.g^{-1}$, which like in the case of NPCu sample demonstrates a divergence of ~ 20%. As for PSD, according to BJH model, the distribution maximum corresponds to the pore diameter of 47 nm for both adsorption and desorption curves, and the average pore size as of adsorption-desorption graphs was 36.5 nm. It should be noted that according to certain research groups, correct interpretation of PSD data high reliability of information requires approximately 20 m^2 surface of material S_{tot} in the experimental cell. However, this was not the case in either of present experiments (the average S_{tot} value for any of the three studied systems did not exceed 3.4 m^2). Hence, we suggest considering the presented in this work PSD data with caution.

ISD mapping has been similarly performed for the selected V_{oi} of the nanoporous silver sample, and its two- and the three-dimensional pattern is exhibited in Figure III.43. As in the case of NPCu, it is homogeneously curved within the medium shape index $S \in [-0.5; 0.75]$ and a most representable patch of the surface with the coordinates in the proximity of (0.25; 0.017) in (S; C) space.

As for the nanoporous cobalt, due to the lack of original sample, described in the section III.1.4, an analogous material, obtained using the local melt-spinning setup in adjusted conditions has been fabricated. After similar chemical treatment, a nanoporous substrate was successfully obtained, although, it is natural to expect certain divergence between the samples in their structural characteristics, which will be revealed further. The aim of FIB nanotomography experiment performed on this newly synthesized sample was to present its morphological difference, expressed through quantified 3D model and ISD pattern and consequently compare all the three studied systems.

According to the model, reconstructed from the sequence of 32 SEM images of the representative cross-section area of dealloyed ribbon, current nanostructure possesses finer interconnected ligaments and pores comparing to the previous analog. It was characterized by 35 ± 3 % of porous space, with the 40-50 nm ligament and 30 nm pore size, as a result of granulometry calculations. More importantly, its S_{spec}, determined from numerical model = 8.3 $m^2.g^{-1}$ in good agreement with the BET experiment that indicated a BET S_{spec} of 7.6 $m^2.g^{-1}$ (almost 4 times higher than for the previous sample which BET surface area was determined 1.96 $m^2.g^{-1}$) and an average 32.5 nm pore size. One of the reasons for smaller structural units of the present sample is the different resultant composition of the as-cast metallic ribbons ($Co_{25.6}Cu_{45.3}Si_{29.04}$ according to EDS data averaged along the cross-section). Having a higher percentage of copper in the pristine material would affect higher porosity after dealloying due to copper-rich phase dissolution. Another factor that might also have had an impact on the refinement of the microstructure would be a quench rate (dependent on the wheel speed, casting temperature, atmosphere in the chamber, etc.). On the 3D reconstruction in Figure III.44, as well as on the SEM image from Figure III.33.b, one may notice a confirmation of preferential direction of ligaments coarsening perpendicular to the ribbons plane surface. This phenomenon is well reflected via the ISD map, where the center of the 2D histogram is shifted towards the rut-like shape factor -0.5, which corresponds to the tubular interfacial structures.

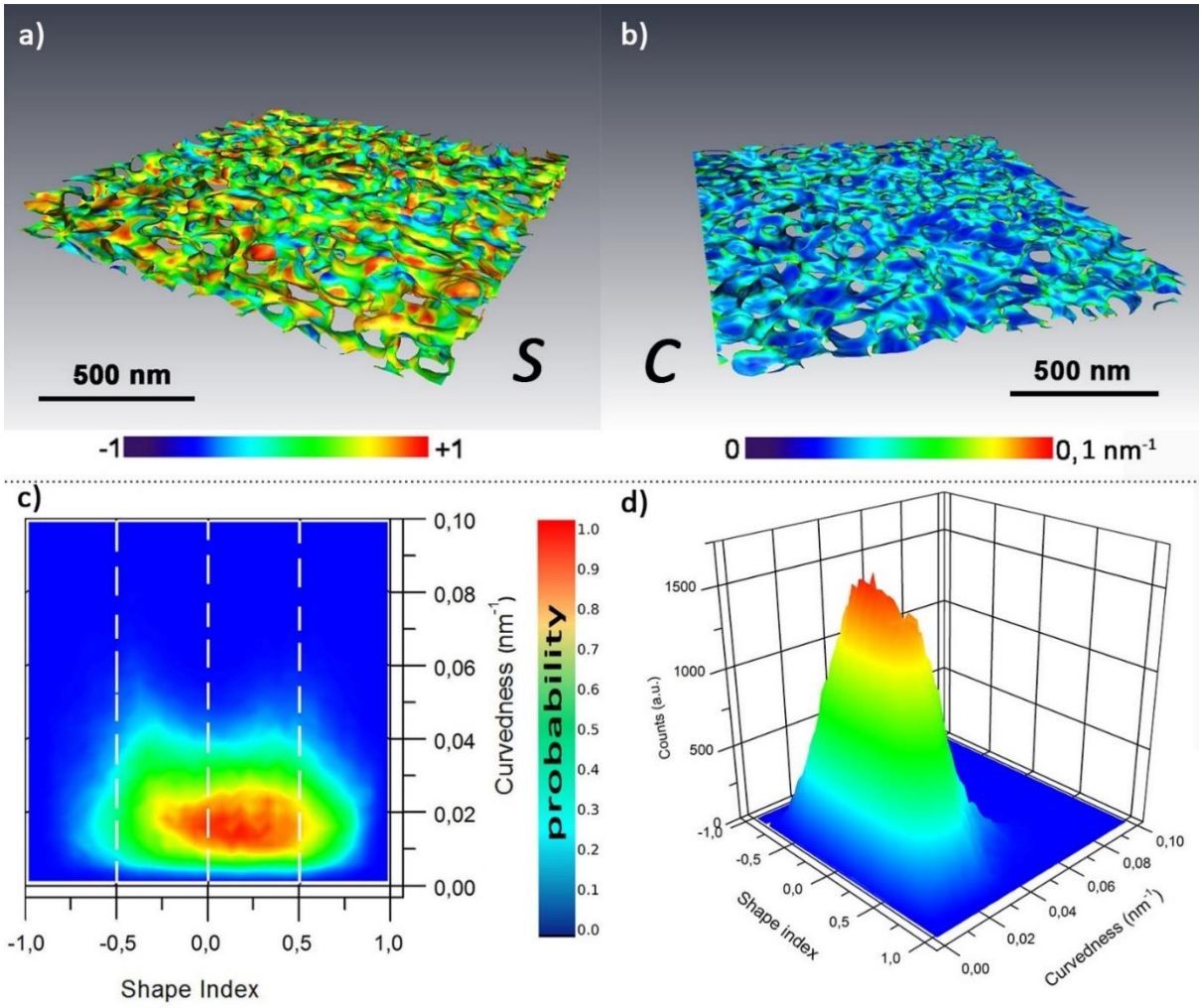

Figure III.43. A color mapping of the NPS surface according to its classification of shape index (a); and curvedness (b). 2D and 3D view of the interfacial shape distributions of a nanoporous silver segment (c and d respectively).

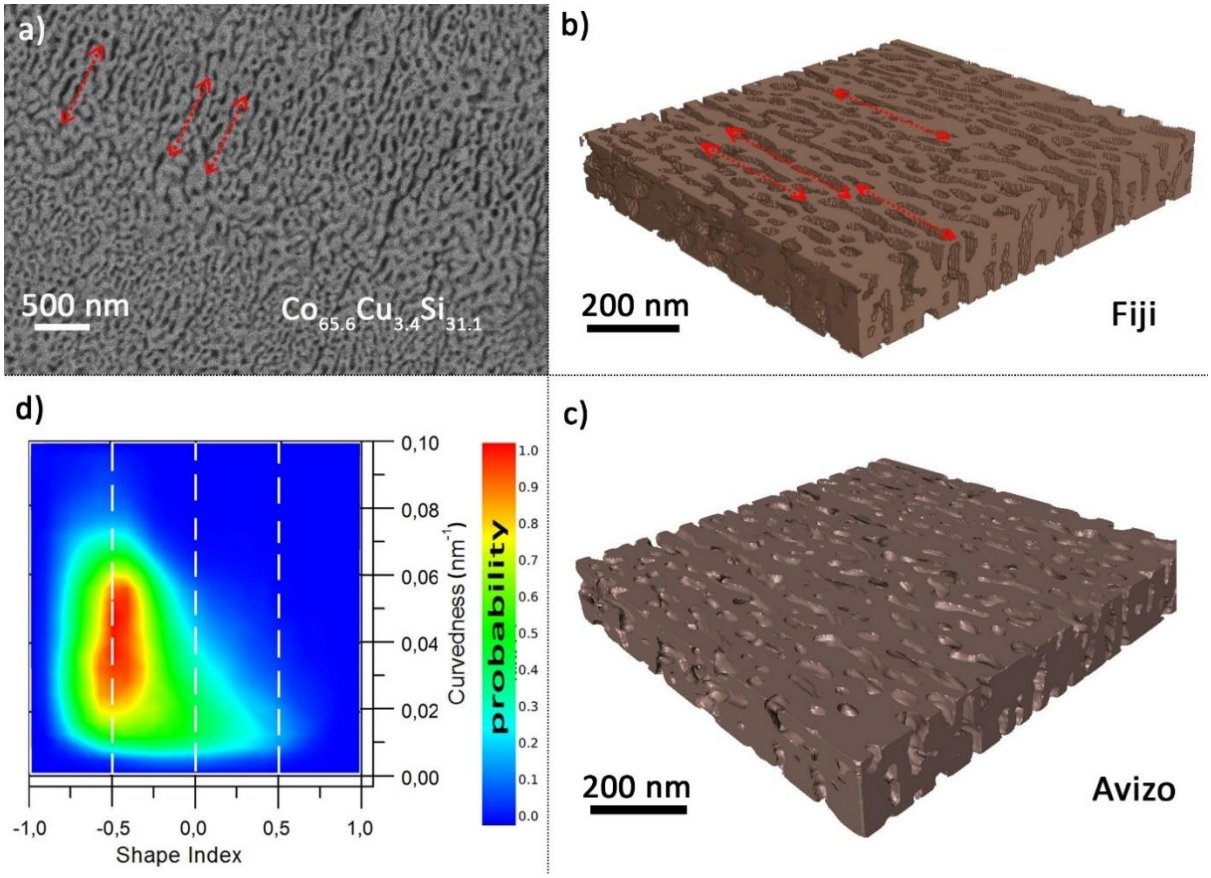

Figure III.44. SEM micrograph of a dealloyed home-cast NPCo ribbon (a) and its reproduced prototype, visualized as a 3D image stack (b) and corresponding surface mesh (c). A corresponding ISD histogram indicates a non-symmetric shape index distribution, shifted towards a rut-like form (d).

III.2.5. Comparisons and conclusions

The comparative chart of ISD patterns for the three most studied nanoporous systems is given in Figure III.45 and vividly presents the morphological diversity between the nanoporous substrates. NPCu possesses the highest curvedness among the represented structures due to its smallest radius of surface curvature, while the lowest C is attributed for NPS. As for the last cobalt substrate, its curvedness is expanded along a relatively wide range of values from 0.018 to 0.06 nm^{-1}. Regarding the shape variations of the discussed morphologies, the near-zero symmetry of copper and silver substrates was well established, as contrasted with NPCo sample, where the existence of the preferential directionality in the microstructures was visually detected and confirmed by the shift of the shape index. A particularly surprising result was that in the case of nanoporous silver and cobalt samples there was a considerable amount of interfacial area that is nearly flat (note the substantial region of nonzero probability in the region $C < 0.01$). Because S is difficult to determine for structures with nearly flat interfaces, such interfaces exhibit a band of probability over a wide range of S for low C as shown on Figure III.45.b-c.

Among general results of this chapter a successful reconstruction of 3D prototypes of the studied nanoporous systems with the limit voxel lateral resolution size of 5 nm should be mentioned. A fairly

good consistency between numerical and physical ways of S_{spec} and PSD determination has been revealed. For all three systems, the S_{spec} error margin did not exceed 20% and prevailing pore sizes obtained by BJH model were in agreement with the granulometric and statistical image analysis of the reconstructed 3D model. NPMs were determined to have bi-continuous morphologies with negligible free-floating volume fraction. Color mapping of curvature characteristics allows supplementary information, useful for the field of catalytic and optically active nanomaterials as for the description of mass-flow transport, the density of catalytically active sites, the location of phonon "hot spots" etc.

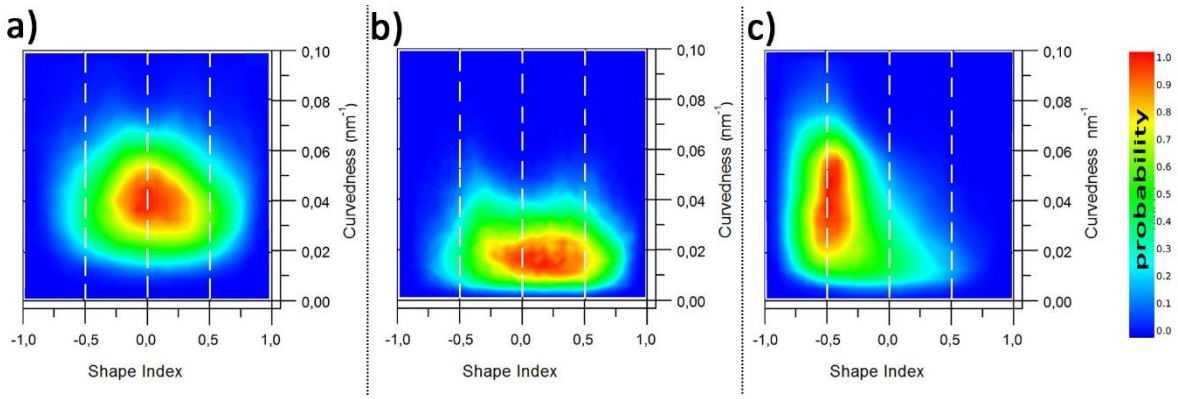

Figure III.45. A comparison of ISD patterns for all nanoporous substrates, reconstructed via FIB-nanotomography: a) NPCu; b) NPS; c) NPCo (home-cast).

III.3.Mechanical behavior of NPMs at nanoindentation.

Nowadays, great attention is paid to the study of synthetic means of new nanoporous metallic substrates and tuning their morphological and functional properties. However, at some point the question comes to the simple handleability of the fabricated substrates during the laboratory experiments not to speak of their integration in the real devices. As it has been discussed at the beginning of section III.1.3, one of our most catalytically perspective NPS material, synthesized from the amorphous precursor, did not possess an adequate integrity to follow its valorization as an anodic catalyst in the frames of half-fuel-cell experiments. This lead to the synthesis of its counterpart from a crystalline precursor, which showed better mechanical stability during casual manipulations and, therefore, this NPS substrate has been subject to further mechanical characterization. Instrumented nanoindentation technique is considered as an ideal solution for testing nano-scale films and materials, as it can limit the indentation depth to reduce substrate effects and is featured by high sensitivity and stability of measurement. It allows to carefully tune the penetration depth of the indent inside the foam and obtain representative mechanical characteristics of material as a whole, avoiding the manifestation of a single-ligament response. Hence, it has been chosen as a main method to evaluate mechanical properties of our porous substrates.

Combining the existing theory on strain gradient plasticity, complemented by the elaborated analytical description of porous network deformation under applied stress, and experimental results

on NPS nanoindentation, we propose an original modelling of the dependence of materials hardness on the morphological parameters and indentation depth.

Among the systems of interest, nanoporous silver was considered as the target NPM for nanoindentation study, since characterization of its mechanical behavior would bring us closer to the comprehensive image of this catalytic and optically active substrate. Moreover, fragile NPCu material has already demonstrated its incapacity as a sustainable substrate, and it would be desirable to improve its integral properties on the step of sample elaboration before any quantitative mechanical characterization. As for NPCo, its viability as an efficient long-functioning catalyst is still not completely clear. Therefore, we save any discussions regarding its mechanical properties for later, although, at present, the material manages to sustain all the electrochemical procedures and manipulations without noticeable physical degradation.

III.3.1. Nanoindentation of NPS samples

Nanoporous and pure bulk silver samples for nanoindentation have been prepared as described in the section II.3.5. It should be noted that, since the as-cast ribbons have been stored in the intended desiccator for a prolonged time (more than 12 months), they suffered from tarnishing which affected their top layer chemical composition and visually added them a dark-gray tone. Even after light surface grinding and polishing, this phenomenon affected the porosity formation throughout dealloying. It resulted in a shift of dealloying times, necessary to acquire the morphologies, previously attributed to the dealloying time of 45, 60, 90 minutes and so on. Therefore, in this section, we no longer refer to the NPS nanostructures, obtained previously, but we use new indications such as "Structure 1" etc. that will imply a corresponding morphology of NPS. This remark does not imply though that the finesse and structural limits of NPS have considerably changed. The same nanoporous silver matrix as in section III.1.3 can be achieved but through longer dealloying times of the aged samples.

Hereafter, studied by nanoindentation NPS samples are described by Figure III.46. "Structure 1" and "structure 2" represent surfaces of nanoporous silver ribbons (glued to the glassy plate) with a φ_{pore} fraction, average ligament's width and length of ~ 45.5 ± 5 % , 50 ± 15 nm, 85 ± 40 nm and 53 ± 6 %, 90 ± 20 nm, and 140 ± 40 nm respectively.

Since nanoindentation is primarily affected by the surface of the sample, our main referential state of the substrate is its surficial characteristics. Nevertheless, a morphological difference of the two considered samples is better revealed while comparing the cross-sections of the substrates (Annex Figure A.2.)

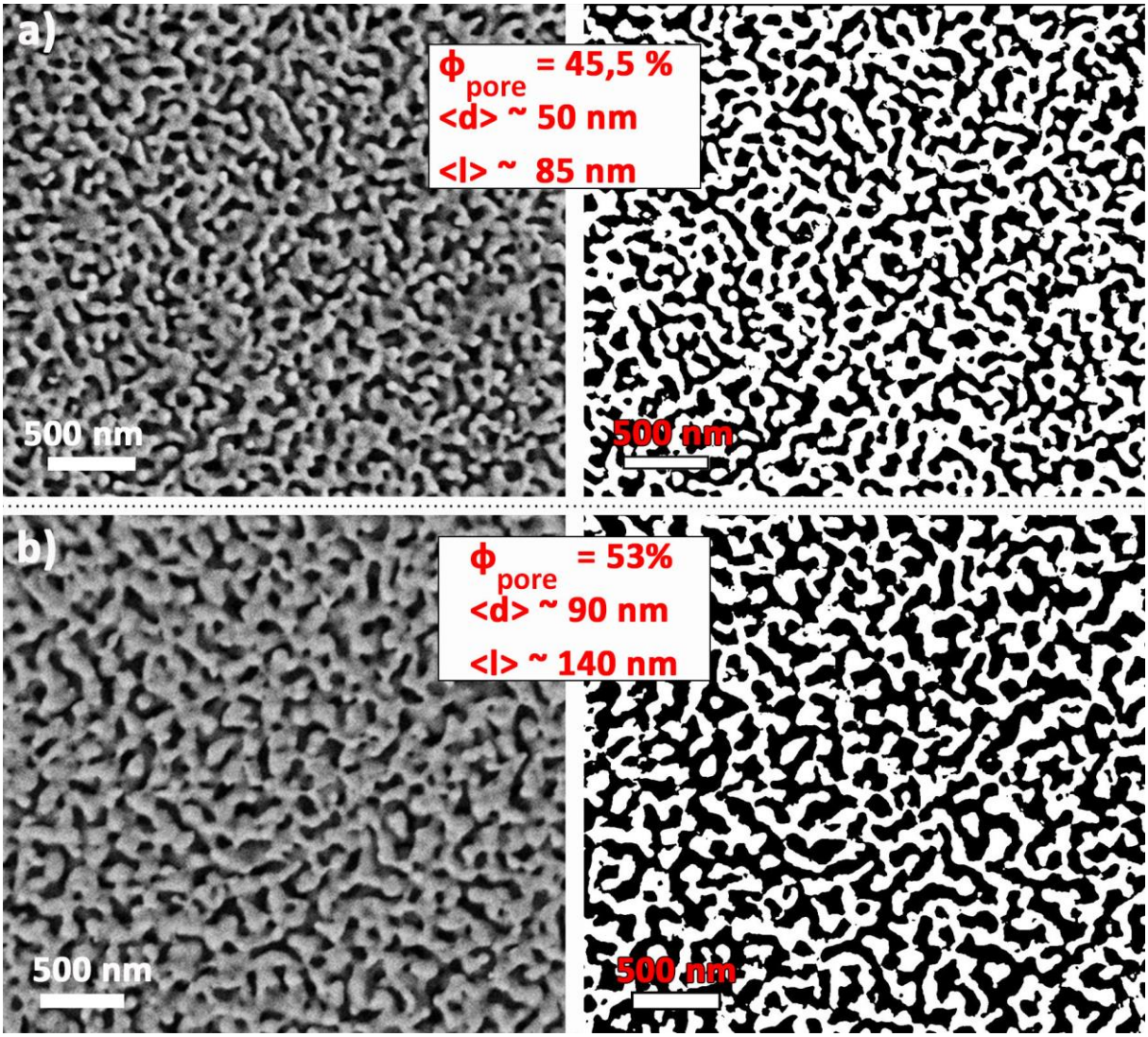

Figure III.46. SEM secondary electrons images and corresponding threshold patterns of a) "structure 1" surface sample of NPS (dealloying time of 45 minutes), and b) "structure 2" surface (dealloying time of 3 hours).

III.3.1.a. Hardness and elastic modulus of NPS

A set of quasistatic nanoindentations at a loading rate 100 µN.s^{-1} with F_{max} = 900 µN was performed on the "structure 1" and "-2" samples and resulting loading-unloading curves for one of the samples are exhibited in Figure III.47.

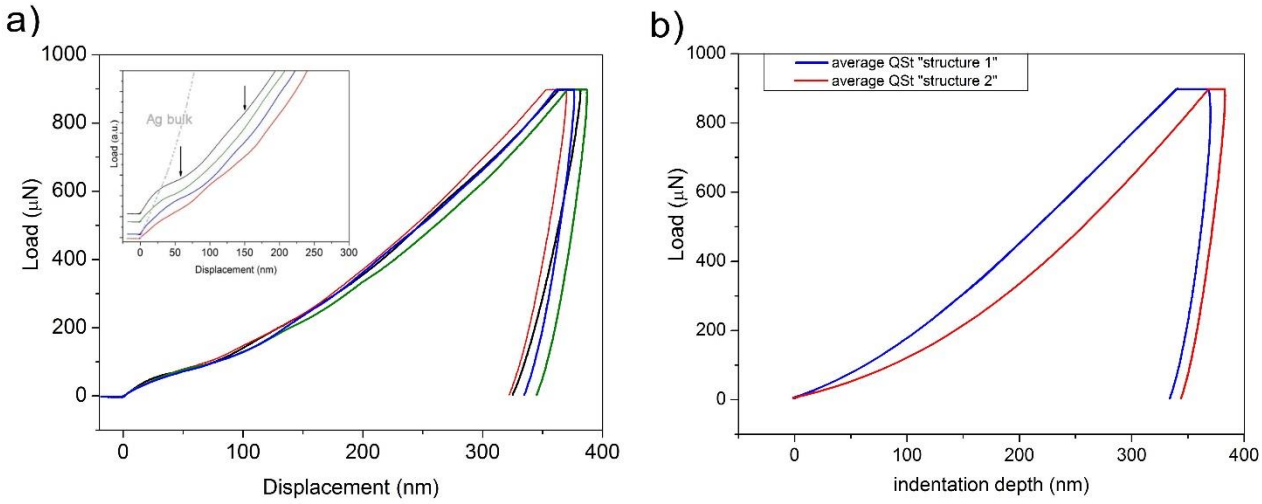

Figure III.47. a) Quasistatic loading-unloading curves (selected 4 out of 64) of the nanoporous silver surface, identified as "Structure 2". An inset represents a magnification of several loading curves at low indentation depth h to exhibit the "bumpy" region, frequently observed in these experiments on nanoporous substrates. A typical quasistatic loading curve for the bulk silver sample is given on the same graph as well (light gray) for comparison; b) Comparison of 2 averaged QSt curves for morphology 1 and morphology 2.

One may see that indentation curves exhibit remarkable slope variation at indent displacement < 200 nm, that may be due to the surface inhomogeneity effect. Generally speaking, data obtained from top 30 nm layer is usually not exploited, since it is affected by multiple errors (mainly, indenter tip roughness and surface forces and adhesion between the indenter and the sample [239]). Nevertheless, it is worth pointing on the tendency to observe humps at the beginning of the loading curves. The first hump can be observed at the indenter displacement below 50 nm, and second not as clear below ~150 nm. For clarification of these phenomena a number of quasi-static slow-rate tests have been performed to define the best experimental conditions. Finally, most revealing measurements were performed at a 1 μm/s loading rate with F_{max} = 80 μN till the 120 nm displacement depth. A corresponding load-displacement curve and scanning probe microscopy images of the indent imprint are presented in Figure III.48-49. The presence of humps is now more pronounced, although, their size-range has shifted to the smaller dimensions (sub-30 and sub-70-nm ranges). We assume that this phenomenon is a result of several factors: structural response of first and second porous layer of NPS, corresponding to the crushing down or buckling of load-bearing ligaments and surface dislocations at h < 50 nm. Although, to produce any certain statements on this account, more experimental data on various morphologies with different loading rates is needed.

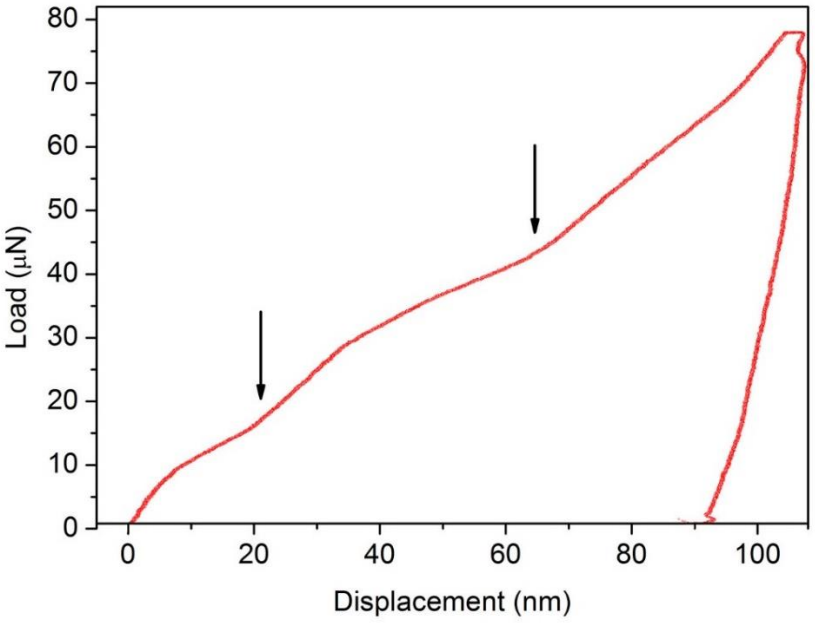

Figure III.48. The loading-displacement curve in a slow-rate quasi-static test on nanoporous "structure 2" silver sample aiming to expose the near-surface phenomena of ligament buckling.

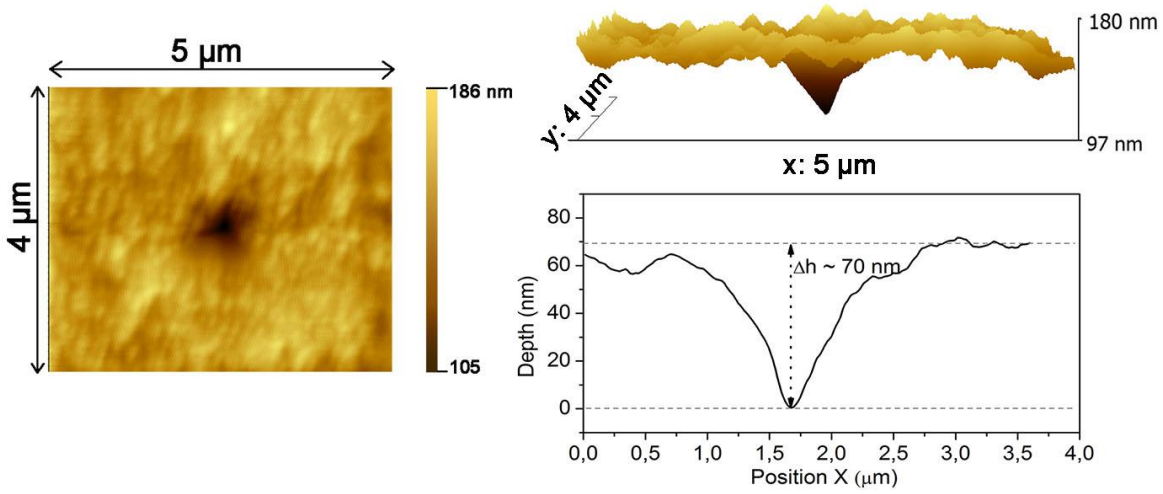

Figure III.49. SPM surface and profile images of the slow-rate quasistatic indent of a 70 nm final depth after the elastic relaxation, performed on "structure 2".

The average values for all QSt indentations result in H = 0.25 ± 0.02 GPa; E = 22.4 ± 1.4 GPa for structure 1 and H = 0.242 ± 0.015 GPa; E = 14 ± 2.2 GPa for "structure 2".

Dynamic mechanical analysis aiming to evaluate viscoelastic time-dependent properties, has been performed on the same sample up to a depth of 1.5 µm (Figure III.50) and at the critical 400 nm displacement depth (see section II.3.4.) corresponds to the $H = 0.21 \pm 0.01$ GPa, $E = 13 \pm 2$ GPa values for "structure 1" and $H = 0.28 \pm 0.01$ GPa, $E = 12.6 \pm 2.2$ GPa for "structure 2". Load-displacement curves in QSt and DMA modes for "structure 1" are not given in this section and can be found in the annexed Figure A.3. For simplicity all obtained *H* and *E* values are assembled in a Table III.2 together with bibliographic data on the pure silver material.

As expected, it is demonstrated that obtained physical values for bulk silver sample largely exceed the values for nanoporous substrates. They also exceed the literature reported values of hardness, performed by Pharr and Oliver [240]: 0.27 (at 4 µm) – 0.5 (at 100 nm) GPa, especially at low displacements, but according to Figure III.51, *H* already reaches 0.92 GPa at 600 nm depth without reaching the plateau of a constant *H* value. The hardness is generally found to decrease with increasing depth [240], and as Figure III.51 exposes, this tendency is confirmed for all the studied samples. Therefore, it is suggested that lower *H* values for bulk Ag sample should be observed at more profound indent depths. In order to estimate the H_0 of the bulk crystalline silver sample, it is possible to apply a Nix and Gao law [241], which predicts a linear dependency of the square of the material's hardness versus the inverse indentation depth (see the following section III.1.3.b), and The H_0 value is found 0,34 ± 0,08 GPa. This value is already in much better agreement with the bibliographic data. It should be noted that the yield strength and hardness of bulk metal depend strongly on the sample's history and may significantly vary. Therefore, one of the reasons of bulk silver high hardness is the impact on the microstructure, left by its preparation (VAR of commercial silver grains).

As for porous samples, it is a peculiar result that at the examined depth both nanoporous materials have very close values of hardness according to QSt and DMA tests. The dynamic mechanical analysis allows to extract hardness as a function of depth for all samples and to estimate the asymptotic value and to observe *H* variation in the near-surface regions. For each curve in Figure III.51-52, the data are averaged over five or more indents made in different regions of the sample, and the error bars represent the range of scattering (standard error). In the near-surface volume (< 200 nm depth) the hardness of a less porous sample expectedly prevailes the other, and as the indent position reaches 200 nm, hardness is almost equal, with a negligible difference. First reflection regarding these results would be to suggest that such hardness alignement can be caused by more dense packing of the ligaments of the material already at 200 nm depth.

The E_r comparison of the NPS samples according to the Table III.2 demonstrates denser "structure 1" withstands the applied stress slightly better than "structure 2". Evolution of E_r with *h* (Figure III.52) in DMA experiments, similarly to *H*, changes with depth. Two curves touch at about 200 nm depth and keep equal values till ~ 500 nm. The explanation of an extraordinary increase of E_r of the "structure 1" at $h > 500$ nm is unexpected at this point and requires additional experiments.

Table III.2. Hardness and elastic modulus of two NPS and pure silver samples, obtained in QSt and DMA modes at 400 nm displacement depth. Literature data is given for comparison

Charact. material	Structure 1	Structure 2	Ag Bulk	Ag bulk (Bibliogr.)
Hardness (DMA), GPa	0.21 ± 0.01	0.28 ± 0.01	1.18 ± 0.02	0.27 – 0.8 [240]
Hardness (QSt), GPa	0.25 ± 0.02	0.24 ± 0.015	1.25 ± 0.05	
E (DMA), GPa	12.4 ± 2	12 ± 2.2	71 ± 1	69 – 82.5 [192,242]
E (QSt), GPa	20.7 ± 3.2	12.7 ± 5.5	76.2 ± 2.5	

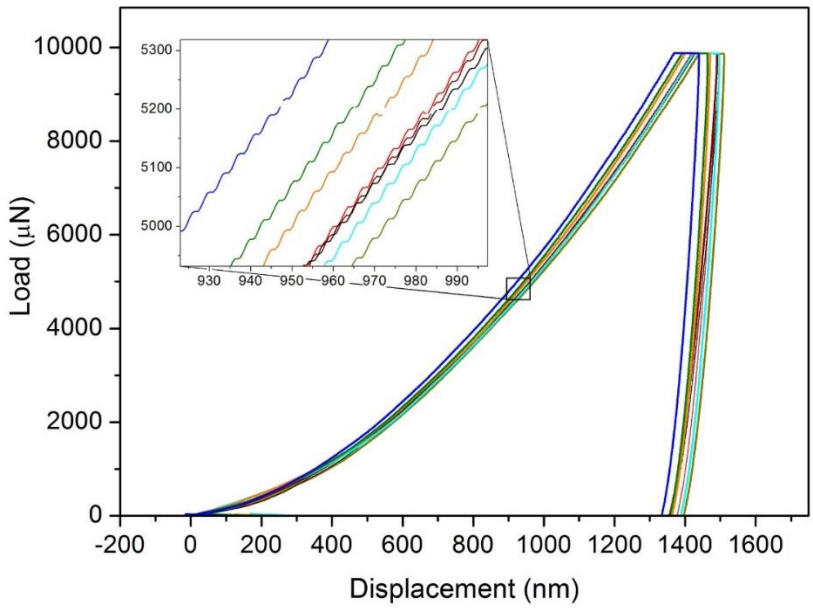

Figure III.50. DMA loading-unloading curves of the "structure 2" NPS surface with a F_{max} applied = 10 mN. The inset represents an oscillating nature of this measurement.

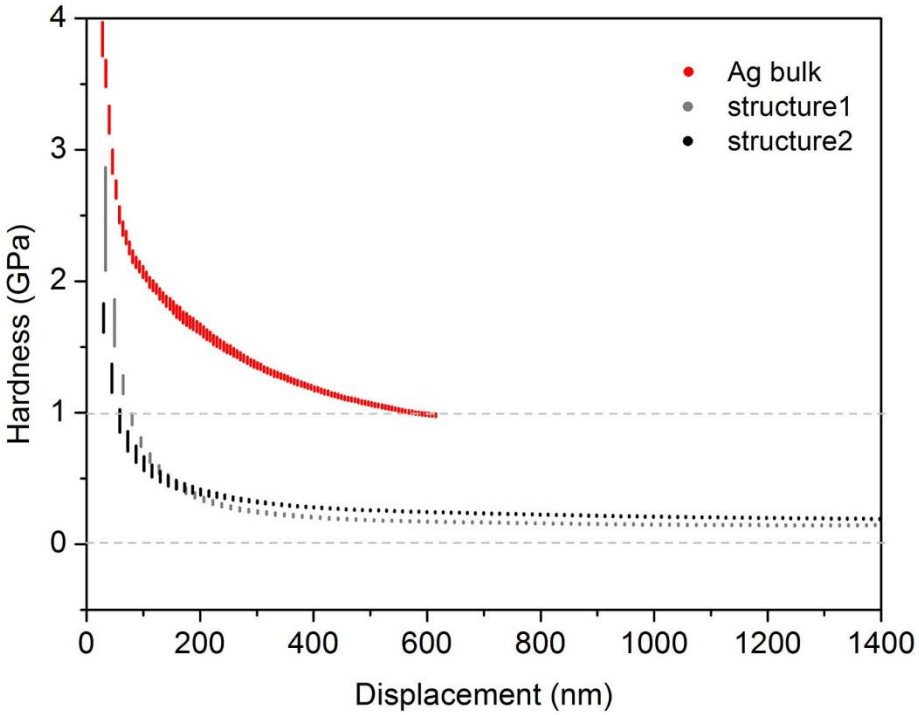

Figure III.51. Hardness as a function of depth for bulk and porous silver substrates up to 1.4 µm deep indents. Each curve is averaged over multiple experimental DMA curves.

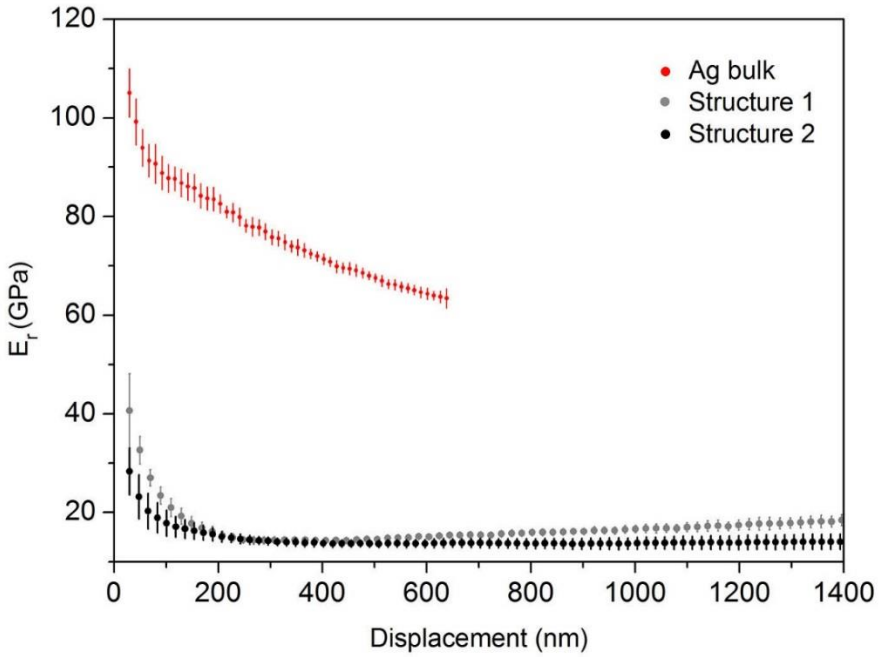

Figure III.52. Storage modulus as a function of depth for bulk and porous silver substrates up to 1.4 µm deep indents. Each curve is averaged over multiple experimental DMA curves.

III.3.1.b. Modeling of the Depth-Dependence of Hardness

As specified in the previous section, the hardness values for the porous samples have been measured at 400 nm depth from the surface, and are most likely overestimated due to the small penetration depth. Therefore, in order to approach true *H* values, we are bringing in a discussion on the possible mathematical calculation of NPS hardness, with the help of known experimental values, existing phenomenological models and new hypothesis.

A hardness-displacement dependence was analysed for all nanoindentation experiments, and an analytical modelling is proposed to explain the observed trends in nanoporous silver substrates. Suggested dependence is slightly different from crystalline and amorphous solids, examined in former works [241,243], where for crystalline materials hardness was found to follow the rule: $H/H_0 = (1 + h^*/h)^{1/2}$, and for amorphous metals: $H/H_0 = 1 + (h^*/h)^{1/2}$ where h^* is a characteristic length that depends on the indenter geometry, shear modulus *G* and the hardness in the limit in the infinite depth H_0. The results presented in this section show that for nanoporous metallic substrates structural properties regarding local ligament arrangement, local density and their variation with deformation can be approached and quantified.

The hardness of material in an indentation experiment is defined as a ratio of applied force to the area *A(h)*, produced by the penetration of indent in the material:

$$H = \frac{F}{A(h)} = \frac{F_0 + f(h)}{A(h)} = H_0 + \frac{f(h)}{A(h)} \qquad \textit{(eq. III.2)}$$

At small *h* the *f(h)/A(h)* supplementary extrinsic contribution to the hardness, originated from the strain gradient, is significant, while at $h \rightarrow \infty$ it becomes negligible and H_0 gives an estimation of the bulk material's hardness, which in this case cannot be obtained directly, but by the extrapolation of the experimental values. *A(h)* in case of Berkovich indenter geometry = $24.56 \cdot h^2$. At displacement *h*, the applied force on *dA(h)* area is $df(h) = \sigma(h)dA(h) = 2 \cdot 24.56 \cdot h\sigma(h)dh$, where σ(h) is a local back stress formed due to the confinement of the deformation.

In order to approach this supplementary contribution term, it is necessary to examine deformation of the NPM in the confined plastic zone around the indent. Considering a model of the NPM as a population of connected ligaments of diameter d_i and length l_i (see Figure III.53), deformation (shear strain) of the population under the indent shear is written as: $\gamma^* = x/l$, with $l = \sum l_i = N\langle l \rangle$, *N* and $\langle l \rangle$, are respectively the average ligament length and the number of ligaments in the population, *x* is the total displacement produced by bending in the population.

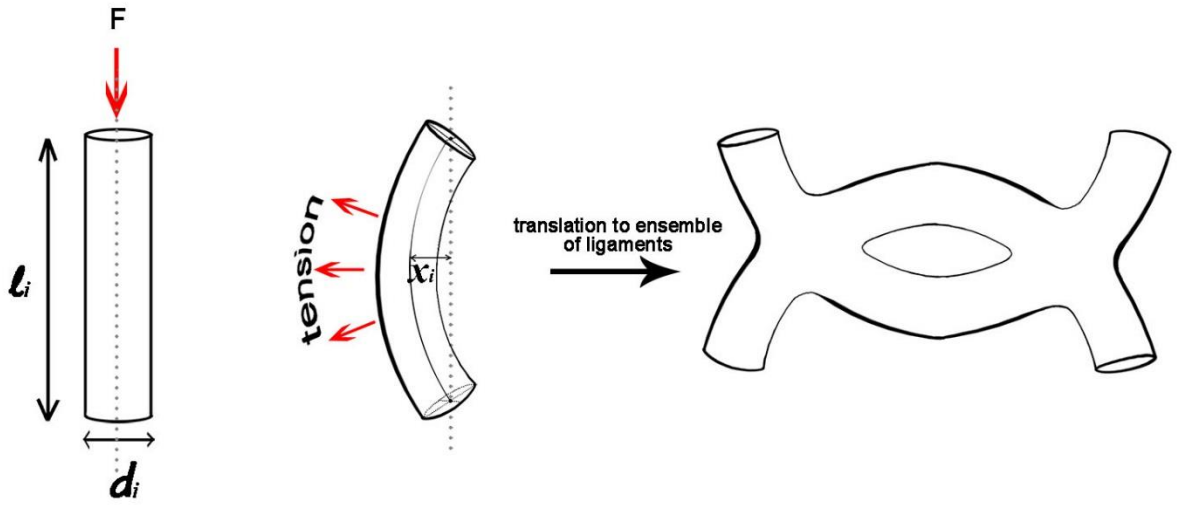

Figure III.53. A schematic representation of a load and deformation, applied to a single ligament, representing a network of connected ligaments in nanoporous structure.

At this stage, it must be emphasized, that bending is necessary as a mode of ligaments rearrangement to accommodate the applied indent shear strain. And whilst the applied indent strain is unidirectional, ligaments have two directions for rearrangement in the plane perpendicular to the indent surface at a given indent depth *h*. Hence, it comes that with increasing *h*, it is less necessary for ligament to bend for accommodating the indent shear since it has more and more available space. Intuitively, the average bending would be varying as the inverse of the surface, following $x \sim 1/h^2$ and, therefore, $\gamma^* \sim 1/h^2$.

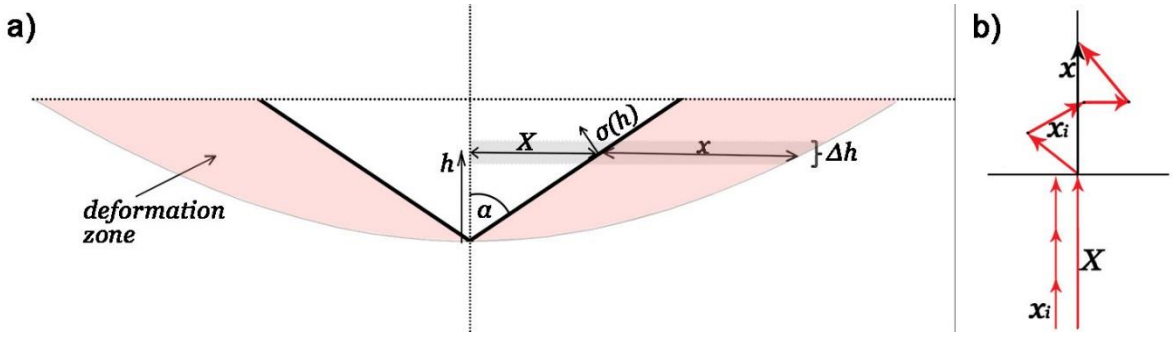

Figure III.54. a) A schematic view of the Berkovich type indent profile, with the material's densification zone, marked as red and a limited layer of volume of the thickness Δh that produces a back stress of σ(h); b) a schematic top view of rearrangement of the ligaments at the height "h", with x_i being an elementary ligament's displacement, x is a total displacement of the population of the ligaments, and X is and indent's surface displacement at "h" height.

Analytically, one can present this conjecture as following. As depicted in the Figure III.54.a, an indent's displacement *X* which produces a displacement *x* in the nanoporous matrix though ligaments

rearrangement of elementary displacements x_i. At a height h, $X=h\cdot tg\alpha$ and in the direction of displacement $X=\sum x_i$. In the porous matrix, ligaments relax this unidirectional displacement imposed, by displacement in the plane as depicted in Figure III.54.b. It follows statistically that $x = (\sum x_i)/N^{1/2} = X/ N^{1/2}$.

Combining the relations for γ* gives the shear strain in NPM:

$$\gamma^* = \frac{x}{l} = \frac{X}{N^{3/2}<l>}$$

For a given slice of a thickness e of material at height h, the number of ligaments is $N \sim \psi h^2 e$, where ψ is the volume density of ligaments. Hence:

$$\gamma^* \sim \frac{1}{h^2} \cdot \frac{tg\alpha}{\psi e^{3/2}<l>}$$

To facilitate the reading, constant parameters are reduced to $B = \frac{tg\alpha}{\psi e^{3/2}<l>}$, therefore:

$$\gamma^* \sim \frac{B}{h^2} \qquad \textit{(eq. III.3)}$$

This assumption is obviously not easy to confirm experimentally. However, it implies that the NPM is less densified as h increases, which could be confirmed at least qualitatively from direct observation on an indent's cross section. Figure III.55 presents such FIB-prepared cross-section obtained from the nanoporous silver matrix with the 45.5 % porosity. Firstly, the image supports the fact that the dominant deformation mechanism during nanoindentation in nanoporous Ag is ductile, plastic densification. Even for a sharp wedge Berkovich indenter cracks or brittle fracture of the substrate has not been observed. The densification gradient of the foam is explicit and is quantitatively presented by the gray level profiles 1-2 (with more frequent dark-light variations at deeper displacements) and indicates that the densification variation clearly depends on h.

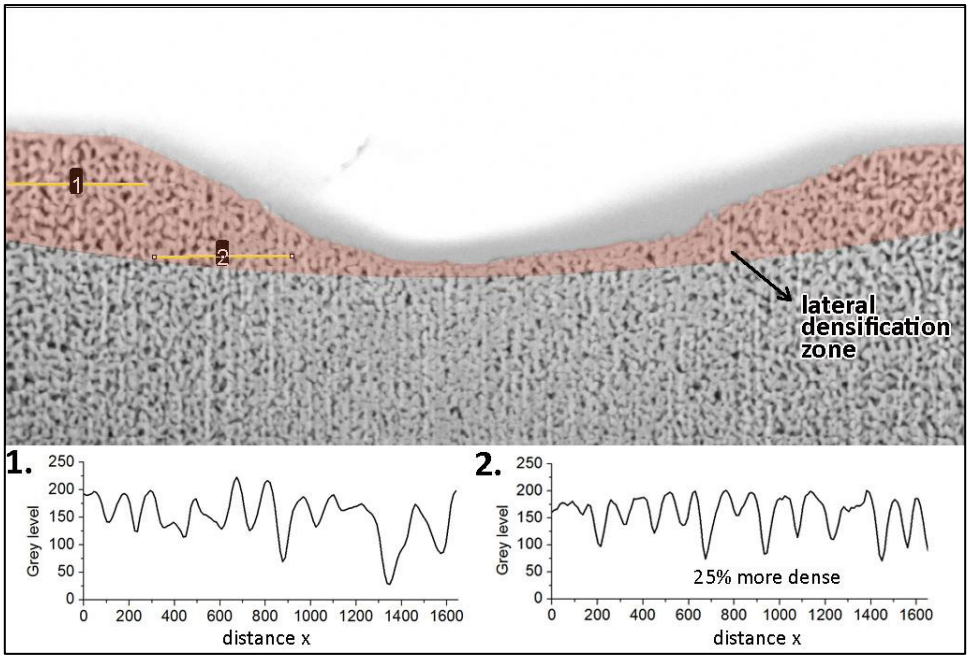

Figure III.55. SEM image displaying a FIB cross section of an indent made on the "structure 1" NPS till the 1.4 µm depth. The insets exhibit gray level variation along the lines 1 and 2 that correspond to the less and more densified regions of the deformed volume under the indent.

In Ashby work on strain gradient [244], the back stress, (what we call here the supplementary contribution term), is a result of the strain gradient which reduces in our model, form relation III.3 to an average representative ligament of length <*l*> and diameter <*d*> and is expressed as: $\gamma^*/<d>$. The back stress is:

$$\sigma(h) \sim C_1\sqrt{\frac{\gamma^*}{<d>}} \qquad \textit{(eq. III.4)}$$

C_1 is a constant related to elastic properties of ligaments. Substituting γ^* by *eq. III.3*, we obtain

$$\sigma(h) \sim \frac{C_1}{h} \cdot \sqrt{\frac{B}{<d>}} \qquad \textit{(eq. III.5)}$$

As it was mentioned above, $df(h) = \sigma(h)dA(h)=49.12 \cdot h\sigma(h)dh$

After substituting $\sigma(h)$ by *eq.III.5* and integrating by h we obtain:

$$H = H_0 + \frac{1}{h} \times \left[C\sqrt{\frac{B}{<d>}} \right] \qquad \textit{(eq. III.6)}$$

Where $C = C_1 = 49.12$.

Expression *III.6* is a comprehensive analytical description of a hardness-displacement behaviour in nanoporous materials. It demonstrates the inverse dependence of hardness on indenter depth, and its direct observation becomes possible, when one plots the *H(1/h)* dependence and observes an almost

perfectly straight fit for the experimental curves for two systems with different porosities as in Figure III.56. It is important to highlight that:

a) The slope $C\sqrt{\frac{tg\alpha}{\psi e^{3/2}<l><d>}}$ of this dependence decreases with increasing average ligament's geometry <l> or <d>. The volume density of ligaments ψ is inverse to porosity level, hence the slope should grow with the growth of porosity. In case of our NPS system, the slope is mainly dictated by the <d> and <l> parameters, rather than porous fraction (see the table in Figure III.56), which is less important since it also has very close values for both samples.

b) Parameter $B = \frac{tg\alpha}{\psi e^{3/2}<l>}$ indicates, that the model is valid as long as ψ does not vary drastically, for instance, at strong compression the material approaches a bulk state, which is beyond the limitations of present model. Large changes in porosity would produce a deviation from the linear *H (1/h)* dependence as observed in the Figure III.56 when $\frac{1}{h} \rightarrow 0$.

Table with the parameters of the analytical model and with the defined intrinsic hardness of porous materials H_0 (Figure III.56), demonstrates that on the range of $h \in [35; 1400]$ nm the slope of less porous structure is higher due to finer ligaments' characteristics, and, consequently, the intrinsic hardness H_0, obtained by extrapolation, is smaller (0.24 GPa) than of more porous one (0.4 GPa).

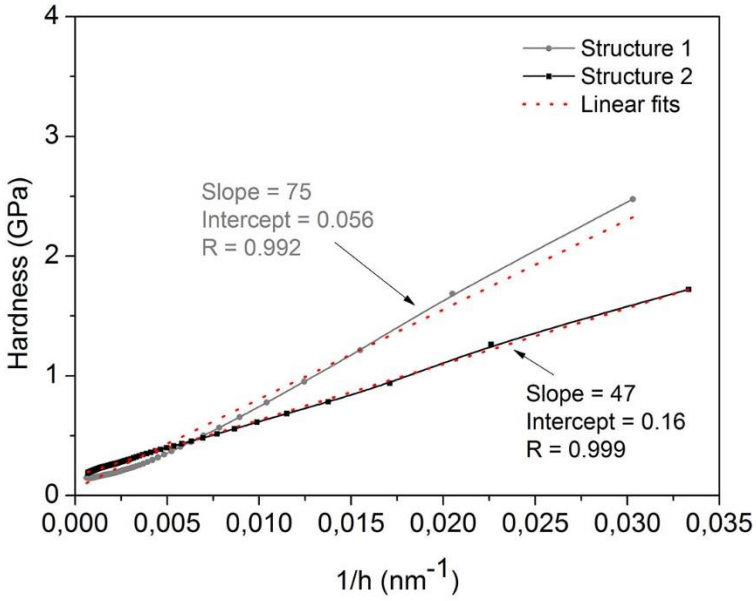

parameters / sample	ϕ_{pore}, %	d, nm	l, nm	H_0,GPa
Structure 1	45.5	50	85	0,24
Structure 2	53	90	140	0,4

Figure III.56. A dependence of NPS averaged hardness H from DMA experiments on the inverse indenter displacement h for the two substrates with different level of the porous fraction. Dashed red line is a straight fit for each of the curves confirming the consistency of eq. III.6. The table represents characteristic information for each sample and determined by extrapolation corresponding H_0 values.

III.3.2. Conclusions

The experiments described in this chapter allowed to evaluate the hardness and Young's modulus of the porous and bulk substrates with indentation depth. It was observed that all characteristics of NPS, measured throughout the nanoindentation experiments show much lower values than the bulk silver sample prepared for comparison, which is expected for metallic foam materials. Although, it is worth mentioning, that our referential bulk Ag sample possesses higher mechanical characteristics even compared to the values, reported in the literature that could be caused by the sample preparation history. Therefore, when compared directly to bibliography data on bulk Ag, nanoporous samples, studied in this work manifest very close hardness values of ~ 0.25 GPa at the h ~ 400 nm.

Hardness and Young's modulus evolution for both morphologies is defined via DMA, where one may observe the values' decrease with the increasing h and is in agreement with the general concept of geometrically necessary dislocations. Although, in present study, the characteristic relation of the depth dependence of hardness differs from well-known equation for crystalline solids and is reported as $H = H_0 + \frac{1}{h} \times \left[C \sqrt{\frac{B}{d}} \right]$, where parameter B contains the information on the materials porosity, morphology's geometry and physical characteristics of solid material, constituting the network of ligaments. The phenomenological model, given here above, is an elementary approach for the description of behaviour of porous metallic systems and has its limitations of application, related to the amount of the fraction of the hollow material. For higher accuracy, it may also need further elaboration and integration of morphological parameters of the material into the qualitative description.

III.4.Functional properties of NPM: Catalysis & SERS

A primary goal of present work was not only the elaboration and characterization of other than commonly used nanoporous Au and Pt materials but a demonstration of their good integrity, effectiveness, and stability of functioning in conditions approached to reality. As it is detailed in the section II.3.5, a half-cell electrochemical characterization method has been used for the testing of the selected NPS and NPCo as catalytically active anodic substrates in further applications in a direct ammonia-borane fuel cell, working on ammonia-borane fuel with a high H_2 capacity. NPCu ribbon substrates were recognized too brittle to perform the evaluation of its functional properties in present experimental conditions. Extending the range of abundant less pricey materials is crucial for the future of alternative energy field, and we believe that in this work a small step forward in this direction has been made.

*To expose the several multi-functionalities of synthesized porous systems, additional experiments demonstrating their advantageous optical properties in surface-enhanced Raman spectroscopy with target Rhodamine 6G molecules were conducted, and the results are reported hereafte*r.

III.4.1. Nanoporous silver as an electrocatalyst

Precious noble metal catalysts are proved to be active for AB dehydrocoupling at room temperature with catalyst loadings as low as 0.5 mol% [245]. In most of the cases these catalysts are used in the form of nanoparticles, supported on highly porous carbon black, which suffers from difficult manipulation and bad electric conductivity. In addition, an important drawback of such composites is their poor stability in strong alkaline media caused by severe carbon corrosion followed by morphological changes of the material and loss of active Pt particles. Working in alkaline media is required to suppress the unwanted reaction of hydrolysis of ammonia-borane: $NH_3BH_3 + 2H_2O = NH_4^+ + BO_2^- + 3H_2$, therefore, finding the appropriate AB catalysts, capable of withstanding the aggressive chemical conditions and demonstrate a good catalytic activity compared to existing commercial solutions would be of a great importance. Silver in the form of nanoparticles, agglomerates, clusters and porous substances has already been widely used as catalysts in fuel cells, and electrochemical actuators [100,220,246,247], and recently also for the electrooxidation of borohydride compounds [248–252]. In that regards, nanoporous silver materials were evaluated as a potential anode catalyst for the DABFC. In the present section, we are going to demonstrate the performance an alternative NPS catalyst for the electrochemical AB oxidation and their valorization in DABFC. In doing so, attention is paid to the catalyst durability and stability of performance.

A nanoporous silver sample obtained after 45 minutes dealloying of the melt-spun crystalline precursor, which characteristics are carefully described in the sections III.1.3 and III.2.4, is used as a principle material for electrochemical characterization tests. Such dealloying time has been selected principally due to the good mechanical resistivity of the sample in the conditions of rapidly rotating disk electrode. In addition, the morphology of the porous layers of this sample exhibit high S_{spec} without considerable traces of Cu and Si impurities, and the matrix is not yet exhibiting an agglomeration of Ag grains, caused by acid aging for longer dealloying times. The conditions of electrochemical experiments including the cell geometry, type of used electrodes and solutions are specified in the section II.3.5.

The electrocatalytic performance of porous silver for the direct electrooxidation of AB fuel in an alkaline medium is presented on Figure III.57. The cyclic voltamperogram of the NPS substrate in the supporting electrolyte (0.1M NaOH) reveals the nature of the silver surface (black curve – is a voltamperogram being recorded at the zero revolution rate of the rotating disk electrode). The large anodic peak centered at ca. E = 0.41 V results from the formation of surface silver oxides.

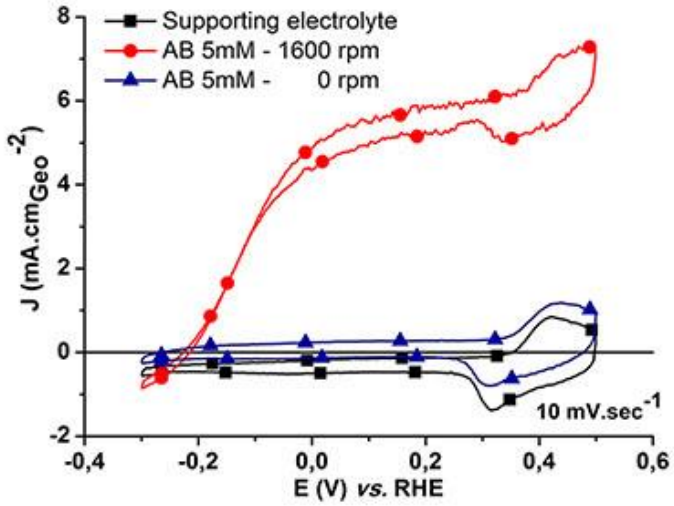

Figure III.57. Electrocatalytic performances of nanoporous silver for direct ammonia borane electrooxidation in 0.1 M NaOH (black) and 0.1 M NaOH +5 mM AB at w = 0 (blue), and at w = 1600 rpm (red). All experiments were performed at 25 °C.

The formation of copper oxides from residual copper coming from the internal bulk layer in the middle of the sample (Figure III.58.b) may also occur in this anodic peak. During the subsequent negative scan, the cathodic reduction of silver oxide proceeds, producing a peak centered at ca. 0.36 V. It is also likely that copper oxides are reduced in this potential domain, as attested by the electrochemical equilibrium between Cu and Cu_2O, expected to proceed around E = 0.471 vs. RHE thermodynamically [120]. Further discussion regarding copper contribution will be given in the following paragraphs.

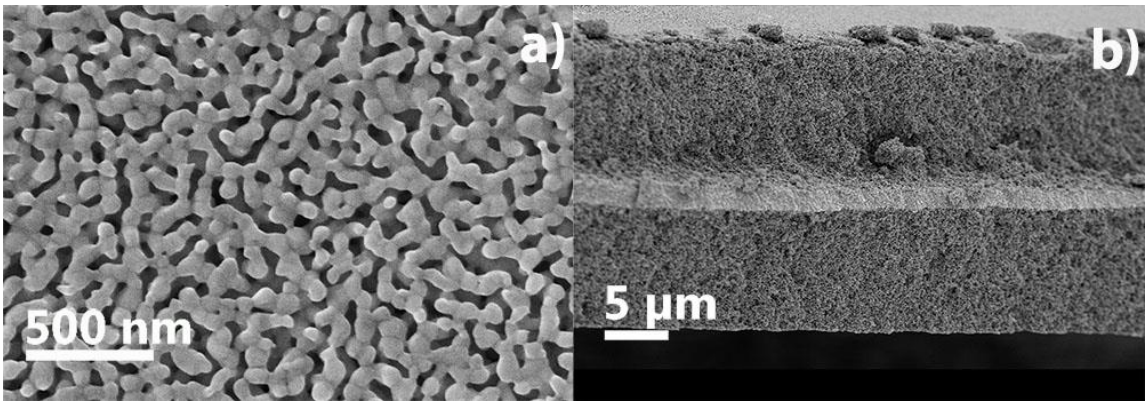

Figure III.58. a) Surface view of the porous Ag microstructure b) Cross section view of the dealloyed ribbon with a bulk non-etched carcass layer in the middle.

The addition of 5 mM of ammonia-borane into the solution modifies the shape of the cyclic voltamperogram, and the obtained shape is strongly depending on the revolution rate of the rotating disk electrode. An oxidation current is observed on the whole potential domain investigated, its magnitude being much larger under diffusion convection regime (ω = 1600 rpm, the upper red curve

in Figure III.57, round symbols) than on a static electrode (ω = 0 rpm, lower blue curve, triangle symbols). The reaction begins at a very low potential value, much lower than the hydrogen oxidation potential in case of Pt/C support. Indeed, the onset for the electrooxidation of ammonia-borane is about $E = -0.25$ V vs. RHE (250 mV below the oxidation of hydrogen in a hydrogen-fed fuel cell [253]), which is of utmost interest for energy production in direct alkaline fuel cells. The kinetic is relatively fast according to the steep slope of the wave in the region up to 0.3 V vs. RHE. Then, the AB oxidation current density reaches a stable maximum value of 6.44 $mA.cm^{-2}$ at about 0.3 V vs. RHE. These values are better than the ones observed for nanoporous gold in 1 M NaOH solution containing higher concentration in ammonia-borane (20 mM), where the V_{onset} of AB electrooxidation reached −0.2 V vs. RHE [254], i.e. was shifted positively by 50 mV compared to the best results with the present nanoporous Ag.

Comparing the voltamperograms after addition of 5 mM of AB (ω = 0 rpm and ω = 1600 rpm), one clearly sees that mass-transport controls the reaction. Figure III.59.a further presents the effect of the rotation rate of the electrode on the electrocatalytic performance measured at $E = 0$ V vs. RHE (i.e. at an electrode potential where a classical H_2-oxidation electrode would not release any quantitative current, which demonstrates the interest of AB oxidation at NPS electrodes); the faster the electrode is rotated, the higher the current density value, in agreement with the Levich theory. This dependency on the mass-transport means that the NPS electrode is indeed a good AB oxidation catalyst (it is not limited by charge-transfer kinetics, even at a potential as low as 0 V vs. RHE and at 25 °C); on the contrary, it implies that the fluidics of the DABFC systems should be considered with care (but this is beyond the focus of the present study). Besides the normal "Levich behavior", the design of our rotating electrode can account to some extent for the mass-transport effect observed. The NPS is inserted at a position about 2 mm deep in a cylindrical shape gap (see Figure II.16), overall limiting the access of "fresh fuel" to the NPS surface. In addition, stagnant AB electrolytes are prone to severe heterogeneous hydrolysis at the NPS electrode; indeed, we observed hydrogen gas bubbles being stacked in the gap. Besides consuming the AB fuel and only being prone to be oxidized above $E = 0$ V vs. RHE, the presence of such H_2 bubbles may interrupt the contact between the NPS catalyst and the AB solution, resulting in lower oxidation current. In any of these cases, the performance of the NPS electrode is improved by increasing the revolution rate of the rotating disk electrode: doing so firstly enables the access of "fresh AB" fuel and secondly favors the removal of hydrogen gas bubbles. It has to be noted that, whatever the steps of revolution rates, the current density rapidly follows the changes of the rotation speed of the working electrode, denoting for the absence of poisoning/deactivation of the NPS electrode in the course of the AB oxidation. Besides, the two scan sequences measured at ω=1600 rpm demonstrate that the NPS proceeds without any quantitative loss in activity versus time (within the time frame of the present experiments).

The stability of the oxidation reaction current was further analyzed; samples were held at the potential $E = 0$ V vs. RHE (Figure III.59.b) for 10 min. Here NPS electrode presents a stable short-term activity for AB oxidation, which is observable by the very small loss of activity during the period of tests, represented by the slight decrease in the oxidation current density.

In addition, the structural stability of the nanoporous silver and its AB oxidation activity have been investigated for long-term operation (the accelerated stress test, AST, consisted of up to 15.000 voltamperometric cycles between −0.3 and 0.5 V vs. RHE at 100 $mV.s^{-1}$) in the same electrolyte (0.1 M NaOH + 5 mM AB, at 25 °C). Cyclic voltamperograms and representative SEM images are given

in Figure III.60 and III.61, respectively. In Figure III.60, one can clearly see that the behavior of nanoporous silver remains similar even after 15.000 cycles; only minor diminution of the anodic current density values can be observed by cycling in the electrolyte: it is a consequence of the AB rare faction in the electrolyte due to its progressive consumption at the working electrode. In spite of this globally decreasing anodic current contribution from AB oxidation, there are no major changes in the equilibrium between the silver/silver oxides (and possibly copper/copper oxides) peaks and for the capacitive current values (in particular, the silver (and copper) oxides reduction peak at ca 0.3 V vs. RHE in the negative sweep, which is not biased by the AB oxidation current is literally unchanged from the 1st to 15,000th cycle of the AST); this indicates that neither metal dissolution, nor active surface area loss, nor structural changes of the silver nanoporous do happen during the cycling. As one can observe in Figure III.61, there are neither significant changes in the morphology of the ligaments or pores of the NPS material after this accelerated stress test. The conjunction of these two results suggests the chemical and electrochemical stabilities of the catalyst in long-term operation. Nevertheless, occasional agglomerates have appeared on the electrode surface. EDS analyses demonstrate that they are rich in copper; such copper-rich islands were not observed for the fresh electrode. Copper has therefore migrated from the bulk to the surface of the sample in the course of the aging test. This, in fact, confirms that the oxidation/reduction peaks observed around 0.4 V vs. RHE in Figure III.58 are related both to silver (majorly) and copper (minorly). Copper necessarily comes from the bulk layer in the middle of the sample (Figure III.58.b) where the alloying elements (Cu and Si) remained unaltered after the leaching procedure.

However, such changes are overall very minor, and the porosity of the NPS sample remains essentially unaltered even after 15,000 cycles; this stability is already larger than what has been observed for noble electrocatalysts of platinum nanoparticles supported on high surface area carbon as previously reported in [193,194].

In addition, such dissolution (from the bulk of the NPS sample) and precipitation (at its surface) of Cu-rich agglomerates is another indication that the whole NPS sample is accessible to reactants, owing to its porous architecture. If such diffusion of Cu atoms/ions from the bulk to the surface of the NPS proceeds, it is likely that AB and its oxidation products can do as well, in agreement with the good electrochemical performances monitored above. To be more specific, the porous architecture of the NPS, formed by the conjunction of very small channels in diameter with large surface area in the middle, channels which enlarge in diameter towards the surface, facilitate the intrusion of the AB-containing liquid solution and the release of the hydrogen bubbles possibly formed from heterogeneous hydrolysis and other AB oxidation products. These textural properties coupled with the intrinsic ability of Ag to promote AB oxidation reaction enable to understand the steep wave monitored on Figure III.57, indicating large overall AB oxidation activity.

From these results, NPS seems both very active and durable for the direct electrooxidation of ammonia-borane in alkaline medium. In addition, the residuals of the secondary η-phase in the final porous structure do not perturbed the oxidation process of AB, which means that material does not require any remarkable purity level to be exploited in real conditions.

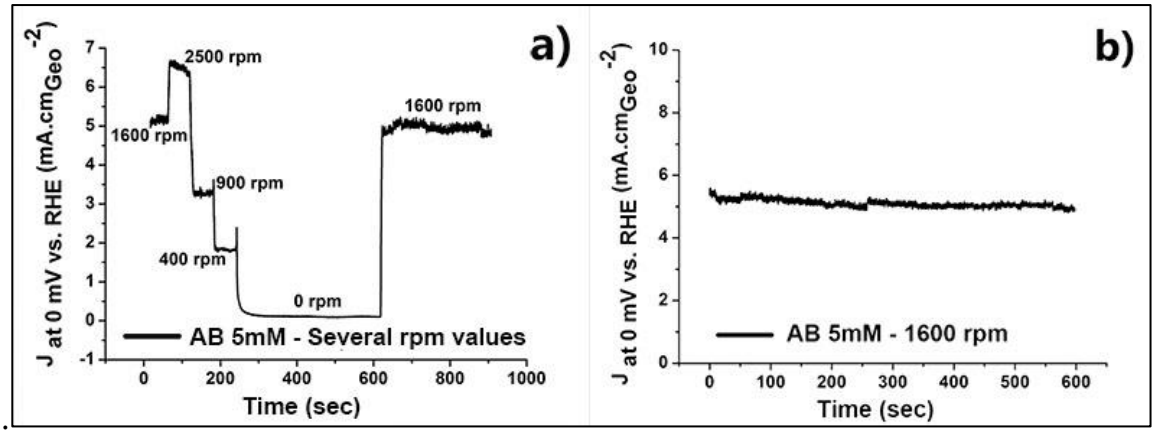

Figure III.59. a) Effect of the electrode's rotation speed and b) Signal stability, for direct ammonia -borane electrooxidation. All performed in 0.1MNaOH+5mMAB, at 0 V vs. RHE and 25 °C.

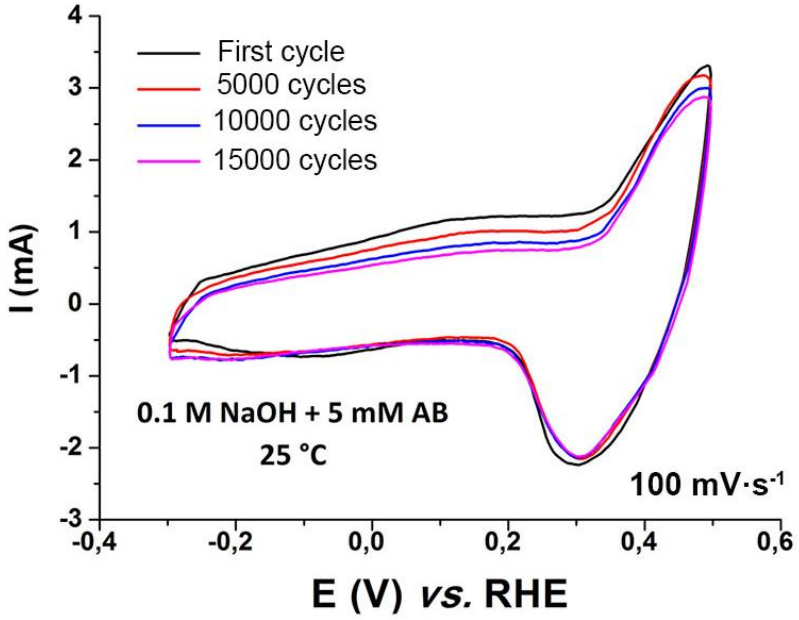

Figure III.60. Cyclic voltammetry of NPS material after 0, 5000, 10,000 and 15,000 cycles in 0.1 M NaOH + 5 mM AB at 100 mV/s and 25 °C.

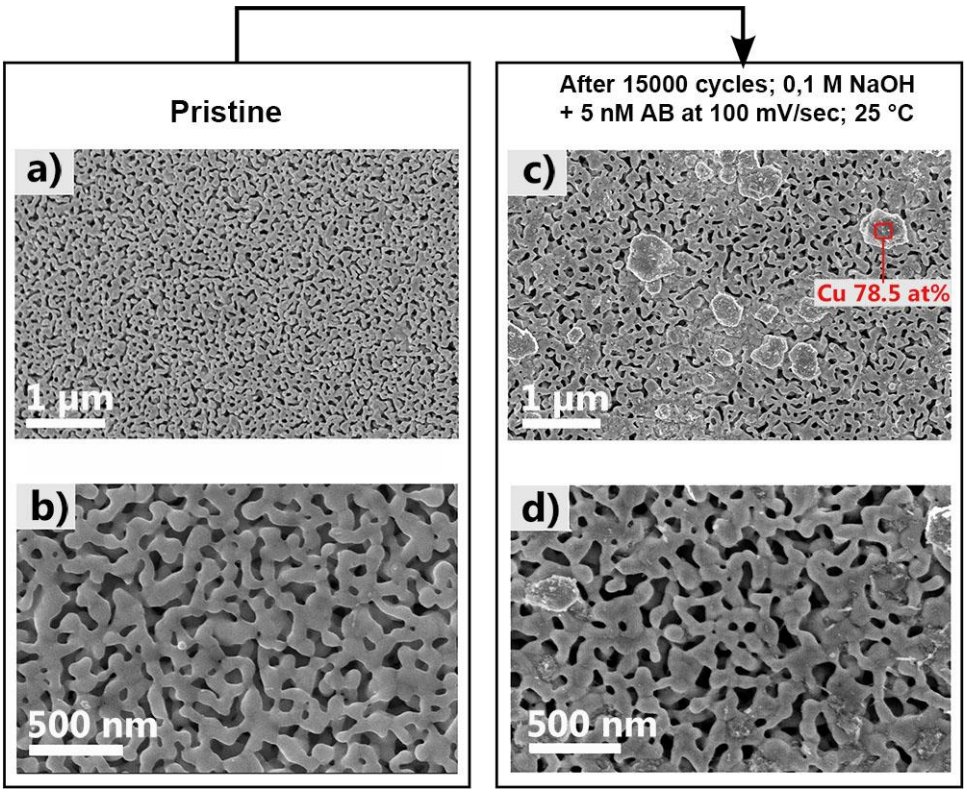

Figure III.61. SEM images of porous silver before (a.–b.) and after (c.–d.) 15,000 Cyclic voltammetry performed between−0.3 and 0.5 V vs. RHE at 100 mV/s in 0.1 M NaOH + 5 mM AB, at 25 °C.

III.4.2. Perspectives of nanoporous cobalt as an electrocatalyst

Similar experiments as in the previous section have been performed on the synthesized nanoporous cobalt based substrate, obtained according to the section III.1.4 by dealloying in the diluted nitric acid for at least 1 hour to reach a maximum dissolution of copper and silicon atoms while preserving the integrity of the melt-spun ribbons. According to the previously carried out characterization, this porous material is a bi-phase alloy, principally constituted of a σ-cobalt and Cu_9Si phases. The latest one is considered here as a "contaminant", since Si atoms are likely to react with the alkaline electrolyte and cause parasitic electrochemical signals on the cyclovoltamperometric diagrams and, moreover, contribute to the fouling of the porous matrix of the catalyst. The overall procedure of the electrochemical test corresponds the one, established in the section II.3.5.

The electrocatalytic performance of the NPCo for the direct electrooxidation of AB fuel is presented on Figure III.62.a. The cyclic voltamperogram of the material in the 0.1M solution of NaOH demonstrates almost complete neutrality of the substrate in the alkaline media (black curve – is a voltamperogram unaffected by the revolution rate of the rotating disk electrode). As in the case of NPS, the addition of 5 mM of ammonia-borane into the supporting electrolyte promotes the appearance of current thanks to the AB oxidation on the surface of the active NPCo support and due to the partial hydrolyses of AB. Similarly, as demonstrated in the Figure III.62.b, the CV scan shape directly depends on the revolution rate of the RDE, although, in present experiment the stability of the oxidation current is poorer than in case of nanoporous Ag supports (see the signal variations at ω = 1600 rpm

revolution rate during 6 minutes, Figure III.62.b). An oxidation current is observed in the whole domain of applied potentials from -0.4 V to 0.5 V *vs.* RHE, with the larger magnitude under diffusion convection regime (upper red curve in Figure III.62.a, square symbols) than in static conditions (lower green curve, triangle symbols). The onset potential V_{onset} of the target reaction is ~ -0.3 V at 1600 rpm. In the low potential region the kinetic of the reaction is relatively fast, untill the moment when the oxidation current stabilizes at ~ to 0.2 V reaching the value of 4 mA.cm^{-2}.

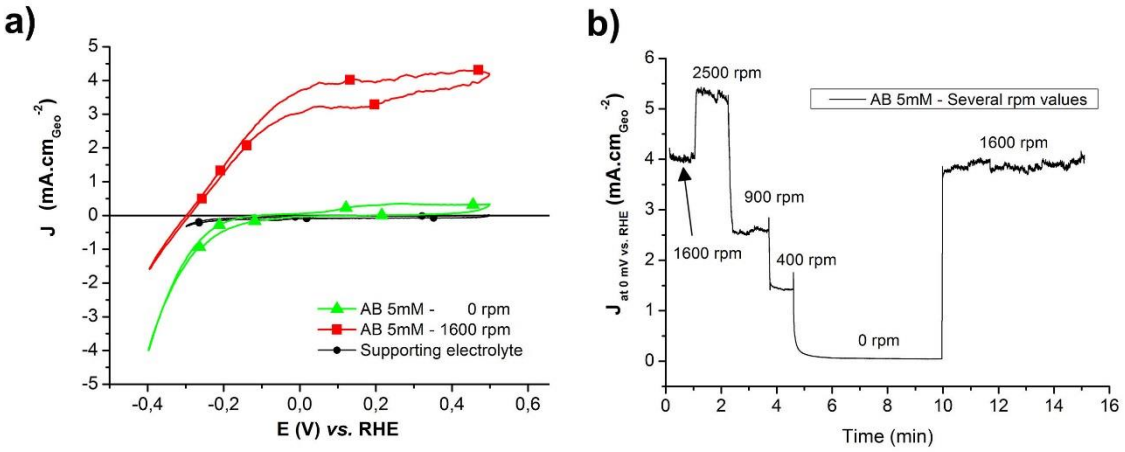

Figure III.62. a) Electrocatalytic performances of nanoporous cobalt for direct ammonia borane electrooxidation in 0.1 M NaOH (black) and 0.1 M NaOH +5 mM AB at w = 0 (green), and at w = 1600 rpm (red). b) Effect of the electrode's rotation speed performed in 0.1 M NaOH +5 mM AB, at 0 V vs. RHE. All experiments were performed at 25 °C

In the both electrochemical test on nanoporous Ag and Co, current values in the Figure III.57 and III.62.a are normalized by the investigated geometric surface area of the substrates, which is of the order of 0.5 cm^2. The following comparison Table III.3 reveals even higher catalytic capacity per specific surface area of the less noble NPCo material, when compared to the previously tested silver anodic material. Keeping in mind that the V_{onset} for both materials is very close (-0.3 V), such profit in the specific current in the Co-based substrate represents a great advantage of its intrinsic catalytic properties. In addition, the cost of raw materials for the Co-based substrate is several times more profitable, than that of Ag.

*Table III.3. Comparison of electrochemical properties of nanoporous silver and cobalt-based substrates. * According to BET.*

material / property	NPS	NPCo
S^*_{spec} (m²/g)	5,02	1,96
Max. current of AB oxidation (mA·cm^{-2})	5,8	4
$\frac{\mathbf{Current}}{\mathbf{S_{spec}}}$	**1,15**	**2,04**

In its turn, the accelerated stress test of the cobalt-based catalyst, performed via in the non-revolution mode of the RDE, showed poor stability of the material. As one may see from Figure III.63, the material is "activated" during first 100 cycles, and, later, on the shape of the voltamperometric curve goes through noticeable changes with the sharp decrease of the AB oxidation current that approach a stable value after about 5.000 cycles. Consequent observation of the substrate via SEM (Figure III.64) demonstrated homogeneously distributed products of materials transformation covering the surface of the porous scaffold. EDS point analysis suggests that these precipitants are oxide-rich formations, principally constituted of cobalt oxides, although, proper examination of the reaction products by other means would be more appropriate. In particular, the ongoing experiments at the high energy diffraction line on the European Synchrotron Research Facility will shed some light on the substrate's modifications during the AST, and the results will be published elsewhere.

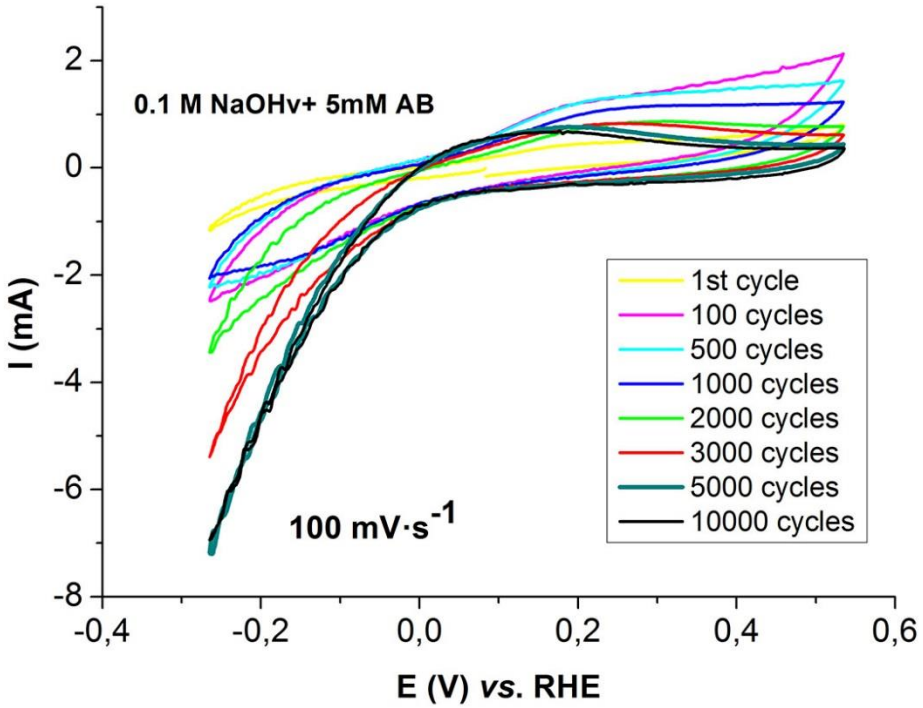

Figure III.63. Cyclic voltammetry of NPCo material at up to 10,000 cycles in 0.1 M NaOH + 5 mM AB at 100 mV.s^{-1} and 25 °C.

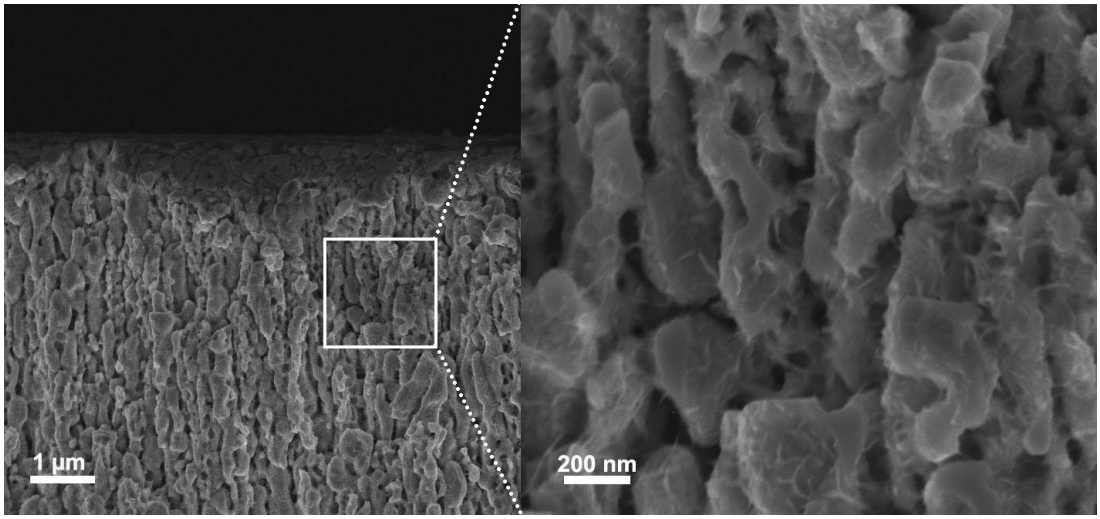

Figure III.64. SEM image of the cross section of the nanoporous cobalt specimen after its static degradation in 0.1 M NaOH + 5 mM AB solution after 10,000 cycles.

From these results, NPCo shows certain advantages as a material for anodic catalytic supports, namely its doubtless catalytic activity for AB conversion. Although, when it comes to durability properties, it obviously lacks chemical stability and suffers degradation in alkaline media (principally due to the reactivity of Si component of the porous support). Unlike the case of NPS, where no remarkable chemical purity of material was required to obtain a stable functioning catalyst, Co-based support obviously needs further compositional improvements to be exploited in real conditions.

III.4.3. Nanoporous silver as a SERS-active substrate

Valorization of synthesized nanoporous metallic systems as optically active substrates was not an eventual objective of present work; most of the studied materials were created in according to their impact on the electrochemical energy conversion field as catalysts. Nevertheless, in the light of the increasing trend of surface enhanced Raman technique for biosensing, spectroelectrochemistry and other related domains, it became a matter of interest to explore the potential of present nanomaterials as SERS supports. Gold, silver and copper have already been known as classic SERS substrates. Au and Ag are most often used because, unlike Cu, they are air stable materials, from here comes the motivation to primarily examine SERS properties of our silver-based nanoporous materials.

The techniques, described in the section II.3.6, suggests recording of the signal's intensity, obtained as a result of illumination of the examined substrate with adsorbed test molecules by the laser light (λ = 514 nm). Depending on the concentration of the probe molecules the intensity of the signal will vary. Finding the appropriate substrate capable of reflecting the presence of the probe molecules contained in low concentration on the examined surface is a required condition for a successful SERS material.

Two types of nanoporous silver morphologies were used throughout present experiments (Figure III.65). First morphology corresponds to the as-spun crystalline silver ribbons, dealloyed for 45

minutes in mixed acid solution as in III.1.3, and the second corresponds to the completely dealloyed material (90 minutes), exposing the agglomerated silver clusters as a result of aging in the etching bath.

Preliminary SERS tests demonstrated that in our case the exposure time of NPS to the solution, containing R6G probe molecules, had little impact on the final intensity of Raman signal, in other words, the immersion of NPS substrates in the solution for 10 seconds was similar to the 48 hours immersion, therefore, 10 seconds exposure times were chosen as a reference timescale for further measurements.

The results of preliminary tests are presented in Figure III.66. The signal and stability of R6G detection for the completely dealloyed substrate were of higher quality than for the case of 45 minutes dealloyed silver sample. With this in mind, further experiments have been conducted on this more "sensitive" substrate with the goal to approach the R6G detection limit.

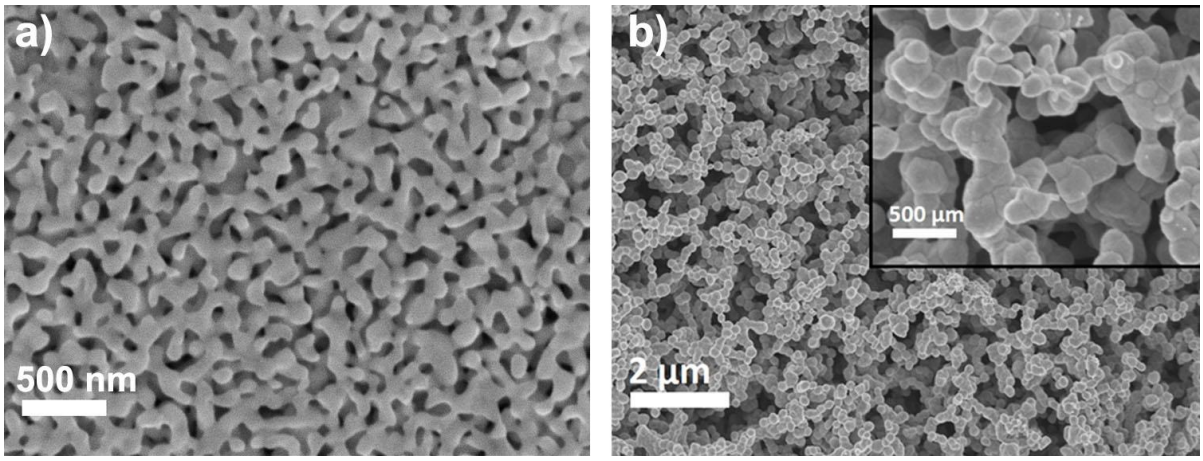

Figure III.65. The two morphologies of nanoporous Ag, examined in the frames of SERS experiments; a) an NPS after 45 minutes and b) 90 minutes of dealloying.

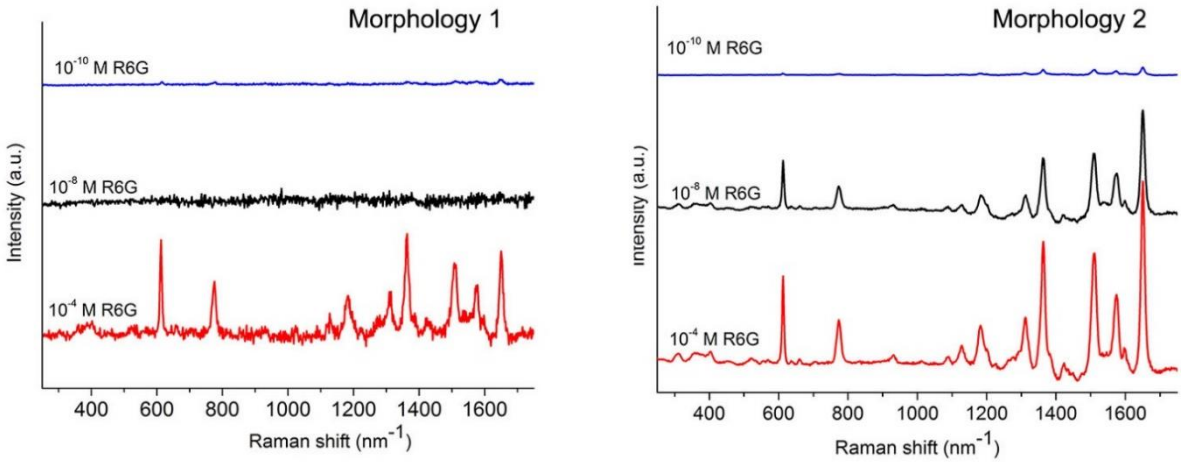

Figure III.66. R6G Raman spectrum evolution with the molecule's concentration in water. Left and right images are associated with the SERS properties of NPS morphology 1 and morphology 2 respectively.

As one may observe in Figure III.66, SERS capability of the selected NPS drastically decrease for the solutions with an R6G concentration below 10^{-10} M. As a matter of fact, at 10^{-11} M concentration none of the 6 random spot measurements on the investigated surface have resulted in a corresponding Raman shift pattern. This observation does not exclude the possibility of local morphology disturbance or uneven wetting of the surface by the probe molecule solution. Nevertheless, as demonstrated in the same figure, the substrate is still SERS viable with a distinct detection of the characteristic R6G peaks at the concentrations down to 10^{-12} M. Further measurements at higher dilution rates gave no R6G signal, therefore, it is possible to conclude that the R6G detection limit of present nanoporous silver morphology is 10^{-12} M. In contrast with this, a pristine Ag-Cu-Si alloy (melt-spun ribbon) did not exhibit any SERS properties already at the probe molecules concentration of 10^{-4} M (red bottom scan in Figure III.67). Hence, it would be accurate to attribute the Raman enhancement effect to the particular nanostructured surface of silver substrates.

It is rather curious, that among the two studied NPS morphologies, the one with less regular (as it seems from SEM graphs in Figure III.65.b) architecture showed more active optical properties. An explanation of such phenomena should be based on the generation of better surface resonance conditions for the used incident light wavelength, appearance of the higher concentration of system's irregularities: isolated Ag agglomerates, grain boundaries and sharp edges, leading to the increased concentration of "hot spots", responsible for SERS amplification, as noted in the section I.8.

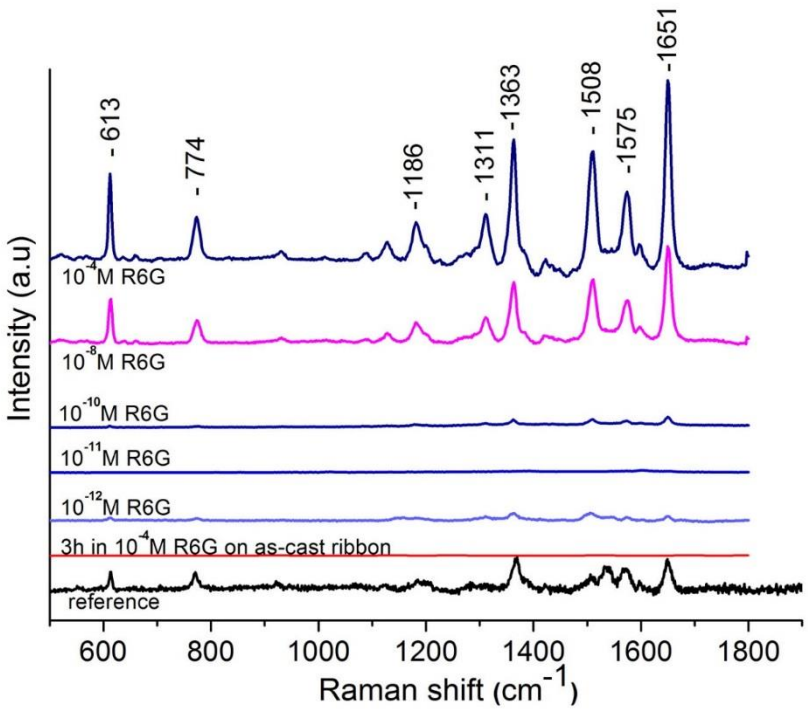

Figure III.67. Evolution of the SERS signal, obtained on the NPS (morphology 2), with the R6G probe molecule concentration in distilled water. Black bottom curve is a reference Raman spectrum, recorded from a droplet of concentrated R6G solution, dried on a Si monocrystal plate.

III.4.4. Conclusions

As a result of half-cell electrochemical experiments, it is for the first time that NPS and NPCo foils have been successfully tested as an active material for direct ammonia-borane electrooxidation in an alkaline medium. This was not possible for the Ag nanoporous analog, produced from the amorphous precursor (the material could not self-stand and could not be handled to prepare electrodes). Hence, observed mechanical integrity was another clear advantageous for application in self-supporting catalysts. Moreover, the materials appeared to be competitive to PGM substrates, and economically are more advantageous, owing to the smaller cost and larger availability of Ag, Co (Cu and Si) compared to gold and platinum, that are mostly used commercial catalysts at the moment. Stability of the material under exploitation is an important characteristic of any potential catalyst, and in the case of NPS, its functioning in the given experimental conditions considerably outlasts the one, reported for conventional Pt/C composite, previously studied in LEMPI laboratory for AB oxidation. As for cobalt-based substrates, the presence of residual phases (Cu_9Si and minor Co_2Si) is a non-negligible even after dealloying in appropriate etchant proceeds. This fact affects the durability of cobalt catalysts in alkaline media by releasing dissolution of Si atoms during the electrochemical cycling and contributing to the poisoning of the nanoporous catalyst matrix.

Surface enhanced Raman spectroscopy analytical technique that allows target molecule detection if an opto-magnetically appropriate substrate is used. Superior SERS properties of nanoporous metals have been brought to evidence rather recently. One of the valorizing results of present research concerns a successful functioning of our NPS system as an SERS-active material for R6G probe molecule detection. Among the selected morphologies of NPS, the one exhibiting most irregular sponge-like architecture showed the best SERS sensitivity (10^{-12} M concentration of R6G), although both morphologies demonstrated a capacity for a single-molecule detection ($< 10^{-8}$ M). Further systematic study of NPS with diverse adsorbed probe molecules, material's surface functionalization or more elaborate structural modifications is a perspective way to create cheap, high-functioning architectured SERS supports.

GENERAL CONCLUSIONS

The research performed within the scope of the present project aimed to contribute to the knowledge about nanoporous metallic materials based on non-platinum group metals. The guiding principles for these works were: the novelty of the elaborated system, the possibility of its microstructural control during synthesis, use of abundant Earth materials and obviously its viability in real applications, namely, electrocatalysts and SERS supports. Another goal pursued throughout the present work was the valorization of amorphous precursors for nanoporous metals fabrication – the field where my research group has a strong background. This last point was well exploited while fabrication of amorphous Cu-Ca foils and further synthesis on the nanoporous copper matrix by simple dissolution of Ca from the bulk alloy. Unfortunately, the systems lack mechanical stability and experiences problems with metal's oxidation, troubling any further applicative actions.

Having established a close collaboration with the laboratory of materials electrochemistry and physicochemistry of the University of Grenoble Alpes and making available the related experimental conditions was a fortunate case. It resulted in focusing on the study of catalytic properties of present NPMs for the application in the direct alkaline fuel cells – the thematic, the preserves its significance in the development plan for alternative energy systems.

Three main types of systems have been studied in the present work: ternary crystalline Ag-Cu-Si and Co-Cu-Si, and a binary amorphous Cu-Ca for consequent synthesis to nanoporous Ag, Co, and Cu substrates respectively. Almost all the pristine materials have been made in the form of metallic ribbons by melt-spinning technique and were systematically characterized by conventional means of microstructural, thermal, and microscopy analysis. Dealloying, being relatively fast and simple in manipulation, was the main method used for the synthesis of NPMs from as-spun precursors.

The most significant amount of performed work is related to the nanoporous silver material, obtained from the $Ag_{38.75}Cu_{38.75}Si_{22.5}$ ribbons. The initiation of this research direction was due to the earlier study, conducted in our group, regarding the use of amorphous precursor with the identical composition for the NPS fabrication. The transition towards its crystalline counterpart was, first of all, because Ag-Cu-Si has a poor glass-formation ability and therefore difficult to reproduce. Secondly, mechanical properties of the porous scaffold after dealloying of amorphous foils were such that poor rigidity of material challenged further realization of electrochemical tests. In its turn, NPS from crystalline precursor showed improved mechanical resistance and allowed to perform catalytic experiments in rather violent agitating conditions set by rotation disk electrode.

The quantitative characterization of the mechanical properties of NPS, performed via instrumented nanoindentation with Berkovich type indenter, resulted in the values for hardness and reduced Young's modulus much lower than those for bulk silver, prepared via vacuum arc melting. Although, when compared directly to bibliography data on bulk Ag, nanoporous samples, studied in this work manifest very close hardness values of ~ 0.25 GPa in the depth $h < 400$ nm. Another ensuing result of a set of statistical indentation experiments was a suggestion for a phenomenological model, describing the hardness-displacement dependence for the type of nanoporous metallic materials. Using a certain conjecture and basic geometrical assumptions for ligaments network behavior, it was possible to demonstrate that the hardness of NPS is inversely related to the displacement h. Present dependence found its confirmation for two different nanoporous Ag morphologies. Even though it follows the trend

of geometrically necessary dislocations, it differs from alternative models, known for crystalline and amorphous systems.

An important part of the work concerned the analysis of geometric characteristics of NPM: calculation of the average ligaments and pore dimensions, their statistical distribution, specific surface area and implied porous fraction. Detailed knowledge about interconnected ligaments forming a porous matrix, the presence of dominating shape or preferential direction of orientation is crucial for the field of catalysts and SERS since these applications strongly depend on substrate's design. Along with trivial SEM observations and gas adsorption/desorption method, that allowed the primary morphological analysis, more elaborated SEM-FIB tomography tool has been additionally used. This technique is particularly attractive for our study, since it does not imply any specific sample preparation (especially if they are already fragile by nature), and accessible magnification allows one to record desirable nano-scale details. The volume reconstructed by FIB nanotomography can be numerically visualized with the use of software-implemented algorithms (Avizo light 9.2.0, FEI™). Here, every point of the reconstructed model is described mathematically. Therefore, it possesses its own curvature characteristics. Owing to this fact, Avizo allows performing color cartography, describing the shape and curvedness of each surface patch. The information, contained in such interfacial shape distribution patterns, together with other structural characteristics is extremely useful for the description of catalytically and optically active materials. All three types of studied NPMs have been reconstructed by the present type of tomography. A comparison of their patterns helps to see the difference between each morphology that can be expressed quantitatively.

The key moment of the present research, determining the real value of elaborated systems, was the applications testing. The applications concerned were: i) anodic NPS and NPCo substrates for a half-cell electrode and ii) SERS-active NPS support. An experimental setup for electrochemical tests included a cooled triple-neck flask, filled with ammonia-borane fuel and NaOH supporting electrolyte, with three electrodes, among which a working electrode was of the RDE type. RDE was used to study the evolution of the mass-transport process with a change of a revolution mode. Related changes of the registered current would be a direct observation of the intrinsic catalytic capacity of the nanoporous catalyst. At very high rotation speeds (1600 – 2500 rpm), turbulent forces seriously affect the studied support attached to the RDE. Therefore, it was to take into consideration the structural integrity of the materials. Exactly this last factor made us eliminate the too brittle NPCu from these tests.

In their turn, both NPS and NPCo showed attractive performance as catalysts for AB oxidation. The onset potential for starting the reaction was set around – 0.3 V *vs.* RHE for both materials, which is lower than in a common H_2 oxidation reaction on Pt. At given experimental conditions, the specific current extracted at high rotation regime reached 5.02 and 4 $mA.cm^{-2}$ for nanoporous Ag and Co respectively, although, taking into account lower S_{spec} of NPCo substrate, it is found to have better intrinsic catalytic activity towards this particular reaction compared to NPS. In spite of good preliminary results, there is one fact that poison the image of good NPCo catalyst: it is its unstable functioning. Unlike NPS that can sustain at least 15.000 cyclovoltamperometric cycles (67 hours) without considerable degradation or loss of activity, NPCo performance is not stable already during 2000 experimental cycles (9 hours). Such functioning is supposedly related to the presence of contaminating residues in the porous scaffold, primarily, Si-containing phases that cause catalyst poisoning upon dissolution. A solution that seems reasonable to fight this malfunctioning is to fabricate a different NPCo precursor, avoiding the formation of intermetallic phases with unwanted elements

upon dealloying. For example, Co-Cu alloy would be a good candidate, nevertheless, in present work, a scenario with such composition hasn't been realized due to its high temperatures of melting, which troubles the established casting procedure.

In addition to catalytic aspects, the studied NPMs were shown to possess SERS-active properties. On the example of nanoporous Ag, it was shown that the detection of R6G probe molecules is highly effective when one uses a dealloyed for 90 minutes sponge-like silver substrate. The detection limit on the surface of the material, in this case, can already reach 10^{-12} M, which is within the range of single-molecule detection concentration. This result lays on the edge of existing detection limit for nanoarchitectured silver and even exceeds such for nanoporous gold substrates in similar experimental conditions. Possible improvements that can be made to increase the SERS activity are related to further variations of NPS morphology, for instance, it is a recent trend to deposit the solution with probe's molecules on material's cross section, since it has higher roughness and, therefore, richer in "hot spots" compared to smoother surface.

Coming to the final part of the conclusions, it is worth bringing up the essential ideas I would like to deliver in this work. Primarily, it is a fact of successful synthesis via a simple dealloying process and characterization of novel porous metallic materials on the base of silver, cobalt, and copper with nano-scale architecture. For the first time, NPS and NPCo have been actually tested as substrates for anode materials in alkaline fuel cells and their potential as such is doubtless. It is certain that each of the fabricated materials has its limitations and imperfections (mechanical and functional stability, the purity of porous matrix, lifetime, flexibility, etc.). In particular, the question of molding and processing is always an actual question for novel materials that cannot be definitely answered regarding the extension of the casting shapes beyond ones used herein. Nevertheless, apart from (always) existing drawbacks, I believe that this work properly demonstrates the potential of NPMs based on abundant metals and that the continuance of related researches should not intermit. In the end, together with the field of materials for energy, the gain will be brought to other vital domains such as biomedicine, biosensing, microelectronics and so forth.

ANNEXES

A.1. Definition of the smoothing parameters of the surface-reconstructed mesh

As it has been detailed in chapter II.3.3, an image stack, binarized and registered via Fiji can be further imported in Avizo, FEI™ that allows surface reconstruction, based on the triangulate surface grid via the "generate surface" module with an appropriate type and level of smoothing. In our case, level 5 of "unconstrained" smoothing type has been selected for the reconstruction of our nanoporous system, basing on the procedure in the Figure A.1. This model represents the evaluation of a surface of a basic three-dimensional object as different smoothing is applied. We consider that level 5 of "unconstrained" smoothing represents a real sphere in a most appropriate way, preserving its symmetry and size. Therefore, we allow to transfer the obtained parameters on the models with comparable scale of morphology.

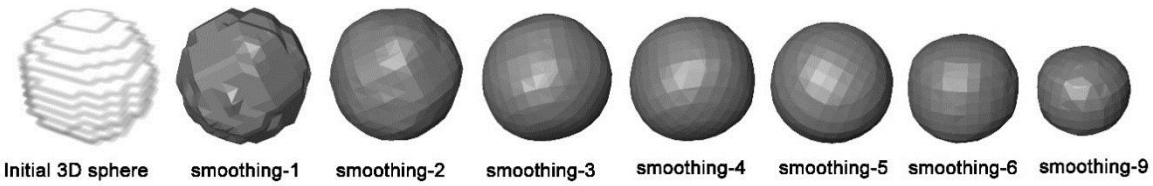

Figure A.1. Three-dimensional numerical representation via Avizo of a spherical surface with different smoothing parameters. Initial diameter of the sphere is 6 pixels.

A.2. Morphological differences from the cross-sections of the studied by nanoindentation NPS samples

Figure A.2 represents the electron microscopy image if the "structure 1" and "structure 2" cross-sections in addition to the Figure III.46 in order to confirm the tridimensional differences of the ligaments network morphologies of the studied by nanoindentation NPS samples.

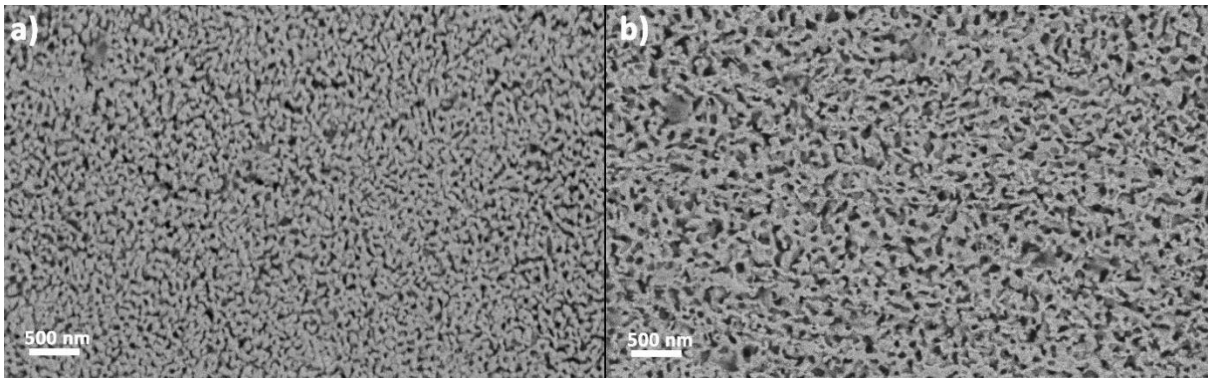

Figure A.2. SEM secondary electrons images of cross sections a) of the "structure 1" sample of NPS (dealloying time of 45 minutes), and b) "structure 2" (dealloying time of 3 hours).

A.3. Load-displacement nanoindentation curves

All the load-displacement nanoindentation curves, obtained in quasistatic (Figure A.3.a) and dynamic mode (Figure A.3.b) for a NPS "structure 1" sample. The top left inset exposes similar as in "structure 2" bumps, characteristic for the top 150nm surface layer of the porous matrix. It is apparent that the slope of the loading part of the QSt curves varies significantly at indent displacement < 200 nm, that may be due to the surface inhomogeneity effect at the different indentation sites.

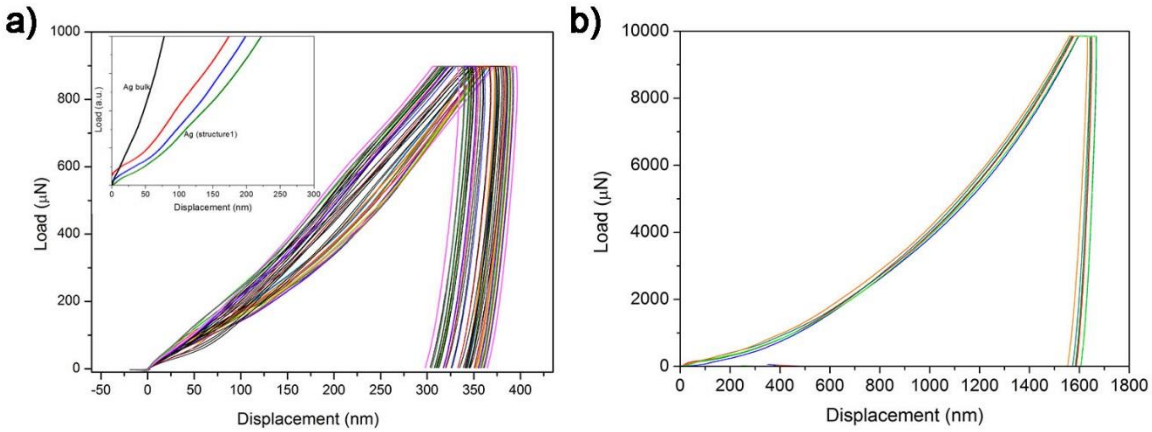

Figure A.3. Load-displacement nanoindentation curves, performed in a) a quasistatic and b) dynamic mode on NPS "structure 1" sample.

REFERENCES

(1) Lakes, R. Materials with Structure Hierarchy. *Nature* **1993**, *361*, 511–515.

(2) Schaedler, T. A.; Jacobsen, A. J.; Torrents, A.; Sorensen, A. E.; Lian, J.; Greer, J. R.; Valdevit, L.; Carter, W. B. Ultralight Metallic Microlattices. *Science (80-.).* **2011**, *334* (6058), 962–965.

(3) Liu, P. S.; Chen, G. F. *Porous Materials, Processing and Applications*, First Edit.; Butterworth-Heinemann, Elsevier, 2014.

(4) Nic, M.; Jirat, J.; Kosata, B. *Compendium of Chemical Terminology Gold Book*, Version 2.; International Union of Pure and Applied Chemistry, 2014.

(5) Society, R.; Engineering, R. A. of. *Nanoscience and Nanotechnologies: Opportunities and Uncertainties*; Latimer Trend Ltd, Plymouth, UK, 2004.

(6) Vajtai, R. *Springer Handbook of Nanomaterials*; 2013.

(7) Eliseev, A. .; Lykashin, A. *Functional Nanomaterials*; Tretiakov, U., Ed.; Fizmatlit: Moscow, 2010.

(8) Murray, R. Method of Producing Finely-Divided Nickel. US001628190, 1926.

(9) Ding, Y.; Erlebacher, J. Nanoporous Metals with Controlled Multimodal Pore Size Distribution. *J. Am. Chem. Soc.* **2003**, *125* (26), 7772–7773.

(10) Zhang, J.; Li, C. M. Nanoporous Metals: Fabrication Strategies and Advanced Electrochemical Applications in Catalysis, Sensing and Energy Systems. *Chem. Soc. Rev.* **2012**, *41* (21), 7016.

(11) Lei, Y.; Cai, W.; Wilde, G. Highly Ordered Nanostructures with Tunable Size, Shape and Properties: A New Way to Surface Nano-Patterning Using Ultra-Thin Alumina Masks. *Prog. Mater. Sci.* **2007**, *52* (4), 465–539.

(12) Xie, Y.; Kocaefe, D.; Chen, C.; Kocaefe, Y. Review of Research on Template Methods in Preparation of Nanomaterials. *J. Nanomater.* **2016**, *2016*, 1–10.

(13) Pylypenko, S.; Mukherjee, S.; Olson, T. S.; Atanassov, P. Non-Platinum Oxygen Reduction Electrocatalysts Based on Pyrolyzed Transition Metal Macrocycles. *Electrochim. Acta* **2008**, *53* (27), 7875–7883.

(14) Zhang, Z.; Wang, Y.; Qi, Z.; Zhang, W.; Qin, J.; Frenzel, J. Generalized Fabrication of Nanoporous Metals (Au, Pd, Pt, Ag, and Cu) through Chemical Dealloying. *J. Phys. Chem. C* **2009**, *113* (29), 12629–12636.

(15) Geslin, P.-A.; McCue, I.; Gaskey, B.; Erlebacher, J.; Karma, A. Topology-Generating Interfacial Pattern Formation during Liquid Metal Dealloying. *Nat. Commun.* **2015**, *6*, 8887.

(16) Detsi, E.; van de Schootbrugge, M.; Punzhin, S.; Onck, P. R.; De Hosson, J. T. M. On Tuning the Morphology of Nanoporous Gold. *Scr. Mater.* **2011**, *64* (4), 319–322.

(17) Seker, E.; Reed, M. L.; Begley, M. R. Nanoporous Gold: Fabrication, Characterization, and Applications. *Materials (Basel).* **2009**, *2* (4), 2188–2215.

(18) Ding, Y.; Kim, Y. J.; Erlebacher, J. Nanoporous Gold leaf: "Ancient Technology "/advanced Material. *Adv. Mater.* **2004**, *16* (21), 1897–1900.

(19) Ding, Y.; Chen, M. Nanoporous Metals for Catalytic and Optical Applications. *MRS Bull.* **2009**, *34* (8), 569–576.

(20) Wada, T.; Setyawan, A. D.; Yubuta, K.; Kato, H. Nano- to Submicro-Porous β-Ti Alloy Prepared from Dealloying in a Metallic Melt. *Scr. Mater.* **2011**, *65* (6), 532–535.

(21) *Springer Handbook of Nanomaterials*; Vajtai, R., Ed.; Springer Berlin Heidelberg: Berlin, Heidelberg, 2013.

(22) Andreasen, G. Kinetics of Particle Coarsening at Gold Electrode/Electrolyte Solution Interfaces Followed by In Situ Scanning Tunneling Microscopy. *J. Electrochem. Soc.* **1996**, *143* (2), 466.

(23) Seebauer, E. Estimating Surface Diffusion Coefficients. *Prog. Surf. Sci.* **1995**, *49* (3), 265–330.

(24) Weissmüller, J.; Newman, R. C.; Jin, H.-J.; Hodge, A. M.; Kysar, J. W. Nanoporous Metals by Alloy Corrosion: Formation and Mechanical Properties. *MRS Bull.* **2009**, *34* (8), 577–586.

(25) McCue, I. D. Frontiers Of Dealloying – Novel Processing For Advanced Materials, Johns Hopkins University, 2015.

(26) Erlebacher, J. An Atomistic Description of Dealloying. *J. Electrochem. Soc.* **2004**, *151* (10), C614.

(27) Erlebacher, J.; Aziz, M. J.; Karma, A.; Dimitrov, N.; Sieradzki, K. Evolution of Nanoporosity in Dealloying. *Nature* **2001**, *410* (6827), 450–453.

(28) Forty, A. J. Corrosion Micromorphology of Noble Metal Alloys and Depletion Gilding. *Nature* **1979**, *282* (5739), 597–598.

(29) Dixon, M. C.; Daniel, T. A.; Hieda, M.; Smilgies, D. M.; Chan, M. H. W.; Allara, D. L. Preparation, Structure, and Optical Properties of Nanoporous Gold Thin Films. *Langmuir* **2007**, *23* (5), 2414–2422.

(30) Sieradzki, K.; Corderman, R. R.; Shukla, K.; Newman, R. C. Computer Simulations of Corrosion: Selective Dissolution of Binary Alloys. *Philos. Mag. A* **1989**, *59* (4), 713–746.

(31) Sieradzki, K. Curvature Effects in Alloy Dissolution. *J. Electrochem. Soc.* **1993**, *140* (10), 2868.

(32) Forty, A. J.; Rowlands, G. A Possible Model for Corrosion Pitting and Tunneling in Noble-Metal Alloys. *Philos. Mag. A* **1981**, *43* (1), 171–188.

(33) Yan, M. Development of New Catalytic Performance of Nanoporous Metals for Organic Reactions, Springer Japan: Tokyo, 2014.

(34) Cahn, J. W. On Spinodal Decomposition. *Acta Metall.* **1961**, *9* (9), 795–801.

(35) Carter, W.-C.; Balluffi, R. W.; Allen, S. *Kinetics of Materials*; John Wiley & Sons, 2005.

(36) Erlebacher, J. Mechanism of Coarsening and Bubble Formation in High-Genus Nanoporous Metals. *Phys. Rev. Lett.* **2011**, *106* (22), 225504.

(37) Pickering, H. W.; Wagner, C. Electrolytic Dissolution of Binary Alloys Containing a Noble Metal. *J. Electrochem. Soc.* **1967**, *114* (7), 698.

(38) Detsi, E. Metallic Muscles: Enhanced Strain and Electrolyte-Free Actuation, 2012.

(39) Brunauer, S.; Emmett, P. H.; Teller, E. Adsorption of Gases in Multimolecular Layers. *J. Am. Chem. Soc.* **1938**, *60* (2), 309–319.

(40) Tan, Y. H.; Davis, J. A.; Fujikawa, K.; Ganesh, N. V.; Demchenko, A. V.; Stine, K. J. Surface Area and Pore Size Characteristics of Nanoporous Gold Subjected to Thermal, Mechanical, or Surface Modification Studied Using Gas Adsorption Isotherms, Cyclic Voltammetry, Thermogravimetric Analysis, and Scanning Electron Microscopy. *J. Mater. Chem.* **2012**, *22* (14), 6733.

(41) Ding, Y.; Zhang, Z. *Nanoporous Metals for Advanced Energy Technologies*; Springer International Publishing: Cham, 2016.

(42) Detsi, E.; De Jong, E.; Zinchenko, A.; Vuković, Z.; Vuković, I.; Punzhin, S.; Loos, K.; ten Brinke, G.; De Raedt, H. A.; Onck, P. R.; De Hosson, J. T. M. On the Specific Surface Area of Nanoporous Materials. *Acta Mater.* **2011**, *59* (20), 7488–7497.

(43) Fritz, J. D. Selective Anodic Dissolution of Cu-Au Alloys: TEM and Current Transient Study. *J. Electrochem. Soc.* **1991**, *138* (11), 3209.

(44) Hayes, J. R.; Hodge, a. M.; Biener, J.; Hamza, a. V.; Sieradzki, K. Monolithic Nanoporous Copper by Dealloying Mn–Cu. *J. Mater. Res.* **2006**, *21* (10), 2611–2616.

(45) Detsi, E.; Vuković, Z.; Punzhin, S.; Bronsveld, P. M.; Onck, P. R.; Hosson, J. T. M. De. Fine-Tuning the Feature Size of Nanoporous Silver. *CrystEngComm* **2012**, *14* (17), 5402.

(46) Zhang, Q.; Zhang, Z. On the Electrochemical Dealloying of Al-Based Alloys in a NaCl Aqueous Solution. *Phys. Chem. Chem. Phys.* **2010**, *12* (7), 1453–1472.

(47) Yu, J.; Ding, Y.; Xu, C.; Inoue, A.; Sakurai, T.; Chen, M. Nanoporous Metals by Dealloying Multicomponent Metallic Glasses. *Chem. Mater.* **2008**, *20* (14), 4548–4550.

(48) Yan, M. Nanoporous Copper Metal Catalyst in Click Chemistry: Nanoporosity Dependent Activity Without Supports and Bases; 2014; pp 17–53.

(49) Barsuk, D.; Zhang, M.; Panagiotopoulos, N. T.; Jorge, A. M.; Georgarakis, K.; Yavari, A. R. Fabrication of Nanoporous Copper Surface by Leaching of Chill-Zone Cu-Zr-Hf Alloys. *Scr. Mater.* **2015**, *104*, 64–66.

(50) Panagiotopoulos, N. T.; Jorge, A. M.; Rebai, I.; Georgarakis, K. Microporous and Mesoporous Materials Nanoporous Titanium Obtained from a Spinodally Decomposed Ti Alloy. *Microporous Mesoporous Mater.* **2016**, *222*, 23–26.

(51) Erlebacher, J.; Seshadri, R. Hard Materials with Tunable Porosity. *MRS Bull.* **2009**, *34* (8), 561–568.

(52) Scaglione, F.; Gebert, A.; Battezzati, L. Dealloying of an Au-Based Amorphous Alloy. *Intermetallics* **2010**, *18* (12), 2338–2342.

(53) Li, R.; Liu, X.; Wang, H.; Wu, Y.; Lu, Z. P. Bendable Nanoporous Copper Thin Films with Tunable Thickness and Pore Features. *Corros. Sci.* **2016**, *104*, 227–235.

(54) Battezzati, L.; Scaglione, F. De-Alloying of Rapidly Solidified Amorphous and Crystalline Alloys. *J. Alloys Compd.* **2011**, *509*, S8–S12.

(55) Scaglione, F.; Celegato, F.; Rizzi, P.; Battezzati, L. A Comparison of de-Alloying Crystalline and Amorphous Multicomponent Au Alloys. *Intermetallics* **2015**, *66*, 82–87.

(56) Rizzi, P.; Scaglione, F.; Battezzati, L. Nanoporous Gold by Dealloying of an Amorphous Precursor. *J. Alloys Compd.* **2014**, *586*, S117–S120.

(57) Zhang, M.; Jorge Junior, A. M.; Pang, S. J.; Zhang, T.; Yavari, A. R. Fabrication of Nanoporous Silver with Open Pores. *Scr. Mater.* **2015**, *100*, 21–23.

(58) Antoniou, A.; Bhattacharrya, D.; Baldwin, J. K.; Goodwin, P.; Nastasi, M.; Picraux, S. T.; Misra, A. Controlled Nanoporous Pt Morphologies by Varying Deposition Parameters. *Appl. Phys. Lett.* **2009**, *95* (7), 73116.

(59) Scaglione, F.; Rizzi, P.; Celegato, F.; Battezzati, L. Synthesis of Nanoporous Gold by Free Corrosion of an Amorphous Precursor. *J. Alloys Compd.* **2014**, 1–6.

(60) Gibson, L. J.; Ashby, M. F. *Cellular Solids Structure and Properties*; Cambridge University Press, UK, 1999.

(61) Uchic, M. D. Sample Dimensions Influence Strength and Crystal Plasticity. *Science (80-.).* **2004**, *305* (5686), 986–989.

(62) Greer, J. R.; Nix, W. D. Size Dependence of Mechanical Properties of Gold at the Sub-Micron Scale. *Appl. Phys. A* **2005**, *80* (8), 1625–1629.

(63) Greer, J. R.; Oliver, W. C.; Nix, W. D. Size Dependence of Mechanical Properties of Gold at the Micron Scale in the Absence of Strain Gradients. *Acta Mater.* **2005**, *53* (6), 1821–1830.

(64) Volkert, C. A.; Lilleodden, E. T. Size Effects in the Deformation of Sub-Micron Au Columns. *Philos. Mag.* **2006**, *86* (33–35), 5567–5579.

(65) Biener, J.; Hodge, A. M.; Hamza, A. V.; Hsiung, L. M.; Satcher, J. H. Nanoporous Au: A High Yield Strength Material. *J. Appl. Phys.* **2005**, *97* (2), 24301.

(66) Biener, J.; Hodge, A. M.; Hayes, J. R.; Volkert, C. A.; Zepeda-Ruiz, L. A.; Hamza, A. V.; Abraham, F. F. Size Effects on the Mechanical Behavior of Nanoporous Au. *Nano Lett.* **2006**, *6* (10), 2379–2382.

(67) Liu, R.; Gruber, J.; Bhattacharyya, D.; Tucker, G. J.; Antoniou, A. Mechanical Properties of Nanocrystalline Nanoporous Platinum. *Acta Mater.* **2016**, *103*, 624–632.

(68) Sun, X.-Y.; Xu, G.-K.; Li, X.; Feng, X.-Q.; Gao, H. Mechanical Properties and Scaling Laws of Nanoporous Gold. *J. Appl. Phys.* **2013**, *113* (2), 23505.

(69) Hakamada, M.; Asao, Y.; Kuromura, T.; Chen, Y.; Kusuda, H.; Mabuchi, M. Density Dependence of the Compressive Properties of Porous Copper over a Wide Density Range. *Acta Mater.* **2007**, *55* (7), 2291–2299.

(70) Hodge, a M.; Hayes, J. R.; Caro, J. a; Biener, J.; Hamza, a V. Characterization and Mechanical Behavior of Nanoporous Gold. *Adv. Eng. Mater.* **2006**, *8* (9), 853–857.

(71) Bobji, M. S.; Pendyala, P.; Gupta, P.; Kalode, P. Effect of Porosity on the Indentation Behaviour of Nanoporous Alumina Films. *Int. J. Surf. Sci. Eng.* **2011**, *5* (1), 51.

(72) Jang, B.-K.; Matsubara, H. Influence of Porosity on Hardness and Young's Modulus of Nanoporous EB-PVD TBCs by Nanoindentation. *Mater. Lett.* **2005**, *59* (27), 3462–3466.

(73) Esqué-de los Ojos, D.; Zhang, J.; Fornell, J.; Pellicer, E.; Sort, J. Nanomechanical Behaviour of Open-Cell Nanoporous Metals: Homogeneous versus Thickness-Dependent Porosity. *Mech. Mater.* **2016**, *100*, 167–174.

(74) Gall, K.; Liu, Y.; Routkevitch, D.; Finch, D. S. Instrumented Microindentation of Nanoporous Alumina Films. *J. Eng. Mater. Technol.* **2006**, *128* (2), 225.

(75) Oliver, W. C.; Pharr, G. M. Measurement of Hardness and Elastic Modulus by Instrumented Indentation: Advances in Understanding and Refinements to Methodology. *J. Mater. Res.* **2004**, *19* (1), 3–20.

(76) Oliver, W. C.; Pharr, G. M. An Improved Technique for Determining Hardness and Elastic Modulus Using Load and Displacement Sensing Indentation Experiments. *J. Mater. Res.* **1992**, *7* (6), 1564–1583.

(77) Li, R.; Sieradzki, K. Ductile-Brittle Transition in Random Porous Au. *Phys. Rev. Lett.* **1992**, *68* (8), 1168–1171.

(78) De Schampheleire, S.; De Jaeger, P.; De Kerpel, K.; Ameel, B.; Huisseune, H.; De Paepe, M. How to Study Thermal Applications of Open-Cell Metal Foam: Experiments and Computational Fluid Dynamics. *Materials (Basel).* **2016**, *9* (2), 94.

(79) Banhart, J. Manufacture, Characterisation and Application of Cellular Metals and Metal Foams. *Prog. Mater. Sci.* **2001**, *46* (6), 559–632.

(80) Haberling, C.; Banhart, J.; Hipke, T.; Neugebauer, R.; Kretz, R.; Maine, E. M. A.; Ashby, M. F. Service Properties and Exploitability. In *Handbook of Cellular Metals*; Wiley-VCH Verlag GmbH & Co. KGaA: Weinheim, FRG; pp 299–354.

(81) Tappan, B. C.; Steiner, S. A.; Luther, E. P. Nanoporous Metal Foams. *Angew. Chemie Int. Ed.* **2010**, *49* (27), 4544–4565.

(82) Wang, G.; Coppens, M.-O. Rational Design of Hierarchically Structured Porous Catalysts for Autothermal Reforming of Methane. *Chem. Eng. Sci.* **2010**, *65* (7), 2344–2351.

(83) Zhang, C.; Zhu, W.; Zheng, J.-P.; Liang, Z.; Wang, B. Catalytic Electrode with Gradient Porosity and Catalyst Density for Fuel Cells. US 8703355 B2, 2014.

(84) Hammer, B.; Norskov, J. K. Theoretical Surface Science and Catalysis — Calculations and Concepts. *Adv. Catal.* **2000**, *45*, 71–129.

(85) Cordonna, G. W.; Kosanovich, M.; Becker, E. R. Gas Turbine Emission Control. Platinum and Platinum-Palladium Catalysts for Carbon Monoxide and Hydrocarbon Oxidation. *Platin. Met. Rev.* **1989**, *33* (2).

(86) Kua, J.; Goddard, W. A. Oxidation of Methanol on 2nd and 3rd Row Group VIII Transition Metals (Pt, Ir, Os, Pd, Rh, and Ru): Application to Direct Methanol Fuel Cells. *J. Am. Chem. Soc.* **1999**, *121* (47), 10928–10941.

(87) Moskaleva, L. V; Röhe, S.; Wittstock, A.; Zielasek, V.; Klüner, T.; Neyman, K. M.; Bäumer, M. Silver Residues as a Possible Key to a Remarkable Oxidative Catalytic Activity of Nanoporous Gold. *Phys. Chem. Chem. Phys.* **2011**, *13* (10), 4529–4539.

(88) Zhang, J.; Liu, P.; Ma, H.; Ding, Y. Nanostructured Porous Gold for Methanol Electro-Oxidation. *J. Phys. Chem. C* **2007**, *111* (28), 10382–10388.

(89) Xu, C.; Wang, L.; Mu, X.; Ding, Y. Nanoporous PtRu Alloys for Electrocatalysis. *Langmuir* **2010**, *26* (10), 7437–7443.

(90) InfoMine Inc. http://www.infomine.com/investment/metal-prices/ (accessed Feb 7, 2017).

(91) Tables of Physical & Chemical Constants www.kayelaby.npl.co.uk.

(92) Clement, J. L.; Jarrett, P. S. Antibacterial Silver. *Met. Based. Drugs* **1994**, *1* (5–6), 467–482.

(93) Xu, C.; Li, Y.; Tian, F.; Ding, Y. Dealloying to Nanoporous Silver and Its Implementation as a Template Material for Construction of Nanotubular Mesoporous Bimetallic Nanostructures. *ChemPhysChem* **2010**, *11* (15), 3320–3328.

(94) Wang, X.; Qi, Z.; Zhao, C.; Wang, W.; Zhang, Z. Influence of Alloy Composition and Dealloying Solution on the Formation and Microstructure of Monolithic Nanoporous Silver through Chemical Dealloying of Al−Ag Alloys. *J. Phys. Chem. C* **2009**, *113* (30), 13139–13150.

(95) Kim, M.-S.; Nishikawa, H. Fabrication of Nanoporous Silver and Microstructural Change during Dealloying of Melt-Spun Al–20 at.%Ag in Hydrochloric Acid. *J. Mater. Sci.* **2013**, *48* (16), 5645–5652.

(96) Zhang, C.; Sun, J.; Xu, J.; Wang, X.; Ji, H.; Zhao, C.; Zhang, Z. Formation and Microstructure of Nanoporous Silver by Dealloying Rapidly Solidified Zn–Ag Alloys. *Electrochim. Acta* **2012**, *63*, 302–311.

(97) Li, Z. Q.; Li, B. Q.; Qin, Z. X.; Lu, X. Fabrication of Porous Ag by Dealloying of Ag–Zn Alloys in H2SO4 Solution. *J. Mater. Sci.* **2010**, *45* (23), 6494–6497.

(98) Ji, H.; Wang, X.; Zhao, C.; Zhang, C.; Xu, J.; Zhang, Z. Formation, Control and Functionalization of Nanoporous Silver through Changing Dealloying Media and Elemental Doping. *CrystEngComm* **2011**, *13* (7), 2617.

(99) Jin, Y.; Li, R.; Zhang, T. Formation of Nanoporous Silver by Dealloying Ca–Ag Metallic Glasses in Water. *Intermetallics* **2015**, *67*, 166–170.

(100) Luft, T. A. www.strem.com http://www.strem.com/uploads/technical_notes/47-0645tech.pdf (accessed Feb 7, 2016).

(101) Lu, Q.; Rosen, J.; Zhou, Y.; Hutchings, G. S.; Kimmel, Y. C.; Chen, J. G.; Jiao, F. A Selective and Efficient Electrocatalyst for Carbon Dioxide Reduction. *Nat. Commun.* **2014**, *5*, 3242.

(102) Pattabiraman, R.; Muzhumathim, S.; Vasu, K. I. Electro-Oxidation of Formaldehyde and Glycol on Silver Alloys in Alkaline Solutions. *Bull. Electrochem.* **1990**, *6* (6), 590–591.

(103) BeŁtowska-Brzezinska, M. Electrochemical Oxidation of Formaldehyde on Gold and Silver. *Electrochim. Acta* **1985**, *30* (9), 1193–1198.

(104) Detsi, E.; Sellès, M. S.; Onck, P. R.; De Hosson, J. T. M. Nanoporous Silver as Electrochemical Actuator. *Scr. Mater.* **2013**, *69* (2), 195–198.

(105) Li, R.; Liu, X. J.; Wang, H.; Wu, Y.; Chu, X. M.; Lu, Z. P. Nanoporous Silver with Tunable Pore Characteristics and Superior Surface Enhanced Raman Scattering. *Corros. Sci.* **2014**, *84*,

159–164.

(106) Marsden, W. L.; Wainwright, M. S.; Friedrich, J. B. Zinc-Promoted Raney Copper Catalysts for Methanol Synthesis. *Ind. Eng. Chem. Prod. Res. Dev.* **1980**, *19* (4), 551–556.

(107) Patart, G. Procédé de Production D'alcools, D'aldéhydes et D'acides À Partir de Mélanges Gazeux Maintenus Sous Pression et Soumis À L'action D'agents Cat Aly Ligues Ou de L'électricité. 540.543, 1921.

(108) Chinchen, G. C.; Denny, P. J.; Jennings, J. R.; Spencer, M. S.; Waugh, K. C. Synthesis of Methanol. *Appl. Catal.* **1988**, *36*, 1–65.

(109) Davies, P.; Snowdon, F. F. Production of Oxygenated Hydrocarbons. U.S. Patent 3,326,956, 1967.

(110) Keir, D. S. The Dealloying of Copper-Manganese Alloys. *J. Electrochem. Soc.* **1980**, *127* (10), 2138.

(111) Hayes, J. R.; Hodge, A. M.; Biener, J.; Hamza, A. V.; Sieradzki, K. Monolithic Nanoporous Copper by Dealloying Mn–Cu. *J. Mater. Res.* **2006**, *21* (10), 2611–2616.

(112) Qi, Z.; Zhao, C.; Wang, X.; Lin, J.; Shao, W.; Zhang, Z.; Bian, X. Formation and Characterization of Monolithic Nanoporous Copper by Chemical Dealloying of Al−Cu Alloys. *J. Phys. Chem. C* **2009**, *113* (16), 6694–6698.

(113) Liu, W.; Xin, C.; Chen, L.; Yan, J.; Li, N.; Shi, S.; Zhang, S. A Facile One-Pot Dealloying Strategy to Synthesize Monolithic Asymmetry-Patterned Nanoporous Copper Ribbons with Tunable Microstructure and Nanoporosity. *RSC Adv.* **2016**, *6* (4), 2662–2670.

(114) Zhao, C.; Qi, Z.; Wang, X.; Zhang, Z. Fabrication and Characterization of Monolithic Nanoporous Copper through Chemical Dealloying of Mg–Cu Alloys. *Corros. Sci.* **2009**, *51* (9), 2120–2125.

(115) Sattayasamitsathit, S.; Thavarungkul, P.; Thammakhet, C.; Limbut, W.; Numnuam, A.; Buranachai, C.; Kanatharana, P. Fabrication of Nanoporous Copper Film for Electrochemical Detection of Glucose. *Electroanalysis* **2009**, *21* (21), 2371–2377.

(116) Lin, B.; Kong, L.; Hodgson, P.; Dumée, L. Impact of the De-Alloying Kinetics and Alloy Microstructure on the Final Morphology of De-Alloyed Meso-Porous Metal Films. *Nanomaterials* **2014**, *4* (4), 856–878.

(117) Luo, X.; Li, R.; Huang, L.; Zhang, T. Nucleation and Growth of Nanoporous Copper Ligaments during Electrochemical Dealloying of Mg-Based Metallic Glasses. *Corros. Sci.* **2013**, *67*, 100–108.

(118) Wang, Z.; Liu, J.; Qin, C.; Yu, H.; Xia, X.; Wang, C.; Zhang, Y.; Hu, Q.; Zhao, W. Dealloying of Cu-Based Metallic Glasses in Acidic Solutions: Products and Energy Storage Applications. *Nanomaterials* **2015**, *5* (2), 697–721.

(119) Liu, L.; Scholz, R.; Pippel, E.; Gösele, U. Microstructure, Electrocatalytic and Sensing Properties of Nanoporous Pt46Ni54 Alloy Nanowires Fabricated by Mild Dealloying. *J. Mater. Chem.* **2010**, *20* (27), 5621.

(120) Pourbaix, M. *Atlas D'équilibres Électrochimiques*, Gauthier-V.; 1963.

(121) Abe, H.; Sato, K.; Nishikawa, H.; Takemoto, T.; Fukuhara, M.; Inoue, A. Dealloying of Cu-Zr-Ti Bulk Metallic Glass in Hydrofluoric Acid Solution. *Mater. Trans.* **2009**, *50* (6), 1255–1258.

(122) Wang, Z.; Wang, L.; Qin, C.; Liu, J.; Li, Y.; Zhao, W. Tailored Dealloying Products of Cu-Based Metallic Glasses in Hydrochloric Acid Solutions. *Mater. Res.* **2014**, *17* (4), 1003–1009.

(123) Dan, Z.; Qin, F.; Makino, A.; Sugawara, Y.; Muto, I.; Hara, N. Fabrication of Nanoporous Copper by Dealloying of Amorphous Ti – Cu – Ag Alloys. *J. Alloys Compd.* **2014**, *586*, S134–S138.

(124) Qin, C. L.; Wang, Z. F.; Liu, H.; Liu, L.; Wang, H.; Ding, J.; Zhao, W. M. Monolithic Nanoporous Copper with Novel Electrochemical Properties Fabricated by Dealloying Cu-Zr(-Al) Metallic Glasses. *Mater. Sci. Forum* **2014**, *783–786*, 1925–1930.

(125) Chen, L. Y.; Yu, J. S.; Fujita, T.; Chen, M. W. Nanoporous Copper with Tunable Nanoporosity for SERS Applications. *Adv. Funct. Mater.* **2009**, *19*, 1221–1226.

(126) Zhang, S.; Xing, Y.; Liu, W.; Zheng, J. Preparation of Nanoporous Copper through Chemical Dealloying and Its Application in Lithium Ion Battery. In *The 15th International Meeting on Lithium Batteries - IMLB 2010*; © 2010 The Electrochemical Society, 2010.

(127) Hou, C.; Lang, X.-Y.; Han, G.-F.; Li, Y.-Q.; Zhao, L.; Wen, Z.; Zhu, Y.-F.; Zhao, M.; Li, J.-C.; Lian, J.-S.; Jiang, Q. Integrated Solid/Nanoporous Copper/Oxide Hybrid Bulk Electrodes for High-Performance Lithium-Ion Batteries. *Sci. Rep.* **2013**, *3* (1), 2878.

(128) Liu, W.; Chen, L.; Yan, J.; Li, N.; Shi, S.; Zhang, S. Nanoporous Copper from Dual-Phase Alloy Families and Its Technology Application in Lithium Ion Batteries. **2015**, *33* (5), 203–231.

(129) Grass, G.; Rensing, C.; Solioz, M. Metallic Copper as an Antimicrobial Surface. *Appl. Environ. Microbiol.* **2011**, *77* (5), 1541–1547.

(130) Liu, Z.; Hu, Y.; Liu, C.; Zhou, Z. Surface-Independent One-Pot Chelation of Copper Ions onto Filtration Membranes to Provide Antibacterial Properties. *Chem. Commun.* **2016**, *52* (82), 12245–12248.

(131) Hans, M.; Mathews, S.; Mücklich, F.; Solioz, M. Physicochemical Properties of Copper Important for Its Antibacterial Activity and Development of a Unified Model. *Biointerphases* **2016**, *11* (1), 18902.

(132) Hunt, E. M.; Pantoya, M. L. *Nanostructured Metallic Alloys: Synthesis, Properties and Applications*; VDM Verlag Dr. Muller publisher, 2007.

(133) Varíola, F.; Vetrone, F.; Richert, L.; Jedrzejowski, P.; Yi, J. H.; Zalzal, S.; Clair, S.; Sarkissian, A.; Perepichka, D. F.; Wuest, J. D.; Rosei, F.; Nanci, A. Improving Biocompatibility of Implantable Metals by Nanoscale Modification of Surfaces: An Overview of Strategies, Fabrication Methods, and Challenges. *Small* **2009**, *5* (9), 996–1006.

(134) Flint, S. H.; Brooks, J. D.; Bremer, P. J. Properties of the Stainless Steel Substrate, Influencing the Adhesion of Thermo-Resistant Streptococci. *J. Food Eng.* **2000**, *43* (4), 235–242.

(135) Fused Quartz Properties & Usage Guide http://www.quartz.com/gedata.html (accessed Feb 20, 2017).

(136) Nishizawa, T.; Ishida, K. The Co−Cu (Cobalt-Copper) System. *Bull. Alloy Phase Diagrams* **1984**, *5* (2), 161–165.

(137) Nanoporous Cobalt and Copper Metal Foam Made by Combustion Synthesis. *Anti-Corrosion Methods Mater.* **2006**, *53* (5), acmm.2006.12853ead.001.

(138) Kim, Y. K.; Cha, S. I.; Hong, S. H. Nanoporous Cobalt Foam and a Co/Co(OH)2 Core–shell Structure for Electrochemical Applications. *J. Mater. Chem. A* **2013**, *1* (34), 9802.

(139) Silberberg, M. *Chemistry: The Molecular Nature Of Matter and Change*; McGraw-Hill Companies, 2004.

(140) Khodakov, A. Y.; Chu, W.; Fongarland, P. Advances in the Development of Novel Cobalt Fischer−Tropsch Catalysts for Synthesis of Long-Chain Hydrocarbons and Clean Fuels. *Chem. Rev.* **2007**, *107* (5), 1692–1744.

(141) Khassin, A. A.; Yurieva, T. M.; Kustova, G. N.; Itenberg, I. S.; Demeshkina, M. P.; Krieger, T. A.; Plyasova, L. M.; Chermashentseva, G. K.; Parmon, V. N. Cobalt–aluminum Co-Precipitated Catalysts and Their Performance in the Fischer–Tropsch Synthesis. *J. Mol. Catal. A Chem.* **2001**, *168* (1–2), 193–207.

(142) Okabe, K.; Li, X.; Wei, M.; Arakawa, H. Fischer–Tropsch Synthesis over Co–SiO2 Catalysts Prepared by the Sol–gel Method. *Catal. Today* **2004**, *89* (4), 431–438.

(143) Roucoux, A.; Schulz, J.; Patin, H. Reduced Transition Metal Colloids: A Novel Family of Reusable Catalysts? *Chem. Rev.* **2002**, *102* (10), 3757–3778.

(144) Group, F. World Catalysts http://www.freedoniagroup.com/World-Catalysts.html (accessed Feb 7, 2017).

(145) Herz, R. K. *Chemical Engineering Design of CO Oxidation Catalysts*; 1987.

(146) Bérubé, V.; Radtke, G.; Dresselhaus, M.; Chen, G. Size Effects on the Hydrogen Storage Properties of Nanostructured Metal Hydrides: A Review. *Int. J. Energy Res.* **2007**, *31* (6–7), 637–663.

(147) Davis, M. E.; Davis, R. J. Fundamentals of Chemical Reaction Engineering.; McGraw-Hill Higher Education: New York, NY, 2003.

(148) Ertl, G. *Catalysis: Science and Technology*; Anderson, J. R., Boudart, M., Eds.; Springer-Verlag: Berlin, 1983.

(149) Lang, X.; Guan, P.; Zhang, L.; Fujita, T.; Chen, M. Characteristic Length and Temperature Dependence of Surface Enhanced Raman Scattering of Nanoporous Gold. *J. Phys. Chem. C* **2009**, *113* (25), 10956–10961.

(150) Zhang, L.; Lang, X.; Hirata, A.; Chen, M. Wrinkled Nanoporous Gold Films with Ultrahigh Surface-Enhanced Raman Scattering Enhancement. *ACS Nano* **2011**, *5* (6), 4407–4413.

(151) Qian, L. H.; Yan, X. Q.; Fujita, T.; Inoue, A.; Chen, M. W. Surface Enhanced Raman Scattering of Nanoporous Gold: Smaller Pore Sizes Stronger Enhancements. *Appl. Phys. Lett.* **2007**, *90* (15), 23–25.

(152) Ovchinnikov, V. Surface Enhanced Raman Scattering. In *The Sixth International Conference on Quantum, Nano and Micro Technologies, ICQNM 2012*; 2012.

(153) Sharma, B.; Frontiera, R. R.; Henry, A.-I.; Ringe, E.; Van Duyne, R. P. SERS: Materials, Applications, and the Future. *Mater. Today* **2012**, *15* (1–2), 16–25.

(154) Moskovits, M. Surface-Enhanced Spectroscopy. *Rev. Mod. Phys.* **1985**, *57* (3), 783–826.

(155) Jeanmaire, D. L.; Van Duyne, R. P. Surface Raman Spectroelectrochemistry. *J. Electroanal. Chem. Interfacial Electrochem.* **1977**, *84* (1), 1–20.

(156) Albrecht, M. G.; Creighton, J. A. Anomalously Intense Raman Spectra of Pyridine at a Silver Electrode. *J. Am. Chem. Soc.* **1977**, *99* (15), 5215–5217.

(157) Asao, N.; Ishikawa, Y.; Hatakeyama, N.; Menggenbateer; Yamamoto, Y.; Chen, M.; Zhang, W.; Inoue, A. Nanostructured Materials as Catalysts: Nanoporous-Gold-Catalyzed Oxidation of Organosilanes with Water. *Angew. Chemie - Int. Ed.* **2010**, *49*, 10093–10095.

(158) Krause, C. New Probe Detects Trace Pollutants in Groundwater. *Oak Ridge Natl. Lab. Rev.* **1993**, *26* (2), 65–67.

(159) McQuillan, A. J. The Discovery of Surface-Enhanced Raman Scattering. *Notes Rec. R. Soc.* **2009**, *63* (1), 105–109.

(160) Tamma, V. A.; Huang, F.; Nowak, D.; Kumar Wickramasinghe, H. Stimulated Raman Spectroscopy and Nanoscopy of Molecules Using near Field Photon Induced Forces without Resonant Electronic Enhancement Gain. *Appl. Phys. Lett.* **2016**, *108* (23), 233107.

(161) Talley, C. E.; Jackson, J. B.; Oubre, C.; Grady, N. K.; Hollars, C. W.; Lane, S. M.; Huser, T. R.; Nordlander, P.; Halas, N. J. Surface-Enhanced Raman Scattering from Individual Au Nanoparticles and Nanoparticle Dimer Substrates. *Nano Lett.* **2005**, *5* (8), 1569–1574.

(162) Kneipp, K.; Wang, Y.; Kneipp, H.; Perelman, L. T.; Itzkan, I.; Dasari, R. R.; Feld, M. S. Single Molecule Detection Using Surface-Enhanced Raman Scattering (SERS). *Phys. Rev. Lett.* **1997**, *78* (9), 1667–1670.

(163) García-Vidal, F. J.; Pendry, J. B. Collective Theory for Surface Enhanced Raman Scattering. *Phys. Rev. Lett.* **1996**, *77* (6), 1163–1166.

(164) Campion, A.; Kambhampati, P. Surface-Enhanced Raman Scattering. *Chem. Soc. Rev.* **1998**, *27* (4), 241.

(165) Nie, S. Probing Single Molecules and Single Nanoparticles by Surface-Enhanced Raman Scattering. *Science (80-.).* **1997**, *275* (5303), 1102–1106.

(166) Creighton, J. A.; Eadon, D. G. Ultraviolet–visible Absorption Spectra of the Colloidal Metallic Elements. *J. Chem. Soc., Faraday Trans.* **1991**, *87* (24), 3881–3891.

(167) Zhang, L.; Lang, X.; Hirata, A.; Chen, M. Wrinkled Nanoporous Gold Films with Ultrahigh Surface-Enhanced Raman Scattering Enhancement. *ACS Nano* **2011**, *5* (6), 4407–4413.

(168) Ling, X.; Xie, L.; Fang, Y.; Xu, H.; Zhang, H.; Kong, J.; Dresselhaus, M. S.; Zhang, J.; Liu, Z. Can Graphene Be Used as a Substrate for Raman Enhancement? *Nano Lett.* **2010**, *10* (2), 553–561.

(169) Qiu, C.; Zhou, H.; Yang, H.; Chen, M.; Guo, Y.; Sun, L. Investigation of N -Layer Graphenes as Substrates for Raman Enhancement of Crystal Violet. *J. Phys. Chem. C* **2011**, *115* (20), 10019–10025.

(170) Livingstone, R.; Zhou, X.; Tamargo, M. C.; Lombardi, J. R.; Quagliano, L. G.; Jean-Mary, F. Surface Enhanced Raman Spectroscopy of Pyridine on CdSe/ZnBeSe Quantum Dots Grown by Molecular Beam Epitaxy. *J. Phys. Chem. C* **2010**, *114* (41), 17460–17464.

(171) Qian, L. H.; Inoue, A.; Chen, M. W. Large Surface Enhanced Raman Scattering Enhancements from Fracture Surfaces of Nanoporous Gold. *Appl. Phys. Lett.* **2008**, *92* (9), 2006–2009.

(172) Lang, X. Y.; Chen, L. Y.; Guan, P. F.; Fujita, T.; Chen, M. W. Geometric Effect on Surface Enhanced Raman Scattering of Nanoporous Gold: Improving Raman Scattering by Tailoring Ligament and Nanopore Ratios. *Appl. Phys. Lett.* **2009**, *94* (21), 10–13.

(173) Chen, L.-Y.; Yu, J.; Fujita, T.; Chen, M. Nanoporous Copper with Tunable Nanoporosity for SERS Applications. *Adv. Funct. Mater.* **2009**, *19* (8), 1221–1226.

(174) Chen, L. Y.; Zhang, L.; Fujita, T.; Chen, M. W. Surface-Enhanced Raman Scattering of Silver@Nanoporous Copper Core−Shell Composites Synthesized by an In Situ Sacrificial Template Approach. *J. Phys. Chem. C* **2009**, *113* (32), 14195–14199.

(175) Qian, L.; Das, B.; Li, Y.; Yang, Z. Giant Raman Enhancement on Nanoporous Gold Film by Conjugating with Nanoparticles for Single-Molecule Detection. *J. Mater. Chem.* **2010**, *20* (33), 6891.

(176) Lye, W.-K.; Owens, G. K.; Wamhoff, B. R.; Hudson, M. S.; Spradlin, J. Methods for Using a Stent Having Nanoporous Layers. US 8449602 B2, 2013.

(177) Owens, G.; Lye, W.-K.; Reed, M.; Spradlin, J.; Wamhoff, B.; Hudson, M.; Looi, K. Dealloyed Nanoporous Stents. US 20060276878 A1, 2006.

(178) Lye, W.-K.; Owens, G.; Reed, M.; Wamhoff, B.; Looi, K.; Spradlin, J. Nanoporous Stents with Improved Radiolucency. US 20060276885 A1, 2006.

(179) Hingston, J.; Robichaud, M.; Weber, J.; McNamara, A.; Flanagan, A.; Horgan, F. Medical Devices Containing Therapeutic Agents. US20110045055 A1, 2011.

(180) Helmus, M. N. Medical Devices Having Vapor Deposited Nanoporous Coatings For Controlled Therapeutic Agent Delivery. US 20100280612 A1, 2010.

(181) Tenney, B.; Xu, Y.; Helmus, M. Medical Devices Having Nanoporous Coatings for Controlled Therapeutic Agent Delivery. US 20070224235 A1, 2007.

(182) Gombert, D.; Richardson, J. G. *Cold Crucible Induction Melter Technology: Results of Laboratory Directed Research and Development*; 2001.

(183) Budhani, R. C.; Goel, T. C.; Chopra, K. L. Melt-Spinning Technique for Preparation of Metallic Glasses. *Bull. Mater. Sci.* **1982**, *4* (5), 549–561.

(184) Cotton, F. A.; Wilkinson, G. *Advanced Inorganic Chemistry*, 5th editio.; New York: John Wiley & Sons, 1988.

(185) Vilador, D.; Veron, M.; Gemmi, M.; Peiro, F.; Portillo, J.; Estrade, S.; Mendoza, J.; Llorca-Isern, N.; Nicilopoulos, S. Orientation and Phase Mapping in the Transmission Electron Microscope Using Precession-Assisted Diffraction Spot Recognition: State-of-the-Art Results. *J. Microsc.* **2013**, *252* (1), 23–34.

(186) Barrett, E. P.; Joyner, L. G.; Halenda, P. P. The Determination of Pore Volume and Area Distributions in Porous Substances. I. Computations from Nitrogen Isotherms. *J. Am. Chem. Soc.* **1951**, *73* (1), 373–380.

(187) Rasband, W. S. https://imagej.nih.gov/ij/ http://imagej.nih.gov/ij/ (accessed May 2, 2016).

(188) Boulos, V.; Salvo, L.; Fristot, V.; Lhuissier, P.; Houzet, D. Investigating Performance Variations of an Optimized GPU-Ported Granulometry Algorithm. In *18th International European Conference on Parallel and Distributed Computing*; Rhodes Island, Greece, 2012.

(189) Koenderink, J. J.; van Doorn, A. J. Surface Shape and Curvature Scales. *Image Vis. Comput.* **1992**, *10* (8), 557–564.

(190) Gibbs, J. W.; Mohan, K. A.; Gulsoy, E. B.; Shahani, A. J.; Xiao, X.; Bouman, C. A.; De Graef, M.; Voorhees, P. W. The Three-Dimensional Morphology of Growing Dendrites. *Sci. Rep.* **2015**, *5* (1), 11824.

(191) Maciejak, O.; Aubert, P. Mesure de Dureté Par Nano-Indentation. *Tech. l'Ingénieur* **2007**, *NM 7 200*, 1–12.

(192) AZoM.com. Silver - Applications and Properties of Silver www.azom.com.

(193) Zadick, A.; Dubau, L.; Chatenet, M.; Demirci, U.; Serov, A.; Atanassov, P. Instability Of Commercial Pt/C And Pd/C Electrocatalysts In Alkaline Media. *ECS Trans.* **2015**, *69* (17), 553–558.

(194) Zadick, A.; Dubau, L.; Sergent, N.; Berthomé, G.; Chatenet, M. Huge Instability of Pt/C Catalysts in Alkaline Medium. *ACS Catal.* **2015**, *5* (8), 4819–4824.

(195) Zadick, A.; Dubau, L.; Demirci, U. B.; Chatenet, M. Effects of Pd Nanoparticle Size and Solution Reducer Strength on Pd/C Electrocatalyst Stability in Alkaline Electrolyte. *J. Electrochem. Soc.* **2016**, *163* (8), F781–F787.

(196) Kabir, S.; Zadick, A.; Atanassov, P.; Dubau, L.; Chatenet, M. Stability of Carbon-Supported Palladium Nanoparticles in Alkaline Media: A Case Study of Graphitized and More Amorphous Supports. *Electrochem. commun.* **2017**, *78*, 33–37.

(197) Zadick, A. Pile À Combustible Alcaline Directe À Hydrazine-Borane Par, Grenoble-INP, 2016.

(198) Wang, Y. Q.; Ma, S.; Yang, Q. Q.; Li, X. J. Size-Dependent SERS Detection of R6G by Silver Nanoparticles Immersion-Plated on Silicon Nanoporous Pillar Array. *Appl. Surf. Sci.* **2012**, *258* (15), 5881–5885.

(199) Qiu, H.; Zhang, Z.; Huang, X.; Qu, Y. Dealloying Ag-Al Alloy to Prepare Nanoporous Silver as a Substrate for Surface-Enhanced Raman Scattering: Effects of Structural Evolution and Surface Modification. *ChemPhysChem* **2011**, *12* (11), 2118–2123.

(200) Yavari, A. R.; Ota, K.; Georgarakis, K.; LeMoulec, A.; Charlot, F.; Vaughan, G.; Greer, A. L.; Inoue, A. Chill Zone Copper with the Strength of Stainless Steel and Tailorable Color. *Acta Mater.* **2008**, *56* (8), 1830–1839.

(201) Kanaya, K.; Okayama, S. Penetration and Energy-Loss Theory of Electrons in Solid Targets. *J. Phys. D. Appl. Phys.* **1972**, *5* (1), 308.

(202) Link-Systems. *Energy Dispersive X-Ray Spectroscopy User's Manual*; Perrygraf Division of Nashua Corp., Printed in USA: Los Angeles, 1982.

(203) Ai, J.; Chen, Y.; Urquidi-Macdonald, M.; Macdonald, D. D. Electrochemical Impedance Spectroscopic Study of Passive Zirconium. *J. Electrochem. Soc.* **2007**, *154* (1), C43.

(204) Stansbury, E. E.; Buchanan, R. A. *Fundamentals of Electrochemical Corrosion*; ASM International, 2000.

(205) Holmes, D. R.; Chang, W. Corrosion of Hafnium and Hafnium Alloys. In *ASM Handbook*; ASM International, 2005; pp 1–6.

(206) St.Amand, R.; Giessen, B. C. Easy Glass Formation in Simple Metal Alloys: Amorphous Metals Containing Calcium and Strontium. *Scr. Metall.* **1978**, *12* (11), 1021–1026.

(207) Jin, Y.; Li, R.; Zhang, T. Intermetallics Formation of Nanoporous Silver by Dealloying Ca E Ag Metallic Glasses in Water. *Intermetallics* **2015**, *67*, 166–170.

(208) Glinka, N. L. *General Chemistry*; KNORUS: Moscow, 2009.

(209) Walker, P.; Tarn, W. H. *Handbook of Metal Etchants*; 1991.

(210) Laporte, V.; Mortensen, A. Intermediate Temperature Embrittlement of Copper Alloys. *Int. Mater. Rev.* **2009**, *54* (2), 94–116.

(211) Luo, X.; Li, R.; Huang, L.; Zhang, T. Nucleation and Growth of Nanoporous Copper Ligaments during Electrochemical Dealloying of Mg-Based Metallic Glasses. *Corros. Sci.* **2013**, *67*, 100–108.

(212) Patterson, A. L. The Scherrer Formula for X-Ray Particle Size Determination. *Phys. Rev.* **1939**, *56* (10), 978–982.

(213) Williamson, G. .; Hall, W. . X-Ray Line Broadening from Filed Aluminium and Wolfram. *Acta Metall.* **1953**, *1* (1), 22–31.

(214) Izumi, F.; Ikeda, T. Implementation of the Williamson – Hall and Halder – Wagner Methods into RIETAN-FP. *Nagoya Inst. Technol. Adv. Ceram. Res. Cent. Annu. Rep. Adv. Ceram. Res. Cent. Nagoya Inst. Technol.* **2014**, *3* (d), 33–38.

(215) Wang, J.-I.; Harrison, I. R. 6.2 Crystallite Size and Lamellar Thickness by X-Ray Methods. In *Methods in Experimental Physics*; Fava, R. A., Ed.; 1980; pp 128–184.

(216) Rothman, S. J., and Peterson, N. L. *Isotope Effect and Divacancies for Self−Diffusion in Copper*; Vol. 35, p 305−312.

(217) Butrymowicz, D. B.; Manning, J. R.; Read, M. E. Diffusion in Copper and Copper Alloys. *Journal of Physical and Chemical Reference Data*. 1973, pp 643–656.

(218) Mizutani, U.; Yoshino, K. Formation and Low-Temperature Electronic Properties of Liquid-Quenched Ag-Cu-X (X=Mg, Si, Sn and Sb) Metallic Glasses. *J. Phys. F Met. Phys.* **1984**, *14* (5), 1179–1192.

(219) Liu, Z.; Luo, X.; Guo, G.; He, C.; Li, G.; Zhang, Q. The Liquidus Of The Ternary Ag-Cu-Si Alloy System. *Acta Metall. Sin.* **1999**, *1*.

(220) Detsi, E.; Sellès, M. S.; Onck, P. R.; De Hosson, J. T. M. Nanoporous Silver as

Electrochemical Actuator. *Scr. Mater.* **2013**, *69*, 195–198.

(221) Nakagawa, Y. Liquid Immiscibility in Copper-Iron and Copper-Cobalt Systems in the Supercooled State. *Acta Metall.* **1958**, *6* (11), 704–711.

(222) Co-Cu-Si (Cobalt-Copper-Silicon). In *Non-Ferrous Metal Systems. Part 2: Selected Copper Systems*; Effenberg, G., Ilyenko, S., Eds.; Springer Berlin Heidelberg: Berlin, Heidelberg, 2007; pp 159–166.

(223) Hedges, E. S. LXXIX.—The Action of Nitric Acid on Some Metals. *J. Chem. Soc.* **1930**, 561–569.

(224) Hayzelden, C.; Rayment, J. J.; Cantor, B. Rapid Solidification Microstructures in Austenitic Fe□Ni Alloys. *Acta Metall.* **1983**, *31* (3), 379–386.

(225) Wronski, Z.; Boyd, J. Effect of Cooling Rate on Solidification Microstructures in Pseudoeutectics 304SS-Zr Alloys. *J. Met.* **1988**, *39* (7), 69.

(226) Huang, S. C.; Laforce, R. P.; Ritter, A. M.; Goehner, R. P. Rapid Solidification Characteristics in Melt Spinning a Ni-Base Superalloy. *Metall. Trans. A* **1985**, *16* (10), 1773–1779.

(227) Ward, E. P. W.; Yates, T. J. V.; Fernández, J.-J.; Vaughan, D. E. W.; Midgley, P. A. Three-Dimensional Nanoparticle Distribution and Local Curvature of Heterogeneous Catalysts Revealed by Electron Tomography. *J. Phys. Chem. C* **2007**, *111* (31), 11501–11505.

(228) Mangipudi, K. R.; Radisch, V.; Holzer, L.; Volkert, C. A. A FIB-Nanotomography Method for Accurate 3D Reconstruction of Open Nanoporous Structures. *Ultramicroscopy* **2016**, *163*, 38–47.

(229) Ziehmer, M.; Hu, K.; Wang, K.; Lilleodden, E. T. A Principle Curvatures Analysis of the Isothermal Evolution of Nanoporous Gold: Quantifying the Characteristic Length-Scales. *Acta Mater.* **2016**, *120*, 24–31.

(230) Caractérisation Des Matériaux. In *Traité des matériaux*; S. Degallaix, Ilschner, B., Eds.; Presses Polytechniques et Universitaires Romandes: Lausanne, 2007.

(231) Lorensen, W. E.; Cline, H. E. Marching Cubes: A High Resolution 3d Surface Construction Algorithm. *Comput. Graph. (ACM).* **1987**, *21* (4), 163–169.

(232) *Avizo User's Guide*; 1995-2016 Konrad-Zuse-Zentrum fur Informationstechnik Berlin (ZIB), Germany, 2016.

(233) Rösner, H.; Parida, S.; Kramer, D.; Volkert, C. A.; Weissmüller, J. Reconstructing a Nanoporous Metal in Three Dimensions: An Electron Tomography Study of Dealloyed Gold Leaf. *Adv. Eng. Mater.* **2007**, *9* (7), 535–541.

(234) Fujita, T.; Qian, L.-H.; Inoke, K.; Erlebacher, J.; Chen, M.-W. Three-Dimensional Morphology of Nanoporous Gold. *Appl. Phys. Lett.* **2008**, *92* (25), 251902.

(235) Holzer, L.; Indutnyi, F.; Gasser, P.; Munch, B.; Wedmann, M. Three-Dimensional Analysis of Porous BaTiO3 Ceramics Using FIB Nanotomography. *J. Microsc.* **2004**, *216* (1), 84–95.

(236) Klobes, P.; Meyer, K.; Munro, R. G. *Porosity and Specific Surface Area Measurements for Solid Materials*; U.S. Government Printing Office: Washington, 2006.

(237) Klobes, P.; Meyer, K.; Munro, R. Porosity and Specific Surface Area Measurements for Solid

Materials. National Institute of Standards and Technology (NIST) 2006.

(238) Thommes, M. Physical Adsorption Characterization of Nanoporous Materials. *Chemie Ing. Tech.* **2010**, *82* (7), 1059–1073.

(239) Menk, J. Uncertainties and Errors in Nanoindentation. In *Nanoindentation in Materials Science*; InTech, 2012.

(240) Pharr, G. M.; Oliver, W. C. Nanoindentation of Silver-Relations between Hardness and Dislocation Structure. *J. Mater. Res.* **1989**, *4* (1), 94–101.

(241) Nix, W. D.; Gao, H. Indentation Size Effects in Crystalline Materials: A Law for Strain Gradient Plasticity. *J. Mech. Phys. Solids* **1998**, *46* (3), 411–425.

(242) Smith, D. R.; Fickett, F. R. Low-Temperature Properties of Silver. *J. Res. Natl. Inst. Stand. Techn ology* **1995**, *100* (2), 119–171.

(243) Champion, Y.; Perri?re, L. Strain Gradient in Micro-Hardness Testing and Structural Relaxation in Metallic Glasses. *Adv. Eng. Mater.* **2015**, *17* (6), 885–892.

(244) Fleck, N. A.; Muller, G. M.; Ashby, M. F.; Hutchinson, J. W. Strain Gradient Plasticity: Theory and Experiment. *Acta Metall. Mater.* **1994**, *42* (2), 475–487.

(245) Jaska, C. A.; Temple, K.; Lough, A. J.; Manners, I. Transition Metal-Catalyzed Formation of Boron−Nitrogen Bonds: Catalytic Dehydrocoupling of Amine-Borane Adducts to Form Aminoboranes and Borazines. *J. Am. Chem. Soc.* **2003**, *125* (31), 9424–9434.

(246) Shimizu, K.; Satsuma, A. Silver Cluster Catalysts for Green Organic Synthesis. *J. Japan Pet. Inst.* **2011**, *54* (6), 347–360.

(247) Spassov, T.; Lyubenova, L.; Liu, Y.; Bliznakov, S.; Spassova, M.; Dimitrov, N. Mechanochemical Synthesis, Thermal Stability and Selective Electrochemical Dissolution of Cu–Ag Solid Solutions. *J. Alloys Compd.* **2009**, *478* (1–2), 232–236.

(248) Chatenet, M.; Micoud, F.; Roche, I.; Chainet, E.; Vondrák, J. Kinetics of Sodium Borohydride Direct Oxidation and Oxygen Reduction in Sodium Hydroxide Electrolyte. *Electrochim. Acta* **2006**, *51* (25), 5452–5458.

(249) Cheng, H.; Scott, K. Investigation of Non-Platinum Cathode Catalysts for Direct Borohydride Fuel Cells. *J. Electroanal. Chem.* **2006**, *596* (2), 117–123.

(250) Sanli, E.; Celikkan, H.; Zuhtyuusal, B.; Aksu, M. Anodic Behavior of Ag Metal Electrode in Direct Borohydride Fuel Cells. *Int. J. Hydrogen Energy* **2006**, *31* (13), 1920–1924.

(251) Atwan, M. H.; Northwood, D. O.; Gyenge, E. L. Evaluation of Colloidal Ag and Ag-Alloys as Anode Electrocatalysts for Direct Borohydride Fuel Cells. *Int. J. Hydrogen Energy* **2007**, *32* (15), 3116–3125.

(252) Sanli, E.; Uysal, B. Z.; Aksu, M. L. The Oxidation of NaBH4 on Electrochemicaly Treated Silver Electrodes. *Int. J. Hydrogen Energy* **2008**, *33* (8), 2097–2104.

(253) Durst, J.; Siebel, A.; Simon, C.; Hasché, F.; Herranz, J.; Gasteiger, H. A. New Insights into the Electrochemical Hydrogen Oxidation and Evolution Reaction Mechanism. *Energy Environ. Sci.* **2014**, *7* (7), 2255.

(254) Nagle, L. C.; Rohan, J. F. Nanoporous Gold Catalyst for Direct Ammonia Borane Fuel Cells.

J. Electrochem. Soc. **2011**, *158* (7), B772.

PUBLICATIONS

- "*Nanoporous silver for electrocatalysis application in alkaline fuel cells*", Daria Barsuk, Anicet Zadick, Marian Chatenet, Konstantinos Georgarakis, Nikolaos T. Panagiotopoulos, Yannick Championa, Alberto Moreira Jorge Jr, Materials and Design, 111 (2016), 528-536. DOI: 10.1016/j.matdes.2016.09.037

- "*Fabrication of nanoporous copper surface by leaching of chill-zone Cu–Zr–Hf alloys*", Daria Barsuk, Min Zhang, Nikolaos T. Panagiotopoulos, Alberto M. Jorge Jr., Konstantinos Georgarakisa, Alain R. Yavari, Scripta Materialia, 104 (2015) 64–66. DOI: 10.1016/j.scriptamat.2015.03.026

CONFERENCES AND COMMUNICATIONS

- "*Fabrication of nanoporous copper surface by leaching of chill-zone Cu–Zr–Hf alloys*", Daria Barsuk, Min Zhang, Nikolaos T. Panagiotopoulos, Alberto M. Jorge Jr., Konstantinos Georgarakisa, Alain R. Yavari, ISMANAM-2015, July 2015, Paris, France, (Poster presentation);

- "*Novel integral nanoporous silver for anode catalytic applications in alkaline fuel cells*", Daria Barsuk, Anicet Zadik, Konstantinos Georgarakis, Nikolaos T. Panagiotopoulos, Marian Chatenet, Yannick Champion, Alberto Moreira Jorge Jr, ISMANAM-2016, July 2016, Nara, Japan, (Oral presentation);

- "*Nanoporous Cobalt Catalyst For Direct Ammonia Borane Fuel Cells*", Daria Barsuk, Anicet Zadick, Yaofeng Guo, Nikolaos T. Panagiotopoulos, Yannick Champion, Marian Chatenet, Alberto M. Jorge Jr, MH 2016, August 2016, Interlaken, Switzerland (Poster presentation);

- "*Nanoporous Cobalt and Silver Catalysts for Direct Ammonia-Borane Fuel Cells*" Daria Barsuk, Anicet Zadick, Yaofeng Guo, Nikolaos T. Panagiotopoulos, Konstantinos Georgarakis, Yannick Champion, Marian Chatenet, Alberto M. Jorge Jr., ECOSS-32, Sept. 2016, Grenoble, France (Poster presentation);

- "*Nanoporous copper from binary Cu-Ca amorphous precursor by simple dealloying in water*", Daria Barsuk, Nikolaos Panagiotopoulos, Frederic Charlot, Gilles Renou, Alberto Moreira Jorge Jr, Yannick Champion, NanoMat 2017, March 2017, Brotas, Brazil (Oral presentation)

- "*Structure and approach of the mechanical strength and deformation of nanoporous metals prepared by de-alloying of crystalline precursor*", PPG-CEM's International Workshop on Applications of Amorphous, Metastable, Nanostructured and Advanced Metallic Alloys, March 2017, São Carlos, Brazil (Oral presentation).

Available online at www.sciencedirect.com

ScienceDirect

Scripta Materialia 104 (2015) 64–66

Scripta MATERIALIA

www.elsevier.com/locate/scriptamat

Fabrication of nanoporous copper surface by leaching of chill-zone Cu–Zr–Hf alloys

Daria Barsuk,[a,*] Min Zhang,[a,b] Nikolaos T. Panagiotopoulos,[a] Alberto M. Jorge, Jr.,[a,c] Konstantinos Georgarakis[a,d] and Alain R. Yavari[a]

[a] *Laboratory of Science, Material Engineering and Procedures, CNRS UMR 5266, Polytechnical Institute of Grenoble, Saint-Martin-d'Heres 38402, France*

[b] *Key Laboratory of Aerospace Materials and Performance (Ministry of Education), School of Materials Science and Engineering, Beihang University, Beijing 100191, China*

[c] *Universidade Federal de Sao Carlos, São Paulo 13565-905, Brazil*

[d] *WPI-AIMR, Tohoku University, Sendai 980-8577, Japan*

Received 6 February 2015; revised 27 March 2015; accepted 29 March 2015
Available online 15 April 2015

In present work we report the synthesis of nanoporous surface using a copper-based alloy via leaching the less noble element-rich phase out of nanostructured ternary Cu–Hf–Zr alloys. The removal of Hf and Zr by mixed acid etchants in the chill-zone region of rapidly solidified ingots leads to the formation of a nano-roughened surface layer constituted of copper. The average pore and grain size of the obtained structure were shown to be less than 100 nm and 50 nm respectively.

Keywords: Nanoporous; Copper alloys; Leaching; Chill-zone; Eutectic solidification

Since nanoporous metals (NPM) and alloys have shown unique mechanical, adhesive, structural and functional properties [1–4], the development of such compounds has become a focus point of current investigations in material and especially in surface engineering. Among multiple ways of fabricating NPMs, template synthesis and dealloying are most widely used [5]. In most cases dealloying (or selective leaching) of metallic alloys is more favorable because it allows to produce NPMs in a controllable way. For example, dealloying under electrochemical conditions [6], changing of corrosion parameters such as etchant solution, leaching time, temperature strongly affect the final structure of NPM. Copper surfaces have been demonstrated to show anti-bactericidal properties and to be active catalysts [5,7–9]. According to present knowledge bactericidal efficacy of copper-, silver- and titanium-based alloys increases with increasing the specific surface area and metallic nanofoams can prevent the growth of bacteria [10–12]. Furthermore, view that surface roughness of 1 μm range is believed to be a critical value for bacteria adhesion due to their similar size [13], nanoporous copper is expected to exhibit better bactericidal properties comparing to nonporous ones and to ones with the large characteristic size of pores. Most nanoporous copper (NPC) materials are made by dealloying of Cu-based alloys, and the final products represent porous structures with large surface areas. Successful fabrication of NPC foils was reported [14,15] using dealloying of Al–Cu alloys in diluted NaOH and HCl water solutions.

In a previous work, we developed a series of $Cu_{90}(ZrHf)_{10}$ crystalline alloys with remarkable mechanical strength better than those of stainless steels and tailorable color using copper-moldcasting [16]. Since Cu–Zr and Cu–Hf binary phase diagrams on the copper-rich side are quite similar [17], one may consider the $Cu_{90}(ZrHf)_{10}$ family as quasi-binary alloys. The slightly-hypereutectic starting solution was selected to avoid early fcc-Cu nucleation on the copper mold. For such hypereutectic compositions, Cu_5Zr –type intermetallic phase is the first phase expected to nucleate on the copper matrix. However, its interfacial energy on copper is high because of different crystalline symmetries and interatomic distances, leading to the achievement of significant undercooling and a fine crystalline microstructure. Upon rapid solidification, a scratch-resistant chill-zone adjacent to the mold surface is formed with a submicron eutectic structure (Fig. 1).

This zone makes a dominant contribution to mechanical strength of the material which we use as precursor for further modifications in the present work. It is worth noting

* Corresponding author at: 1130, rue de la Piscine, 38402 Saint-Martin d'Hères, France. Tel.: +33 678660241; e-mail: barsukd@simap.grenoble-inp.fr

http://dx.doi.org/10.1016/j.scriptamat.2015.03.026
1359-6462/

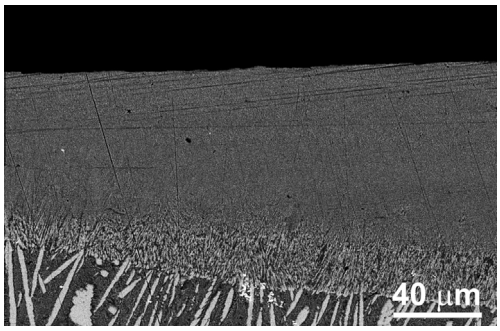

Figure 1. SEM images of cross-section perpendicular to the mold surface and to the casting length of hypereutectic $Cu_{90}(ZrHf)_{10}$. An apparently featureless layer appears next to the mold contact surface and wraps the core of the casting.

that sub-micron scale structures do not form during solidification of hypoeutectic Cu(HfZr) liquids where copper crystals form on the casting copper-mold surface and result in more coarse-grained dendrite growth into the melt [16].

The fine-grained sub-microstructure present in the chill-zone provides a new opportunity for fabrication of nanoporous surfaces by leaching the chill-zone "skin".

According to our previously reported work, the chill-zone of hypereutectic $Cu_{90}Zr_5Hf_5$ is nanostructured as shown in Figure 2(a) (magnified image of the chill-zone structure). The thickness of the chill-zone was estimated to be near 200 μm. Typical size of the Zr- and Hf-rich intermetallic compounds is around 100 nm. In order to create a pure copper nanoporous surface, free corrosion conditions were provided to remove Zr and Hf-rich component from the chill-zone region of the ternary alloys by selective leaching.

Samples of $Cu_{90}Zr_5Hf_5$ alloys were etched in water solutions of hydrofluoric acid (HF) with addition of nitric acid (HNO_3) (acid contents of 0.05 M and 0.01 M respectively) [18,19] at room temperature. Different etching times were set from 300 to 600 s. Characterization of morphological evolution of the etched samples was performed in a high-resolution field emission gun-equipped scanning electron microscope (FEG-SEM) coupled to an energy dispersive X-ray spectrometer (EDX).

The evolution of surface morphology of $Cu_{90}Zr_5Hf_5$ alloy chill-zone with leaching time is shown in Figure 2(b and c). After leaching the chill-zone for more than 300 s, the Zr- and Hf- rich intermetallic compounds are removed from the alloy and the surface of the material is shown to be nanoroughened. The most homogeneous structure of the surface was obtained after leaching for 600 s (Fig. 2(c)). According to the EDX spectra on Figure 2(d), after 600 s only Cu peaks (O and C are from the residual atmosphere) are detected. Zr and Hf atoms with some associated copper atoms have been removed and replaced by pores in the Cu skeleton. The size of surface pore distribution is below 100 nm, while the grain size is below 50 nm. The thickness of the porous layer can be controlled by varying the etching time. In the conditions used to perform the EDX (15 keV), the penetration depth can be calculated as being at least ~0.4 μm while maintaining the bulk material with unchanged structural features and high mechanical properties.

In conclusion, we report fabrication of a novel nanoporous copper surface on a bulk $Cu_{90}Zr_5Hf_5$ alloy with remarkable mechanical properties. The chill-zone of the alloy was etched in mixed HF and HNO_3 acid solution. As a result, the Zr and Hf element-rich phase was removed and nanoscale pores were formed. Pore size was below 100 nm and typical grain size of copper below 50 nm. Such new material can find applications in different areas of medical industry where bactericidal, high strength and nanostructural surface properties are required.

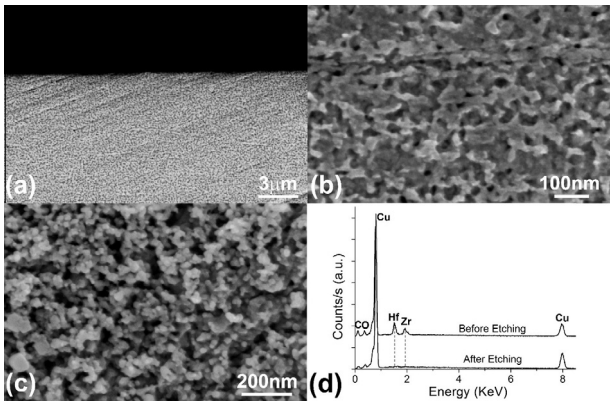

Figure 2. (a) Backscattered secondary electron FEG-SEM (BSE) image of the cross-section of the $Cu_{90}Zr_5Hf_5$ chill-zone near the mold contact. A layer of some 50 μm large below the surface shows an extremely fine isotropic eutectic-type two-phase structure on a length scale of ~100 nm with the bright phase representing the Zr–Hf containing intermetallic component [16]. (b and c) Magnified SE profile of the Cu90Zr5Hf5 surface after leaching in 0.05 M HF 0.01 M HNO_3 water solution for 300 and 600 s respectively. (d) EDX spectrum showing elemental composition before and after leaching.

This work was funded by the European ITN Network project No. 607080 (VitriMetTech). Alberto Moreira Jorge Jr gratefully acknowledges fellowship of the Fundação de Amparo à Pesquisa do Estado de São Paulo (Brazil) under Grant No. FAPESP# 2012/13179–6. Min Zhang gratefully acknowledges China Scholarship Council (No. 201303070184), Beijing Natural Science Foundation No. 2122033, and NSFC (Grant No. 51161130526).

[1] H. Nakajama, Proc. Jpn. Acad., Ser. B 86 (2010) 884–899.
[2] F. Variola, F. Vetrone, L. Richert, P. Jedrzejowski, J.-H. Yi, S. Zalzal, S. Clair, A. Sarkissian, D.F. Perepichka, J.D. Wuest, F. Rosei, A. Nanci, Small 5 (2009) 996–1006.
[3] W.-F. Lee, T.-S. Yang, Y.-C. Wu, P.-W. Peng, J. Exp. Clin. Med. 5 (3) (2013) 92–96.
[4] J. Weissmüller, R. Newman, H. Jin, A. Hodge, J. Kysar, Mater. Res. Soc. Bull. 34 (2009) 577–586.
[5] Y. Ding, Z. Zhang, in: R. Vajtai (Ed.), Springer Handbook of Nanomaterials, Springer-Verlag, Berlin Heidelberg, 2013, pp. 779–818.
[6] J. Zheng, S. Zhang, W. Liu, Y. Xing, Z. Du, J. N. Mat. Electrochem. Syst. 14 (2011) 213–216.
[7] L.Y. Chen, J.S. Yu, T. Fujita, M.W. Chen, Adv. Funct. Mater. 19 (2009) 1221–1226.
[8] T. Jin, M. Yan, Menggenbateer, T. Minato, M. Bao, Y. Yamamoto, Adv. Synth. Catal. 353 (2011) 3095–3100.
[9] F. Gao, H. Pang, S. Xu, Q. Lu, Chem. Commun. 24 (2009) 3571–3573.
[10] E.M. Hunt, M.L. Pantoya, Nanostructured Metallic Alloys: Synthesis, Properties and Applications, VDM Verlag Dr. Muller publisher, 2007.

[11] J.-S. Lee, Y.-S. Lee, M.-S. Kim, S.-K. Hyum, Ch.-H. Kang, J.-S. So, Y.-H. Yoon, Adv. Mater. Sci. Eng. 2013 (2013).
[12] H. Jing, Z. Yu, L. Li, J. Biomed, Mater. Res. A 87 (2008) 33–37.
[13] S.H. Flint, J.D. Brooks, P.J. Bremer, J. Food Eng. 43 (2000) 235–242.
[14] Z. Qi, C. Zhao, X. Wang, J. Lin, W. Shao, Z. Zhang, X. Bian, J. Phys. Chem. C 113 (2009) 6694–6698.
[15] M. Li, Y. Zhou, H. Geng, J. Porous Mater. 19 (2012) 791–796.
[16] A.R. Yavari, K. Ota, K. Georgarakis, A. LeMoulec, F. Charlot, G. Vaughan, A.L. Greer, A. Inoue, Acta Mater. 56 (2008) 1830–1839.
[17] ASM Alloy Phase Diagram Center. <http://www.asminternational.org/asmenterprise/apd/> (accessed Oct 15, 2014).
[18] P. Walker, W.H. Tarn (Eds.), CRC Handbook of Metal Etchants, CRC Press LLC, Boston, MA, 1991, p.1358.
[19] H. Abe, K. Sato, H. Nishikawa, T. Takemoto, M. Fukuhara, A. Inoue, Mater. Trans. 50 (2009) 1255–1258.

Materials and Design 111 (2016) 528–536

Contents lists available at ScienceDirect

Materials and Design

journal homepage: www.elsevier.com/locate/matdes

Nanoporous silver for electrocatalysis application in alkaline fuel cells

Daria Barsuk [a,b,*], Anicet Zadick [c,d,1], Marian Chatenet [c,d,e,1], Konstantinos Georgarakis [a,b,f], Nikolaos T. Panagiotopoulos [a,b], Yannick Champion [a,b], Alberto Moreira Jorge Jr [a,b,c,d,g,1]

[a] Université Grenoble Alpes, SIMAP, F-38000 Grenoble, France
[b] CNRS, SIMAP, F-38000 Grenoble, France
[c] Université Grenoble Alpes, LEPMI, F-38000 Grenoble, France
[d] CNRS, LePMI, F-38000 Grenoble, France
[e] French University Institute (IUF), Paris 75231, France
[f] WPI-AIMR, Tohoku University, Sendai 980-8577, Japan
[g] Federal University of São Carlos, DEMa, São Paulo 13565-905, Brazil

HIGHLIGHTS

- Nanoporous silver is obtained via dealloying of Cu_3Si phase from the crystalline precursor.
- Bulk thin middle layer of nanoporous foil reinforces its mechanical integrity.
- Pores of <100 nm and high surface area of 5 m^2/g is advantageous for catalytic applications.
- Designed material is successfully tested for applications in Direct Ammonia-Borane Fuel Cell as porous anodic catalyst.
- Materials show very high stability and lower onset voltage comparing to H_2-fed fuel cell.

GRAPHICAL ABSTRACT

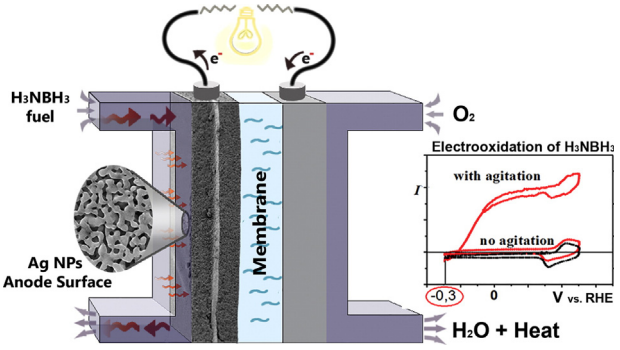

ARTICLE INFO

Article history:
Received 20 June 2016
Received in revised form 2 September 2016
Accepted 9 September 2016
Available online 10 September 2016

Keywords:
Nanoporous
Silver alloys
Dealloying
Ammonia-borane
Fuel cell
Electrooxidation

ABSTRACT

Self-supporting porous silver foils with an average pore size <100 nm were produced from a crystalline silver-based ternary alloy as a precursor by removing second phases present in the silver matrix. The final Ag-based porous foil shows good mechanical properties when comparing to its previous amorphous analogues. Its activity for direct electrochemical oxidation of ammonia-borane (AB), a fuel of interest for direct liquid fuel cells, has been investigated in alkaline media. The material exhibits promising electrochemical properties in long-term operation; indeed, material composition and nanostructure remain similar after 15,000 cyclic-voltammetries between −0.3 and 0.5 V vs. RHE in a 0.1 M NaOH + 5 mM AB solution thermostated at 25 °C. Nanoporous materials, and in particular nanoporous silver, can therefore represent a relevant choice as anode in direct ammonia-borane fuel cell.

1. Introduction

With the crescent global warming due to greenhouse gas emissions, the political and environmental climates are increasingly affected, and the demand for alternative fuels becomes unquestionably clear.

* Corresponding author at: Université Grenoble Alpes, SIMAP, F-38000 Grenoble, France.
E-mail address: daria.barsuk@simap.grenoble-inp.fr (D. Barsuk).
[1] These authors contributed equally.

http://dx.doi.org/10.1016/j.matdes.2016.09.037
0264-1275/

Hydrogen arises as a clean-energy option, generating only water after burning or electrooxidation. However, current technologies for hydrogen production, storage and transportation still require several shortcomings to be solved, for instance, green origin of the mother fuel (at present H_2 is processed from fossil fuel for >95% of its production) safety, energy-density, efficiency and cost.

Chemical hydrogen storage, in which hydrogen covalently bonded to molecules is released in gaseous form through (catalyzed) chemical reactions, offers a promising future for hydrogen storage and distribution. Considering the US Department of Energy target for the entire system weight (9.0 wt% H) [1,2], the compound ammonia-borane (H_3NBH_3, AB), with a molecular weight of 30.9 g/mol and an inherent capacity of 19.6 wt% H_2, is an obvious prime candidate as hydrogen storage compound. Solution and solid-state thermal dehydrogenation [3–5], as well as acid-catalyzed dehydrocoupling [6], have been reported for hydrogen production from amine-boranes. Transition-metal-catalyzed dehydrogenation reactions have only recently been described in the literature [7–11]. Precious noble metal catalysts (platinum-group metals - PGM) are active for AB dehydrocoupling at room temperature with catalyst loadings as low as 0.5 mol% [5].

Nevertheless, the above methodologies still suffer some drawbacks, which limit their utilization. PGMs are too expensive and poorly available. As such, PGM nanoparticles are usually supported on carbon black, which are of difficult manipulation and are not so good electron conductors. Finally, the degradation of these catalyst materials is another issue: noble metal nanoparticles were recently found highly instable in strong alkaline solutions [12–14].

Ammonia-borane is chemically stable in an alkaline medium [15] and its direct oxidation in Alkaline Fuel Cells (AFCs) can solve many of those issues. Indeed, AFCs present many advantages: for instance, the kinetics of many complex reactions is non-negligibly improved in an alkaline medium, and several metals (or metal oxides) are both active and stable in alkaline media (spreading the possibilities for material candidates to be used as electrodes) [16].

More importantly, by using an appropriate catalyst, the direct electrooxidation of ammonia-borane can initiate below the hydrogen oxidation potential [17] (<0 V vs. RHE, and as low as −0.3 V vs. RHE [18]), enhancing the energy efficiency of a Direct Ammonia-Borane Fuel Cell (DABFC) versus a hydrogen fuel cell fed after catalytic decomposition of borane fuels (in other words, the same number of electrons can be generated, but at much lower electrode potential). As such, the DABFC technology represents an interesting solution, in principle capable both of storing chemical energy and releasing it on demand with a reasonable efficiency and power density. Strong efforts have been realized to develop and improve AB oxidation catalysts [15,19–21] and use them in (hopefully efficient and economically viable) DABFC [18].

Given that both Zadick et al. [12,13] and Olu et al. [18] have brought evidences of the huge instability of platinum, and to a lesser extent of palladium nanoparticles supported on high surface area carbon in alkaline medium, the present research aims to develop cheaper and more abundant alternative catalysts for the electrochemical oxidation amine-boranes and their valorization in DABFC. In doing so, attention is paid to the catalyst durability and stability of performance. Silver in the form of nanoparticles, agglomerates, clusters and porous substances has already been widely used as catalysts in fuel cells and electrochemical actuators [22–25], in particular recently for the electrooxidation of borohydride compounds [26–30]. In that regards, nanoporous silver materials was evaluated as a potential anode catalyst for the DABFC.

There are many ways to elaborate metal-based porous catalysts. For instance, dissolution, a simple but powerful elaboration strategy, is commonly used to obtain nanoporous metallic systems. As a result of dissolution, less-noble elements are selectively leached from the mother alloy, driving a reorganization of nobler elements of the alloy-electrolyte interface into a 3-dimensional pattern [31,32]. This is commonly constituted by the noblest element, but it can also have a multi-elemental composition [33–36]. Crystalline alloys preserve their original microstructure after leaching: in other words, each grain becomes a crystal surrounded by a porous structure [37].

Nanoporous metals find their application as sensors, [38,39] catalysts [23,35,36,40–42], actuators [43,44], SERS substrates [42,45,46], and often combine advantageous structural properties with bactericidal and biocompatible ones [47–49]. Due to their very high specific surface area, nanoporous metals may present excellent catalytic properties for a series of important heterogeneous reactions, because of interconnected ligaments and 3D channels that may allow free transport of medium molecules and electrons [50–52].

Since the development of the field of nanoporous metals, a great number of works has been dedicated to the design of noble metal-based nanoporous architectured structures, among which silver plays an important role [46,53–56]. Among others, nanoporous silver (NPS) was obtained in the group of De Hosson by dealloying Al from the amorphous Ag—Al precursor alloy [57]. Another interesting "clean" method of its fabrication was recently suggested by the group of T. Zhang when amorphous Ag—Ca foils were simply immersed in water to remove calcium atoms [55].

In the previous work by M. Zhang et al. [56] was reported the fabrication of a porous silver material with a submicron pore size. The precursor of the given work was an amorphous $Ag_{38.75}Cu_{38.75}Si_{22.5}$ alloy that was exposed to an appropriate etching condition in order to eliminate Cu and Si atoms, leaving a single Ag porous carcass. Homogeneous distribution of elements in the amorphous state is a key to obtain the fine ultimate porous architecture upon reorganization of Ag atoms while etching; on the contrary, when in crystalline precursors are used, the final characteristic features are determined by the phases present in the ingot [24]. However, in spite of the finely architectured structure, the bulk material produced from the amorphous precursor [56] did not possess sufficient mechanical integrity and robustness to allow any further experiments revealing its advantages, particularly in the field of catalysis where good failure resistance is required.

The general aim of our work is firstly to approach the structural composition of previously elaborated NPS foils so as to enhance their mechanical characteristics. In the present paper, we make a step beyond and characterize a porous silver material from an electrochemical viewpoint, in particular versus the direct electrooxidation reaction of ammonia-borane in an alkaline medium, a model reaction of interest towards the development of direct alkaline fuel cells. Besides, the stability of this material is also investigated in accelerated stress-test operation.

2. Experimental section

2.1. Materials' preparation and characterization

A set of Ag-based polycrystalline alloys of composition $Ag_{38.75}Cu_{38.75}Si_{22.5}$ were prepared by arc melting of pure Ag, Cu and Si (99,99% purity, Alfa Aesar) in helium atmosphere. To homogenize the alloy, minimum 5 additional melting steps were made before the rapid solidification casting of the material on the copper wheel. Foils with thicknesses ranging between 20 and 60 μm were produced by varying the rotating speed of the copper wheel. After analyzing X-ray diffraction (XRD) results and preliminary chemical treatment tests of the obtained samples, the 20 μm thick foils showed finer porous architecture and were chosen for further careful characterization and ammonia-borane electrooxidation tests.

The XRD patterns of as-spun and dealloyed components were obtained using a PANalytical X'Pert Pro MRD instrument with a copper (Kα) radiation (0.051°/step, in variable mode).

The microstructures and chemical compositions of the ribbons were observed using a high-resolution ZEISS Ultra 55 scanning electron microscope equipped with a field emission gun (FEG-SEM) and energy-dispersive X-ray analyzer (EDS).

To analyze the pore size of the as-dealloyed ribbons an imaging tool ImageJ [58] was used.

Brunauer-Emmett-Teller (BET) surface area was measured by Nitrogen adsorption/desorption experiments carried out at 77 K using a Micromeritics A2020 instrument. Dealloying of the as-cast ribbons was performed at the ambient conditions using a few chemical etchants including the one reported in [56] – 13.4 wt% (2.12 M) of HNO_3, and another solution of 0.67 M of HNO_3 and 0.64 M of HF in deionized water. The intensity of magnetic stirring while etching was 250 rpm, the etching time was chosen in the way to leave the desirable thickness of the middle bulk non-etched layer.

2.2. Electrochemical characterization

For the electrochemical experiments, silver materials were carefully cut and placed on a glassy carbon electrode to be used as working electrode; the geometrical surface of silver materials in contact with the electrolyte was 0.048 cm^2. The counter-electrode was a carbon plate, and the reference electrode was a mercury/mercury oxide electrode (Hg/HgO) filled with 0.1 M NaOH solution; to ease the comparison with the literature, all potential values are given versus the Reversible Hydrogen Electrode scale (RHE).

Electrolytes were freshly prepared with NaOH monohydrated provided from Merck (Suprapur), ammonia-borane provided from Sigma-Aldrich (complex, 97%) and MQ-grade water (18.2 MΩ cm, <3 ppb total organic carbon, Elix + Milli-Q Gradient, Millipore). The electrochemical set-up was thermostated at 25 °C.

3. Results and discussions

3.1. Production and characterization of nanoporous silver

The architectural design of nanoporous silver in this work was based on the composition and structure previously elaborated by our group [56]. However, the aim was to improve the mechanical stability, and to produce self-supporting electrodes that enable their use in electrocatalysis. Firstly, $Ag_{38.75}Cu_{38.75}Si_{22.5}$ alloys were produced using the planar flow casting technique aiming to obtain wider and thicker amorphous ribbons. The low glass forming ability of this system has disallowed the production of samples with amorphous structure and desired properties. Then, sets of crystalline ribbons of composition $Ag_{38.75}Cu_{38.75}Si_{22.5}$ were obtained by melt spinning in helium atmosphere with rotation speeds of 14–28 m/s. The foils had widths of ~2 mm. According to the rotation speed, their thickness varied within the range of 20 to 60 μm. The sample with the thickness of 20 μm was chosen for further chemical treatment. Its X-ray diffraction (XRD) pattern (Fig. 1) confirmed that the majority of the samples was composed by the crystalline face-centered cubic silver and the hexagonal η Cu_3Si phase.

Fig. 2 represents a SEM micrograph obtained after 10 min of etching of the as cast selected sample in 3.32 M of HNO3 solution. It reveals an irregular morphology and difficulties for solution penetration, without a well-defined tridimensional porous structure. Compositional analysis based on energy dispersive X-ray spectroscopy (EDS) confirmed that the atomic concentration of the residual Si atoms was ~19 at.%.

Another etching solution: a mixture of 0.67 M of HNO_3 and 0.64 M of HF, was tested for as spun ribbons in order to accelerate the dissolution of the Si atoms. The etching time of 45 min was selected as an optimal time to generate a fairly regular porous structure (Figs. 3 a, b).

A 3D-architecture was readily produced, leaving in the center a thin carcass layer of few microns thick (Fig. 3c). This carcass will play a load-bearing function of the material. After etching, XRD analysis reveals only the presence of fcc-Ag (Fig. 3d).

Fig. 4a confirms this finding. The chemical analysis, performed on the cross-section of ribbons before and after etching, reveals that all the copper and silicon have been removed after etching (although traces may subsist, below the detection limit of the EDS analyses). After longer etching time, Ag crystallites start agglomerating and the porous network of the crystalline precursor collapses, leaving a sponge-like structure, as presented in Fig. 4b.

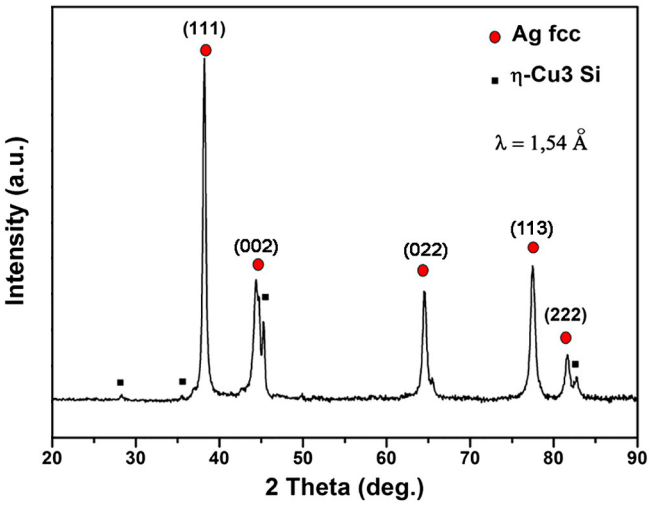

Fig. 1. XRD pattern of as cast $Ag_{38.75}Cu_{38.75}Si_{22.5}$ ribbon.

The higher chemical stability of Ag in the given acid media, in contrast to copper and silicon, is supported by the difference between standard electrode potentials of the pure elements, which, in fact, globally reflects the material nature: φ_0 Ag = 0.799 V > φ_0 Cu = 0.337 V > φ_0 Si = −0.91 V. All the values here are given according to the hydrogen scale [59].

By using image analysis, the average surface pore size is calculated as ~98 nm. The ligaments on the surface are very similar. Their direct dimensions measurements gave the average values of ~80 nm and ~250 nm for the width and length, respectively. The quality of such geometry appears to be inferior to the one obtained using an amorphous precursor of the same composition, which is characterized by regular pore size distribution and its smaller dimensions (Fig. 5). Nevertheless, porosity was analyzed by the method of Brunauer, Emmet and Teller (BET) [60]. Fig. 6 presents the pore size distribution of such measurement. Almost 76% in volume of pores falls in a wide range of size distribution, between 4 and 102 nm. As one can observe, the size of the pores tangibly decreases going towards the bulk. It is expected that greater pore size will prevail on the surface (which is consistent with the image analyses above) while the finest ones in the interior of the foil, thus creating a sort of porosity gradient from the bulk (interior) to the surface (exterior) of the ribbons.

In the above sense, the obtained architecture, which usually consists of interconnected networks, appears to be the ideal for catalyst

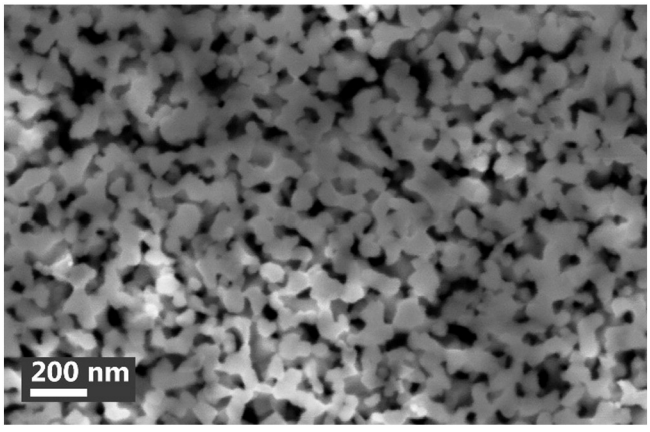

Fig. 2. SEM image of a porous Ag-based pattern after dealloying in nitric acid solution for 10 min.

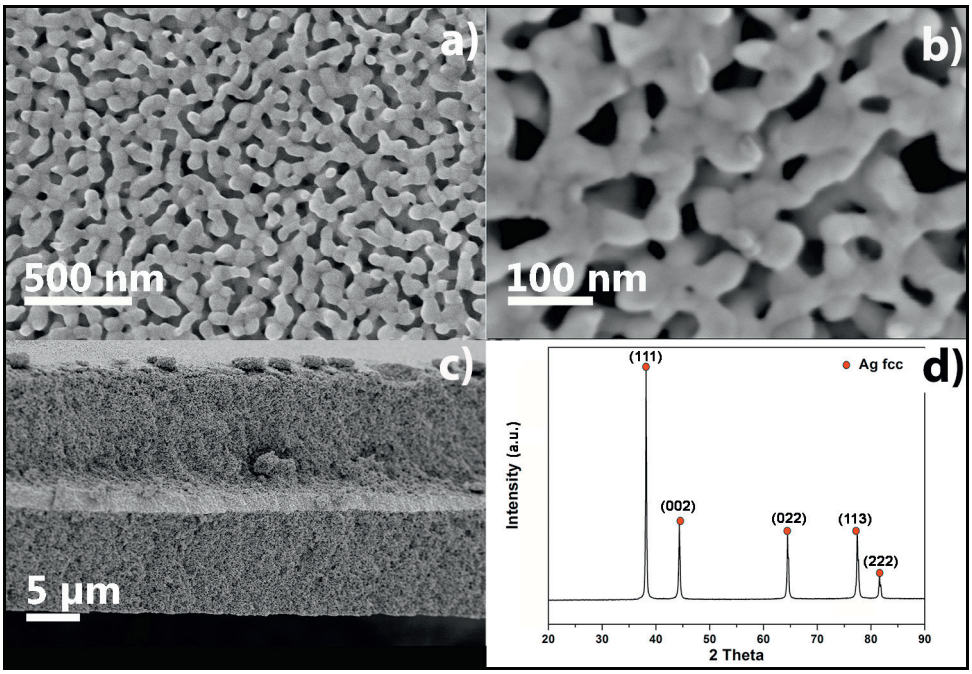

Fig. 3. a), b) Surface view of the final porous microstructure c) Cross section view of the dealloyed ribbon with a bulk non-etched carcass layer in the middle d) XRD pattern of as-dealloyed $Ag_{38.75}Cu_{38.75}Si_{22.5}$ ribbons.

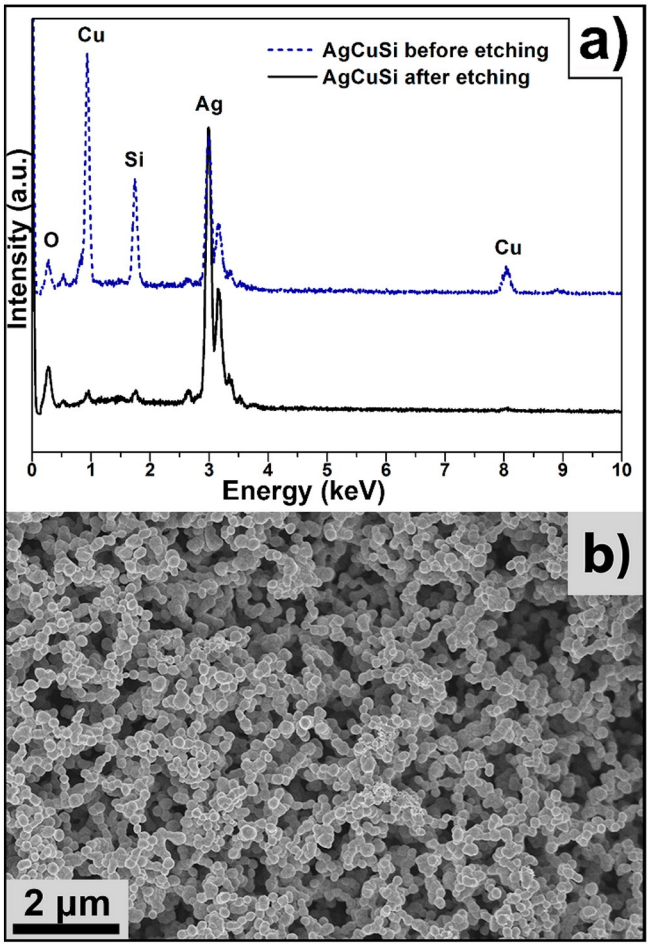

Fig. 4. a) EDS spectra obtained on of the cross section of the foil before and after dealloying in the solution of mixed nitric and hydrofluoric acids for 45 min. b) SEM image of a sponge-like silver based structure after 2 h etching.

materials. In other words, the smaller pores will have the largest surface area. They will be the responsible for most of the catalytic reactions, while the larger pores will facilitate both fuel access and gas release, a strategy already used with success by the group of Atanassov for the alkaline oxidation of several fuels [50–52,61–65]. The total surface area calculated by BET is ~5 m^2/g. The average pore size of 36 nm was calculated by the Barrett-Joyner-Halenda (BJH) method, which uses the Kelvin Model for pore-filling, being applicable to the present type of material [66]. Eventually, the final material presented a huge total surface area, and better integrity makes it possible to apply this material as a self-supporting electrode, allowing to perform electroactivity measurements in the scope of the present work. The corresponding data are discussed below.

3.2. Electrochemical test

The electrocatalytic performance of porous silver for the direct electrooxidation of ammonia borane in an alkaline medium is presented

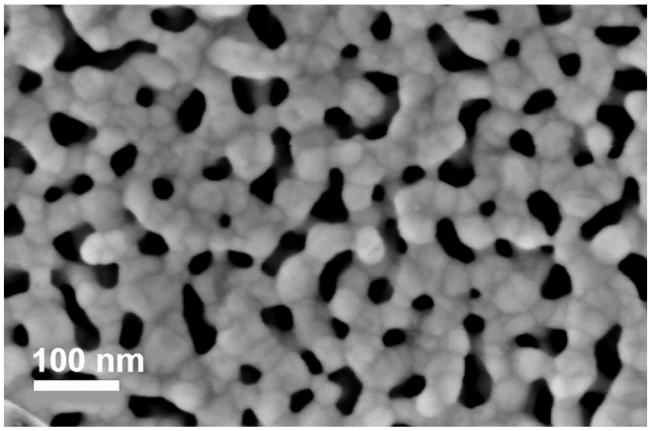

Fig. 5. Nanoporous silver, obtained from the amorphous $Ag_{38.75}Cu_{38.75}Si_{22.5}$ precursor [56].

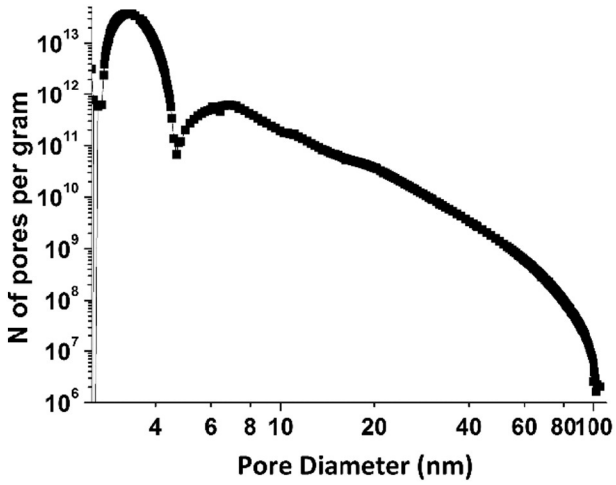

Fig. 6. Pore size distribution measured by BET.

on Fig. 7. The cyclic voltamperogram of the nanoporous Ag substrate in the supporting electrolyte (0.1 M NaOH) reveals the nature of the silver surface (black curve – this voltamperogram being unaffected by the revolution rate of the rotating disk electrode). The large anodic peak centered at ca. $E = 0.41$ V results from the formation of surface silver oxides. The formation of copper oxides from residual copper coming from the bulk layer in the middle of the sample (Fig. 3c) may also occur in this anodic peak. During the subsequent negative scan, the cathodic reduction of silver oxide proceeds, producing a peak centered at ca. 0.36 V. It is also likely that copper oxides are reduced in this potential domain, as attested by the electrochemical equilibrium between Cu and Cu_2O, expected to thermodynamically proceed around $E = 0.471$ vs. RHE [67]. Further discussion regarding copper will be given in the following sections.

The addition of 5 mM of ammonia-borane into the solution noticeably modifies the shape of the cyclic voltammogram, and the obtained shape is strongly depending on the revolution rate of the rotating disk electrode. An oxidation current is observed on the whole potential domain investigated, its magnitude being much larger under diffusion convection regime ($\omega = 1600$ rpm, upper red curve in Fig. 7, round symbols) than on a static electrode ($\omega = 0$ rpm, lower red curve in Fig. 7, triangle symbols). The reaction begins at a very low potential

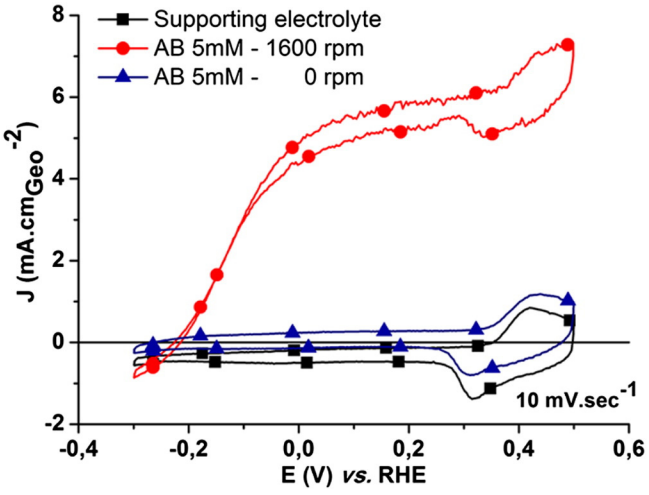

Fig. 7. Electrocatalytic performances of nanoporous silver for direct ammonia borane electrooxidation in 0.1 M NaOH (black) and 0.1 M NaOH + 5 mM AB (blue), at w = 0 and w = 1600 rpm (red). All experiments were performed at 25 °C. (For interpretation of the references to color in this figure legend, the reader is referred to the web version of this article.)

value, much lower than the hydrogen oxidation potential. Indeed, the onset for the electrooxidation of ammonia-borane is about $E = -0.3$ V vs. RHE (300 mV below the oxidation of hydrogen in a hydrogen-fed fuel cell), which is of utmost interest for energy production in direct alkaline fuel cells. The kinetic is relatively fast according to the steep slope of the wave in the region up to 0.3 V vs. RHE. Then, the AB oxidation current density reaches a stable maximum value of 6,44 mA/cm^2 at about 0.3 V vs. RHE. These values are better than the ones observed for NPGold in 1 M NaOH containing higher concentration in ammonia-borane (20 mM) or $NaBH_4$ the onset potential for the electrooxidation of $NaBH_4$: on NPGold was at best as high as ca 0.1 V vs. RHE [68], while that of AB electrooxidation could reach −0.2 V vs. RHE [19], i.e. was at best shifted positive by 0.1 V compared to the best results with the present nanoporous Ag.

Comparing the voltamperograms after addition of 5 mM of ammonia-borane ($\omega = 0$ rpm and $\omega = 1600$ rpm) in Fig. 7, one clearly sees that the reaction is controlled by mass-transport. Fig. 8.a further presents the effect of the rotation rate of the electrode on the electrocatalytic performance measured at $E = 0$ V vs. RHE (i.e. at an electrode potential where a classical H_2-oxidation electrode would not release any quantitative current, which demonstrates the interest of AB oxidation at NPS electrodes); the faster the electrode is rotated, the higher the current density value, in agreement with the Levich theory. This dependency on the mass-transport means that the NPS electrode is indeed a good AB oxidation catalyst (it is not limited by charge-transfer kinetics, even at a potential as low as 0 V vs. RHE and at 25 °C); on the contrary, it

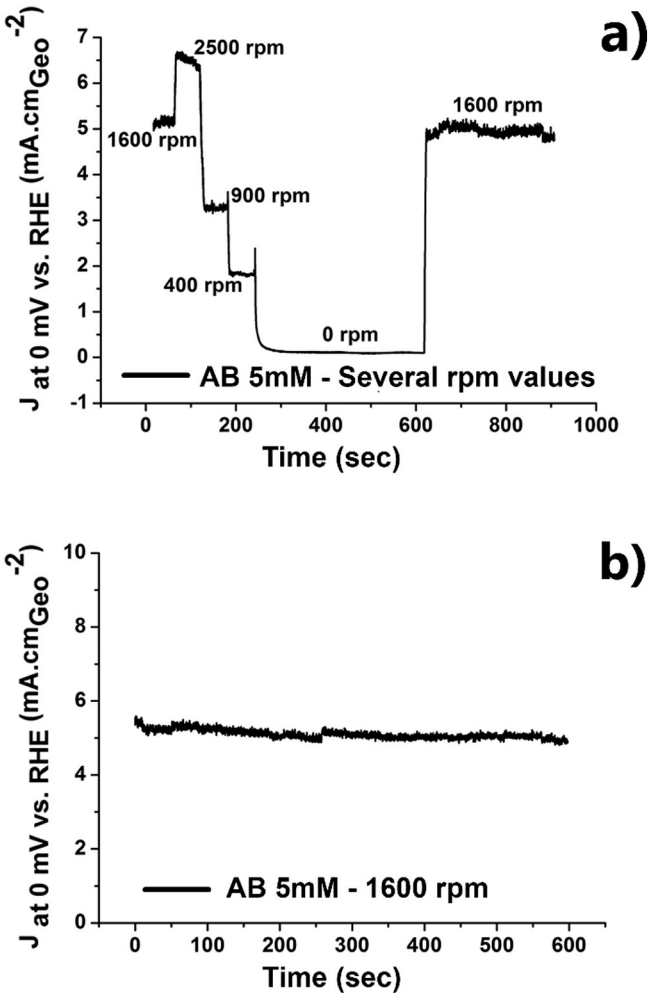

Fig. 8. a) Effect of the electrode's rotation speed and b) Signal stability, for direct Ammonia Borane electrooxidation. All performed in 0.1 M NaOH + 5 mM AB, at 0 V vs. RHE and 25 °C.

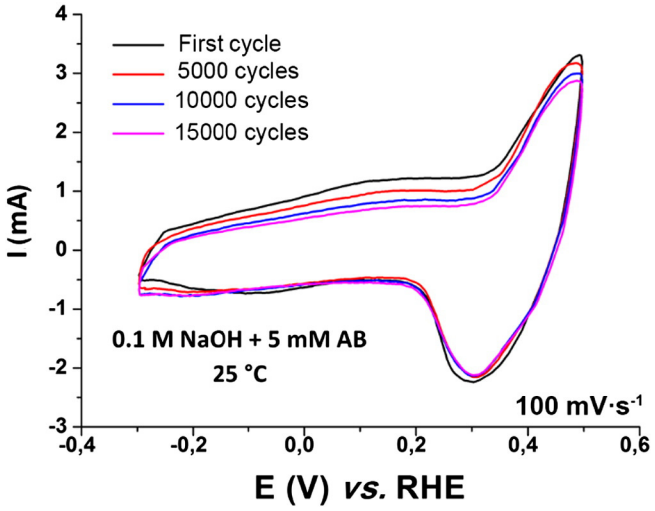

Fig. 9. Cyclic voltammetries of NPS material after 0, 5000, 10,000 and 15,000 cycles in 0.1 M NaOH + 5 mM AB at 100 mV/s and 25 °C.

implies that the fluidics of the DABFC systems should be considered with care (but this is beyond the focus of the present contribution). Besides the normal "Levich behavior", the design of our rotating electrode can account to some extent to the mass-transport effect observed. The NPS is inserted at a position about 2 mm deep in a cylindrical shape gap, overall limiting the access of "fresh fuel" to the NPS surface. In addition, stagnant AB electrolytes are prone to severe heterogeneous hydrolysis at the NPS electrode; indeed, we observed hydrogen gas bubbles being stacked in the gap. Besides consuming the AB fuel and only being prone to be oxidized above $E = 0$ V vs. RHE, the presence of such H_2 bubbles may interrupt the contact between the NPS catalyst and the AB solution, resulting in lower oxidation current. In any of these cases, the performance of the NPS electrode is improved by increasing the revolution rate of the rotating disk electrode: doing so firstly enables the access of "fresh AB" fuel and secondly favors the removal of hydrogen gas bubbles. It has to be noted that, whatever the steps of revolution rates, the current density increases/decreases rapidly as soon as the rotation of the working electrode is changed, denoting for the absence of poisoning/deactivation of the NPS electrode in the course of the AB oxidation. Besides, the two sequences measured at $\omega = 1600$ rpm demonstrate that the NPS proceeds without any quantitative loss in activity versus time (within the time frame of the present experiments).

The stability of the oxidation reaction current was further analyzed; samples were held at $E = 0$ V vs. RHE (Fig. 8.b) for 10 min. The NPS electrode presents a stable short-term activity for AB oxidation; this is promptly observable by the very small loss of activity during the period of tests, represented by the small decrease in the oxidation current density and rules out any severe effect of poisoning of the Ag surface by reaction intermediates, as shown for the electrooxidation of $NaBH_4$ at Pt surfaces [17,69,70].

In addition, the structural stability of the nanoporous silver and its AB oxidation activity have been investigated for long-term operation (the accelerated stress test, AST, consisted of up to 15,000,000 voltamperometric cycles between −0.3 and 0.5 V vs. RHE at 100 mV/s) in the same electrolyte (0.1 M NaOH + 5 mM AB, at 25 °C). Cyclic voltammograms and representative SEM images are given in Figs. 9 and 10, respectively. In Fig. 9, one can clearly see that the behavior of nanoporous silver remains similar even after 15,000 cycles; only minor diminution of the anodic current density values can be observed by cycling in the electrolyte: it is a consequence of the ammonia-borane rarefaction in the electrolyte due to its progressive consumption at the working electrode. In spite of this globally decreasing anodic current contribution from AB oxidation, there are no major changes in the equilibrium between the silver/silver oxides (and possibly copper/copper oxides) peaks and for the capacitive current values (in particular, the silver (and copper) oxides reduction peak at ca.

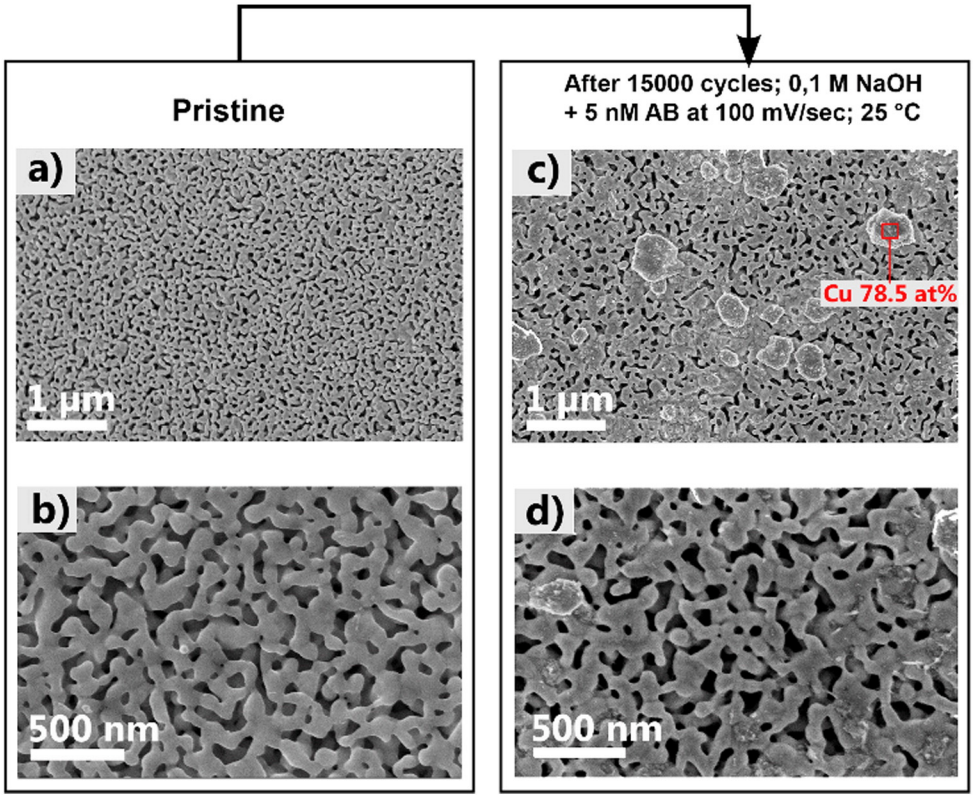

Fig. 10. SEM images of porous silver before (a.–b.) and after (c.–d.) 15,000 Cyclic voltammetries performed between −0.3 and 0.5 V vs. RHE at 100 mV/s in 0.1 M NaOH + 5 mM AB, at 25 °C.

0.3 V vs. RHE in the negative sweep, which is not biased by the AB oxidation current is literally unchanged from the 1st to 15,000th cycle of the AST); this indicates that neither metal dissolution, nor active surface area loss, nor structural changes of the silver nanoporous do happen during the cycling. As one can observe in Fig. 10, there are neither significant changes in the morphology of the ligaments or pores of the NPS material after this accelerated stress test. The conjunction of these two results suggests the chemical and electrochemical stabilities of the catalyst in long-term operation. Nevertheless, occasional agglomerates have appeared on the electrode surface. EDS analyses demonstrate that they are rich in copper; such copper-rich islands were not observed for the fresh electrode. Copper has therefore migrated from the bulk to the surface of the sample in the course of the aging test. This, in fact confirms that the oxidation/reduction peaks observed around 0.4 V vs. RHE in Fig. 7 are related both to silver (majorly) and copper (minorly). Copper necessarily comes from the bulk layer in the middle of the sample (Fig. 3c) where the alloying elements (Cu and Si) remained unaltered after the leaching procedure.

However, such changes are overall very minor and the porosity of the NPS sample remains essentially unaltered even after 15,000 cycles; this stability is already larger than what has been observed for noble electrocatalysts of platinum nanoparticles supported on high surface area carbon as previously reported in [12,13].

In addition, such dissolution (from the bulk of the NPS sample) and precipitation (at its surface) of Cu-rich agglomerates is another indication that the whole NPS sample is accessible to reactants, owing to its porous architecture. If such diffusion of Cu atoms/ions from the bulk to the surface of the NPS proceeds, it is likely that AB and its oxidation products can do as well, in agreement with the good electrochemical performances monitored above. To be more specific, the porous architecture of the NPS, formed by the conjunction of very small channels in diameter with large surface area in the middle, channels which enlarge in diameter towards the surface, facilitate the intrusion of the AB-containing liquid solution and the release of the hydrogen bubbles possibly formed from heterogeneous hydrolysis and other AB oxidation products. These textural properties coupled to the intrinsic ability of Ag to promote AB oxidation reaction enable to understand the steep wave monitored on Fig. 7, indicating large overall AB oxidation activity.

From these results, NPS seems both very active and durable for the direct electrooxidation of ammonia-borane in alkaline medium. In addition, the residuals of the secondary η-phase in the final porous structure do not perturbate the oxidation process of AB, which means that material does not require any remarkable purity level in order to be exploited in real conditions.

4. Summary and conclusions

Foils of nanoporous silver were synthesized from a crystalline $Ag_{38.75}Cu_{38.75}Si_{22.5}$ precursor by free corrosion in an acid solution. Further, by controlling the etching parameters, nanoporous silver foils were designed to have a thick nanoporous layer and a bulk thin layer of the nominal composition, which contributed to their mechanical stability a clear advantageous for application in self-supporting catalysts. It is for the first time that NPS foils have been successfully tested as an active and stable material for direct ammonia-borane electrooxidation in an alkaline medium, which was not possible for its nanoporous analogue, produced from amorphous precursor (the material could not self-stand and could not be handled to prepare electrodes). Moreover, the material appeared to be competitive to nanoporous gold substrate, and economically is more advantageous, owing to the smaller cost and larger availability of silver compared to gold. The architecture of the present porous material follows the design of the most modern current catalysts. These are formed by very small pore channels, in which the reaction will occur due to the extremely active large surface area and increased pore channel diameters going towards to the surface, which favors both liquid and gas transportation.

The results presented in this work are inspiring and they open optimistic prospects for nanoporous silver and likely for other cheaper transition metal-based materials for their direct application in fuel cells as a lower-cost integral/ergonomic alternative for platinum nanoparticles supported on high surface area carbon materials.

Author contributions

All authors have given approval to the final version of the manuscript.

Funding sources

This work was partially supported by the European ITN Network project “VitriMetTech” (grant No. FP7-PEOPLE-2013-ITN-607080) in frames of Marie Sklodowska-Curie actions program; and by the Rhône-Alpes Academic Research Community l'ARC Energies (grant No. 13-009671-01).

Acknowledgment

A. Zadick acknowledges Centre of Excellence of Multifunctional Architectured Materials “CEMAM”, project No. AN-10-LABX-44-01. M. Chatenet thanks the French IUF for its support. A. M. Jorge Junior thanks Fundação de Amparo à Pesquisa do Estado de São Paulo (Brazil), Grant No. FAPESP# 2012/13179–6. Authors are grateful to the specialists of the characterization platform CMTC of Grenoble for careful measurements and discussion.

This work is dedicated to the memory of Prof Alain Reza Yavari, who was a mentor and insightful supervisor for some of the authors (DB, KG, NTP, AMJ).

Supplementary data

The supporting information includes EDS data on the material, dealloyed for 10 min in 13,4 wt% HNO_3 solution. Optical images of as-cast and dealloyed material, and images exhibiting structure evolution with the dealloying time. Supplementary data associated with this article can be found in the online version, at http://dx.doi.org/10.1016/j.matdes.2016.09.037.

References

[1] M. Dresselhaus, G. Crabtree, M. Buchanan (Eds.), Basic Energy Needs for the Hydrogen Economy, Washington, DC, 2003.
[2] Targets for Onboard Hydrogen Storage Systems for Light-Duty Vehicles, 5, 2009 http://www1.eere.energy.gov/hydrogenandfuelcells/storage/pdfs/targets_onboard_hydro_storage_explanation.pdf (accessed March 20, 2016).
[3] M.E. Bluhm, M.G. Bradley, R. Butterick, U. Kusari, L.G. Sneddon, Amineborane-based chemical hydrogen storage: enhanced ammonia borane dehydrogenation in ionic liquids, J. Am. Chem. Soc. 128 (2006) 7748–7749, http://dx.doi.org/10.1021/ja062085v.
[4] F. Baitalow, J. Baumann, G. Wolf, K. Jaenicke-Rößler, G. Leitner, Thermal decomposition of B–N–H compounds investigated by using combined thermoanalytical methods, Thermochim. Acta 391 (2002) 159–168, http://dx.doi.org/10.1016/S0040-6031(02)00173-9.
[5] C.A. Jaska, K. Temple, A.J. Lough, I. Manners, Transition metal-catalyzed formation of boron–nitrogen bonds: catalytic dehydrocoupling of amine-borane adducts to form aminoboranes and borazines, J. Am. Chem. Soc. 125 (2003) 9424–9434, http://dx.doi.org/10.1021/ja030160l.
[6] F.H. Stephens, R.T. Baker, M.H. Matus, D.J. Grant, D.A. Dixon, Acid initiation of ammonia–borane dehydrogenation for hydrogen storage, Angew. Chem. Int. Ed. 46 (2007) 746–749, http://dx.doi.org/10.1002/anie.200603285.
[7] M. Chandra, Q. Xu, A high-performance hydrogen generation system: transition metal-catalyzed dissociation and hydrolysis of ammonia–borane, J. Power Sources 156 (2006) 190–194, http://dx.doi.org/10.1016/j.jpowsour.2005.05.043.
[8] M. Chandra, Q. Xu, Room temperature hydrogen generation from aqueous ammonia-borane using noble metal nano-clusters as highly active catalysts, J. Power Sources 168 (2007) 135–142, http://dx.doi.org/10.1016/j.jpowsour.2007.03.015.
[9] J. Hannauer, O. Akdim, U.B. Demirci, C. Geantet, J.-M. Herrmann, P. Miele, Q. Xu, High-extent dehydrogenation of hydrazine borane $N_2H_4BH_3$ by hydrolysis of BH_3 and decomposition of N_2H_4, Energy Environ. Sci. 4 (2011) 3355, http://dx.doi.org/10.1039/c1ee01886h.

[10] J. Hannauer, U.B. Demirci, C. Geantet, J.-M. Herrmann, P. Miele, Transition metal-catalyzed dehydrogenation of hydrazine borane $N_2H_4BH_3$ via the hydrolysis of BH_3 and the decomposition of N_2H_4, Int. J. Hydrog. Energy 37 (2012) 10758–10767, http://dx.doi.org/10.1016/j.ijhydene.2012.04.102.

[11] A. Yousef, N.A.M. Barakat, M.H. EL-Newehy, M.M. Ahmed, H.Y. Kim, Catalytic hydrolysis of ammonia borane for hydrogen generation using Cu(0) nanoparticles supported on TiO_2 nanofibers, Colloids Surf. A Physicochem. Eng. Asp. 470 (2015) 194–201, http://dx.doi.org/10.1016/j.colsurfa.2015.02.004.

[12] A. Zadick, L. Dubau, M. Chatenet, U. Demirci, A. Serov, P. Atanassov, Instability of commercial Pt/C and Pd/C electrocatalysts in alkaline media, ECS Trans. 69 (2015) 553–558, http://dx.doi.org/10.1149/06917.0553ecst.

[13] A. Zadick, L. Dubau, N. Sergent, G. Berthomé, M. Chatenet, Huge instability of Pt/C catalysts in alkaline medium, ACS Catal. 5 (2015) 4819–4824, http://dx.doi.org/10.1021/acscatal.5b01037.

[14] A. Zadick, L. Dubau, U.B. Demirci, M. Chatenet, Effects of Pd nanoparticle size and solution reducer strength on Pd/C electrocatalyst stability in alkaline electrolyte, J. Electrochem. Soc. 163 (2016) F781–F787, http://dx.doi.org/10.1149/2.0141608jes.

[15] L.C. Nagle, J.F. Rohan, Ammonia borane oxidation at gold microelectrodes in alkaline solutions, J. Electrochem. Soc. 153 (2006) C773, http://dx.doi.org/10.1149/1.2344842.

[16] E.H. Yu, X. Wang, U. Krewer, L. Li, K. Scott, Direct oxidation alkaline fuel cells: from materials to systems, Energy Environ. Sci. 5 (2012) 5668–5680, http://dx.doi.org/10.1039/C2EE02552C.

[17] J. Durst, A. Siebel, C. Simon, F. Hasché, J. Herranz, H.A. Gasteiger, New insights into the electrochemical hydrogen oxidation and evolution reaction mechanism, Energy Environ. Sci. 7 (2014) 2255, http://dx.doi.org/10.1039/c4ee00440j.

[18] P.-Y. Olu, F. Deschamps, G. Caldarella, M. Chatenet, N. Job, Investigation of platinum and palladium as potential anodic catalysts for direct borohydride and ammonia borane fuel cells, J. Power Sources 297 (2015) 492–503, http://dx.doi.org/10.1016/j.jpowsour.2015.08.022.

[19] L.C. Nagle, J.F. Rohan, Nanoporous gold catalyst for direct ammonia borane fuel cells, J. Electrochem. Soc. 158 (2011) B772, http://dx.doi.org/10.1149/1.3583637.

[20] M. Belén Molina Concha, M. Chatenet, F.H.B. Lima, E.A. Ticianelli, In situ Fourier transform infrared spectroscopy and on-line differential electrochemical mass spectrometry study of the NH3BH3 oxidation reaction on gold electrodes, Electrochim. Acta 89 (2013) 607–615, http://dx.doi.org/10.1016/j.electacta.2012.11.027.

[21] X. Zhang, S. Han, J. Yan, H. Shioyama, N. Kuriyama, T. Kobayashi, Q. Xu, Electrochemical oxidation of ammonia borane on gold electrode, Int. J. Hydrog. Energy 34 (2009) 174–179, http://dx.doi.org/10.1016/j.ijhydene.2008.09.083.

[22] K. Shimizu, A. Satsuma, Silver cluster catalysts for green organic synthesis, J. Japan Pet. Inst. 54 (2011) 347–360, http://dx.doi.org/10.1627/jpi.54.347.

[23] T.A. Luft, www.strem.com http://www.strem.com/uploads/technical_notes/47-0645tech.pdf accessed February 7, 2016.

[24] E. Detsi, M.S. Sellès, P.R. Onck, J.T.M. De Hosson, Nanoporous silver as electrochemical actuator, Scr. Mater. 69 (2013) 195–198, http://dx.doi.org/10.1016/j.scriptamat.2013.04.003.

[25] T. Spassov, L. Lyubenova, Y. Liu, S. Bliznakov, M. Spassova, N. Dimitrov, Mechanochemical synthesis, thermal stability and selective electrochemical dissolution of Cu–Ag solid solutions, J. Alloys Compd. 478 (2009) 232–236, http://dx.doi.org/10.1016/j.jallcom.2008.12.005.

[26] M. Chatenet, F. Micoud, I. Roche, E. Chainet, J. Vondrák, Kinetics of sodium borohydride direct oxidation and oxygen reduction in sodium hydroxide electrolyte, Electrochim. Acta 51 (2006) 5452–5458, http://dx.doi.org/10.1016/j.electacta.2006.02.014.

[27] H. Cheng, K. Scott, Investigation of non-platinum cathode catalysts for direct borohydride fuel cells, J. Electroanal. Chem. 596 (2006) 117–123, http://dx.doi.org/10.1016/j.jelechem.2006.07.031.

[28] E. Sanli, H. Celikkan, B. Zuhtyuusal, M. Aksu, Anodic behavior of Ag metal electrode in direct borohydride fuel cells, Int. J. Hydrog. Energy 31 (2006) 1920–1924, http://dx.doi.org/10.1016/j.ijhydene.2006.04.003.

[29] M.H. Atwan, D.O. Northwood, E.L. Gyenge, Evaluation of colloidal Ag and Ag-alloys as anode electrocatalysts for direct borohydride fuel cells, Int. J. Hydrog. Energy 32 (2007) 3116–3125, http://dx.doi.org/10.1016/j.ijhydene.2005.12.022.

[30] E. Sanli, B.Z. Uysal, M.L. Aksu, The oxidation of NaBH4 on electrochemicaly treated silver electrodes, Int. J. Hydrog. Energy 33 (2008) 2097–2104, http://dx.doi.org/10.1016/j.ijhydene.2008.01.049.

[31] J. Erlebacher, M.J. Aziz, A. Karma, N. Dimitrov, K. Sieradzki, Evolution of nanoporosity in dealloying, Nature 410 (2001) 450–453, http://dx.doi.org/10.1038/35068529.

[32] J. Erlebacher, An atomistic description of dealloying, J. Electrochem. Soc. 151 (2004) C614, http://dx.doi.org/10.1149/1.1784820.

[33] J. Zhang, H. Ma, D. Zhang, P. Liu, F. Tian, Y. Ding, Electrocatalytic activity of bimetallic platinum–gold catalysts fabricated based on nanoporous gold, Phys. Chem. Chem. Phys. 10 (2008) 3250, http://dx.doi.org/10.1039/b718192b.

[34] M. Zhang, M.P. Li, T. Yin, T. Zhang, Fabrication of nanoporous bi-metallic Ag–Pd alloys with open pores, Mater. Lett. 162 (2016) 273–276, http://dx.doi.org/10.1016/j.matlet.2015.10.014.

[35] C. Xu, R. Wang, M. Chen, Y. Zhang, Y. Ding, Dealloying to nanoporous Au/Pt alloys and their structure sensitive electrocatalytic properties, Phys. Chem. Chem. Phys. 12 (2010) 239–246, http://dx.doi.org/10.1039/B917788D.

[36] C. Xu, L. Wang, X. Mu, Y. Ding, Nanoporous PtRu alloys for electrocatalysis, Langmuir 26 (2010) 7437–7443, http://dx.doi.org/10.1021/la9041474.

[37] S. Van Petegem, S. Brandstetter, R. Maass, A.M. Hodge, B.S. El-Dasher, J. Biener, B. Schmitt, C. Borca, H. Van Swygenhoven, On the microstructure of nanoporous gold: an X-ray diffraction study, Nano Lett. 9 (2009) 1158–1163, http://dx.doi.org/10.1021/nl803799q.

[38] J. Biener, G.W. Nyce, A.M. Hodge, M.M. Biener, A.V. Hamza, S.A. Maier, Nanoporous plasmonic metamaterials, Adv. Mater. 20 (2008) 1211–1217, http://dx.doi.org/10.1002/adma.200701899.

[39] L. Liu, R. Scholz, E. Pippel, U. Gösele, Microstructure, electrocatalytic and sensing properties of nanoporous $Pt_{46}Ni_{54}$ alloy nanowires fabricated by mild dealloying, J. Mater. Chem. 20 (2010) 5621, http://dx.doi.org/10.1039/c0jm00113a.

[40] V. Zielasek, B. Jürgens, C. Schulz, J. Biener, M.M. Biener, A.V. Hamza, M. Bäumer, Gold catalysts: nanoporous gold foams, Angew. Chem. Int. Ed. 45 (2006) 8241–8244, http://dx.doi.org/10.1002/anie.200602484.

[41] A. Wittstock, B. Neumann, A. Schaefer, K. Dumbuya, C. Kübel, M.M. Biener, V. Zielasek, H.-P. Steinrück, J.M. Gottfried, J. Biener, A. Hamza, M. Bäumer, Nanoporous Au: an unsupported pure gold catalyst? J. Phys. Chem. C 113 (2009) 5593–5600, http://dx.doi.org/10.1021/jp808185v.

[42] M. Yan, Development of New Catalytic Performance of Nanoporous Metals for Organic Reactions, Springer, Japan, 2014, http://dx.doi.org/10.1007/978-4-431-54931-4.

[43] D. Kramer, R.N. Viswanath, J. Weissmüller, Surface-stress induced macroscopic bending of nanoporous gold cantilevers, Nano Lett. 4 (2004) 793–796, http://dx.doi.org/10.1021/nl049927d.

[44] J. Biener, a. Wittstock, L.a. Zepeda-Ruiz, M.M. Biener, V. Zielasek, D. Kramer, R.N. Viswanath, J. Weissmüller, M. Bäumer, a.V. Hamza, Surface-chemistry-driven actuation in nanoporous gold, Nat. Mater. 8 (2009) 47–51, http://dx.doi.org/10.1038/nmat2335.

[45] L.Y. Chen, J.S. Yu, T. Fujita, M.W. Chen, Nanoporous copper with tunable nanoporosity for SERS applications, Adv. Funct. Mater. 19 (2009) 1221–1226, http://dx.doi.org/10.1002/adfm.200801239.

[46] H. Qiu, Z. Zhang, X. Huang, Y. Qu, Dealloying Ag-Al alloy to prepare nanoporous silver as a substrate for surface-enhanced Raman scattering: effects of structural evolution and surface modification, ChemPhysChem 12 (2011) 2118–2123, http://dx.doi.org/10.1002/cphc.201100205.

[47] P. Ranga Reddy, K. Varaprasad, N. Narayana Reddy, K. Mohana Raju, N.S. Reddy, Fabrication of Au and Ag Bi-metallic nanocomposite for antimicrobial applications, J. Appl. Polym. Sci. 125 (2012) 1357–1362, http://dx.doi.org/10.1002/app.35192.

[48] L.Y. Chen, L. Zhang, T. Fujita, M.W. Chen, Surface-enhanced Raman scattering of silver@nanoporous copper core–shell composites synthesized by an in situ sacrificial template approach, J. Phys. Chem. C 113 (2009) 14195–14199, http://dx.doi.org/10.1021/jp904081s.

[49] T.N. Martin, Nanoporous and Thin Film Gold and Silver Metal Alloys and Their Medical Applications in Drug Delivery and Antimicrobial Activity, North Carolina State University, 2012.

[50] A. Zalineeva, A. Serov, M. Padilla, U. Martinez, K. Artyushkova, S. Baranton, C. Coutanceau, P.B. Atanassov, Self-supported Pd × Bi catalysts for the electrooxidation of glycerol in alkaline media, J. Am. Chem. Soc. 136 (2014) 3937–3945, http://dx.doi.org/10.1021/ja412429f.

[51] A. Zalineeva, A. Serov, M. Padilla, U. Martinez, K. Artyushkova, S. Baranton, C. Coutanceau, P. Atanassov, Nano-structured Pd-Sn catalysts for alcohol electro-oxidation in alkaline medium, Electrochem. Commun. 57 (2015) 48–51, http://dx.doi.org/10.1016/j.elecom.2015.05.006.

[52] A. Zalineeva, A. Serov, M. Padilla, U. Martinez, K. Artyushkova, S. Baranton, C. Coutanceau, P.B. Atanassov, Glycerol electrooxidation on self-supported Pd1Snx nanoparticules, Appl. Catal. B Environ. 176-177 (2015) 429–435, http://dx.doi.org/10.1016/j.apcatb.2015.04.037.

[53] C. Xu, Y. Li, F. Tian, Y. Ding, Dealloying to nanoporous silver and its implementation as a template material for construction of nanotubular mesoporous bimetallic nanostructures, ChemPhysChem 11 (2010) 3320–3328, http://dx.doi.org/10.1002/cphc.201000313.

[54] C. Xu, Y. Liu, F. Su, A. Liu, H. Qiu, Nanoporous PtAg and PtCu alloys with hollow ligaments for enhanced electrocatalysis and glucose biosensing, Biosens. Bioelectron. 27 (2011) 160–166, http://dx.doi.org/10.1016/j.bios.2011.06.036.

[55] Y. Jin, R. Li, T. Zhang, Formation of nanoporous silver by dealloying Ca–Ag metallic glasses in water, Intermetallics 67 (2015) 166–170, http://dx.doi.org/10.1016/j.intermet.2015.08.011.

[56] M. Zhang, A.M. Jorge Junior, S.J. Pang, T. Zhang, A.R. Yavari, Fabrication of nanoporous silver with open pores, Scr. Mater. 100 (2015) 21–23, http://dx.doi.org/10.1016/j.scriptamat.2014.11.040.

[57] E. Detsi, Z. Vuković, S. Punzhin, P.M. Bronsveld, P.R. Onck, J.T.M. De Hosson, Fine-tuning the feature size of nanoporous silver, CrystEngComm 14 (2012) 5402, http://dx.doi.org/10.1039/c2ce25313e.

[58] W.S. Rasband, U. S. Natl. Institutes Heal., Bethesda, Maryland, USA, 1997–2016 http://imagej.nih.gov/ij/ (accessed May 2, 2016).

[59] N.L. Glinka, General Chemistry, KNORUS, Moscow, 2009.

[60] P. Klobes, K. Meyer, R.G. Munro, Porosity and Specific Surface Area Measurements for Solid Materials, U.S. Government Printing Office, Washington, 2006 http://www.ncbi.nlm.nih.gov/pubmed/22544181.

[61] U. Martinez, K. Asazawa, B. Halevi, A. Falase, B. Kiefer, A. Serov, M. Padilla, T. Olson, A. Datye, H. Tanaka, P. Atanassov, Aerosol-derived Ni1–xZnx electrocatalysts for direct hydrazine fuel cells, Phys. Chem. Chem. Phys. 14 (2012) 5512, http://dx.doi.org/10.1039/c2cp40546f.

[62] A. Serov, U. Martinez, A. Falase, P. Atanassov, Highly active PdCu catalysts for electrooxidation of 2-propanol, Electrochem. Commun. 22 (2012) 193–196, http://dx.doi.org/10.1016/j.elecom.2012.06.023.

[63] T. Sakamoto, K. Asazawa, U. Martinez, B. Halevi, T. Suzuki, S. Arai, D. Matsumura, Y. Nishihata, P. Atanassov, H. Tanaka, Electrooxidation of hydrazine hydrate using Ni–La catalyst for anion exchange membrane fuel cells, J. Power Sources 234 (2013) 252–259, http://dx.doi.org/10.1016/j.jpowsour.2013.01.181.

[64] A. Serov, U. Martinez, P. Atanassov, Novel Pd–In catalysts for alcohols electrooxidation in alkaline media, Electrochem. Commun. 34 (2013) 185–188, http://dx.doi.org/10.1016/j.elecom.2013.06.003.
[65] T. Sakamoto, K. Asazawa, J. Sanabria-Chinchilla, U. Martinez, B. Halevi, P. Atanassov, P. Strasser, H. Tanaka, Combinatorial discovery of Ni-based binary and ternary catalysts for hydrazine electrooxidation for use in anion exchange membrane fuel cells, J. Power Sources 247 (2014) 605–611, http://dx.doi.org/10.1016/j.jpowsour.2013.08.107.
[66] Micromeritics, ASAP 2020 Accelerated Surface Area and Porosimetry System Operator's Manual, V4.01, http://www.cif.iastate.edu/sites/default/files/uploads/Other_Inst/BET/ASAP2020 Operator's Manual.pdf (accessed February 10, 2016).
[67] M. Pourbaix, Atlas d'équilibres électrochimiquesGauthier-V 1963.
[68] L.C. Nagle, J.F. Rohan, Nanoporous gold anode catalyst for direct borohydride fuel cell, Int. J. Hydrog. Energy 36 (2011) 10319–10326, http://dx.doi.org/10.1016/j.ijhydene.2010.09.077.
[69] P.-Y. Olu, C.R. Barros, N. Job, M. Chatenet, Electrooxidation of NaBH4 in alkaline medium on well-defined Pt nanoparticles deposited onto flat glassy carbon substrate: evaluation of the effects of Pt nanoparticle size, inter-particle distance, and loading, Electrocatalysis 5 (2014) 288–300, http://dx.doi.org/10.1007/s12678-014-0195-0.
[70] D.A. Finkelstein, C.D. Letcher, D.J. Jones, L.M. Sandberg, D.J. Watts, H.D. Abruña, Self-poisoning during BH 4 – oxidation at Pt and Au, and in situ poison removal procedures for BH 4 – fuel cells, J. Phys. Chem. C 117 (2013) 1571–1581, http://dx.doi.org/10.1021/jp308677f.

Abstract

New nanoporous metallic materials based on non-Pt group metals have been synthesized via dealloying of rapidly solidified alloys and aimed to demonstrate competitive catalytic performance in the field of direct alkaline fuel cells and SERS-active substrates. Nanostructured copper surface and nanoporous copper matrix with very fine morphology and specific surface area were obtained by chemical dealloying of bulk $Cu_{90}(HfZr)_{10}$ and melt-spun amorphous CuxCa100-x (x ranging from 35 to 80 at.%) family of alloys accordingly. Nanoporous silver and cobalt substrates were produced by dealloying of $M_{38,75}Cu_{38,75}Si_{22,5}$ crystalline ribbons (M = Co and Ag) as a result of the removal of Cu and Si-rich phases. In addition to conventional characterization methods, all nanoporous structures have been reconstructed by FIB-nanotomography, clearly exposing the morphological diversity of the three systems with transversal porosity when visualized and color-mapped in 3D by a special numerical tomography tool. It is for the first time that a practical significance of these materials has been explored in the scope of self-supported anodic catalysts, suggested throughout this study as an alternative to the unstable Pt-based carbon-supported commercial composites. Half-cell electrochemical tests demonstrated an excellent catalytic activity towards the oxidation of a borane fuel and superior stability of functioning in the alkaline environment compared to Pt/C catalyst. In similar conditions, nanoporous Co showed higher efficiency but lower stability, attributed to the complex chemical composition of its porous scaffold. Nanoporous Cu has not been exploited for the mentioned applications due to its high brittleness and is suggested to go through improvements on the step of precursor synthesis. Lastly, while exploring the mechanical behavior of the NPMs by instrumented nanoindentation of different nanoporous Ag substrates, a load-displacement dependence phenomenological model has been suggested for this class of metallic materials.

Keywords: Nanostructures, nanoporous, microstructures, microporosity, dealloying

Résumé

De nouveaux matériaux métalliques nanoporeux à base d'éléments n'appartenant pas à la famille du Pt ont été synthétisés par le "dealloying" (ou dissolution sélective) d'alliages rapidement solidifiés. L'objectif est d'examiner les propriétés catalytiques en vue d'utilisation dans des piles à combustible alcalines directes ou en tant que substrats actifs pour la spectroscopie SERS. Des surfaces et des matrices nanostructurées de cuivre de morphologie très fines et une forte surface spécifique ont été obtenues respectivement par le dealloying aqueux de rubans CuxCa100-x amorphe (35 <x< 80 % at.) et par le dellaoying chimique d'échantillons massifs de $Cu_{90}(HfZr)_{10}$. Des substrats nanoporeux d'Ag et de Co ont été produits par dealloying en retirant les phases riches en Cu et Si de rubans $M_{38,75}Cu_{38,75}Si_{22,5}$ cristallin (avec M = Co ou Ag). En complément des techniques de caractérisations conventionnelles, toutes les structures nanoporeuses ont pu être reconstruites par nanotomographie à partir de découpes FIB. Des outils numériques spécifiques à la nanotomographie de visualisation et de cartographie en 3 dimensions ont permis de révéler la diversité morphologique des trois systèmes avec la porosité traversante. Ces matériaux ont pour la première fois été étudiés pour leur utilisation pratique en tant que catalyseurs anodiques auto-supportés. Cette étude suggérent qu'ils constituent une alternative sérieuse aux composites commerciaux instables à base de Pt et supportés par du C. Des essais électrochimiques en demi-cellule ont montré une excellente activité catalytique vis-à-vis de l'oxydation d'un combustible en borane ainsi qu'une stabilité de fonctionnement supérieure dans un environnement alcalin en comparaison d'un catalyseur Pt/C. Le Co nanoporeux a montré dans des conditions similaires une meilleure efficacité mais une stabilité moindre, attribuée à la composition chimique complexe de son réseau poreux. Le Cu nanoporeux n'a pas été étudié pour les applications mentionnées précédemment en raison de sa grande fragilité. Il est suggéré d'améliorer la voie de synthèse de son précurseur pour augmenter sa tenue mécanique. Enfin le comportement mécanique de ces nouveaux matériaux métalliques nanoporeux a été abordé par des mesures de nanoindentation sur des substrats nanoporeux d'Ag. L'étude a permis de proposer un modèle phénoménologique de dépendance entre la charge et le déplacement pour cette classe de matériaux métalliques.

Mots clés : Nanostructures, nanoporeux, microstructures, microporosités, désalliage